UNIVERSITÉ DU QUÉBEC À TROIS-RIVIÈRES

CONCEPTION, SYNTHÈSES, PROPRIÉTÉS ET APPLICATIONS DES RÉSEAUX DE COORDINATION À BASE DE LIGANDS PYRIDONES

DESIGN, SYNTHESIS, PROPERTIES AND APPLICATIONS OF PYRIDONE BASED COORDINATION NETWORKS

THÈSE PRÉSENTÉE
COMME EXIGENCE PARTIELLE DU
DOCTORAT EN SCIENCES DE L'ÉNERGIE ET DES MATÉRIAUX

PAR
MIDHUN MOHAN

DÉCEMBRE 2020

UNIVERSITÉ DU QUÉBEC À TROIS-RIVIÈRES

DOCTORAT EN SCIENCES DE L'ÉNERGIE ET DES MATÉRIAUX (PH. D.)

Direction de recherche :

Adam Duong	Directeur de recherche

Jury d'évaluation de la thèse :

Adam Duong	Directeur de recherche
François Brouillette	Président de jury
Daniel Montplaisir	Évaluateur interne
Almir Oliveira Neto	Évaluateur externe

Thèse soutenue le 2 novembre 2020.

"Dream, Dream, Dream

Dreams transform into thoughts

And thoughts result in action.

Dream is not that which you see while sleeping,

It is something that does not let you sleep"

- A. P. J. Abdul Kalam

"Energy is this invisible link that connects everything;
the materials provide us the evidence"

DuongLab quote

ACKNOWLEDGEMENT

I would like to express my gratitude to my supervisor, Prof. Adam Duong, for his inspiring guidance, motivation, support and encouragement. His strenuous efforts and valuable advices for my endeavour without which it would have been impossible for me to complete this work in time.

My sincere gratitude for the thesis evaluation committee for their valuable time and suggestions. I take this opportunity to thank all my funding sources which made my Ph. D. dream possible. I thank the Queen Elizabeth Diamond Jubilee Scholarship for the financial support which I received for the duration of 3 years with which I arrived in Canada. After which, I was also supported by the *Fonds de Recherche du Québec – Nature et Technologies*. Apart from my Ph. D. funding, the works were also supported by the Natural Sciences and Engineering Research Council of Canada (RGPIN-2015-06425) and the Canada Foundation for Innovation.

I would like to express my sincere thanks to Dr. Thierry Maris from the *Université de Montréal* for his valuable support for my project work. Profound gratitude goes to Dr. Follivi Kloutse Ayevide for all the support and time he has spent with me along with the adsorption measurements. It was great fun to have discussions with him. I also thank David Durette for the simulation studies he conducted. On this occasion, I also thank Sarah Zaye for her great support through the projects she worked with me and for her willingness and patience over my mentorship. I would like to thank Mohamed Essalhi and Dr. Love Karan Rana for their collaborative works. I am thankful to all my past and present colleagues from DuongLab and specially Dr. Prabhjyot Kaur for the constructive suggestion and comment on my thesis. I take this opportunity to express my sincere thanks to all the members of the *Département de chimie, biochimie et physique* (DCBP),

Institut de Recherche sur l'hydrogène (IRH) and *Institut d'Innovations en Écomatériaux, Écoproduits et Écoénergies, à base de biomasse* (I2E3) for providing me with the facilities to carry out my works. My gratitude will never be complete without mentioning Dr. Sadesh Kumar Natarajan, Dr. Ahmed Hourri, Dr. Agnes Lejeune, Jocelyn Bouchard, Marie-Eve Marchand-Lamarche, Dr. Hatem Titi for the experiments and access to various instrumentations. A sincere thanks to Micromeritics Analysis services for the BET studies conducted. I am also thankful to my beloved friends and family in Canada and India for their love and support.

ABSTRACT

A steep rise in the demand of energy and technology has been an evident scenario which is addressed globally due to the exponential population growth. With the extensive use of fossil fuels and industrialization to develop these sectors, humans have caused adverse effects on the environment including global warming. As a result, the global climatic conditions have been altered which are evident from the annual temperature rise and reduction of lands due to the increasing sea levels caused by the melting of polar ice caps. This climate change is also the primary culprit for extinction of living beings both in mainland and aquatic. In many major cities as well as the nearby lands, pollution of air and waterbodies is so extreme that it has started to become uninhabitable. The perpetual growing demand for energy has also resulted in the depletion of fossil fuels which urges us to search for alternate clean and renewable energies. Thus, a great deal of research has been concentrated on the development of smart materials that can focus on these issues.

Coordination polymers play a key role in structuring novel smart materials due to the versatility in the available precursors which includes organic and inorganic species forming hybrid materials. A wide class of materials has been developed in the field of material chemistry due to the eclectic diversity of organic moieties with which the properties of the materials developed can be precisely controlled. Thus, designing of organic species predominantly influences the characteristics of the polymers. Inorganic species comprises of the metal ions or clusters forming the connectors between the organic linkers which also contributes to the properties exhibited by the materials and so, a judicious selection of metal component is needed to address various applications. Most importantly, these polymers can have predictable organizations depending on the precursors which facilitates the ease of the selection procedure.

The major concern on the coordination polymers being the thermal and chemical stability, we propose to use rigid, flat, poly-conjugated, nitrogen-rich aromatic systems as organic ligands. To explore this strategy, we have constructed organic moieties consisting of pyridonyl-based functionalities which include triple ring fused cyamelurate. Due to the versatility in number of coordination modes and similarity with carboxylate groups with addressing the issues related to the polymeric materials formed by the latter, these pose to be the best candidates that can form a new class of coordination polymers including Metal-Organic Frameworks. A series of pyridonyl-based bidentate ditopic and tritopic organic ligands were designed and synthesized which emphasize on the formation of coordination bonding with metal species. The ability of transition and lanthanide metals to have higher coordination numbers ease the formation of extended framework structures.

In this thesis, studies will be directed towards (i) the development of novel series of pyridonyl-based organic ligands with multiple coordination sites and the study of their self-assembly, (ii) rational design and synthesis of novel pyridone based coordination polymers with transition metals with chromic properties for sensing applications, (iii) synthesis of novel 2D Metal-Organic Frameworks using pyridone based organic ligands, (iv) rational design of nitrogen-rich lanthanide Metal-Organic Frameworks using cyamelurate ligand for gas selective separation.

Keywords: energy and technology, coordination polymers, Metal-Organic Frameworks, hybrid materials, supramolecular chemistry, pyridone, cyamelurate, selectivity.

RÉSUMÉ

Une forte augmentation de la demande en énergie et technologie à l'échelle mondiale en raison de la croissance exponentielle de la population est un scénario inévitable. Avec une utilisation extensive des combustibles fossiles et l'industrialisation pour développer ces secteurs, les humains ont causé des effets néfastes sur l'environnement, y compris le réchauffement climatique. En conséquence, les conditions climatiques mondiales ont été modifiées, ce qui se manifeste par l'augmentation annuelle de la température et la réduction de l'espace terrestre en raison de l'élévation du niveau de la mer causée par la fonte des glaces polaires. Elles sont également les principales responsables de l'extinction de certaines espèces vivantes à la fois sur le continent et en milieu aquatique. Dans de nombreuses grandes villes, la pollution de l'air et des plans d'eau sont extrêmes et commencent à devenir inhabitables. L'industrialisation et la consommation abusives de ces ressources non renouvelables ont entrainé l'épuisement des combustibles fossiles. De ce fait, il est primordial de trouver des énergies alternatives propres et renouvelables. Ainsi, de nombreuses recherches se concentrent sur le développement de matériaux avancés pour répondre à la demande en énergie.

Les polymères de coordination jouent un rôle clé dans le domaine de l'énergie en raison de la polyvalence des précurseurs disponibles, qui comprend des espèces organiques et inorganiques formant des matériaux hybrides avec diverses propriétés. Une large gamme de matériaux hybrides a été développée dont les propriétés peuvent être modifiées en variant les fragments organiques et inorganiques. Ainsi, la conception de ces fragments (organiques et inorganiques) constituant le matériau influence grandement son architecture et ses propriétés. Les espèces inorganiques comprennent les ions métalliques ou les clusters formant les connecteurs entre les ligands organiques, ce qui contribuent

également aux propriétés des matériaux. Ainsi, une sélection judicieuse des composantes métalliques et organiques sont nécessaires pour les diverses applications. Plus importants encore, ces polymères peuvent avoir des organisations prévisibles en fonction des précurseurs ce qui permet de moduler l'architecture de ces matériaux.

Une des préoccupations majeures dans la conception des polymères de coordination est la stabilité thermique et chimique de ces matériaux. Ainsi, nous proposons dans cette thèse d'utiliser des systèmes aromatiques rigides, planaires, polyconjuguées, riches en azote comme ligands organiques. Pour explorer cette stratégie, nous avons conceptualisé des composés organiques avec des fonctionnalités à base de pyridonyle qui incluent le cyamelurate fusionné à trois cycles. En raison de la polyvalence du nombre de modes de coordination, de la similitude avec le groupement carboxylique (-COOH) et afin de résoudre les problèmes liés aux polymères de coordination une série de ligands ditopiques et tritopiques basés sur la pyridone et de ces dérivés ont été conceptualisés au cours de cette thèse pour développer des matériaux innovants. Ces composés organiques présentent la capacité de former des liaisons de coordination avec les espèces métalliques ou de s'auto-assembler par liaison hydrogène pour générer des structures variées. Pour les réseaux de coordination, nous avons choisi d'utiliser les métaux de transition et les lanthanides, car ils présentent les caractéristiques suivantes (i) géométrie de coordination prédictible (ii) nombre important de liens de coordination et (iii) nombreuses propriétés intéressantes (rédox, catalytique, luminescence, chromisme etc.).

Dans cette thèse, les activités de recherches seront orientées vers 1) le développement de nouvelles séries de ligands organiques à base de pyridonyle avec de multiples sites de coordination et l'étude de leur auto-assemblage, 2) la conception rationnelle et la synthèse de nouveaux polymères de coordination à base de pyridone et de métaux de transition avec des propriétés chromiques pour les applications de détection, 3) la synthèse de

nouveaux réseaux de coordination (*Metal-Organic Frameworks* = MOFs) utilisant des ligands organiques à base de pyridone, 4) la conception rationnelle des MOFs avec des lanthanides et riche en azote par l'utilisation du cyamelurate (ligand riche en azote) pour la séparation sélective de gaz.

Mots-clés : énergie et technologie, polymères de coordination, *Metal-Organic Framework*, matériaux hybrides, chimie supramoléculaire, pyridone, cyamelurate, sélectivité.

Table of Contents

List of Figures

Appendix 1

Appendix 2

Appendix 3

Appendix 4

μm); b) UV-Vis spectra changes for MMOP-7. Black solid lines: MMOP-7 as synthesized; purple solid lines: heated at 130 °C, black dash lines: sample on exposure in water and red dash lines: sample on exposure in methanol. Insert: chromism images of MMOP-7; c) FTIR spectra of the MMOP-7 as-synthesized, heated at 130 °C, exposed to water and then exposed to methanol; d) PXRD patterns of the samples taken at different cycles and the simulated patterns calculated from the single-crystal X-ray diffraction data; e) TG curves of MMOP-7 as synthesized and dehydrated. One cycle is referred to a transformation that brings the cyan species to yellow species and return to the original colour.

Appendix 5

List of Tables

Appendix 4

Appendix 5

List of Schemes

List of Charts

List of Abbreviations

Abbreviations	Expansion
DNA	Deoxyribonucleic acid
IPCC	Intergovernmental Panel on Climate Change
IUPAC	International Union of Pure and Applied Chemistry
ID	One-dimensional
2D	Two-dimensional
3D	Three-dimensional
MOF	Metal-Organic Framework
SBU	Secondary Building Unit
BET	Brunauer–Emmett–Teller
IDE	Interdigitated Electrode
RH	Relative Humidity
API	Active Pharmaceutical Ingredient
MRI	Magnetic Resonance Imaging
LED	Light Emitting Diode
GSS	Gas Sweetening System
FTIR	Fourier Transform Infrared
EA	Elemental Analysis
UV-Vis	Ultraviolet-Visible
Nm	Nanometer
MHz	Megahertz
Mm	Millimetre
XPS	X-ray Photoelectron Spectroscopy
EDS	Energy-Dispersive X-ray Spectroscopy
TGA	Thermogravimetric Analysis
DTA	Differential Thermal Analysis
CIF	Crystallographic Information File
FWHM	Full Width Half Maximum
Å	Angstrom
kV	Kilo Voltage
mA	Milli Ampere

Mg	Milli Gram
Hrs	Hours
XRD	X-ray Diffraction
NMR	Nuclear Magnetic Resonance
MS	Mass Spectroscopy
CP	Coordination Polymer
DMF	Dimethylformamide
PXRD	Powder X-ray Diffraction
ORTEP	Oak Ridge Thermal Ellipsoid Plot
EtOH	Ethanol
DMSO	Dimethylsuphoxide
DSC	Differential Scanning Calorimetry
MeOH	Methanol
DCM	Dichloromethane
Mmol	Milli Mole
mL	Milli Litre
HCl	Hydrochloric acid
SEM	Scanning Electron Microscopy
MOP	Metal-Organic Polymer
MMOP	Mixed Metal-Organic Polymer
eV	Electron Volt
a.u.	Atomic Unit

Personal CV

During my Ph. D, I published three articles as 1st author and one article as a co-author in world renowned journals. Two other manuscripts were submitted to journals with high impact factors. In total since my academic study, I have 11 articles.

1 **Mohan, M.**; Rana, L. K.; Maris, T.; Duong, A., Intercalated 2D + 2D hydrogen-bonded sheets in co-crystals of cobalt salt with 1 H, 1′ H-[3, 3′] bipyridinyl-6, 6′-dione. *Can. J. Chem.* **2020**, *98 (3)*, 347-351.

2 **Mohan, M.**; Maris, T.; Duong, A., Building coordination polymers using dipyridone ligands. *CrystEngComm.* **2020**, *22* (3), 441-447.

3 **Mohan, M.**; Rajak, S.; Tremblay, A. A.; Maris, T.; Duong, A., Syntheses of mono and bimetallic cyamelurate polymers with reversible chromic behaviour. *Dalton Trans.* **2019**, *48* (20), 7006-7014.

4 **Mohan, M.**; Essalhi, M.; Durette, D.; Rana L. K.; Ayevide, F. K.; Maris, T.; Duong, A., A rational design of microporous nitrogen-rich lanthanide metal-organic frameworks for CO_2/CH_4 separation*ACS Appl. Mater. Interfaces*, **2020**, *12* (45), 50619-50627..

5 **Mohan, M.;** Essalhi, M.; Zaye, S.; Rana, L. K.; Maris, T.; Duong, A., Hydrogen bonds patterns in co-crystals of dipyridone (Submitted in *CrystEngComm.*).

6 Rajak, S.; **Mohan, M.**; A. Tremblay, A.; Maris, T.; Leal do Santos, S.; Venancio, E. C.; Ferreira Santos, S.; Duong, A., Programmed molecular construction: driving the self-assembly by coordination and hydrogen bonds using 6-(pyridin-2-yl)-1, 3, 5-triazine-2, 4-diamine with $M(NO_3)_2$ salts. *ACS Omega* **2019**, *4* (2), 2708-2718.

7 Peter, A.; **Mohan, M.**; Maris, T.; Wuest, J. D.; Duong, A., Comparing crystallizations in three dimensions and two dimensions: behavior of isomers of [2, 2′-bipyridine] dicarbonitrile and [1, 10-phenanthroline] dicarbonitrile. *Cryst. Growth Des.* **2017**, *17* (10), 5242-5248.

8 Panneri, S.; Ganguly, P.; **Mohan, M.**; Nair, B. N.; Mohamed, A. A. P.; Warrier, K. G.; Hareesh, U. S., Photoregenerable, Bifunctional granules of carbon-doped g-C_3N_4 as adsorptive photocatalyst for the efficient removal of tetracycline antibiotic. *ACS Sustain. Chem. Eng.* **2017**, *5* (2), 1610-1618.

9 **Mohan, M.**; Suzuki, T.; Nair, A. K.; Pillai, S.; Warrier, K.; Hareesh, U.; Nair, B. N.; Gale, J., Surface modification induced enhanced CO_2 sorption in cucurbit [6] uril, an organic porous material. *Phys. Chem. Chem. Phys.* **2017**, *19* (37), 25564-25573.

10 **Midhun, M.**; Pragatheeswaran, A.; Sankar, S.; Shijina, K.; Firozkhan, M.; Mohamed, A. P.; Ananthapadmanabhan, P.; Warrier, K.; Hareesh, U. S., Synthesis, spray granulation and plasma spray coating of lanthanum phosphate nanorods for thermal insulation coatings. *Ceram. Int.* **2017**, *43* (6), 4858-4865.

11 Shijina, K.; Sankar, S.; **Midhun, M.**; Firozkhan, M.; Nair, B. N.; Warrier, K. G.; Hareesh, U. S., Very low thermal conductivity in lanthanum phosphate–zirconia ceramic nanocomposites processed using a precipitation–peptization synthetic approach. *New J. Chem.* **2016**, *40* (6), 5333-5337.

12 Manjumol, K.; Sankar, S.; Nair, B. N.; **Midhun, M.**; Mohamed, P. A.; Warrier, K., A novel approach to formulate high flux multifunctional ultrafiltration membranes from photocatalytic titania composite precursors on multi-channel tubular substrates. *RSC Adv.* **2016**, *6* (63), 58813-58822.

13 Siji Narendran, N.; **Midhun, M.**; Soman, R.; Arunkumar, C.; Chandrasekharan, K. Synthesis and third order optical investigations of nitrophenyl porphyrins, *AIP Conference Proceedings*, **2013**, 1536 (1), 851-852.

Chapter 1: Introduction

1.1 General Introduction

Material designing has led to a drastic change in the development of modern technologies, with which the civilization has achieved all technological advancements.[1,2] A steady growth in the needs of mankind thrives the scientific community in pursuing more progressive materials therein improving the knowledge. A prodigious consideration has been given to the development and use of innovative smart materials to enhance environmental sustainability, economic, eco-friendly and easy processability.[3,4] Latest technologies with high-performance materials are being developed to meet these needs, this in turn, has contributed towards creating innovative solutions to long-established problems, especially the undesirable impact on the environment.[5-7] These improvements have benefited in moulding the structural stability of the material and in modifying the preservation policies for environmental conservation and rehabilitation, which effectively influences the architectural design thinking. The frontier objective of the research community in the field of smart materials is developing a new class of multi-functional materials which can be achieved by either incorporating components possessing diverse properties or by designing components delivering multiple properties.[8] The current approach will discuss and analyse the integration of smart materials, their construction and impact on technologies which can potentially transform architectural thoughts in ways we can hardly imagine today. It will bring a paradigm shift in material designing and performance.

1.2 Structure-Property Relationship

Understanding the structure, components and the interaction between the building blocks is the origin to comprehend the function of many things.[9] Like many other fields such as mechanical engineering, macromolecular biology and architecture, this ideology is relevant even in the field of particle physics and it forms the central idea to the fundamentals of chemistry.[10-13] This correlation between the structure and function forms the core to enlighten the subject, ranging from atomic structure to the complex chemical and physical properties exhibited by the materials. Even, the classification of elements can never be fulfilled without clear visualization of the structure of atoms. Likewise, chemical properties that can also be rationalized based on the chemical structure of different species. For an illustrative example, carbon is a tetravalent element with atomic number 6. The three well-known allotropes of carbon are amorphous carbon, graphite and diamond. In the free form, carbon exists in amorphous form. When combined with other carbon atoms arranged in a hexagonal lattice with sp^2 hybridization, it forms well-defined two-dimensional sheets which are conductive in nature. Similarly, when carbon is connected to other carbon atoms in a tetrahedral fashion, elemental carbon takes the form of one of the hardest naturally occurring material known viz. diamond. Further, the structure of fullerene comes by similar connectivity to that of graphite. Nevertheless, due to the versatility in the structure, they exhibit entirely new properties. Finally, when graphitic layers are bent and joined in one direction so as to form hollow cylinders, they form carbon nanotubes, one of the strongest and stiffest materials in terms of its tensile strength and elastic modulus (Figure 1.1). Thus, a clear understanding of the structure of the materials is a vital phase in determining the desired properties. More properties depend on more variables; hence a greater knowledge of the structure and composition of

the system is required. Explaining the reactivity, conductivity or even the adsorption properties of material requires an increasing amount of understanding of the electronic and bonding structure, including the intermolecular interactions taking place in the system.[14,15]

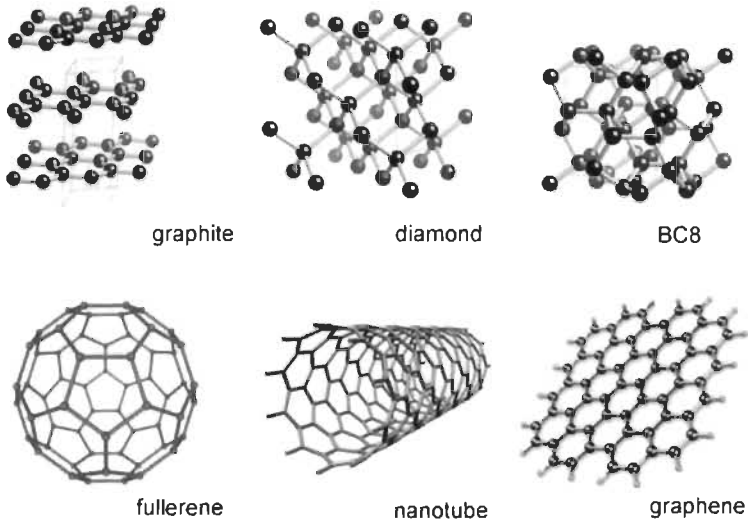

Figure 1.1. Different allotropes of carbon.

A major scientific upgradation was achieved during the early 1900's which led to the birth of a new era of nanotechnology allowing a deeper insight into the exact arrangement of atoms.[16-18] This field of science proved to be a diverse and interdisciplinary area concerning the understanding of chemical and biological structures in the range of 1-100 nanometres. The major breakthrough in the scientific world can be considered after the discovery of X-rays by Roentgen in 1895 which opened the knowledge in illuminating the exact chemical structures.[19] This discovery eventually led to the development of single crystal X-ray crystallographic analysis, after which more complex structures were revealed thereby advancing our understanding of intermolecular interactions hence enlightening the chemical and physical properties of the systems.[20,21]

A famous American theoretical physicist, Richard Feynman, once had quoted that "what would happen if we could arrange the atoms one by one the way we want?". Following the quote, arranging atoms and molecules with a strategical design would eventually lead us to materials with desired properties. Just as in the case of Lego, which was constructed by a Denmark company, where a set of six bricks of 2 x 4 studs can have a combination of 915,103,765 ways to arrange (Figure 1.2). With an enormous number of combinations, any structure models can be constructed by interlocking the bricks.

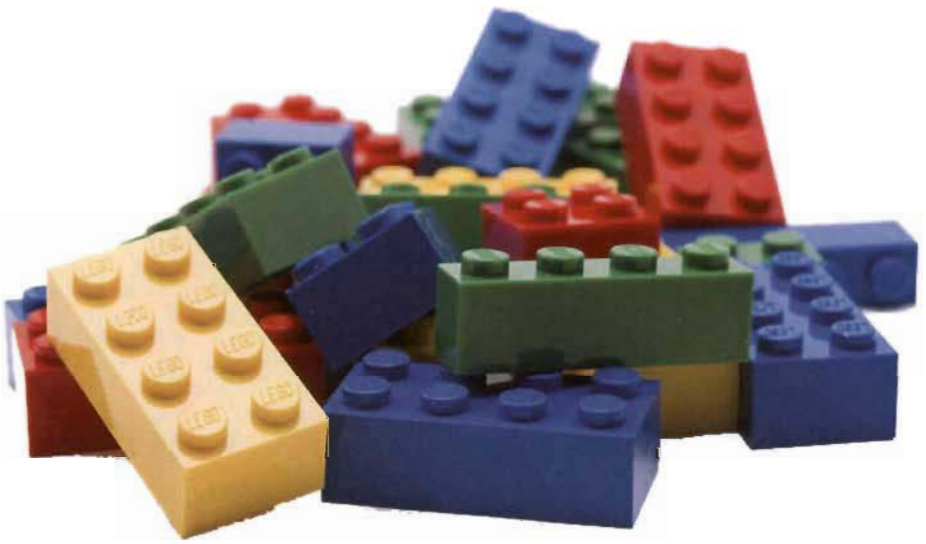

Figure 1.2. Different types of Lego bricks.

Nature has provided us with the perfect examples for designing and constructing, starting from the atomic level. The control of molecules at atomic levels can be achieved by self-assembly. For instance, DNA and peptides are readily assembled from the basic building blocks namely nucleotides and amino acids respectively. Scientists often investigate nature for clues to help in developing new methods for synthesizing polymers, micelles and porous functional materials.[22-25] Subsequently, the concept of self-assembly was adapted into coordination chemistry to allow actual control over the structure and

functional properties at the molecular level which would lead to synthesizing complex coordination compounds.[26-28]

1.3 General Issues Emphasized

Prerequisite for the advancement in smart materials has driven the researchers for the betterment of social and economic consciences. A major transformation began in the fields of transportation and energy production.[29,30] A great deal of achievements has been accomplished in these fields which resulted in the ease of living style the *homo sapiens* created for themselves. Development in these fields made us build large ships, trucks, trains, aeroplanes and even space shuttles, which has elevated our knowledge and motivated us to look beyond our own planet. Since then, the growth in science and technology has been exponential and has brought us significantly closer to achieve our targets. Nevertheless, the advancement in most of the sectors such as agriculture, biomedical, informatics and textiles, the adverse effects of the changes can profoundly be seen in nature, one of the major issues being global warming. The extensively high amounts of greenhouse gases induced by the aftereffects of the industrialization and cattle farming are the primary cause of global warming.[31] Extensive use of fossil fuels has also led to yet another major blow in the environmental and economic sectors by causing energy crisis.[32] As these energy sources are non-renewable, their availability diminishes as their demand and usage increases. Judicious use of the energy has become an out of the box theme mainly due to the apathetic technological advancement in the fields of machinery. This may lead to a day with no fossil fuels left.

1.3.1 Global Warming

Climate influences our growth and our well-being. Each species on earth has adapted to live within a specific climatic niche. Global warming has led to an average increase in earth surface temperature of about 0.6 °C in the 21st century, according to the 2018 Intergovernmental Panel on Climate Change (IPCC) report (Figure 1.3).[33] These effects are the results of human activities which changes the chemical composition of the atmosphere. This continuous change in climate has perilous effects on ecosystems that are not able to adapt themselves to these climatic variations. Carbon dioxide and methane are the primary cause of these climatic changes. Recent studies confirm that the annual emission of CO_2 is over 36 billion tons, which has been the highest in the past 4,20,000 years.[34] CO_2 is expelled into the atmosphere mainly through the burning of fossil fuels, volcanic activities, industrial and automobile exhausts, and so on.

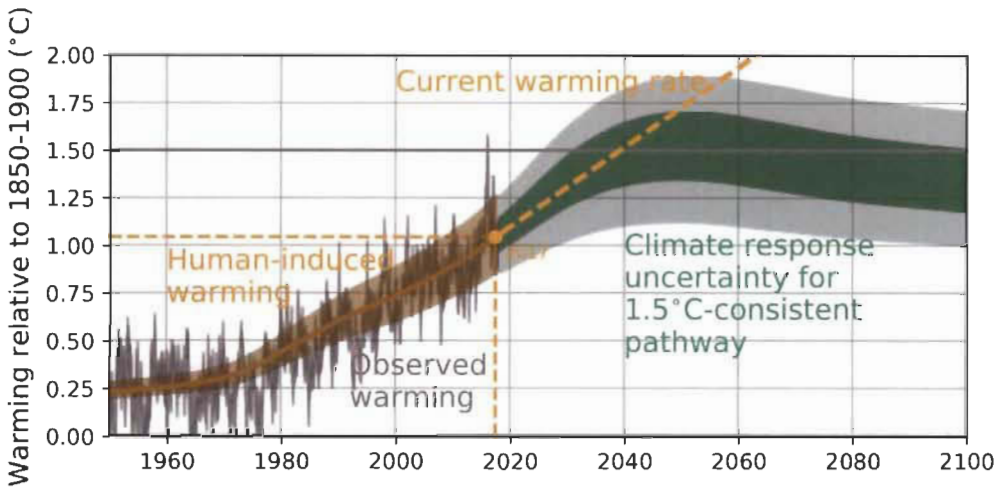

Figure 1.3. Special report on global warming of 1.5 °C by Intergovernmental Panel on Climate Change (IPCC).

1.3.2 Energy Crisis

Fuel efficiency can be elucidated as the ratio of effort to result of a process converting the chemical potential energy from the fuel to kinetic energy. Nevertheless, efficiency largely depends on the purity of the fuel. With exponential growth in the human population, a steep hike has been evident on the use of fossil fuels for the fulfilment of improving living standards. This rapid consumption has had a wide implication on depletion of fossil fuel reserves whose complete exhaustion might be landmarked in the near future. Not only is the price of fossil fuels continuously increasing, but their burning is also generating notorious moieties including greenhouse gases, which pose a serious threat to the very survival of life on Earth.

The best alternative is the use of renewable energy resources, but it has many setbacks one being that the issues cannot be rectified at an immediate pace. The lack of conventional technologies to effectively convert these energy to usable fuel forms has been the primary cause of the hindrance in using renewable energy resources. The technological transformation of conventional engines for the usage of these energies might be time consuming as well as expensive. As a result, there has been a keen interest in search of alternative fuels for internal combustion engines which can improve the engine fuel economy and reduce exhaust emissions. Natural gas has emerged and proven to be the promising alternative fuel as it belongs to the clean fuel category.[35] Combustion of natural gas produces significantly lower emissions of pollutant gases when compared with traditionally used gasoline and diesel. Natural gas comprises a mixture of varying gas that includes 75-98% methane with varying percentages of CO_2 and other gases. The major issue in using natural gas as an alternative fuel is the presence of high amounts of

CO_2 in the mixture of natural gas causing a lower heating value thereby leading to a reduction in the burning velocity that ultimately affects the performance of the engine.

Recent data on the global energy consumption which includes domestic as well as industrial usage reveals that the major contributions are received from the non-renewable sources such as oil, coal, natural gas and nuclear fuel which subsidizes to around 90% of the total (Figure 1.4).[36] Only around 10% is contributed by renewable sources such as solar, hydro, wind and biomass. This can be conjunctively related to the growing global population and their demands that enlighten the need to develop materials to harvest renewable sources of energy with more competence.

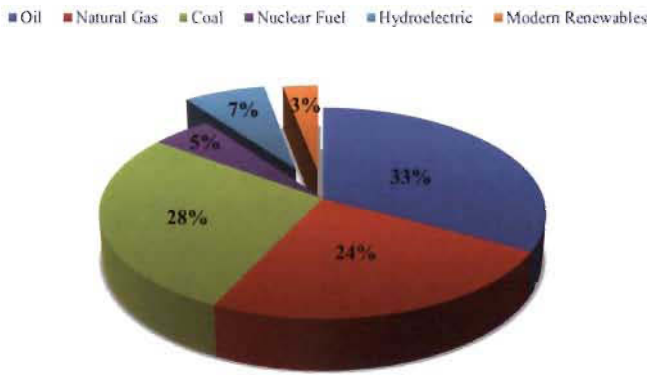

Figure 1.4. Pie chart representation of the global energy consumption (2017).

1.4 Introduction to Coordination Polymers and Metal-Organic Frameworks

During the last few decades, tremendous researches have been going on to develop new materials for addressing the energy related motifs. In this context, coordination polymers are one of the most promising candidates owing to their structural versatility and tunable properties.[37,38] They exhibit various properties such as porosity, catalysis, electronic and

photophysical. They can be used for gas storage and sequestration, sensor applications, electronic applications, as molecular sieves, photovoltaics, molecular machines, optoelectronics, photoluminescence, biomimetic and pharmaceuticals.[39-42] It is worth mentioning that among the best coordination polymers, zeolites are known for their industrial applications as adsorbents and catalysts.[43]

Coordination compounds are a class of materials composed of organic ligands forming coordinating bonds with metal ions or clusters. These compounds are best defined by the IUPAC as "*A coordination compound is any compound that contains a coordination entity. A coordination entity is an ion or neutral molecule that is composed of a central atom, usually that of a metal, to which is attached a surrounding of atoms or group of atoms, each of which is called a ligand.*" The first exploration of coordination compounds dates to the nineteenth century when Alfred Werner discovered the octahedral cobalt Werner complexes.[44] Coordination complexes are classified as zero, one and two/three-periodic based on the periodicity of the resultant networks (0-P, 1-P and 2-P/3-P, respectively).[45] Prior to the discussion on the same, a short introduction to the node-and-spacer model developed by Wells would be more appropriate for better understanding.[46] This model defines crystal structure by reducing the complexity using joints of the respective geometries linked by spacers. The model was developed further by Robson and has been the standard model of representing coordination polymers to date.[47] Figure 1.5 shows a representation of this model. The nodes represent the ligand systems or metal ions/clusters with more than two points of extension. These nodes are linked through spacers or linkers. The spacers can be linear ligands, 2-connected metal or a portion of the ligand which connects with the metal.

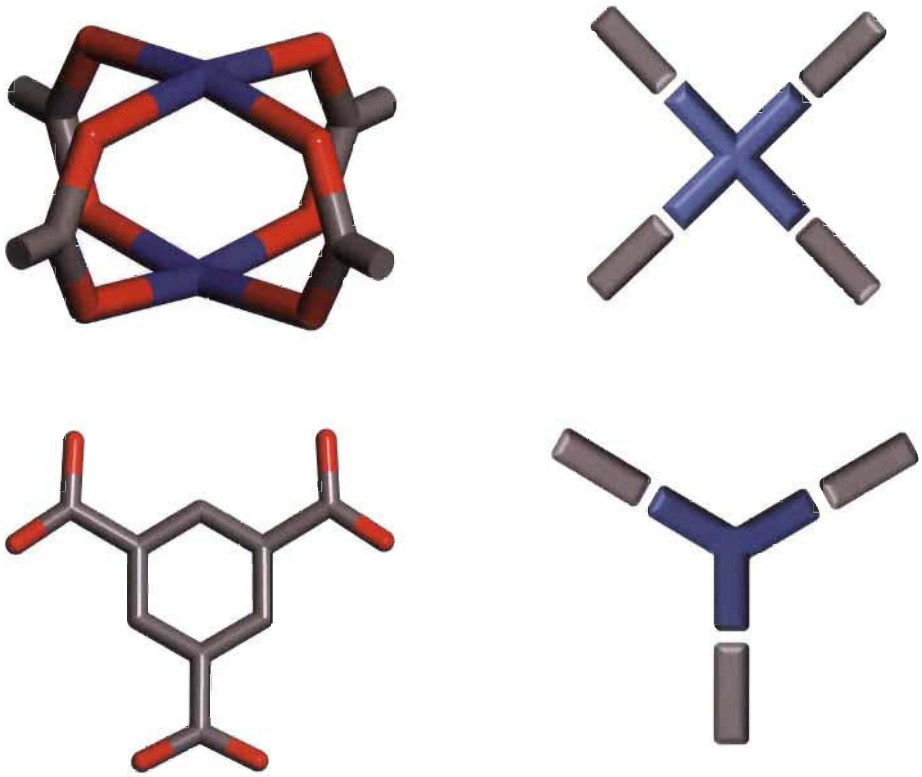

Figure 1.5. Schematic representation of node-and-spacer model.

Coordination polymers were also classified in different ways among which the most common classification was in accordance with their structure and composition as porous and non-porous coordination polymers.[48] Porous coordination polymers comprise of large surface area which is further classified as flexible and rigid porous coordination polymers. Additionally, coordination polymers are also categorized depending upon their structural dimensionality as one-dimensional (1D), two-dimensional (2D) and three-dimensional (3D) coordination polymers (Figure 1.6).[49-51] This classification is in accordance with the number of directions in space in which the array is extending.

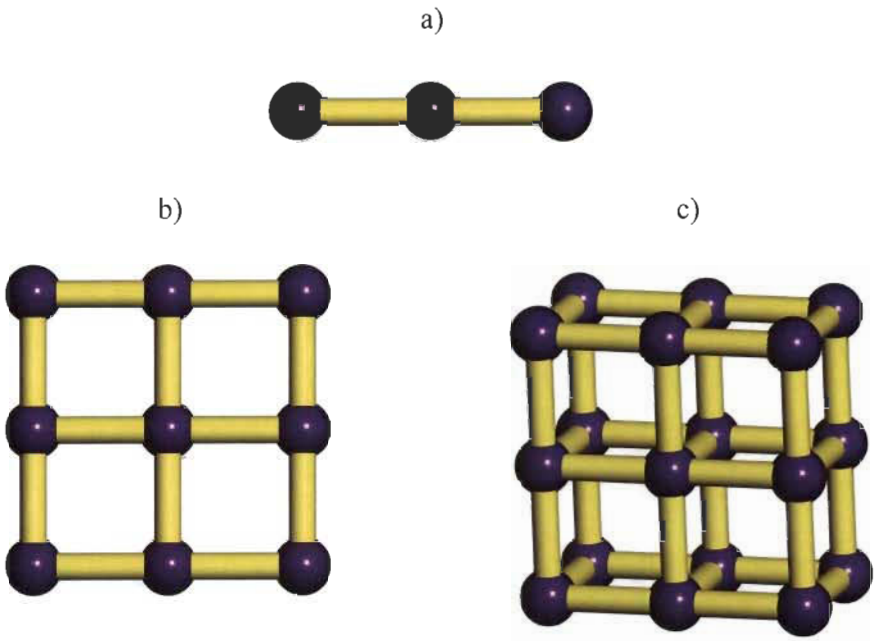

Figure 1.6. Illustrative representation of a) 1D coordination polymer, b) 2D coordination polymer and c) 3D structure coordination polymer. Purple balls denote metal centres and yellow sticks denote ligand species.

Metal-Organic Frameworks (MOFs) are an important class of coordination polymers consisting of metal ions or clusters coordinated to organic linkers to form one, two or three-dimensional structures.[52] Due to the versatility in selection of the two counterparts, MOFs can variegate claiming unusual diversities in their properties such as porosity, functionalisation and structure.[53] They have attracted considerable attention which makes them potential candidates for various applications such as gas storage and separation, catalysis, drug delivery, photoluminescence, magnetism, sensors, and so on.[54-58] The diversity in applications is mainly due to the possibility of forming them from a wide range of metals and various functional groups in the organic linkers. MOFs have a large and permanent porosity that can interact with guest molecules and ions. One of the important areas of MOF application has been focussed on the gas storage and separation

with high selectivity, mainly CO_2 due to its adverse effects on the ecosystem associated with climate change.[59] Many MOFs and other porous materials have reportedly addressed this issue; however, considerable effort needs to be made to develop efficient porous materials for gas separation. The current issue causing a slowdown of their applications is their instability-thermally, chemically and in vacuum.[60] Until now, only a very few MOFs reported have found industrial applications. Thus, improvement is needed to create energy technologies using MOFs.

1.4.1 Brief History of MOFs

The earliest examples of crystalline materials comprising metal centres and organic linkers dates to 1943 with the Werner-type complexes.[61] These complexes have a general formula MX_2L_4 where M is the metal species with divalent octahedral geometry, X is the anionic ligand, most commonly, CN^-, NO_3^- and SCN^- and L is the pyridine coordination molecule (Figure 1.7).

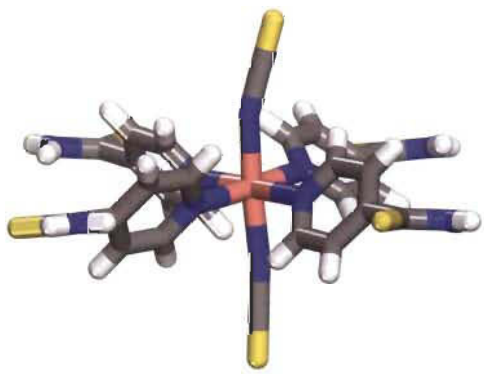

Figure 1.7. Crystal structure of a Werner complex, tetrakis(pyridine-4-carbothioamide)-bis(isothiocyanate)-cobalt (II). Colour code: Co- pink, N- blue, C- grey and S- yellow.

By the end of 1960s, Iwamoto and co-workers studied the Hofmann-type clathrate compounds derived from the parental compound discovered by K. A. Hofmann exhibiting the molecular formula of $Ni(NH_3)_2(CN)_4(C_6H_6)$ (Figure 1.8).[62,63]

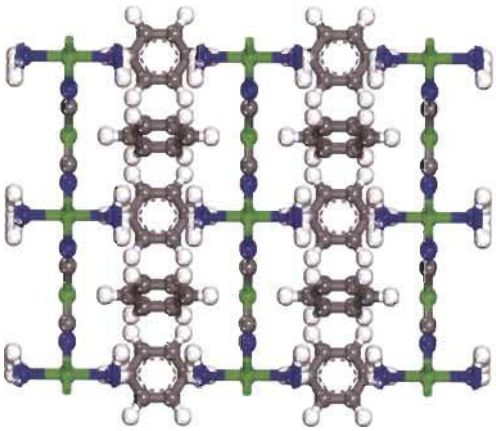

Figure 1.8. Crystal structure of a Hofmann clathrate structure, catena (bis(hexadeuterobenzene)tetrakis(μ2-cyano)-tetrakis(ammonio)-di-nickel clathrate). Colour code: Ni- green, N- blue and C- grey.

Since the discovery of the first zeolite in 1756 to the latest researches on the porous materials, the evolution has had irregularities which are evident from the recent developments in the field of porous materials.[64] In 1990, Robson and co-workers explored the functionality in the porous coordination polymers, especially in the ion-exchange properties.[65] Subsequently, Yaghi and co-workers developed porous coordination polymers with bipyridine followed by the first robust and highly porous material, MOF-5 or IRMOF-1 which revolutionized the field of porous materials (Figure 1.9).[66]

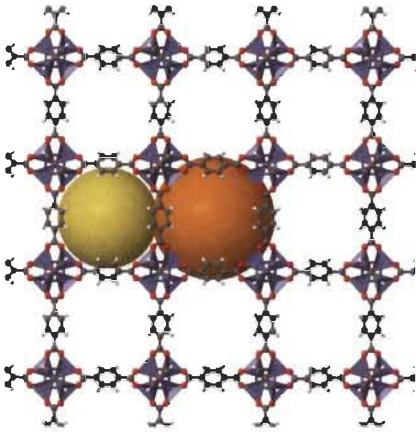

Figure 1.9. Crystal structure of MOF-5. Colour code: C- grey, O- red, Zn tetrahedra- pale blue, empty voids- yellow and orange spheres.

Since then the terminology of Metal-Organic Frameworks or, in short, MOFs have grown exponentially to become a crucial part of material chemistry and porous materials. Mainstream focus on MOFs was achieved notably after understanding the methods to activate the pores thereby delivering the potential applications associated with. Until now, more than 20,000 MOFs have been synthesized with various potential applications of which a few have drawn a quite lot of attraction from the scientific community. Williams and co-workers developed HKUST-1, also known as Cu_3-$(btc)_2$ which finds applications in gas storage and separation.[67] This MOF exhibited a face-centred cubic crystal that consists of large square pores with dimensions of 9 Å by 9 Å. Few other examples of revolutionary MOFs are MIL-101, MOF-74, NU-110, NU-1000, etc.

1.4.2 Design and Synthesis of Metal-Organic Frameworks

Inorganic connectors and organic linkers are the two key components for the construction of MOFs. Fascination with the field of MOFs arises mainly due to the versatility in the

selection of these components. Through judicious choice, it can be made possible to specify the properties exhibited by the MOFs with a wide range of options in structural, optical, magnetic, electrical and catalytic properties.[68,69] As far as the metallic part, also known as the Secondary Building Unit (SBU), transition metals have been most commonly employed due to their different coordination numbers and variety in the coordination geometries such as linear, trigonal (T- or Y-shaped), tetrahedral, square-planar, square-pyramidal, trigonal bipyramidal, octahedral, trigonal-prismatic and pentagonal bipyramidal geometries (Figure 1.10). As an example, Nickel (II) has an oxidation state of +2 with an electronic configuration of d_8. In the preferred six coordination, Ni (II) has an octahedral geometry but can also be found in other geometries such as square planar and tetrahedral with four coordination number. Other metallic systems include lanthanide ions that are mostly used to generate new and unusual network topologies due to the higher coordination numbers ranging from 8-12.

In the case of an organic linker, the choice is more diverse as the structural versatility in organic compounds is greater. Ligands with rigid structures are preferred since they result in the easier and advanced prediction of the geometry of the MOF, along with the advantage of improving the structural stability and sustaining the open-pore structure after solvent removal. These linkers can be neutral, cationic or anionic species (Figure 1.11).[70-72] The most common neutral organic linkers are pyrazine and 4,4'-bipyridine compounds which serve best for construction of pillared layers to form 3D networks. Among the different categories of linkers, anionic organic linkers are the most preferred as they have a higher affinity towards the cationic metal ions. Carboxylates are the most used anionic linkers since they aggregate metal ions into clusters thereby forming stable MOFs. Cationic organic linkers are the least preferred as they have the lower affinity towards metal ions.

Number of functional sites	Connectors
2	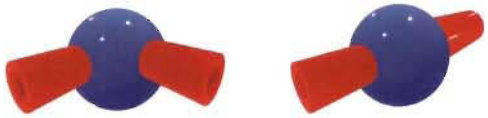
3	
4	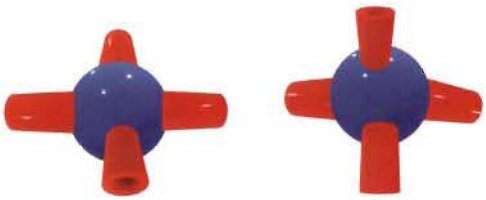
5	
6	

Figure 1.10. Components of MOFs with the number of functional sites.

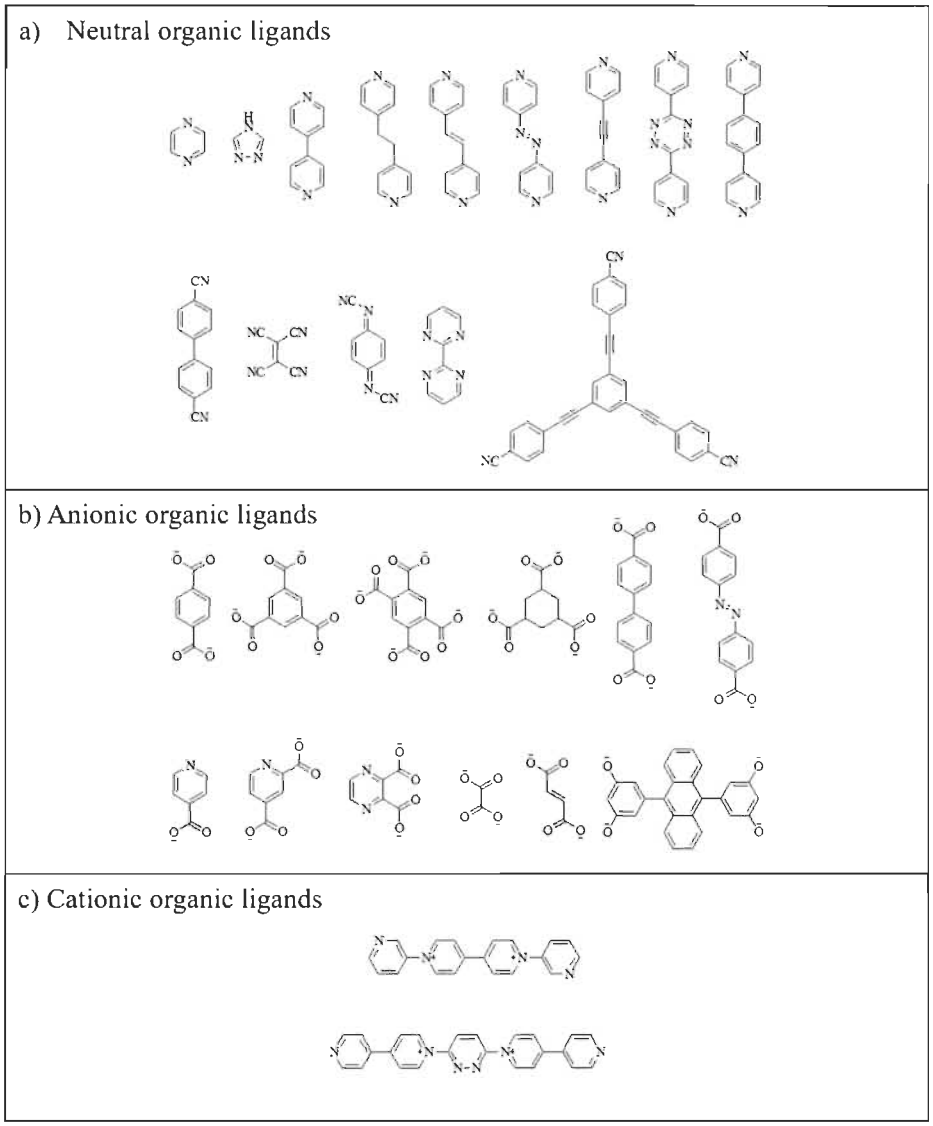

Figure 1.11. Examples of linkers used in MOFs. a) Neutral organic ligands, b) Anionic organic ligands and c) Cationic organic ligands.

1.4.3 Co-crystallization

Co-crystals are single phase crystalline solids containing more than one molecule or ionic compounds having unique properties. Co-crystals not only gives us an idea about the fundamental understanding of various supramolecular interaction and molecular

recognition, but also overlays the ways to new specialty chemicals with improved performances.[73] Synthesizing co-crystals is considered as one of the focus in the field of crystal engineering. The study on co-crystals originated from the Wohler's work in 1850s on quinhydrone, a 1:1 co-crystal of quinone and hydroquinone.[74] The contribution of co-crystals can be unnoticeably seen in pharmaceuticals, smart materials and agrochemical sectors.[75]

Hydrogen bonding has been the relied as the centre of protocol for the synthesis of co-crystals.[76] Nevertheless, in order to construct complex co-crystals, halogen bonding can also be employed to build co-crystals of higher order using logical strategies derived from an improved awareness of the balance and competition between many other intermolecular interactions. Apart from the judicious selection of synthons for the construction of co-crystals, it is also important to carefully select the solvent system in which all the components have relatively good solubility. The role of solvents can be more than merely solubilizing all components as sometimes have an impact on the structural outcome by amplifying certain synthons. They can also take part in the formation of co-crystals and afford unintended solvates.

Co-crystallization plays a key role in material designing by offering a degree of predictable periodicity. This can improve the understanding of the molecular arrangement, crystal structure and physical properties of the resulting crystalline solids. By fixing the structural framework of the active site in the co-crystals and replacing by closely related components without any change to the overall crystal structure can deliver materials with specific properties. A reliable synthetic methodology for the developing co-crystals and multicomponent molecular solids has become the new aspect of material chemistry using self-assembly and crystal engineering.

1.5 Applications of Coordination Polymers

Due to the intrinsic nature exhibited by the coordinated metal ion(s) along with other remarkable structural uniqueness such as porosity, coordination polymers such as Metal-Organic Frameworks have been regarded as the most effective remedy in many applications. Porosity adjoined with the pore properties makes them the potential candidates for applications associated with the gas adsorption, molecular sieves, catalysis, sensors, bioluminescence, magnetic material, etc.[39-42] Some of these are discussed in the following sections.

1.5.1 Adsorption

The word "adsorption" was coined in 1881 by German physicist *Heinrich Kayser*. Adsorption is the process in which atoms, ions, or molecules in gaseous, liquid or dissolved solid forms have adhered to a surface. This phenomenon associates with the substance accumulating in the vicinity of an interface. The material, mostly solids, on which the adsorption occurs is called the adsorbent, whereas, the material (gas, liquid or dissolved solids) that gets adsorbed is known as the adsorbate. This process contrasts from absorption, in which, a fluid is dissolved by or permeates in a liquid or solid, respectively. Adsorption is a surface phenomenon, while absorption is a bulk phenomenon. The amount of adsorbate adsorbed is mainly influenced by the surface properties such as porosity, affinity towards the adsorbent, temperature and pressure of the adsorption process and mobility of the adsorbate in the adsorbent system.

1.5.1.1 Modes of Adsorption

In general, there are two modes of adsorption, namely, physisorption and chemisorption.[77,78]

1.5.1.1. a) Physisorption

In physisorption, the target molecules are attracted to the surface of pore walls within a high surface-area sorbent by van der Waals attractive forces and have a low heat of adsorption that is slightly greater than the heat of sublimation of the adsorbate. This is the result of long-range attraction forces and short-range repulsion forces between the adsorbate and adsorbent. Figure 1.12a shows a schematic representation of physisorption onto a substrate.

Physisorption has low enthalpy of adsorption, i.e., ΔH_{ads} is ~20-40 kJ/mol.[77,78] In general, there exists no specificity since any adsorbate can be adsorbed onto the surface and highly liquefiable adsorbates are physically adsorbed more strongly. As the adsorption process is exothermic, the physisorption is higher at lower temperatures and it decreases as the temperature increases. This is represented in the graph below (Figure 1.12b).

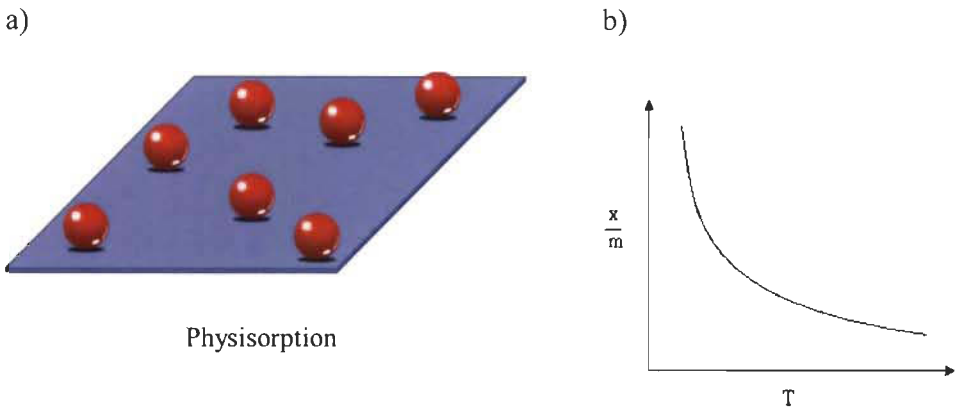

Figure 1.12. Physisorption. a) Schematic representation of physisorption on a surface. b) Graphical representation of physisorption showing rate of adsorption with an increase in temperature where x is the amount of adsorbate, m is the amount of adsorbent and T is the temperature.

1.5.1.1 b) Chemisorption

Chemisorption is the process which involves valence forces with the same magnitude exhibited during the formation of a chemical bond. The mechanism is characterized by chemical specificity. The chemical nature of the adsorbent and adsorbate systems may be altered during the process due to the chemical bond formation between them. The energy of chemisorption is of the same magnitude as the energy change during the chemical reaction between adsorbent and adsorbate, which indicates that chemisorption may be exothermic or endothermic. Figure 1.13 shows a schematic representation of the chemisorption process.

High enthalpy of adsorption, i.e., ΔH_{ads} is ~200-400 kJ/mol is observed due to the chemical bond formation between adsorbate and adsorbent.[77,78] As a matter of fact,

chemisorption occurs only in the adsorption sites present on the surface of the adsorbent, resulting in monolayer adsorption. The mechanism of chemisorption normally requires activation energy. Thus, temperature also influences the kinetics of the chemisorption by accelerating the amount adsorbed. As the temperature increases, the rate of adsorption also increases till it reaches the activation energy level, and then decreases with further increase in temperature.

1.5.1.2 Adsorption Isotherm

The process of adsorption is usually studied through a graph denoted as the adsorption isotherm. It is the graphical representation of the amount of adsorbate adsorbed by the adsorbent in the function of equilibrium pressure at a constant given temperature.

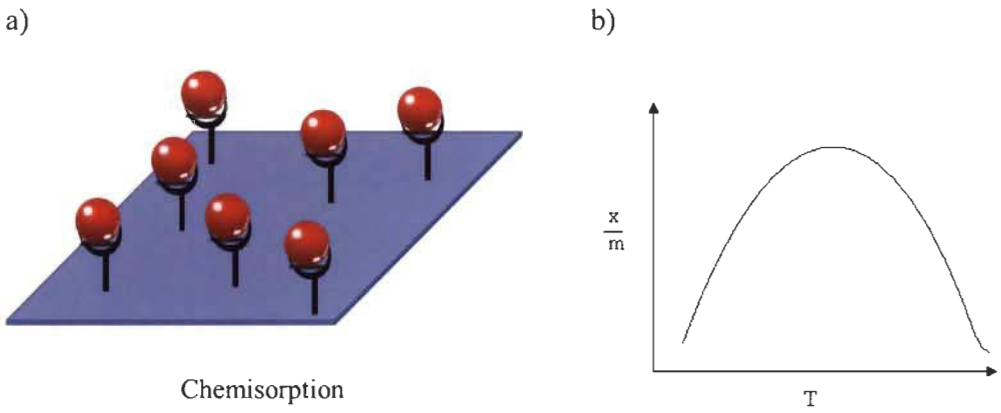

Figure 1.13. Chemisorption. a) Schematic representation of chemisorption. b) Graphical representation of chemisorption showing the amount of adsorption with an increase in temperature where x is the amount of adsorbate, m is the amount of adsorbent and T is the temperature.

Adsorption data is obtained from the concept of understanding the amount of adsorbate removed in its gaseous/liquid phase during the adsorption. Various methods can be adopted to measure the amount of the adsorbate on the adsorbent such as volumetric method, gravimetric method, etc.

In general, six types of adsorption isotherms are observed (Figure 1.14).[79] Type I isotherms are characteristic of microporous materials with a relatively small proportion of the outer surface. A marginal variation of the pore size, as well as the microporous nature of the pores in the materials, exhibit a quicker saturation at lower pressures resulting in Type I isotherm. Type II isotherms refer to poly-molecular adsorption in non-porous or microporous adsorbents. They show a gradual change in thickness of the adsorbed layer from monolayer filling to the formation of several layers. Type III isotherms are the characteristic of non-porous sorbents with low energy of adsorbent-adsorbate interaction. As the pressure increases, more layers of adsorbate are formed over the adsorbent which is merely due to the adsorbate-adsorbate interaction rather than adsorbate-adsorbent interaction. Type IV isotherms are similar to Type II at lower pressures. However, as the pressure increases, a saturation plateau is obtained. Unlike Type II isotherms shown by non-porous materials, Type IV isotherms are exhibited by mesoporous adsorbents. This adsorption is also irreversible as they follow a hysteresis between the adsorption and desorption curves. Similar is the case with Type V isotherms which resemble Type III isotherms except that a saturation plateau is observed at higher pressures. This deviation at high pressure is due to the mesoporous nature of the materials. These are characterized by weak interactions between the adsorbent and adsorbate with the presence of hysteresis. Type VI isotherms are characteristic of non-porous adsorbents with homogeneous surfaces.

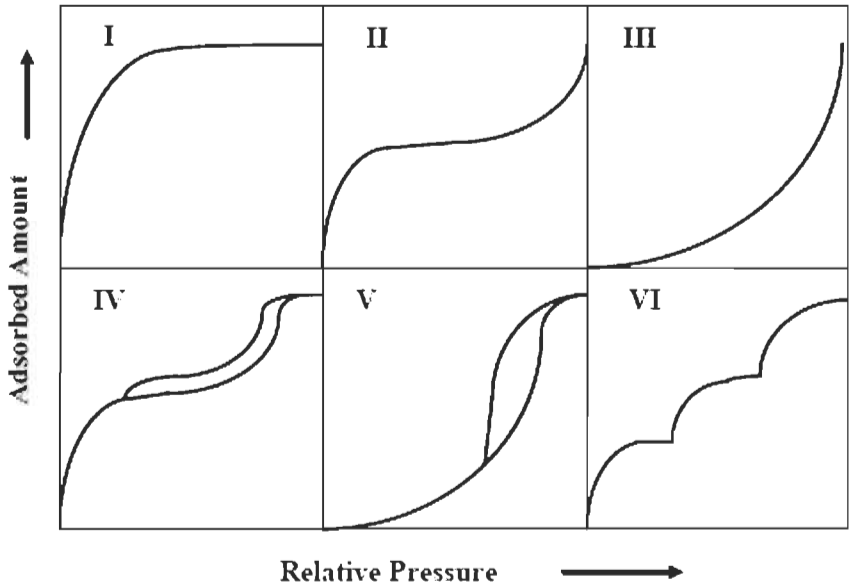

Figure 1.14. Different types of adsorption isotherms.

1.5.1.3 Adsorption Models

The absolute amounts of adsorbate adsorbed are estimated using adsorption models. There are various adsorption models developed, a few are described in the following sections.

1.5.1.3 a) Langmuir Adsorption Isotherm

Langmuir isotherm model was proposed by Irving Langmuir in 1916 which explained the variation of adsorption with pressure.[80] Through this theory, Langmuir equation was depicted which gave a relationship between the number of active sites of the surface undergoing adsorption and the pressure. The assumptions made for the Langmuir isotherm are as follows: i) Fixed number of vacant or adsorption sites are available on the

surface of solid. ii) All the vacant sites are of equal size and shape on the surface of the adsorbent. iii) Each site can hold a maximum of one gaseous molecule and a constant amount of heat energy is released during this process. iv) Dynamic equilibrium exists between the adsorbed gaseous molecules and the free gaseous molecules. v) Adsorption is monolayer.[81] According to the approximation and calculations, the derived Langmuir equation is:

$$\Theta = \frac{KP}{1+KP} \qquad \text{(Equation. 1)}$$

where Θ = number of sites of the adsorbent covered by the adsorbate

K = equilibrium constant

P = partial pressure

The major drawbacks of this theory are that firstly, the gas fulfils these conditions only at lower pressures. As such, the theory does not incorporate the multilayer adsorption. Another assumption in this theory states that the adsorption sites are homogeneous and there is no adsorbate-adsorbate interaction, which is not the real case.

1.5.1.3 b) Freundlich Adsorption Isotherm

Freundlich adsorption isotherm is a modified version of Langmuir isotherm.[82] It considers surface heterogeneity giving an empirical expression representing the adsorption of a quantity of gas adsorbed. The equation of Freundlich adsorption isotherm is:

$$\Theta = KP^{1/n} \qquad \text{(Equation 2)}$$

where Θ = number of sites of the adsorbent covered by the adsorbate

K, n = constants

P = partial pressure

Using Freundlich isotherm, the amount of adsorbate varies with the pressure to the power of 1/n until the saturation pressure beyond which the adsorption tends to saturate even with an increase in pressure, in contrast with the experimental situation, where, the adsorption increases as the pressure is increased. Thus, Freundlich isotherm fails at higher pressures.[83]

1.5.1.3 c) Brunauer, Emmet, Teller Model (BET)

The BET model was primarily designed to describe adsorption isotherms of type II observed in gases close to their boiling points.[84] This model extends to the formation of several layers as compared to monolayer formation by Langmuir. Indeed, improvising Langmuir's hypotheses, the BET model assumes that the molecules adsorbed on the surface of the solid may themselves become adsorption sites for subsequent layers. In addition, the energy of the higher layers is uniform and equal to the liquefaction energy of the gas. The isotherm of BET is represented by the following equation:

$$\frac{P}{V_{total}(P_0-P)} = \frac{1}{V_{mono}c} + \frac{c-1}{V_{mono}c}\left(\frac{P}{P_0}\right) \qquad \text{(Equation 3)}$$

where V_{total} is the volume of the gas adsorbed at the pressure P, V_{mono} is the volume adsorbed when the surface of the solid is covered completely with a monolayer of the

adsorbed molecules of the gas, P_0 is the saturation pressure and c is the constant depending upon the nature of the gas. Its numerical value is given approximately by the expression:

$$c = \exp(E_1 - E_L)/RT \qquad \text{(Equation 4)}$$

in which E_1 is the heat of adsorption in the first layer and E_L is the heat of liquefaction of the gas. The BET model is mainly used to determine the specific surface area of the adsorbent materials.

1.5.1.3 d) Toth Adsorption Isotherm

The Toth isotherm is another empirical modification of the Langmuir equation with the aim of reducing the error between experimental data and the predicted value of equilibrium data.[85] This model is most useful in describing heterogeneous adsorption systems which satisfy both low- and high-end boundary of the adsorbate concentration. The Toth isotherm model is expressed as follows:

$$\theta = \frac{K_e P}{[1+(K_L P)^t]^{1/t}} \qquad \text{(Equation. 5)}$$

where K_L is Toth isotherm constant, K_e is the equilibrium constant, P is the pressure and t are Toth constant. When t = 1, the equation reduces to Langmuir isotherm equation. Therefore, the parameter characterizes the heterogeneity of the adsorption system and if it deviates further away from unity, then the system is said to be heterogeneous. The

values of parameters of the Toth model can be evaluated by non-linear curve fitting method using sigma plot software. This isotherm model has been applied for the modelling of several multilayer and heterogeneous adsorption systems.

1.5.2 Moisture Sensing

Hygrometry is referred to as the measurement of the moisture content of gases. Based on the aspect emphasized, the water vapour content in atmosphere can be defined by absolute humidity, relative humidity, dry-bulb and wet-bulb temperature or the dew-point temperature.[86, 87] These limits can be monitored and studied by mechanical, electrical, optical or temperature measurements.[88] Instrumentation techniques with smart sensing materials in this field have been advancing depending upon the requirements procured from each of them. In general, most humidity sensor techniques include capacitive humidity, resistive humidity, gravimetric humidity and optical humidity.

Capacitive humidity sensors are based on the dielectric constant change of the sensing layer caused by the adsorption of water molecules.[89] This change can be caused by the swelling of the polymer film or the capillary condensation in the porous structures. Capacitance can also be measured by patterned top electrode geometries, such as interdigitated electrodes (IDE) or spiral on top of the sensing layer. These electrodes allow the vapour to diffuse freely into the dielectric material and give a faster response. However, the field distribution is not as uniform as thin film electrodes. Resistive humidity sensors transduce air humidity into an impedance change, which can be measured by current, voltage or resistance.[90] The design of resistive sensors is usually comparable to capacitive sensors. Both polymer and porous ceramic can be built into resistive humidity sensors. The gravimetric humidity sensors are based on the mass

change of the sensing film due to the water vapor uptake.[91] In a vibrating mechanical structure, which is vibrating at its natural frequency, the increase of mass will result in a resonance frequency shift in proportion to the added mass. Gravimetric humidity sensors usually show better sensitivity and accuracy than other sensors at a very low relative humidity (RH). Finally, the most effective method to detect moisture is using the optical humidity sensors.[92] RH can be measured by the optical methods in several ways. One widely used apparatus is the fibre-optical sensor. Light is generated from an optical source, passed through fibre and received by an optical detector. The fibre is coated with water vapour adsorbing layer. The frequency, transmitted power, or wavelength of the received light can be changed as a function of vapour adsorption. The sensing property can be enhanced by functional coatings on the surface of the fibre. The advantages of optical humidity sensors include ease of miniaturization, operation in harsh environments, and potential for remote sensing. However, their main drawbacks are susceptibility to contamination and the complexity of the entire system. Thus, a great deal of past and present research has been focused on developing new materials to enhance the properties and rectify the hitches faced.

The material used for sensing plays a key role to understand the design and operation of humidity sensors. Commonly used humidity sensing materials in the diverse humidity sensor techniques include moisture absorbing polymers, polyimide, polyelectrolytes, porous ceramic (metal oxides), and porous silicon/polysilicon.[93-95] The presence of water molecules in close proximity of these materials' surface could change their mechanical, electrical or optical properties. Organic polymers are an interesting class of water adsorbing sensing elements which include non-conductive and conductive polymers. In non-conductive polymers, a change in their dielectric constants gives the value of the number of water molecules adsorbed. This practice is most used among the polymeric

humidity sensor materials. Another significant method to understand water uptake is by studying the swelling of the films. This will result in mass or dimension change which when detected by techniques can be correlated to the amount of water uptake. In the case of conductive polymers, the conductivity change caused due to the adsorbed water molecules is measured by a pair of electrodes placed on the sensing film. Even though polymer-based humidity sensors have advantages such as fast response, resistance to contaminants, good repeatability and low hysteresis, these sensor materials lose their capacity at high RH level and high temperatures thereby limiting their application in extreme and harsh environments. This is where ceramic-based humidity sensors have an upper hand.[96] Especially metal oxides have been used in humidity sensors, shaped as porous sintered and thin film moieties. Thorough calculation and judgement in developing micromachining and on-chip integration technology have led to the realization of depositing these metal oxides on any desired surfaces by various methods. The electrical properties of ceramics change because of the chemisorption of water vapor on the available sites of the oxide surface, mainly at the grain boundaries. The reaction is related to the dissociation of the water molecule and the formation of one proton and a hydroxyl ion. When the temperature is lower than 100 ^{0}C, physical adsorption of subsequent layers on the first hydroxyl layer also accounts for the property changes. For porous ceramics with microporous structures, capillary condensation is another factor to be considered in the sensing mechanism at high RH level. The advantages of ceramics include ultra-high surface-to-volume ratio, mechanical strength and thermal and physical stability. However, due to the chemisorption reaction, ceramic humidity sensors need periodic regeneration by heat cleaning to recover humidity sensitive properties.[97] The main purpose is to remove the stable chemisorbed –OH on the surface of the porous structure or grain boundaries. This usually requires a temperature up to 400 – 500 °C.

Moreover, adsorption of impurities such as dust and dirt may cause irreversible changes to the sensing layer, as they act the same way as chemisorbed water. This makes ceramics less resistant than polymers to surface contamination.

1.5.2.1 Humidity Sensor with Ordered Porous Structures

The innovative developments in the field of material synthesis have been evolving day by day which continues to gain the attention of new researchers. One of the keen areas of material development is led by the ordered porous materials which have found a very wide range of applications platform. The porosity of these materials ranges from microporous to macroporous depending on the application.[98,99] Organometallics has played a vital role in moulding the design of material synthesis and hence materials itself. Porous materials, nonetheless, organic, inorganic or organometallic hybrid species, are easily processible and thus take form in accordance with the requirements such as thin films. These materials have proved to be advantageous in various chemicals, electrocatalysis and biochemical applications. To optimize their characteristics (electrical or optical), special care during the fabrication process needs to be taken to obtain well-ordered structures with a narrow distribution of open pores and highly accessible surface area. With further development in fabrication technology, the highly ordered porous structure would show huge potential and applications in various chemical sensing systems.

1.5.3 Catalysis

MOFs have been extensively studied as a potential alternative in the field of heterogeneous catalysis for a wide variety of transformations. Though in 1994, the ability of framework materials for catalytic activity were investigated, the ease in tuning the structural functionality of MOFs facilitates their till date usage in catalytic applications.[100-102] The major advantage being the porosity enabling the passage of reactants and products in and out of the active sites located in the pores resulting in an increase in the selectivity of the catalytic activity. Adequate chemical stability while activating the pores as well as during the catalytic conditions is of primary concern when designing MOFs for such applications. Incorporation of highly selective catalytic sites which can be recyclable for a decent number of cycles also plays a key role during the design and synthesis phase. This leaves a greater platform to be explored in order to improve the inputs which have attracted the research community. Various strategies can be adopted to achieve these goals such as incorporating open metal sites, introducing functional groups in ligand moiety, encapsulating catalytic materials inside the pores and grafting catalytic species to metal centres.[103-105]

In 2007, Kitawaga and co-workers reported a breathing cadmium based MOF with tridentate 1,3,5-benzenetricarboxylic acid tris[*N*-(4-pyridyl)amide] (4-BTAPA) ligand.[106] This flexible MOF was found to be suitable for molecular recognition or selective guest inclusion. The organic sites present in it were identified as interesting for the catalytic activity of Knoevenagel condensation of benzaldehyde in benzene with different methylene compounds with an efficiency of about 98%. POST-1, a zinc-based MOF, is an example of catalytic activity induced via pendant organic groups inside the MOF cages.[107] Although very modest enantioselectivity of 8% was obtained during the

transesterification reaction, POST-1 was the first example of an enantioselective catalytic MOF containing enantiopure catalytically active pyridyl groups with tartrate derived ligands. Hupp and co-workers developed a new microporous MOF, NU-601 with urea functionalization catalysing numerous bond-forming reactions such as Diels-Alder or Friedel-Crafts reaction without undergoing self-quenching due to the immobilization of the catalytic sites.[108] Zang *et al.* introduced sulfoxy moiety into Cr-MIL-101 which catalysed the esterification of monohydric alcohols such as *n*-hexanol, *n*-butanol and benzyl alcohol with acetic acid or lauric acid with a yield of around 80 % with highest turnover frequency value of 4.25 min^{-1}.[109] Meanwhile, Wang and co-workers successfully incorporated catalytically active sites on Cr-MIL-101 through post-synthetic grafting of amino groups onto the organic ligand which showed greatly enhanced Knoevenagel condensation reactivity.[110] Similar work was conducted by Hartmann and Fischer forming amine grafted Cr-MIL-101 tested in the Knoevenagel condensation of benzaldehyde with malononitrile and ethyl cyanoacetate, respectively. A superior conversion rate of 90% was obtained with high selectivity of 99%.[111]

1.5.4 Drug Delivery

As MOFs exhibit many desired characteristics required for a drug delivery system, such as exceptionally high surface area, tunable pore sizes, intrinsic biodegradability depending on the labile metal-ligand bonds and versatility in post-synthetic functionality through grafting, these materials are realised to have a great potential in the drug delivery applications.[112,113] Tremendous growth has been seen in the development of MOFs for utility in this field for the above-mentioned features. The ease of introducing specific functionalities into the structure either prior to the synthesis or through post-synthetic

modification has facilitated the ease to regulate the drug loading and realising mechanisms with the utmost consideration. So far, the most used mediums for drug delivery are polymeric and liposome systems, along with a few porous materials such as zeolites.[114] Using organic systems have the propensity of biocompatibility and the flexibility with numerous kinds of drugs but the major drawback is the uncontrolled rate of drug delivery. On the other hand, while inorganic systems have controlled rate of discharge of the drugs, they come with other drawbacks such as regioselectivity and so on. Thus, developing porous systems such as MOFs with desired properties gives an upper hand over the other existing materials as it addresses the drawbacks while keeping the beneficial attributes of both organic and inorganic components. Using MOFs for drug delivery can abate the side effects of the active pharmaceutical ingredient (API) and thereby increasing the drug efficiency.[115]

Horcajada and co-workers were the first to report on the utility of MOFs for the drug delivery systems.[116] In their study, they used Cr-MIL-100 and Cr-MIL-101 for encapsulating anti-inflammatory and analgesic ibuprofen inside the pores. The stability of these MOFs in water prevents their rapid degradation and ensures proper drug delivery. Brenda and co-workers investigated on encapsulating aspirin into Fe-MIL-100.[117] In this study, the MOF was immersed in the aspirin solution and the drug loading efficiency was monitored using time-of-flight mass spectroscopy which came to be about 181 %. The release of the drug took nearly 18 days when dissolved in phosphate buffer saline solution at body temperature. This study shows a direct relationship of drug loading efficiency with the pore volume of the MOF. Nanoscale MOFs are also extensively designed as they are the potential nano-vectors for delivering therapeutic agents to targeted areas of the body, as they can control drug release with their large surface areas, high porosity, and presence of functional groups to interact with loaded moieties. Lin and co-workers

studied on this class of MOFs, especially on nano Fe-MIL-101 for loading fluorophores and anticancer agents via post-synthetic modifications.[118]

1.5.5 Other Applications of MOFs

MOFs have been investigated and eventually have shown excellent potential in a variety of applications, especially in the fields where porosity has been the major criteria. Apart from the applications mentioned above, MOFs find utility in other areas like biomedical applications, for instance in MRI contrast agents, LED and sensor applications, magnetism, molecular sieve, etc.[119-121] Diversity in structural architectures and tunable properties have enabled the use of MOFs in these various fields. Regulating the luminescence properties of the MOFs by modifying the metal and ligand parts, has resulted in their great potential for usage in light-emitting devices. By the same judicious selection of counterparts which can respond to the external stimuli, MOFs have entered the field of sensors. By selecting metal systems with magnetic properties, they have shown a great deal of potential in magnetic applications. In summary, the ease of designing MOFs has enabled the fine controlling of the structure and properties allowing to meet the demand of the specialized application whichsoever is to be fulfilled.

1.6 References

1. Addington, D. M.; Schodek, D. L., *Smart materials and new technologies: for the architecture and design professions*. Routledge: 2005.
2. Kumar, M.; Kumar, S.; Tyagi, S., Design, development and technological advancement in the biomass cookstoves: A review. *Renew. Sust. Energ. Rev.* **2013**, *26*, 265-285.
3. Bogue, R., Smart materials: a review of recent developments. *Assembly Automation* **2012**.
4. Bogue, R., Smart materials: A review of capabilities and applications. *Assembly Automation* **2014**.
5. Saidur, R.; Rahim, N.; Islam, M.; Solangi, K., Environmental impact of wind energy. *Renew. Sust. Energ. Rev.* **2011**, *15* (5), 2423-2430.
6. Mezher, T.; Fath, H.; Abbas, Z.; Khaled, A., Techno-economic assessment and environmental impacts of desalination technologies. *Desalination* **2011**, *266* (1-3), 263-273.
7. Brantley, L. R.; Brantley, R. T., *Building materials technology: structural performance and environmental impact*. McGraw-Hill: 1996.
8. Gandhi, M. V.; Thompson, B., *Smart materials and structures*. Springer Science & Business Media: 1992.
9. Milo, R.; Shen-Orr, S.; Itzkovitz, S.; Kashtan, N.; Chklovskii, D.; Alon, U., Network motifs: simple building blocks of complex networks. *Science* **2002**, *298* (5594), 824-827.
10. Cornelissen, J. J. L. M.; Rowan, A. E.; Nolte, R. J. M.; Sommerdijk, N. A. J. M., Chiral architectures from macromolecular building blocks. *Chem. Rev.* **2001**, *101* (12), 4039-4070.
11. Lei, S.; Tahara, K.; De Schryver, F. C.; Van der Auweraer, M.; Tobe, Y.; De Feyter, S., One building block, two different supramolecular surface-confined patterns: concentration in control at the solid–liquid interface. *Angew. Chem. Int. Ed.* **2008**, *47* (16), 2964-2968.
12. Liu, K.; Zhang, X.; Meng, X.; Shi, W.; Cheng, P.; Powell, A. K., Constraining the coordination geometries of lanthanide centers and magnetic building blocks in frameworks: a new strategy for molecular nanomagnets. *Chem. Soc. Rev.* **2016**, *45* (9), 2423-2439.
13. Evans, O. R.; Lin, W., Crystal engineering of NLO materials based on metal–organic coordination networks. *Acc. Chem. Res.* **2002**, *35* (7), 511-522.
14. Van Krevelen, D. W.; Te Nijenhuis, K., *Properties of polymers: their correlation with chemical structure; their numerical estimation and prediction from additive group contributions*. Elsevier: 2009.
15. Stuart, S. J.; Tutein, A. B.; Harrison, J. A., A reactive potential for hydrocarbons with intermolecular interactions. *J. Chem. Phys.* **2000**, *112* (14), 6472-6486.

16. Sanchez, F.; Sobolev, K., Nanotechnology in concrete–a review. *Construction and building materials* **2010**, *24* (11), 2060-2071.

17. Pokropivny, V.; Lohmus, R.; Hussainova, I.; Pokropivny, A.; Vlassov, S., *Introduction to nanomaterials and nanotechnology*. Tartu University Press Ukraine: 2007.

18. Liu, P.; Qin, R.; Fu, G.; Zheng, N., Surface coordination chemistry of metal nanomaterials. *J. Am. Chem. Soc.* **2017**, *139* (6), 2122-2131.

19. Glasser, O., *Wilhelm Conrad Röntgen and the early history of the Roentgen rays*. Norman Publishing: 1993.

20. Guinier, A., *X-ray diffraction in crystals, imperfect crystals, and amorphous bodies*. Courier Corporation: 1994.

21. Flack, H.; Bernardinelli, G., The use of X-ray crystallography to determine absolute configuration. *Chirality: The Pharmacological, Biological, and Chemical Consequences of Molecular Asymmetry* **2008**, *20* (5), 681-690.

22. Trask, R.; Williams, H.; Bond, I., Self-healing polymer composites: mimicking nature to enhance performance. *Bioinspiration Biomimetics* **2007**, *2* (1), P1.

23. Parton, R. F.; Vankelecom, I. F.; Casselman, M. J.; Bezoukhanova, C. P.; Uytterhoeven, J. B.; Jacobs, P. A., An efficient mimic of cytochrome P-450 from a zeolite-encaged iron complex in a polymer membrane. *Nature* **1994**, *370* (6490), 541-544.

24. Rotem, S.; Mor, A., Antimicrobial peptide mimics for improved therapeutic properties. *Biochim. Biophys. Acta. Biomembr.* **2009**, *1788* (8), 1582-1592.

25. Li, Y.; Fu, Z. Y.; Su, B. L., Hierarchically structured porous materials for energy conversion and storage. *Adv. Funct. Mater.* **2012**, *22* (22), 4634-4667.

26. Ejima, H.; Richardson, J. J.; Liang, K.; Best, J. P.; van Koeverden, M. P.; Such, G. K.; Cui, J.; Caruso, F., One-step assembly of coordination complexes for versatile film and particle engineering. *Science* **2013**, *341* (6142), 154-157.

27. Cook, T. R.; Zheng, Y.-R.; Stang, P. J., Metal–organic frameworks and self-assembled supramolecular coordination complexes: comparing and contrasting the design, synthesis, and functionality of metal–organic materials. *Chem. Rev.* **2013**, *113* (1), 734-777.

28. Friese, V. A.; Kurth, D. G., From coordination complexes to coordination polymers through self-assembly. *Curr. Opin. Colloid Interface Sci.* **2009**, *14* (2), 81-93.

29. Li, G.; Hou, Y.; Wu, A., Fourth Industrial Revolution: technological drivers, impacts and coping methods. *Chin. Geogr. Sci.* **2017**, *27* (4), 626-637.

30. Schwab, K., *The fourth industrial revolution*. Currency: 2017.

31. Anderson, R. C. In *The next industrial revolution*, Forum for Applied Research and Public Policy, University of Tennessee, Energy, Environment and Resources Center: 2000; p 23.

32. Abas, N.; Kalair, A.; Khan, N., Review of fossil fuels and future energy technologies. *Futures* **2015**, *69*, 31-49.

33. Hoegh-Guldberg, O.; Jacob, D.; Bindi, M.; Brown, S.; Camilloni, I.; Diedhiou, A.; Djalante, R.; Ebi, K.; Engelbrecht, F.; Guiot, J., Impacts of 1.5 C global warming on natural and human systems. *Global warming of 1.5° C. An IPCC Special Report* **2018**.

34. Ritchie, H.; Roser, M., CO_2 and Greenhouse Gas Emissions. *OurWorldInData* **2017**.

35. Zárante, P. H. B.; Sodré, J. R., Evaluating carbon emissions reduction by use of natural gas as engine fuel. *J. Nat. Gas Sci. Eng.* **2009**, *1* (6), 216-220.

36. *https://www.bernini-impianti.it/fr/-actualites-et-evenements.html.*

37. Kitagawa, S.; Kitaura, R.; Noro, S. i., Functional porous coordination polymers. *Angew. Chem. Int. Ed.* **2004**, *43* (18), 2334-2375.

38. Chen, C.-T.; Suslick, K. S., One-dimensional coordination polymers: Applications to material science. *Coord. Chem. Rev.* **1993**, *128* (1-2), 293-322.

39. Bureekaew, S.; Shimomura, S.; Kitagawa, S., Chemistry and application of flexible porous coordination polymers. *Sci. Technol. Adv. Mater.* **2008**, *9* (1), 014108.

40. Zhang, X.; Wang, W.; Hu, Z.; Wang, G.; Uvdal, K., Coordination polymers for energy transfer: Preparations, properties, sensing applications, and perspectives. *Coord. Chem. Rev.* **2015**, *284*, 206-235.

41. Yamada, T.; Otsubo, K.; Makiura, R.; Kitagawa, H., Designer coordination polymers: dimensional crossover architectures and proton conduction. *Chem. Soc. Rev.* **2013**, *42* (16), 6655-6669.

42. Ma, Z.; Moulton, B., Recent advances of discrete coordination complexes and coordination polymers in drug delivery. *Coord. Chem. Rev.* **2011**, *255* (15-16), 1623-1641.

43. Barthomeuf, D., Basic zeolites: characterization and uses in adsorption and catalysis. *Catal. Rev.* **1996**, *38* (4), 521-612.

44. Kauffman, G. B., *Alfred Werner: Founder of Coordination Chemistry*. Springer Science & Business Media: 2013.

45. Lawrance, G. A., Complexes. In *Introduction to Coordination Chemistry*, 2009; pp 41-82.

46. Wells, A. F., *Three dimensional Nets and Polyhedra*. Wiley: New York: 1977.

47. Hoskins, B.; Robson, R., Design and construction of a new class of scaffolding-like materials comprising infinite polymeric frameworks of 3D-linked molecular rods. A reappraisal of the zinc cyanide and cadmium cyanide structures and the synthesis and structure of the diamond-related frameworks $[N(CH_3)_4][Cu(I)Zn(II)(CN)_4]$ and Cu(I)[4,4',4",4'"-tetracyanotetraphenylmethane]$BF_4.xC_6H_5NO_2$. *J. Am. Chem. Soc.* **1990**, *112* (4), 1546-1554.

48. Sunday, N. F., Emerging trends in coordination polymers and metal-organic frameworks: perspectives, synthesis, properties and applications. *Arch. Org. Inorg. Chem. Sci.* **2018**, *1* (2), 39-51.

49. Mas-Ballesté, R.; Gómez-Herrero, J.; Zamora, F., One-dimensional coordination polymers on surfaces: towards single molecule devices. *Chem. Soc. Rev.* **2010**, *39* (11), 4220-4233.

50. Vittal, J. J., Supramolecular structural transformations involving coordination polymers in the solid state. *Coord. Chem. Rev.* **2007**, *251* (13-14), 1781-1795.

51. Batten, S. R.; Neville, S. M.; Turner, D. R., *Coordination polymers: design, analysis and application*. Royal Society of Chemistry: 2008.

52. Rowsell, J. L.; Yaghi, O. M., Metal–organic frameworks: a new class of porous materials. *Microporous Mesoporous Mater.* **2004**, *73* (1-2), 3-14.

53. Long, J. R.; Yaghi, O. M., The pervasive chemistry of metal–organic frameworks. *Chem. Soc. Rev.* **2009**, *38* (5), 1213-1214.

54. Zhou, H.-C.; Long, J. R.; Yaghi, O. M., Introduction to metal–organic frameworks. ACS Publications: 2012.

55. Czaja, A. U.; Trukhan, N.; Müller, U., Industrial applications of metal–organic frameworks. *Chem. Soc. Rev.* **2009**, *38* (5), 1284-1293.

56. Schröder, M., *Functional metal-organic frameworks: gas storage, separation and catalysis*. Springer: 2010; Vol. 293.

57. Ma, S.; Zhou, H.-C., Gas storage in porous metal–organic frameworks for clean energy applications. *Chem. Commun.* **2010**, *46* (1), 44-53.

58. Kreno, L. E.; Leong, K.; Farha, O. K.; Allendorf, M.; Van Duyne, R. P.; Hupp, J. T., Metal–organic framework materials as chemical sensors. *Chem. Rev.* **2012**, *112* (2), 1105-1125.

59. Liu, J.; Thallapally, P. K.; McGrail, B. P.; Brown, D. R.; Liu, J., Progress in adsorption-based CO_2 capture by metal–organic frameworks. *Chem. Soc. Rev.* **2012**, *41* (6), 2308-2322.

60. Dhakshinamoorthy, A.; Alvaro, M.; Garcia, H., Commercial metal–organic frameworks as heterogeneous catalysts. *Chem. Commun.* **2012**, *48* (92), 11275-11288.

61. Diercks, C. S.; Kalmutzki, M. J.; Diercks, N. J.; Yaghi, O. M., Conceptual advances from werner complexes to metal–organic frameworks. *ACS Central Science* **2018**, *4* (11), 1457-1464.

62. Iwamoto, T., Aromatic guest molecules enclathrated in hofmann-type and analogous clathrates. *Isr. J. Chem.* **1979**, *18* (3-4), 240-245.

63. Büttner, H.; Kearley, G.; Howard, C.; Fillaux, F., Structure of the Hofmann clathrates $Ni(NH_3)_2Ni(CN)_4.2C_6D_6$ and $Zn(NH_3)2Ni(CN)_4.2C_6H_6$. *Acta Crystallogr. Sect. B: Struct. Sci.* **1994**, *50* (4), 431-435.

64. Bae, Y. S.; Snurr, R. Q., Development and evaluation of porous materials for carbon dioxide separation and capture. *Angew. Chem. Int. Ed.* **2011**, *50* (49), 11586-11596.

65. Hoskins, B. F.; Robson, R., Infinite polymeric frameworks consisting of three dimensionally linked rod-like segments. *J. Am. Chem. Soc.* **1989**, *111* (15), 5962-5964.

66. Li, H.; Eddaoudi, M.; O'Keeffe, M.; Yaghi, O. M., Design and synthesis of an exceptionally stable and highly porous metal-organic framework. *Nature* **1999**, *402* (6759), 276-279.

67. Chui, S. S.-Y.; Lo, S. M.-F.; Charmant, J. P.; Orpen, A. G.; Williams, I. D., A chemically functionalizable nanoporous material $[Cu_3(TMA)_2(H_2O)_3]_n$. *Science* **1999**, *283* (5405), 1148-1150.

68. Fletcher, A. J.; Thomas, K. M.; Rosseinsky, M. J., Flexibility in metal-organic framework materials: Impact on sorption properties. *J. Solid State Chem.* **2005**, *178* (8), 2491-2510.

69. Bennett, T. D.; Goodwin, A. L.; Dove, M. T.; Keen, D. A.; Tucker, M. G.; Barney, E. R.; Soper, A. K.; Bithell, E. G.; Tan, J.-C.; Cheetham, A. K., Structure and properties of an amorphous metal-organic framework. *Phys. Rev. Lett.* **2010**, *104* (11), 115503.

70. Hagrman, P. J.; Hagrman, D.; Zubieta, J., Organic–inorganic hybrid materials: from "simple" coordination polymers to organodiamine-templated molybdenum oxides. *Angew. Chem. Int. Ed.* **1999**, *38* (18), 2638-2684.

71. Eddaoudi, M.; Moler, D. B.; Li, H.; Chen, B.; Reineke, T. M.; O'keeffe, M.; Yaghi, O. M., Modular chemistry: secondary building units as a basis for the design of highly porous and robust metal– organic carboxylate frameworks. *Acc. Chem. Res.* **2001**, *34* (4), 319-330.

72. Zhang, J.; Matsushita, M. M.; Kong, X. X.; Abe, J.; Iyoda, T., Photoresponsive coordination assembly with a versatile logs-stacking channel structure based on redox-active ligand and cupric ion. *J. Am. Chem. Soc.* **2001**, *123* (48), 12105-12106.

73. Tilborg, A.; Springuel, G.; Norberg, B.; Wouters, J.; Leyssens, T., How cocrystallization affects solid-state tautomerism: stanozolol case study, Cryst. Growth Des., 2014, 14 (7), 3408.

74. Wohler, F., Studies on the Quinone, Ann. Chem. Pharm., 1844, 51, 145.

75. Aakeroy, C. B., Is there any point in making co-crystals? Acta Crystallogr., Sect. B: Struct. Sci., Cryst. Eng. Mater., 2015, 71 (4), 387–391.

76. Gunawardana, C. A.; Aakeroy, C. B., Co-crystal synthesis: fact, fancy, and great expectations, Chem. Commun., 2018, 54 (100), 14047.

77. Oura, K.; Lifshits, V.; Saranin, A.; Zotov, A.; Katayama, M., *Surface science: an introduction*. Springer Science & Business Media: 2013.

78. Ruthven, D. M., *Principles of adsorption and adsorption processes*. John Wiley & Sons: 1984.

79. Kinniburgh, D. G., General purpose adsorption isotherms. *Environ. Sci. Technol.* **1986**, *20* (9), 895-904.

80. Langmuir, I., The constitution and fundamental properties of solids and liquids. Part I. Solids. *J. Am. Chem. Soc.* **1916**, *38* (11), 2221-2295.

81. Ayawei, N.; Ebelegi, A. N.; Wankasi, D., Modelling and Interpretation of Adsorption Isotherms. *J. Chem.* **2017**, *2017*, 3039817.

82. Freundlich, H., Over the adsorption in solution. *J. Phys. Chem* **1906**, *57* (385471), 1100-1107.

83. Adamson, A. W.; Gast, A. P., *Physical chemistry of surfaces*. Interscience publishers New York: 1967; Vol. 150.

84. Brunauer, S.; Emmett, P. H.; Teller, E., Adsorption of gases in multimolecular layers. *J. Am. Chem. Soc.* **1938**, *60* (2), 309-319.

85. Toth, J., State equation of the solid-gas interface layers. *Acta Chim. Hung.* **1971**, *69*, 311-328.

86. Schoen Jr, O. W., Dew point hygrometer. Google Patents: 1987.

87. Dunmore, F. W., An electric hygrometer and its application to radio-meteorography. *Bull. Am. Meteorol. Soc.* **1938**, *19* (6), 225-243.

88. Sonntag, D., Advancements in the field of hygrometry. *Meteorol. Z.* **1994**, 51-66.

89. Chen, Z.; Lu, C., Humidity sensors: a review of materials and mechanisms. *Sensor Lett.* **2005**, *3* (4), 274-295.

90. Farahani, H.; Wagiran, R.; Hamidon, M. N., Humidity sensors principle, mechanism, and fabrication technologies: a comprehensive review. *Sensors* **2014**, *14* (5), 7881-7939.

91. Rittersma, Z., Recent achievements in miniaturised humidity sensors—a review of transduction techniques. *Sens. Actuators, A* **2002**, *96* (2-3), 196-210.

92. Kolpakov, S. A.; Gordon, N. T.; Mou, C.; Zhou, K., Toward a new generation of photonic humidity sensors. *Sensors* **2014**, *14* (3), 3986-4013.

93. Kim, S. H.; Jeon, S. Y.; Yoo, P. J.; Pu, L. S.; Lee, J. Y., Metal oxide/polymer hybrid nanofiber as flexible moisture absorbent. *Fibers Polym.* **2013**, *14* (12), 1975-1980.

94. Vogt, B. D.; Soles, C. L.; Lee, H.-J.; Lin, E. K.; Wu, W.-l., Moisture absorption and absorption kinetics in polyelectrolyte films: influence of film thickness. *Langmuir* **2004**, *20* (4), 1453-1458.

95. Wang, Z.; Catabay, W. G.; Zhao, J. W., Process for treating damaged surfaces of low dielectric constant organo silicon oxide insulation material to inhibit moisture absorption. Google Patents: 2000.

96. Traversa, E., Ceramic sensors for humidity detection: the state-of-the-art and future developments. *Sens. Actuators, B* **1995**, *23* (2-3), 135-156.

97. Blank, T.; Eksperiandova, L.; Belikov, K., Recent trends of ceramic humidity sensors development: A review. *Sens. Actuators, B* **2016**, *228*, 416-442.

98. Schueth, F.; Schmidt, W., Microporous and mesoporous materials. *Adv. Eng. Mater.* **2002**, *4* (5), 269-279.

99. Parlett, C. M.; Wilson, K.; Lee, A. F., Hierarchical porous materials: catalytic applications. *Chem. Soc. Rev.* **2013**, *42* (9), 3876-3893.

100. Jiao, L.; Jiang, H.-L., Metal-organic-framework-based single-atom catalysts for energy applications. *Chem* **2019**, *5* (4), 786-804.

101. Huang, Y.-B.; Liang, J.; Wang, X.-S.; Cao, R., Multifunctional metal–organic framework catalysts: synergistic catalysis and tandem reactions. *Chem. Soc. Rev.* **2017**, *46* (1), 126-157.

102. Wu, C.-D.; Hu, A.; Zhang, L.; Lin, W., A homochiral porous metal– organic framework for highly enantioselective heterogeneous asymmetric catalysis. *J. Am. Chem. Soc.* **2005**, *127* (25), 8940-8941.

103. Fei, H.; Cohen, S. M., A robust, catalytic metal–organic framework with open 2, 2′-bipyridine sites. *Chem. Commun.* **2014**, *50* (37), 4810-4812.

104. Vermoortele, F.; Ameloot, R.; Vimont, A.; Serre, C.; De Vos, D., An amino-modified Zr-terephthalate metal–organic framework as an acid–base catalyst for cross-aldol condensation. *Chem. Commun.* **2011**, *47* (5), 1521-1523.

105. Aijaz, A.; Karkamkar, A.; Choi, Y. J.; Tsumori, N.; Rönnebro, E.; Autrey, T.; Shioyama, H.; Xu, Q., Immobilizing highly catalytically active Pt nanoparticles inside the pores of metal–organic framework: a double solvents approach. *J. Am. Chem. Soc.* **2012**, *134* (34), 13926-13929.

106. Hasegawa, S.; Horike, S.; Matsuda, R.; Furukawa, S.; Mochizuki, K.; Kinoshita, Y.; Kitagawa, S., Three-dimensional porous coordination polymer functionalized with amide groups based on tridentate ligand: selective sorption and catalysis. *J. Am. Chem. Soc.* **2007**, *129* (9), 2607-2614.

107. Seo, J. S.; Whang, D.; Lee, H.; Im Jun, S.; Oh, J.; Jeon, Y. J.; Kim, K., A homochiral metal–organic porous material for enantioselective separation and catalysis. *Nature* **2000**, *404* (6781), 982-986.

108. Roberts, J. M.; Fini, B. M.; Sarjeant, A. A.; Farha, O. K.; Hupp, J. T.; Scheidt, K. A., Urea metal–organic frameworks as effective and size-selective hydrogen-bond catalysts. *J. Am. Chem. Soc.* **2012**, *134* (7), 3334-3337.

109. Zang, Y.; Shi, J.; Zhang, F.; Zhong, Y.; Zhu, W., Sulfonic acid-functionalized MIL-101 as a highly recyclable catalyst for esterification. *Catal. Sci. Technol.* **2013**, *3* (8), 2044-2049.

110. Luan, Y.; Qi, Y.; Gao, H.; Andriamitantsoa, R. S.; Zheng, N.; Wang, G., A general post-synthetic modification approach of amino-tagged metal–organic frameworks to access efficient catalysts for the Knoevenagel condensation reaction. *J. Mater. Chem. A* **2015**, *3* (33), 17320-17331.

111. Hartmann, M.; Fischer, M., Amino-functionalized basic catalysts with MIL-101 structure. *Microporous Mesoporous Mater.* **2012**, *164*, 38-43.

112. Sun, C.-Y.; Qin, C.; Wang, X.-L.; Su, Z.-M., Metal-organic frameworks as potential drug delivery systems. *Expert Opin. Drug Del.* **2013**, *10* (1), 89-101.

113. Keskin, S.; Kızılel, S., Biomedical applications of metal organic frameworks. *Ind. Eng. Chem. Res.* **2011**, *50* (4), 1799-1812.

114. Lee, S.-M.; Nguyen, S. T., Smart nanoscale drug delivery platforms from stimuli-responsive polymers and liposomes. *Macromolecules* **2013**, *46* (23), 9169-9180.

115. Teplensky, M. H.; Fantham, M.; Li, P.; Wang, T. C.; Mehta, J. P.; Young, L. J.; Moghadam, P. Z.; Hupp, J. T.; Farha, O. K.; Kaminski, C. F., Temperature treatment of highly porous zirconium-containing metal–organic frameworks extends drug delivery release. *J. Am. Chem. Soc.* **2017**, *139* (22), 7522-7532.

116. Horcajada, P.; Serre, C.; Maurin, G.; Ramsahye, N. A.; Balas, F.; Vallet-Regi, M.; Sebban, M.; Taulelle, F.; Férey, G., Flexible porous metal-organic frameworks for a controlled drug delivery. *J. Am. Chem. Soc.* **2008**, *130* (21), 6774-6780.

117. Singco, B.; Liu, L.-H.; Chen, Y.-T.; Shih, Y.-H.; Huang, H.-Y.; Lin, C.-H., Approaches to drug delivery: Confinement of aspirin in MIL-100 (Fe) and aspirin in the de novo synthesis of metal–organic frameworks. *Microporous Mesoporous Mater.* **2016**, *223*, 254-260.

118. Taylor-Pashow, K. M.; Della Rocca, J.; Xie, Z.; Tran, S.; Lin, W., Postsynthetic modifications of iron-carboxylate nanoscale metal– organic frameworks for imaging and drug delivery. *J. Am. Chem. Soc.* **2009**, *131* (40), 14261-14263.

119. Liu, D.; Lu, K.; Poon, C.; Lin, W., Metal–organic frameworks as sensory materials and imaging agents. *Inorg. Chem.* **2014**, *53* (4), 1916-1924.

120. Cui, Y.; Chen, B.; Qian, G., Lanthanide metal-organic frameworks for luminescent sensing and light-emitting applications. *Coord. Chem. Rev.* **2014**, *273*, 76-86.

121. Coronado, E.; Espallargas, G. M., Dynamic magnetic MOFs. *Chem. Soc. Rev.* **2013**, *42* (4), 1525-1539.

Chapter 2: Projects Overview

2.1 Introduction

In the previous chapter, a general overview of the concerns to be addressed in the thesis was presented. The major issues being the energy crisis and global warming, which seem to be the most discussed areas in various fields of science including material chemistry where tremendous efforts have been put forward for the betterment of the situation. The demand for energy for every nation around the globe has been enormous since the beginning of the industrial revolution. This has been perceived due to the exponentially increasing population and rapidly growing technologies. Traditional methods to harvest and store energies have started to see the limitations due to the rapid depletion of fossil fuels which are the primary sources of energy. The extensive use of fossil fuels has also caused severe disastrous impacts on the ecosystem such as global warming, acid rain, droughts, extinction of many plants and animals, etc. Recent catastrophic events and worldwide climatic studies have proved that the global temperature has increased by around 2 °C over the last decade.[1] The search for an alternate energy form ended up with the most promising renewable energy resources such as solar, wind, geothermal heat, tidal, and various forms of biomass energies which are available in abundance. The major issues concerning the use of these renewable energy resources are the technologies and materials adopted to harvest and convert them into usable energy. Currently none of the energy technologies is efficient enough to meet the growing demand of global consumption, thereby making the energy produced from these resources uneconomical.

One of the best methods to maximize the resource outcome is to improve the existing technologies dealing with energy harvesting approaches. A major part of the energy consumption still comes from fossil fuels with a turnover of about 85% of the energies consumed.[2] Coal and petroleum playing a major role in this sector, the current types of

machinery survive on these sources. Instead of modifying the machineries, the best remedy would be to alter the fuel source which can be used to run the existing machines. Hydrogen is one of the cleanest and efficient fuels in this course. Though hydrogen has been said to be the next-generation fuel, there stands a foremost barrier of storage of the gas. Conventional methods store hydrogen in heavy walled containers, which retrogresses the technology due to the additional energy required for storage. This effect is more pronounced when dealing with automobiles which reduce efficiency. In this case, a large volume of space, as well as the total weight of the system is compensated. Another most widely available source of fuel is natural gas which is generated during the mining process. Natural gas as a fuel is the second most reliable resource. A study by the National Renewable Energy Laboratory estimated that surface mining releases 1.91 grams of methane per kilogram of surface-mined coal and 4.23 grams of methane per kilogram of underground-mined coal.[3,4] Studies show that methane has been a major contributor to greenhouse gases. The negative effect of methane on climate is 23 times higher than the effect of CO_2. Thus, utilizing the methane produced in nature is a simple and effective method to solve two issues, *viz*, energy demand, and global warming.

The chemical composition of natural gas consists of methane (>85%), ethane (3-8%), propane (1-2%), butane (<1%), carbon dioxide (1-2%), oxygen (0-0.2%), nitrogen (1-5%), hydrogen sulphide (<1%), and other rare gases (0-2%).[5,6] Except hydrogen sulphide and CO_2, the rest are active fuel systems. Hydrogen sulphide and a partial amount of CO_2 are initially removed from natural gas using gas sweetening systems (GSS), also known as amine treatment. In the case of gas vents with a higher percentage of CO_2, this method has its limitations leading to an increased amount of CO_2 in natural gas. This adversely affects the performance of the engine and eventually leads to the lower efficiency of the fuel. Thus, several efforts have been made to develop methods to separate CO_2 from CH_4.

Earlier, liquid ammonia spray was employed for this job, but the reusability of the ammonia was impossible due to the strong chemical bondage forming ammonium carbamate. A solution to this issue can also be hired from other industrial and automobile sectors for CO_2 capture thereby reducing the CO_2 emission to the atmosphere. Apart from the energy crisis and global warming, other areas where new materials are gaining ground include sensors, biomedical, pharmaceuticals, etc.

Metal-Organic Frameworks are foreseen as the potential materials for the environmental issues mentioned above mainly due to their versatility and tunable properties. For instance, incorporation of more than one type of metal in coordination polymers can result in the formation of solid solutions, which combines the properties of both the metals. This strategy allows creating advanced materials with hybrid properties. Depending on the ratio of each metal incorporated in the framework, the intrinsic properties can differ thereby facilitating the use of these materials in diverse applications. The development of mixed metal MOFs is also challenging mainly due to the preferential coordination nature of the organic ligands. Isostructural MOFs formed from the same organic ligand and different metal centres can be used to create mixed metal MOFs with intrinsic properties of the diverse metal ions in the framework. Until now, most of the coordination polymers have been synthesized in conditions which are not viable for industrial-scale preparation such as elevated temperatures, toxic solvents, high pressures, etc. Thus, new cost-effective and eco-friendly synthetic methods need to be developed to meet industrial demands.

2.1.1 Metal Selection Criteria

MOFs have found potential applications in many areas including molecular sieves and catalysis. Intense research has been carried on developing novel MOFs for energy storage and gas separation. Transition metals are being commonly employed as metal centres due to their coordination numbers, properties and stability. Promising properties of MOFs are mainly due to the metals incorporated in the system. Depending on the properties exhibited by the transition metals, a drastic variation in material output can be achieved. Among these, the most attractive properties are the *d-d* electronic transitions with different oxidation states due to the relatively lower energy gap and the presence of unpaired *d* electrons. These spectacular features result in selecting transition metals for the formation of infinite frameworks along with additional advantages in the areas of magnetism and sensors. Due to their ability to have multiple oxidation states, transition metals also drive the attention in the catalysis field.

To improve the coordination core, metals with higher coordination numbers are an ideal replacement. Lanthanides are a class of rare-earth metals containing higher coordination numbers than other elements making them good candidates for MOF synthesis. A few of the Lanthanide-based MOFs have driven considerable attention due to their ability to form multifunctional hybrid materials; merging their fundamental porous character with physical properties coming from the rare-earth elements; in the field of magnetism, catalysis, and luminescence.

2.1.2 Ligand Selection Criteria

A major issue in the field of MOFs is the structural, thermal and chemical stability of the frameworks. Ever since the discussion on simple and complex Metal-Organic Frameworks, it has been evident that the functional linkage moiety, which has been extensively used, is the carboxylate group.[7] A few advantages of the carboxylate group include their ready accessibility and their easy perceivable structures in combination with different metals. Despite these advantages, the rigidity of the framework formed by the coordination of metals to carboxylate groups is weak which affects their structural stability. This may be due to the free rotation that is available in the bonds connecting the carboxylate groups to the organic moiety. Most of the MOFs collapse when the pores are emptied which has a direct relationship with the functionality they possess. Thus, there is a great need to develop MOFs with organic functionalities which provide stable architectures.

As an alternate to carboxylate functionality, the replaced systems should possess a few criteria including a similar attachment with the metal species. Additional properties must be exhibited from the ligand. For this, nitrogen-rich systems are encouraged as they are electron-deficient and have a higher affinity towards CO_2 gas. Planar molecules are another preference as they can lead to predictable structures. Ligand species which are aromatic and connected can exhibit planarity. Keeping in consideration all these criteria, the best alternative seems to be the ligands containing pyridone functionality.

A major advantage of replacing carboxylates by pyridines is the versatility in coordination modes compared to carboxylates and an improvement in stability. As the free rotation in the C-C-O axis, in the case of carboxylates is replaced by the rigid N-C-O in pyridines, which cannot rotate due to the aromatic connectivity, the stability of the MOFs formed

with pyridone motifs increases. Shown in Scheme 2.1 is the restriction in rotation induced by the pyridone functionality.

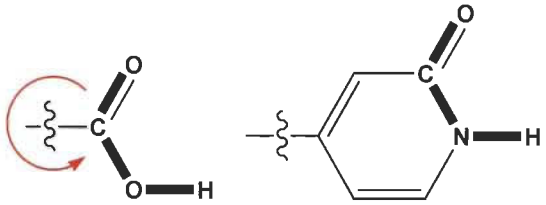

Carboxylic acid **Pyridone**

Scheme 2.1. Schematic representation showing the restriction of free rotation along the carbonyl bond in pyridonyl functionality.

Considering these characteristics, a series of ligands containing pyridonyl groups have been selected with cyamelurate compounds being one of them. Redeman and Lucas were the first to report on the base hydrolysis of melon polymer using aqueous KOH to form the salt, potassium cyamelurate ($K_3C_6N_7O_3$).[8,9] Kroke and co-workers have reported the synthesis of a series of alkali cyamelurates along with their crystal structures.[10] Later, James R. Holst reported the synthesis of various metal cyamelurates.[11,12] Getting inspired from these works and seeing the fact that potassium cyamelurate is water-soluble, the coordination chemistry of this ligand was focussed on prior consideration. Also, the structure of cyamelurate satisfied all the criteria which were focussed, mainly on the planarity and N-rich component. Additionally, the cyamelurates undergo improved pyridonyl coordination modes due to the multiple coordination sites which gives an upper hand to construct versatile coordination polymers and MOFs. Scheme 2.2 shows the different coordination modes available in different organic ligands.

On the other hand, ligands that resemble the various carboxylate moieties were also designed and developed including the dipyridone systems, discussed in chapter 3.

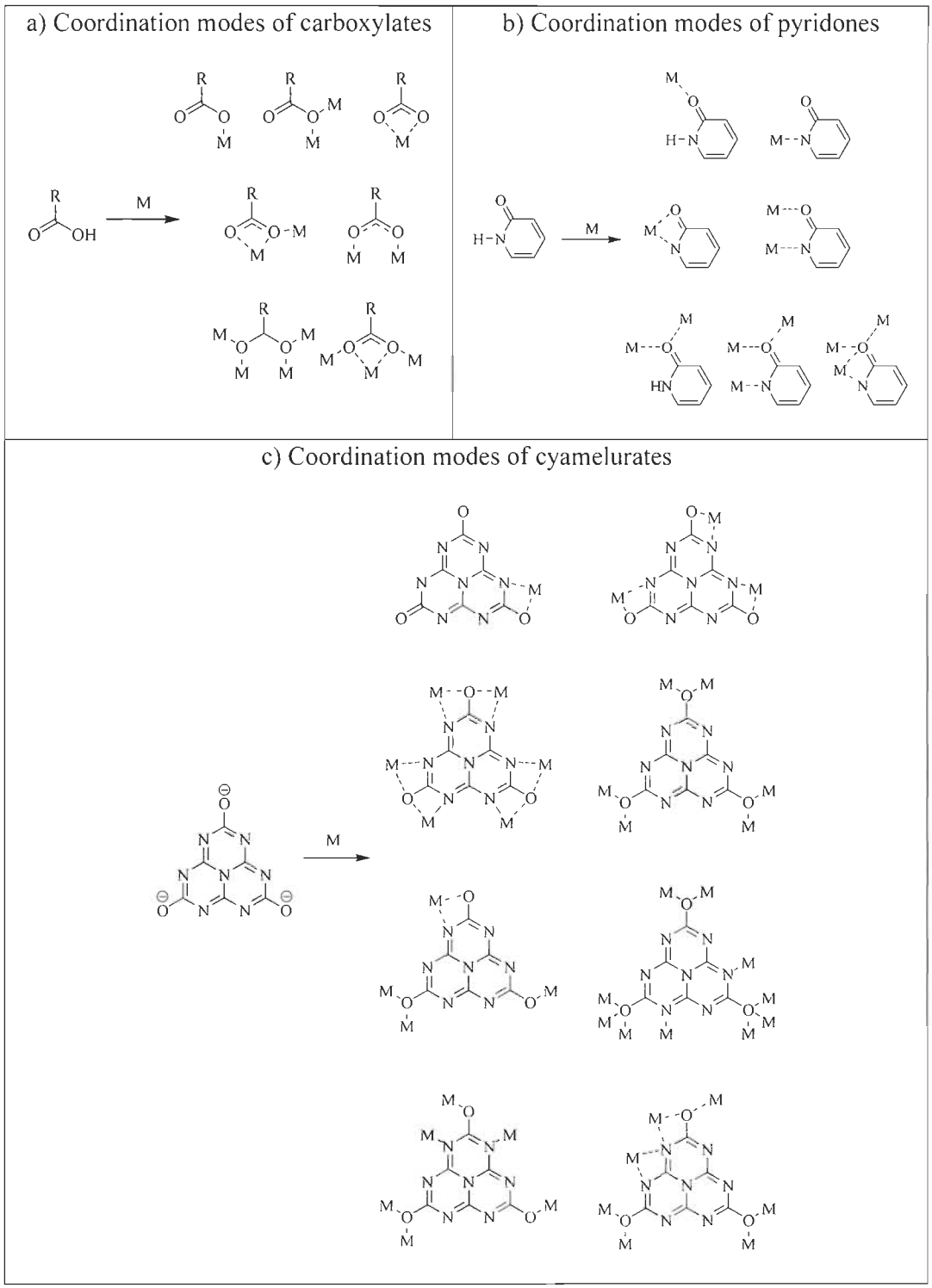

Scheme 2.2. Schematic representation showing coordination modes in different functionalities. a) Carboxylates b) Pyridones c) Cyamelurates.

Table 2.1. Table showing the resemblance of a few of the dipyridone ligands synthesized with the existing carboxylate ligands.

Dipyridone ligands synthesized	Carboxylate ligands	MOFs with the carboxylate ligands
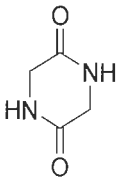	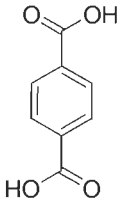	MOF-5[13] UiO-66[16]
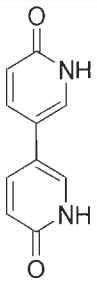	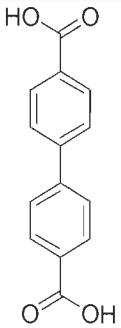	MOF-118[14], IRMOF-10[15],

2.2 Materials and Methods

All chemicals were purchased from either one of the vendors such as Sigma Aldrich, Alfa Aesar, and TCI. Solvents were purchased from Fischer Scientific. All chemicals were purchased in high purity and used without further purification.

2.2.1 Safety measurements

Safety inside as well as outside the laboratory has been the primary and utmost consideration. Prior to the synthesis, all safety measures and trainings were undertaken. Safety trainings include WHMIS, Hydrogen safety training, liquid nitrogen safety

training, fire safety training, and laboratory safety training. Apart from these, a thorough understanding of all the equipment in the laboratory was made sure. Along with these, the hazards associated with the chemicals were also taken into consideration while working in the laboratory.

2.2.2 Waste Management

In a chemical laboratory, it is as important to take care of the chemical wastes as much as the reactions done. All chemical wastes were disposed according to the University norms and regulations. Solvents were either recycled using the rotary evaporator or disposed in the separate containers labelled for specific solvents along with their percentage. Solid chemical wastes, glass wastes and recyclable wastes such as syringes were disposed separately. Silica wastes were dried prior to the disposal in separate containers. Used glass vials were mostly recycled for other purposes. Acid and base wastes were identified in separate containers too. All reactions were carried inside the fume hood to ensure safety as well as to purge out any gaseous wastes produced.

2.2.3 Synthesis of Potassium Cyamelurate

Synthesis of potassium cyamelurate was undergone using reported methods.[11] In the synthesis, melamine used as the precursor was taken in a crucible and heated at 490 °C for 4 days. A yellow powder of melon was obtained which was suspended in 2.5 M KOH solution. The mixture was refluxed for 4 hrs after which the solution becomes clear. The reaction mixture was cooled to room temperature followed by cooling at 0 °C to obtain

white precipitates of potassium cyamelurate. It was then filtered; washed with cold ethanol and dried under vacuum.

2.2.4 General Synthesis and Mechanism of Suzuki Coupling Reaction

Suzuki coupling reaction is a palladium catalysed cross-coupling reaction between organoboronic acids and organohalides.[17] It was first reported in 1979 which later lead to Nobel Prize in 2010. This reaction is employed for the C-C bond formation. A general synthesis of Suzuki coupling is shown in Scheme 2.3.

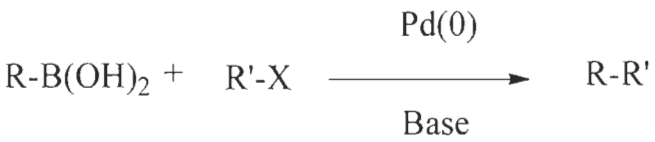

Scheme 2.3. Schematic representation of the Suzuki coupling reaction.

The general mechanism of Suzuki coupling is shown in Scheme 2.4. It involves three basic steps, oxidative addition, trans-metalation and reductive elimination. The reaction initiates with the reduction of Pd(II) to Pd(0) which undergoes oxidative addition with the aryl halide forming organopalladium species. This then undergoes base addition followed by trans-metalation with organoboronate complex (formed by the reaction of base with organoboronic acid) forming organopalladium species containing both aryl groups. In the final step, the desired product is formed by reductive elimination which also regenerates the Pd(0) species.

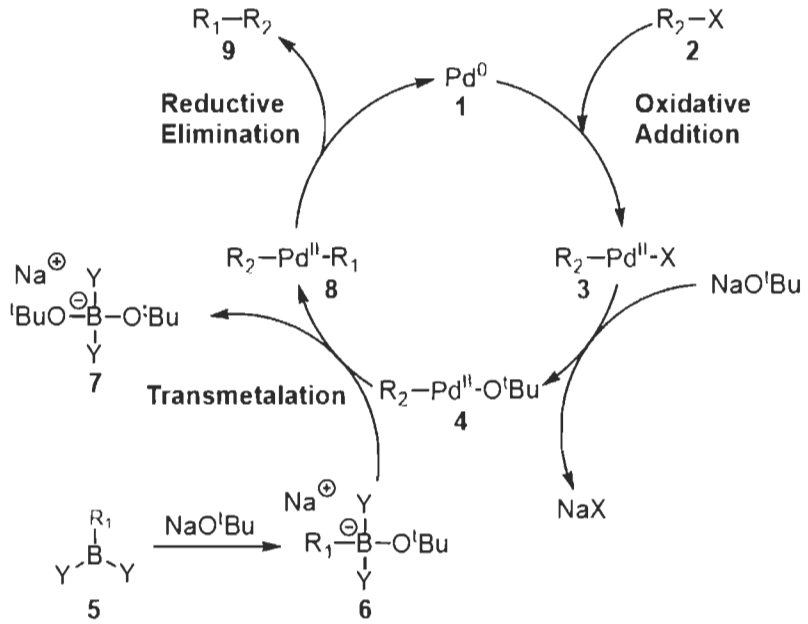

Scheme 2.4. Schematic representation of the mechanism of Suzuki coupling reaction.

2.3 Characterization techniques

The initial progress of the work deals with the design and syntheses of various materials through a thorough understanding of the properties to be exhibited. The second and far most important step is the characterization of the synthesized materials using various techniques including spectroscopic, microscopic, thermogravimetric, diffraction and adsorption techniques. These techniques are meant to provide valuable information including structural integrity, material stability, homogeneity, purity, understanding the functionality and the possession of required properties. A few of the techniques employed during the course of different projects are enlisted below.

2.3.1 Spectroscopic and Gravimetric Analysis Techniques

Fourier transform infrared spectroscopy is the technique to characterize the functional groups in a compound. It is used to obtain the infrared spectrum of absorption or emission of the compound. It calculates the amount of light absorbed by a sample at every 7 wavelengths when a beam of light containing many frequencies is directed towards the sample and the wavelengths that are absorbed by the sample are recorded. FTIR was performed using Nicolet iS10 Smart FT-IR spectrometer with an average range of 4000-600 cm^{-1}.

To determine the purity of the sample, Elemental analysis is carried out where, carbon, hydrogen, nitrogen and sulphur (C, H, N, S) content in the material are determined by combustion methods. Here, the sample analysis was performed using EA 1108 Fisons CHNS Element analyser by the quantitative dynamic flash combustion method. The solid-state UV-Vis spectra were recorded using Cary 5000 spectrophotometer. Samples were sandwiched between two quartz plates and measurement carried from 350-800 nm at a medium scan rate. ^{1}H and ^{13}C Nuclear Magnetic Resonance spectroscopy were recorded with 200 MHz, 400 MHz and 700 MHz in different projects. In a typical ^{1}H NMR 700 MHz, the spectra were recorded using Bruker BioSpin GmbH Version 3.2. XPS was performed using a model Axis Ultra with hybrid lens mode and acquisition time of 46 sec. Energy Dispersive X-ray Spectroscopy was coupled with Scanning Electron Microscopy. EDS was performed using X-Max 20 mm^2. EDS gives an idea of the elemental composition and can establish their relative concentration over the surface of the material. Thermal stability of the materials was determined using Thermogravimetric analyser using a Diamond Pyris TGA/DTA apparatus from Perkin-Elmer.

2.3.2 Microscopic Techniques

The morphology of the materials prepared was imaged using Scanning Electron Microscopy using JEOL 5500 model. This imaging technique gives us the pictorial view of particles at a higher magnification. In situ thermal microscopy was performed using a combination of a microscope Nikon Eclipse E200 and a hot stage microscopy system Mettler Toledo FP82.

2.3.3 Diffraction Techniques

Crystallographic data were collected using a Bruker Venture Metaljet diffractometer with Ga Kα radiation and Bruker Smart APEX 2 diffractometers with Cu Kα radiation. The structures were solved by dual-space algorithm using SHELXT, and non-hydrogen atoms were refined anisotropically with least squares minimization using SHELXL-2018.[18,19] Hydrogen atoms were treated by first locating them from difference Fourier maps, recalculating their positions using standard values for distances and angles, and then refining them as riding atoms. Microcrystalline powders were analysed in transmission-mode geometry using a Bruker D8-Discover instrument (θ–θ geometry) equipped with an XYZ platform and a HI-STAR gas detector. X-rays were generated using a conventional sealed-tube source with a copper anode producing Cu Kα radiation (λ = 1.54178 Å). The samples were gently ground and then mounted on a flat Kapton sample holder. The data collection involved the acquisition of two different sections with an increasing angular position, giving two different 2D frames. These frames were integrated and combined to produce the final 1D X-ray diffraction powder pattern. Calculated X-ray powder diffraction patterns were generated from the structural data in the corresponding

CIFs resulting from single-crystal analyses. The calculation was performed using Mercury software of the Cambridge Crystallographic Data Centre. A unique value of the FWHM for the diffraction peaks was adjusted in order to obtain a better match between the resolution of the experimental and the calculated patterns. Powder X-ray diffraction data were collected on a Bruker D8 Advance diffractometer equipped with a LYNXEYE linear position sensitive detector (Bruker AXS, Madison, WI). Neat samples were smeared directly onto the silicon wafer of a proprietary low-background sample holder. Data was collected using a continuous coupled $\theta/2\theta$ scan with Ni-filtered CuKα (λ = 1.54178 Å) radiation operating at 40 kV and 40 mA.

2.3.4 Adsorption Techniques

The specific surface area of the material was measured using Brunauer-Emmett-Teller (BET) surface area analysis method using Micromeritics 3Flex Version 5.02. Materials were analysed using CO_2 and Ar gases as adsorbates at 0 °C and -186 °C, respectively. Approximately 150 mg of samples were outgassed at 100 °C for 16 hrs.

The pure-component adsorption isotherms were measured using a laboratory-made static volumetric apparatus also referred to as Sievertz apparatus (Scheme 2.5). In this apparatus, the samples to be analysed were initially activated and weighed. The sample chamber was then sealed and connected to the reference chamber interlinked by valves. During the experiment, Gibbs excess adsorption of each component was calculated from material balance upon expanding a known amount of gas from the reference chamber (volume between the valve points of V_1, V_2 and V_3) to the measurement volume (reference volume + the additional volume between V_3 and S) where the sample was filled after activation which was placed in a thermostatic bath whose temperature can be

regulated and monitored through T_2. T_1 and P were employed to note the temperature and pressure changes during the gas expansion.

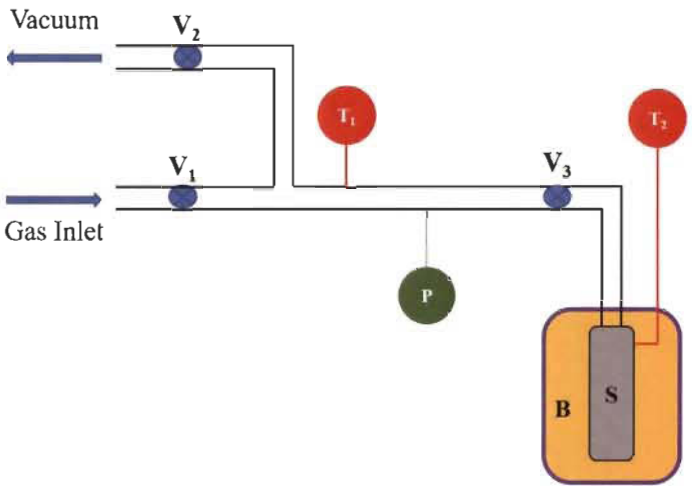

P	Pressure gauge
T_1, T_2	Thermocouples
V_1, V_2, V_3	Valves
S	Sample cell
B	Thermostatic bath

Scheme 2.5. Schematic representation of static volumetric apparatus.

2.4 General Organization of the Thesis

Synthesizing smart materials using coordination chemistry involves the development of two components, namely, organic ligands and metal ions or clusters. While designing the organic ligands, a few criteria were investigated with utmost priority. These include synthesizing stable nitrogen-rich organic ligands and polyconjugate systems for flat ligands with facile solubility especially in water, low cost of production, eco-friendly, cheaper starting materials, easy processability, and finally, containing multiple coordination sites. To address these properties, a novel series of pyridonyl based ligands

have been incorporated in this thesis. Various novel as well as known pyridonyl organic ligands were designed and synthesized during the course of the study. Further, these developed organic ligands were coordinated with transition and lanthanide metals in forming 1D, 2D and 3D coordination polymers including Metal-Organic Frameworks.

The structure of the thesis is as follows:

In chapter 1, general introduction of the material chemistry and issues to be addressed have been discussed. Also, a detailed discussion on various materials, especially Metal-Organic Frameworks and their applications have been discussed.

In chapter 2, a brief overview of the thesis has been presented. This chapter also emphasizes the general methodology incorporated in the thesis. A brief description of the selection criteria of metals and ligands has been discussed along with a summary of the instruments used.

In chapter 3, a series of multivalent pyridonyl compounds were synthesized using Suzuki coupling reaction. The crystal structures of the organic ligands prepared were characterized using XRD, NMR, FTIR, MS, and TGA. This work gives an insight to the development of a new class of organic linkers that pose structural versatility and stability to coordination polymers. The work is submitted to CrystEngComm.

[**Midhun Mohan**, Mohamed Essalhi, Sarah Zaye, Love Karan Rana, Thierry Maris and Adam Duong, Hydrogen bonds patterns in co-crystals of dipyridone, (Submitted in CrystEngComm, August 2020).]

In chapter 4, co-crystals of Co(II) salt and 1H,1'H-[3,3']bipyridinyl-6,6'-dione were prepared. An equivalent mixture of both components was determined from XRD and other characterization techniques. This work has been published in Canadian Journal of Chemistry.

[**Midhun Mohan**, Love Karan Rana, Thierry Maris and Adam Duong, Intercalated 2D + 2D hydrogen-bonded sheets in co-crystals of cobalt salt with 1 H ,1′ H -[3,3′]bipyridinyl-6,6′-dione. *Can. J. Chem.* **2020**, *98 (7)*, 347-351.]

In chapter 5, the self-assembly of 1H,1'H-[3,3']bipyridinyl-6,6'-dione was prepared along with the coordination of the same with Co(II) to form novel CP-**671**. This work shows the first example of extended coordination polymer using pyridonyl functionality. It also showcases the different hydrogen bond patterns by varying the crystallization conditions and emphasizes the potential of multivalent pyridonyl compounds to form infinite frameworks such as MOFs. This work has been published in CrystEngComm.

[Midhun Mohan, Thierry Maris and Adam Duong, Building coordination polymers using dipyridone ligands, *CrystEngComm*, **2020**, *22 (3)*, 441-447.]

In chapter 6, a series of monometallic and bimetallic coordination polymers were prepared using potassium cyamelurate as an organic ligand (MOP-(**1-4**) and MMOP-(**5-7**)). Metals selected for this study were intended to possess chromic behaviour which induced the thermochromic as well as solvochromic properties exhibited by the materials synthesized. The work has been published in Dalton Transaction.

[**Midhun Mohan**, Sanil Shyamshankar Rajak, Alexandre A. Tremblay, Thierry Maris and Adam Duong, Syntheses of mono and bimetallic cyamelurate polymers with reversible chromic behaviour, *Dalton Trans.*, **2019**, *48 (20)*, 7006-7014.]

In chapter 7, a series of isostructural three-dimensional lanthanide-based MOFs were prepared using potassium cyamelurate as an organic ligand. The pores were found to be one-directional with exceptional selectivity towards CO_2 over CH_4, H_2, N_2 and Ar. The low-pressure selectivity of these series of MOFs gives an advantage to these materials over other porous materials used for gas selectivity. This work has been submitted in ACS Applied Materials and Interfaces.

[**Midhun Mohan**, Mohamed Essalhi, David Durette, Love Karan Rana, Follivi Kloutse Ayevide, Thierry Maris and Adam Duong, A rational design of microporous nitrogen-rich lanthanide metal-organic frameworks for CO_2/CH_4 separation, *ACS Appl. Mater. Interfaces*, **2020**, *12* (45), 50619-50627..]

In chapter 8, a detailed conclusion has been presented drawn from the existing work highlighted and the future scope of this work.

2.5 References

1. Hoegh-Guldberg, O.; Jacob, D.; Bindi, M.; Brown, S.; Camilloni, I.; Diedhiou, A.; Djalante, R.; Ebi, K.; Engelbrecht, F.; Guiot, J., Impacts of 1.5 °C global warming on natural and human systems. *Global warming of 1.5° C. An IPCC Special Report* **2018**.
2. https://www.bernini-impianti.it/fr/-actualites-et-evenements.html.
3. Kirchgessner, D. A.; Piccot, S. D.; Masemore, S. S., An improved inventory of methane emissions from coal mining in the United States. *J. Air Waste Manage.* **2000**, *50* (11), 1904-1919.
4. Bogner, J.; Spokas, K.; Burton, E.; Sweeney, R.; Corona, V., Landfills as atmospheric methane sources and sinks. *Chemosphere* **1995**, *31* (9), 4119-4130.
5. Eviany, A.; Kartohardjono, S., The impact of gas production decline to lpg recovery and optimization strategy to prevent lpg facility from shutdown. *International J. Adv. Sci. Technol.* **2020**, *29* (7 Special Issue), 3296-3304.
6. Schloemer, S.; Krooss, B., Molecular transport of methane, ethane and nitrogen and the influence of diffusion on the chemical and isotopic composition of natural gas accumulations. *Geofluids* **2004**, *4* (1), 81-108.
7. Gangu, K. K.; Maddila, S.; Mukkamala, S. B.; Jonnalagadda, S. B., A review on contemporary Metal–Organic Framework materials. *Inorg. Chim. Acta* **2016**, *446*, 61-74.
8. Redemann, C.; Lucas, H., Some derivatives of cyameluric acid and probable structures of melam, melem and melon. *J. Am. Chem. Soc.* **1940**, *62* (4), 842-846.
9. Redemann, C.; Lucas, H., Ionization constants and hydrolytic degradations of cyameluric and hydromelonic acids. *J. Am. Chem. Soc.* **1939**, *61* (12), 3420-3425.
10. Horvath-Bordon, E.; Kroke, E.; Svoboda, I.; Fueß, H.; Riedel, R.; Neeraj, S.; Cheetham, A. K., Alkalicyamelurates, $M_3[C_6N_7O_3]\cdot xH_2O$, M= Li, Na, K, Rb, Cs: UV-luminescent and thermally very stable ionic tri-s-triazine derivatives. *Dalton Trans.* **2004**, (22), 3900-3908.
11. Holst, J. R., Synthesis of inorganic heptazine-based materials. *Theses and Dissertations* **2009**, 242.
12. Holst, J. R.; Gillan, E. G., From triazines to heptazines: deciphering the local structure of amorphous nitrogen-rich carbon nitride materials. *J. Am. Chem. Soc.* **2008**, *130* (23), 7373-7379.
13. Rosi, N. L.; Eckert, J.; Eddaoudi, M.; Vodak, D. T.; Kim, J.; O'Keeffe, M.; Yaghi, O. M., Hydrogen storage in microporous metal-organic frameworks. *Science* **2003**, *300* (5622), 1127-1129.
14. Cavka, J. H.; Jakobsen, S.; Olsbye, U.; Guillou, N.; Lamberti, C.; Bordiga, S.; Lillerud, K. P., A new zirconium inorganic building brick forming metal-organic

frameworks with exceptional stability. *J. Am. Chem. Soc.* **2008**, *130* (42), 13850-13851.

15. Furukawa, H.; Kim, J.; Ockwig, N. W.; O'Keeffe, M.; Yaghi, O. M., Control of vertex geometry, structure dimensionality, functionality, and pore metrics in the reticular synthesis of crystalline metal–organic frameworks and Polyhedra. *J. Am. Chem. Soc.* **2008**, *130* (35), 11650-11661.

16. Eddaoudi, M.; Kim, J.; Rosi, N.; Vodak, D.; Wachter, J.; O'Keeffe, M.; Yaghi, O. M., Systematic design of pore size and functionality in isoreticular MOFs and their application in methane storage. *Science* **2002**, *295* (5554), 469-472.

17. Suzuki, A., Organoborane coupling reactions (Suzuki coupling). *P. Jpn. Acad. B-Phys.* **2004**, *80* (8), 359-371.

18. Sheldrick, G. M., SHELXT–Integrated space-group and crystal-structure determination. *Acta Crystallogr. A* **2015**, *71* (1), 3-8.

19. Sheldrick, G. M., Crystal structure refinement with SHELXL. *Acta Crystallogr. C* **2015**, *71* (1), 3-8.

CHAPTER 3: Synthesis of Organic Ligands

3.1 Introduction

Material characteristics are controlled by the intermolecular interactions which facilitate the properties exhibited. A proper understanding of these interactions helps to monitor and regulate the properties for desired applications. Developing smart materials motivates to judiciously design building blocks. Coordination chemistry gives us the facility to strategize the functionality of the materials by providing a wide choice of metal and organic components. A major contribution can be invested by functionalizing the organic ligands. Most of the coordination polymers are constructed from carboxylate ligands. In this work, we focus on developing organic ligands based on pyridone functionality. Apart from the coordination atmosphere of pyridones, they differ from carboxylates due to the coordinated organic group as they restrict the free rotation of the ligating molecule once coordinated. A series of bipyridone organic compounds were synthesized by Suzuki coupling reaction. These synthesized compounds are potential candidates for the synthesis of a new class of pyridonyl based coordination polymers.

3.2 Objectives

- A detailed survey on the coordination modes of carboxylate groups used for coordination polymers including Metal-Organic Frameworks and comparison with the coordination modes of pyridonyl functionality.
- Designing a series of bidentate pyridonyl compounds incorporating the ideas to form hierarchical frameworks.
- Synthesis of pyridonyl bidentate organic compounds using Suzuki coupling reaction and deprotection reaction.

- Crystallisation of synthesized compounds for understanding the structure using single-crystal X-ray diffraction.
- Other characterizations on the synthesized compounds such as FTIR, ^{1}H-NMR, ^{13}C-NMR, mass spectroscopy and thermogravimetric analysis.

3.3 Authors' Contributions

Midhun Mohan. Conceptualization of the project, visualization and investigation of experiments, all synthesis of ligands and experiments conducted, validation of methodology and curation of data, drafting the original manuscript.

Sarah Zaye. Assistance in synthesis and experiments of pyridone ligands.

Mohamed Essalhi. Assistance in preparation of single crystals of selected pyridone ligand.

Love Karan. Investigation in X-ray diffraction study.

Thierry Maris. Investigation and curation of X-ray diffraction experiments.

Adam Duong. Project administration, supervision, funding acquisition and editing of the manuscript.

3.4 Article 1

Hydrogen Bonds Patterns in Co-Crystals of Dipyridone

Hydrogen Bonds Patterns in Co-Crystals of Dipyridone

Midhun Mohan,[a] Mohamed Essalhi,[a] Sarah Zaye,[a] Love Karan Rana,[a] Thierry Maris[b] and Adam Duong[a,*]

[a]*Département de Chimie, Biochimie et physique and Institut de Recherche sur l'Hydrogène, Université du Québec à Trois-Rivières, Trois-Rivières, Québec, G9A 5H7, Canada.*

[b]*Département de chimie, Université de Montréal, Montréal, Québec, H3T 1J4, Canada*

†Electronic supplementary information (ESI) available: Crystallographic data, NMR, FTIR and TGA of synthesized compounds. CCDC 2011734-2011736 contain the supplementary crystallographic data for this paper. For ESI and crystallographic data in CIF or other electronic format, see DOI: xxx

*To whom correspondence should be addressed. E-mail: adam.duong@uqtr.ca

ABSTRACT

Dipyridonyl-substituted derivatives **2-4** of benzene, pyridine, and pyrazine respectively were synthesized to examine the ability of 2-pyridone to direct the self-assembly by hydrogen bonding. Analysis by single-crystal X-ray diffraction revealed that crystals of **3** grown from DMSO/H_2O demonstrate typical $R_2^2(8)$ cyclic hydrogen bonds motif of 2-pyridone. However, crystallization in trifluoroacetic acid (TFA) of **2** and **4** formed crystals with non-conventional hydrogen bond motifs of 2-pyridone in the structures. The co-crystallization of cationic dipyridones with anionic trifluoracetate prevented 2-pyridonyl groups to associate according to characteristic hydrogen bond motifs. Nevertheless, the resulting association for all compounds **2-4** generated similar networks consisting of chains and sheets.

INTRODUCTION

Since hydrogen bonds were discovered, effort to characterize them and to understand their use to direct the molecular organization have flourished.[1,2] These intermolecular interactions occurred in many kinds of materials. Their study has an important contribution in determining the properties and activities of the materials produced by self-assembly.[2,3] Single-crystal X-ray diffraction (SCXRD) is the main characterization technique that has been extensively used to determine the hydrogen bonding patterns of various compounds which incorporate one or multiples sticky sites such as hydroxy (-OH), carboxylic (-COOH), diaminotriazinyl (DAT), pyridonyl groups and so forth.[4-8] In chemistry, the strategy that uses non-covalent interactions to direct the molecular organization is the concept of crystal engineering.[9] In the last decade, a major study in the field of crystal engineering is related to the development of multi-component crystals also known as co-crystals.[10,11] Up to date, the design of co-crystals is still challenging due to the various recognition possibilities between different molecules which make the task difficult.[12,13] To prepare co-crystals the most often used strategy is to combine components with strong heteromolecular interactions, however, it is not certain that this phenomenon will occur systematically. Understanding the co-assembly of binary and multi-components are of interest to production of energetic materials, pharmaceuticals, and other compounds.[14,15] Among the various sticky site by hydrogen bonds, 2-pyridone group has been the least used to produce crystalline materials.[16,17] 2-Pyridone exists as tautomers in which the proton can be attached to nitrogen or to oxygen to form lactam and 2-hydroxypyridine respectively.[18-20] However, the predominant form in solid-state is 2-pyridone.[21] So far, to the best of our knowledge, only fourteen structures are reported on organic crystal containing from two to four 2-pyridone groups.[22-25] Several crystal

structures of them reveal hydrogen bonds with $R_2^2(6)$ synthon and only few exhibits a C(3) pattern (Chart 1a).

In this present report, we focused our work on the design, synthesis and characterization of novel dipyridone compounds **2-4** (Chart 1b). They consist of 1,4-dipyridone substituted derivatives of benzene, pyridine, and pyrazine. They are interesting owing to their abilities to self-assemble by hydrogen bonds and to co-crystallize depending on the conditions of crystallization.

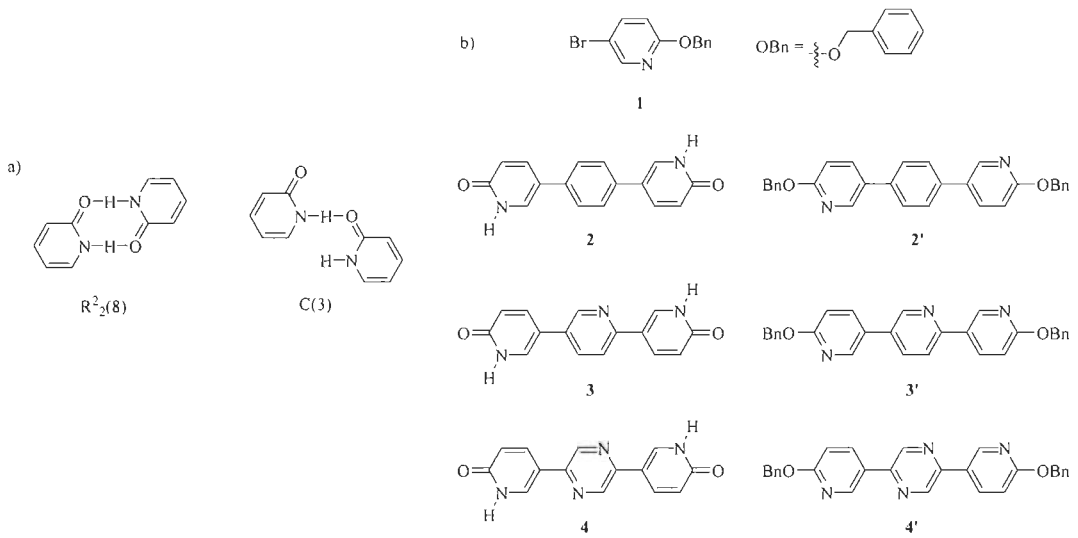

Chart 1 (a) Typical hydrogen bonding synthon of 2-pyridone group and (b) Molecular structures of **1-4** and **2'-4'**.

RESULTS AND DISCUSSION

Syntheses of compounds 1, 2-4 and 2'-4'. 2-(benzyloxy)-5-bromopyridine **1** was prepared following methods reported previously. Compounds **2'-4'** were synthesized with yields ranging from 80-90 % by Suzuki-Miyaura coupling reaction.[26,27] Deprotection of the benzoxyl group in acidic condition gives **2-4** in quantitative yield (Scheme 1).

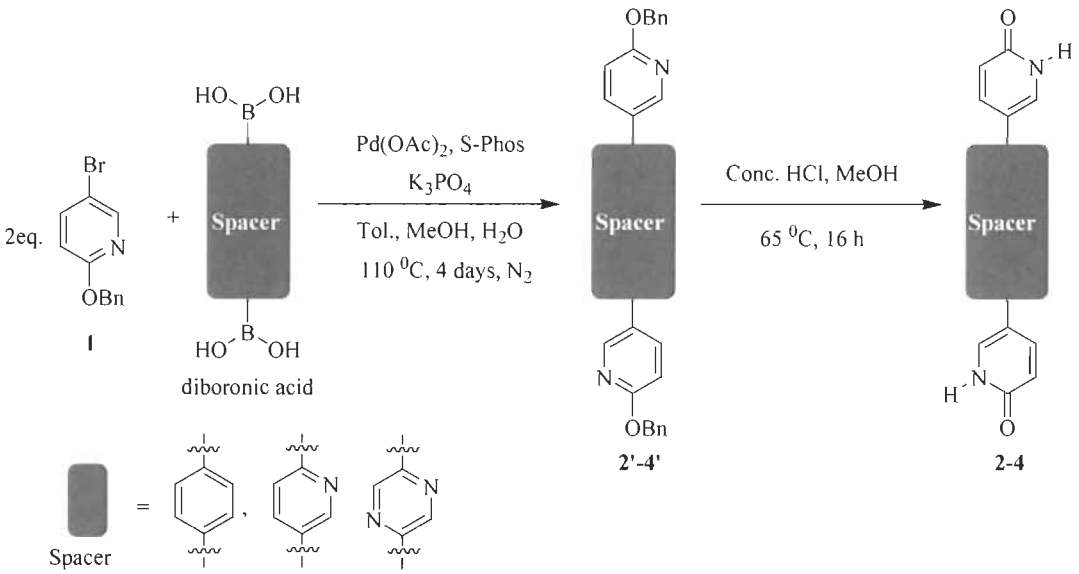

Scheme 1 General synthetic route for the obtention of **2'-4'** and **2-4**.

Structures of **2-4** and **2'-4'** were determined using electrospray ionization mass spectrometry (ESI-MS), infrared (IR) and ^{1}H and ^{13}C nuclear magnetic resonance (NMR) spectroscopies. Their IR indicates the presence of typical bands characteristic of N-H and C=O in the range 3100-3500 and ~ 1650 cm^{-1} respectively (Fig. S16-19†). Thermogravimetry analysis (TGA) shows that **2-4** are thermally stable up to ~350 °C, 370 °C and 415 °C respectively (Fig. S19†). Single-crystal X-ray diffraction (SCXRD) was performed to reveal the molecular organization by hydrogen bonds of **2-4**.

Structure of 5-(4-(1,6-Dihydro-6-oxopyridin-3-yl)phenyl)pyridin-2(1H)-one 2 as a Trifluoroacetate Salt. Crystals of **2** grown from TFA/$CHCl_3$ proved to belong to the triclinic space group $P\bar{1}$ and have the composition $(\mathbf{2}H)^+ \cdot (CF_3COO)^-$. Views of the structures are shown in Fig. 1. Additional crystallographic data are given in Table 1. In the crystal structure, the organic moiety is protonated to give a cation specie $(\mathbf{2}H)^+$. Trifuoroacetate $(CF_3COO)^-$ anion co-crystallized to balance the positive charge of the organic moiety. The molecular structure of $(\mathbf{2}H)^+$ show identical twist angle for both

pyridonyl groups with the phenyl ring (29.24°). The two N-H of pyridonyl groups are *trans*-oriented. In the structure, cationic units $(\mathbf{2}H)^+$ are linked according to $D_1^1(2)$ motifs (O-H···O (2.431 Å)) to form chains which are further interconnected by another $D_1^1(2)$ motif (N-H···O_{TFA} (2.786 Å)) to generate a new binary graph set $\mathbf{R_6^6(42)}$ in a sheet (Fig. 1a). Sheets are then joined by multiple hydrogen bonding involving trifluoro- acetic and acetate molecules to produce the three-dimensional network (Fig. 1b). Selected hydrogen bonds and angles are given in Tables S1-S4†.

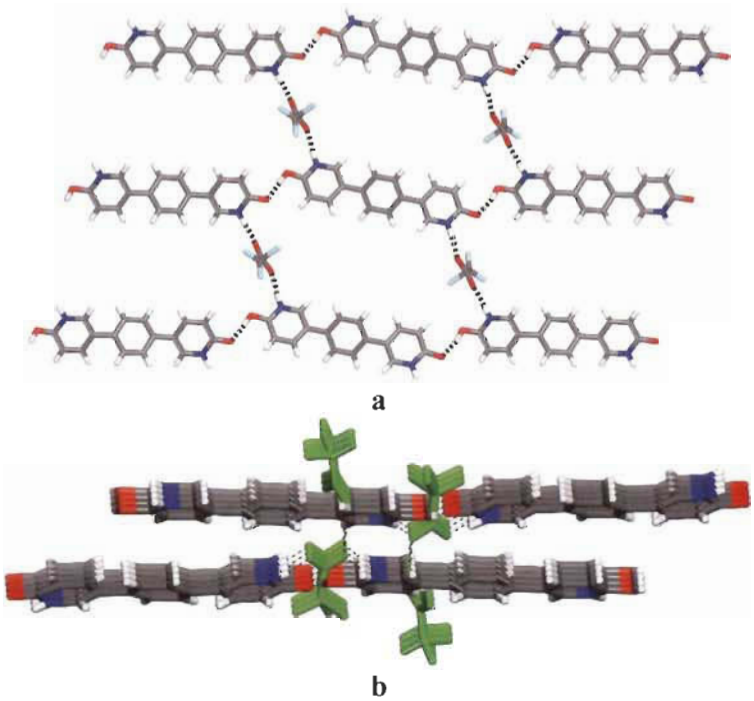

Fig. 1 Representation of the structure of crystals of the trifluoroacetate salt of 5-(4-(1,6-dihydro-6-oxopyridin-3-yl)phenyl)pyridin-2(1H)-one **2** grown from TFA/$CHCl_3$. (a) Cationic $(\mathbf{2}H)^+$ are linked to form chains by O-H···O hydrogen bonds and chains are further interconnected by N-H···O involving bridging trifluoroacetate anions to generate a sheet. (b) View along the *a*-axis showing stacking of sheets maintained together by hydrogen bonding involving bridging of TFA and $(CF_3COO)^-$. For clarity TFA and

$(CF_3COO)^-$ molecules are marked in green. Hydrogen bonds are represented by broken lines. C, grey; O, red; N, blue; H, white and F, cyan.

Table 1. Crystallographic data for **2-4**

	2	**3**	**4**
Formula	$C_{16}H_{12}N_2O_2$ ·$2CF_3COOH$	$C_{15}H_{11}N_3O_2$ ·$2H_2O$	$C_{14}H_{10}N_4O_2$ ·$2CF_3COOH$
Mr	492.33	301.30	494.32
Crystal System	Triclinic	Monoclinic	Monoclinic
Space group	$P\bar{1}$ (2)	$P2_1/n$	$P2_1/n$
a (Å)	10.3431(8)	13.2786(15)	8.5865(3)
b (Å)	10.4169(9)	3.7845(5)	11.2016(4)
c (Å)	10.5799(9)	14.1350(17)	20.1685(7)
α (deg)	92.243(5)	90	90
β (deg)	102.909(5)	104.613(7)	99.148(2)
γ (deg)	103.076(5)	90	90
V (Å^3)	1077.45(16)	687.35(15)	1915.18(12)
Z	2	2	4
ρ_{calcd} (g cm^{-3})	1.518	1.456	1.714
T (K)	100	298(2)	150
Radiation	CuKα	CuKα	GaKα
λ (Å)	1.54178	1.54178	1.34139
μ (mm^{-1})	1.293	0.900	0.949
F (000)	500	316	1000
No. measured reflections	22253	8690	24456
No. independent reflections	3996	1344	3508
No. obsd. reflections I>2σ(I)	3402	1144	2685
Nb Params	372	100	357
R_1, I>2σ (%)	0.0729	0.0751	0.0695
R_1, all data (%)	0.0790	0.0834	0.0837
ωR_2, I>2σ(I) (%)	0.2296	0.2141	0.1980
ωR_2, all data (%)	0.2389	0.2323	0.2151
GoF	1.054	1.023	1.030

Structure of 5-(5-(1,6-dihydro-6-oxopyridin-3-yl)pyridin-2-yl)pyridin-2(1H)-one 3. Compounds **3** and **2** differ only in a single replacement of C-H by N (Chart 1). Crystals of **3** grown from DMSO/EtOH proved to belong to the monoclinic space group $P2_1/n$ and have the composition **3** • $2(H_2O)$. Fig. 2 shows views of structures of **3** and other crystallographic data are provided in Table 1. As expected, molecule **3** adopts similar configurations as that in **2**. However, the twist angle between pyridonyl and phenyl rings (26.10°) is slightly smaller. In the structure, organic species self-assemble by N-H···O

hydrogen bonds (2.790 Å) according to $\mathbf{R_2^2(8)}$ motif to form a zigzag chain (Fig. 2b). Chains are then interconnected by multiple hydrogen bonds involving bridging of water molecules to produce complex graph sets $\mathbf{R_8^8(42)}$ in a three-dimensional network. The network is also strengthened by π-π stacking (3.784 Å) of heterocycles (Fig. 2b). It is noteworthy that the nitrogen of the pyridyl ring is not participating in any hydrogen bonding. Summary of hydrogen bonds and angles are provided in Tables S5 and S6†.

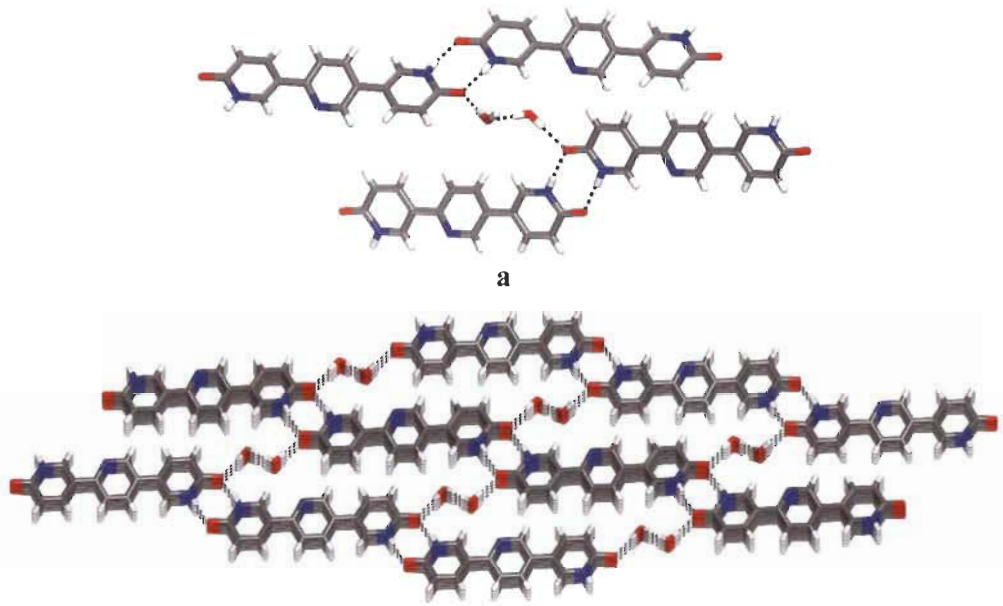

a

b

Fig. 2 Views of the structure of 5-(5-(1,6-dihydro-6-oxopyridin-3-yl)pyridin-2-yl)pyridin-2(1H)-one **3**. (a) Zigzag chains formed by cyclic N-H···O hydrogen bonds and their interconnection by bridging of water molecules. (b) View showing the 3D network produced by hydrogen bonds and π-π stacking. Hydrogen bonds are represented by broken lines. C, grey; O, red; N, blue; H, white.

The replacement from C-H to N does not affect the molecular conformation of molecule **3**. The only slight difference is the twisted angles between pyridonyl and pyridyl rings. However, the hydrogen bonds patterns of 2-pyridone group are entirely different. The use of acidic solvent in the crystallization results in the protonation of the organic moiety

which change the tendency of 2-pyridonyl groups to self-assemble according to known synthons (Chart 1).

Structure of 5-(5-(1,6-dihydro-6-oxopyridin-3-yl)pyridin-3-yl)pyridin-2(1H)-one 4 as a Trifluoroacetate Salt. The behavior of the 2-pyridonyl group in TFA prompted us to examine the corresponding pyrazine **4**, in which two C-H have been replaced by N as compared with **2**. In principle, the molecular structure of **4** should be similar to **2** and **3**. If molecule **4** co-crystallize with TFA the hydrogen bond motifs might be analogous to those observed in the structure of **2**. Crystals of **4** grown from TFA/H_2O proved to belong to the monoclinic space group $P2_1/n$ and have the composition $(\mathbf{4}H)^{2+} \bullet 2(CF_3COO)^-$. The SCXRD show an organic specie diprotonated forming a dication $(\mathbf{4}H)^{2+}$. Molecule $(\mathbf{4}H)^{2+}$ is nearly planar with pyrazinyl and pyridonyl rings twisted angles of 9.10° and 4.96°. Again, the N-H groups are *trans*-oriented. In the structure, dicationic moieties are interconnected by bridged trifluoroacetate anions according to unitary graph sets $D_1^1(\mathbf{2})$ (N-H···O (2.798 Å, 2.699 Å) and O-H···O (2.455 Å, 2.480 Å)) to produce a ring with graph sets symbol $\boldsymbol{R_8^8(50)}$ within a layered structure (Fig. 3a). Sheets are further π-π stacked (3.721 Å) to produce the thickness of crystals (Fig. 3b). Details of hydrogen bonds and angles are provided in Tables S7-S10†.

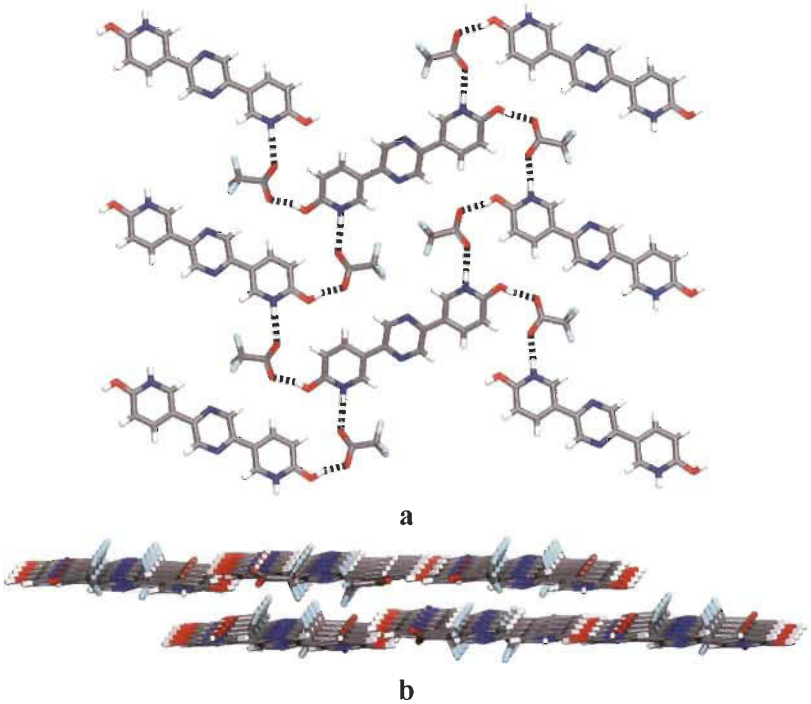

Fig. 3 Views of the structure of 5-(5-(1,6-dihydro-6-oxopyridin-3-yl)pyridin-3-yl)pyridin-2(1H)-one **4** grown from TFA/H_2O. (a) View showing a sheet formed by hydrogen bonds between $(\mathbf{4}H)^{2+}$ and trifluoroacetate. (b) View along the *b*-axis showing packing of sheets. Hydrogen bonds are represented by broken lines. C, grey; O, red; N, blue; H, white and F, cyan.

CONCLUSIONS

Although 2-pyridone group is well known in crystal engineering, only a few organic crystals have shown structures with two or more of these sticky sites. Our work shows that the tendency of dipyridone to form $R_2^2(8)$ and C(3) synthons is not systematic. It is significantly dependent on the conditions of crystallizations. When dipyridone and TFA co-crystallize, it forms co-crystals salts with reliable patterns. In trifluoracetic acid (TFA), the hydrogen bonding patterns of 2-pyridone is not conventional. The aggregation is dictated by the hydrogen bonds and the coulombic interactions between anionic and

cationic species. Our work is useful to understand the molecular organization of dipyridone in acidic condition. We have identified new hydrogen bonding patterns for 2-pyridone group with TFA. It should help researchers that are interested to build reliable molecular networks by hydrogen bonds. Our investigation on the synthetic method of dipyridone promises to be useful for scientists who are involved in the design of coordination polymers *via* the linkage of 2-pyridone with metal ions.

EXPERIMENTAL SECTION

General Notes. All chemicals were purchased from commercial sources are were used without further purification. All solvents were purchased from Fischer Scientific. Compounds **2'-4'** and **2-4** were made by the procedures summarized below.

General method to prepare 2'-4'. A dried Schlenk flask was degassed with $Pd(OAc)_2$ (0.101 g, 0.15 mmol) and S-Phos (0.118 g, 0.288 mmol) dissolved in toluene (20 mL). In continuously bubbled with argon environment addition of (i) 2-(benzyloxy)-5-bromopyridine **1** (0.8451 g, 3.2 mmol) and benzene-1,4-diboronic acid (0.27 g, 1.6 mmol), (ii) 2,5-dibromopyridine (0.38 g, 1.6 mmol) and 2-(benzyloxy)-5-(4,4,5,5-tetramethyl-1,3,2-dioxaborolan-2-yl)pyridine (1 g, 3.2 mmol), and (iii) 2,5-dibromopyrizine (0.38 g, 1.6 mmol) and 2-(benzyloxy)-5-(4,4,5,5-tetramethyl-1,3,2-dioxaborolan-2-yl)pyridine (1 g, 3.2 mmol) were necessary to form of **2'-4'** respectively. To these mixtures, solutions (12 mL) of K_3PO_4 (6.1137 g, 28.8 mmol) in methanol/water 1:1 mixture were added dropwise. The mixtures were then heated at 110 °C under argon. After 4 days, the reactions were cooled to room temperature and extracted with dichloromethane. The organic layers were dried over magnesium sulphate, filtered and

the solvent evaporated under reduced pressure. The residues were purified by column chromatography (silica gel, chloroform/hexane 1:2).

2-(Benzyloxy)-5-(4-(6-(benzyloxy)pyridin-3-yl)phenyl)pyridine 2'. Colourless solid (0.61 g, 1.36 mmol, 85 %). mp 211 °C; FTIR ν 3060, 3042, 3022, 2938, 2885, 1301, 1567, 1524, 1475, 1466, 1453, 1425, 1357, 1286, 1243, 1140, 1010, 995, 825, 817, 742, 693 cm^{-1}; ^1H NMR (700 MHz, DMSO) δ 8.56 (d, J = 2.5 Hz, 1H), 8.11 (dd, J = 8.6, 2.6 Hz, 1H), 7.78 (s, 2H), 7.48 (d, J = 7.3 Hz, 2H), 7.40 (t, J = 7.6 Hz, 2H), 7.34 (t, J = 7.3 Hz, 1H), 7.01 (d, J = 8.6 Hz, 1H), 5.42 (s, 2H); ^{13}C NMR (176 MHz, DMSO) δ 163.04, 145.01, 138.10, 137.73, 136.36, 129.42, 128.86, 128.35, 128.23, 127.36, 111.43, 67.52; HRMS (ESI) calcd for $[C_{30}H_{24}N_2O_2 + H]^+$ m/e 445.1911, found 445.1915.

2,5-bis(6-(benzyloxy)pyridin-3-yl)pyridine 3'. Pale yellow solid (0.58 g, 1.3 mmol, 81.3 %). mp 169 °C; FTIR ν 3061, 3034, 2947, 1602, 1568, 1504, 1468, 1452, 1406,1344, 1308, 1283, 1246, 1134, 1006, 983, 921, 875, 825, 773, 743, 734, 703, 694 cm^{-1}; ^1H NMR (700 MHz, DMSO) δ 8.98 (dd, J = 30.1, 2.3 Hz, 2H), 8.64 (d, J = 2.4 Hz, 1H), 8.47 (dd, J = 8.6, 2.4 Hz, 1H), 8.19 (td, J = 8.1, 2.5 Hz, 2H), 8.08 (d, J = 8.3 Hz, 1H), 7.51 – 7.46 (m, 4H), 7.40 (t, J = 7.5 Hz, 4H), 7.34 (t, J = 7.3 Hz, 2H), 7.08 – 6.98 (m, 2H), 5.44 (d, J = 6.1 Hz, 4H); ^{13}C NMR (176 MHz, DMSO) δ 164.01, 163.39, 153.04, 147.68, 145.75, 124.32, 138.19, 137.83, 137.66, 137.61, 135.21, 128.86, 128.43, 128.36, 128.28, 128.25, 126.70, 120.16, 111.61, 111.37, 67.70, 67.58; HRMS (ESI) calcd for $[C_{29}H_{23}N_3O_2 + H]^+$ m/e 446.1863, found 446.1853.

2,5-Bis(6-(benzyloxy)pyridin-3-yl)pyrazine 4'. Yellow solid (0.56 g, 1.26 mmol, 79 %). mp 208 °C; FTIR ν 3068, 3030, 2874, 1601, 1566, 1517, 1495, 1467, 1452, 1395,

1360, 1308, 1269, 1236, 1185, 1157, 1111, 1076, 1021, 936, 919, 877, 848, 831, 756, 726, 706, 689 cm 1; 1H NMR (700 MHz, DMSO) δ 9.33 (d, J = 1.9 Hz, 1H), 9.01 (s, 1H), 8.50 (dt, J = 8.7, 2.3 Hz, 1H), 7.49 (d, J = 7.6 Hz, 2H), 7.41 (t, J = 7.5 Hz, 2H), 7.35 (t, J = 7.0 Hz, 1H), 7.08 (dd, J = 8.6, 1.6 Hz, 1H), 5.46 (s, 2H); 13C NMR (176 MHz, DMSO) δ 164.41, 148.05, 145.99, 141.20, 137.84, 137.50, 128.88, 128.44, 128.32, 126.01, 111.74, 67.81; HRMS (ESI) calcd for $[C_{28}H_{22}N_4O_2 + H]^+$ m/e 447.1816, found 447.1831.

General method to prepare 2-4. Purified and dried 2-(benzyloxy)-5-(4-(6-(benzyloxy)pyridin-3-yl)phenyl)pyridine **2'** (0.5 g, 1.13 mmol), 2,5-bis(6-(benzyloxy)pyridin-3-yl)pyridine **3'** (0.45 g, 1.01 mmol) and 2,5-bis(6-(benzyloxy)pyridin-3-yl)pyrazine 5' (0.45 g, 1.0 mmol) **4'** were taken in a flask containing methanol (45 mL). Concentrated hydrochloric acid (15 mL) was added dropwise to the above solution making the solution clear. The mixtures were heated to reflux for overnight and then cooled to room temperature and neutralized using saturated solution of sodium bicarbonate until pH 7. The resulting precipitates were washed in water, filtered and dried to give **2-4** respectively.

5-(4-(1,6-Dihydro-6-oxopyridin-3-yl)phenyl)pyridin-2(1H)-one 2. Colourless solid (0.28 g, 1.07 mmol, 95 %). mp 338 °C; FTIR ν 3271, 3122, 3027, 2948, 2829, 1645, 1609, 1548, 1514, 1463, 1434, 1342, 1297, 1239, 1143, 1014, 989, 928, 908, 824, 754, 723, 662 cm^{-1}; ^1H NMR (700 MHz, DMSO) δ 11.86 (s, 1H), 7.89 (ddd, J = 21.8, 9.5, 2.7 Hz, 1H), 7.75 (d, J = 8.4 Hz, 1H), 7.70 – 7.59 (m, 2H), 6.46 (dd, J = 13.1, 9.5 Hz, 1H); ^{13}C NMR (176 MHz, DMSO) δ 162.21, 140.31, 138.16, 135.65, 134.87, 127.34, 126.17, 126.08; HRMS (ESI) calcd for $[C_{16}H_{12}N_2O_2 + H]^+$ m/e 265.0972, found 265.0973.

5-(5-(1,6-Dihydro-6-oxopyridin-3-yl)pyridin-2-yl)pyridin-2(1H)-one 3. Yellow solid (0.25 g, 0.92 mmol, 92 %). mp 330 °C; FTIR ν 3271, 3132, 2953, 2830, 1650, 1614, 1549, 1489, 1469, 1432, 1392, 1310, 1259, 1223, 1143, 996, 882, 821, 768, 668 cm^{-1}; ^1H NMR (700 MHz, DMSO) δ 11.95 (s, 2H), 8.80 (d, J = 2.1 Hz, 1H), 8.22 (dd, J = 9.6, 2.7 Hz, 1H), 8.17 (d, J = 2.4 Hz, 1H), 8.01 (dd, J = 8.4, 2.4 Hz, 1H), 7.92 (dd, J = 9.5, 2.7 Hz, 1H), 7.88 – 7.82 (m, 2H), 6.50 – 6.42 (m, 2H); ^{13}C NMR (176 MHz, DMSO) δ 162.54, 162.21, 151.62, 146.39, 140.06, 139.23, 134.52, 133.95, 133.67, 129.99, 120.76, 120.32, 118.63, 117.05, 115.02; HRMS (ESI) calcd for $[C_{15}H_{11}N_3O_2 + H]^+$ m/e 266.0924, found 266.0922.

5-(5-(1,6-Dihydro-6-oxopyridin-3-yl)pyrazin-2-yl)pyridin-2(1H)-one 4. Orange solid (0.24 g, 0.9 mmol, 90 %). mp 341 °C; FTIR ν 3126, 3046, 2690, 1685, 1645, 1559, 1498, 1471, 1432, 1383, 1333, 1277, 1252, 1239, 1195, 1161, 1078, 1018, 992, 973, 888, 839, 673 cm^{-1}; ^1H NMR (700 MHz, TFA-d) δ 9.43 (s, 1H), 9.43 (s, 1H), 8.87 (s, 1H), 8.79 (d, J = 8.9 Hz, 1H), 7.46 (d, J = 9.1 Hz, 1H); ^{13}C NMR (176 MHz, TFA-d) δ 163.26, 146.42, 14.06, 140.26, 136.40, 120.80, 117.73; HRMS (ESI) calcd for $[C_{14}H_{10}N_4O_2 + H]^+$ m/e 267.0877, found 267.0882.

Crystallization conditions for 2-4. All compounds were crystallized by slow diffusion. **2** (10 mg) was dissolved in TFA (2 mL) and chloroform was diffused to the solution mixture. Compound **3** (10 mg) was dissolve in DMSO (3 mL) and the solution mixture was exposed to vapor of water. **4** (10 mg) was also dissolved in TFA (2 mL) and water vapor was diffused to the solution mixture.

ASSOCIATED CONTENT

Supporting Information. The supporting Information is available free of charge via the internet at ACS Publications website at DOI:

Additional crystallographic details (including thermal atomic displacement ellipsoid plots), Mass spectrum, ORTEP diagrams and other crystallographic data, Infrared and Thermogravimetry analysis (PDF).

Accession Codes

CCDC 2011734-2011736 contain the supplementary crystallographic data for this paper. These data can be obtained free of charge via www.ccdc.cam.ac.uk/data_request/cif, of by email data_request@ccdc.cam.ac.uk, or by contacting The Cambridge Crystallographic Data Centre, 12 Union Road Cambridge CB2 1EZ, UK; fax: +44 1223 336033.

AUTHOR INFORMATION

Corresponding Author

*E-mail: adam.duong@uqtr.ca.

ORCID

Adam Duong : 0000-0002-4927-3603

Notes

The authors declare no competing financial interest.

ACKNOWLEDGMENT

We are grateful to the Natural Sciences and Engineering Research Council of Canada (RGPIN-2015-06425), the Canadian Queen Elizabeth II Diamond Jubilee Scholarships, Mitacs globalink, the Canada foundation for innovation, the Fonds de recherche du Québec – Nature et technologies and the Université du Québec à Trois-Rivières.

REFERENCES

1. L. Pauling, *The Nature of the Chemical Bond*, Cornell university press Ithaca, NY, 1960.
2. P. T. Galek, J. A. Chisholm, E. Pidcock and P. A. Wood, *Acta Crystallogr. B*, 2014, **70**, 91-105.
3. M. J. Zaworotko, *Cryst. Growth Des.*, 2007, **7**, 4-9.
4. N. G. White, V. Carta and M. J. MacLachlan, *Cryst. Growth Des.*, 2015, **15**, 1540-1545.
5. A. Lemmerer, D. A. Adsmond, C. Esterhuysen and J. Bernstein, *Cryst. Growth Des.*, 2013, **13**, 3935-3952.
6. A. Duong, S. Rajak, A. A. Tremblay, T. Maris and J. D. Wuest, *Cryst. Growth Des.*, 2019, **19**, 1299-1307.
7. A. Peter, M. Mohan, T. Maris, J. D. Wuest and A. Duong, *Cryst. Growth Des.*, 2017, **17**, 5242-5248.
8. M. Mohan, L. K. Rana, T. Maris and A. Duong, *Can. J. Chem.*, 2020, DOI: 10.1139/cjc-2019-0415, 1-5.
9. C. B. Aakeröy and K. R. Seddon, *Chem. Soc. Rev.*, 1993, **22**, 397-407.
10. G. Springuel, B. Norberg, K. Robeyns, J. Wouters and T. Leyssens, *Cryst. Growth Des.*, 2012, **12**, 475-484.
11. K. Biradha, C. Y. Su and J. J. Vittal, *Cryst. Growth Des.*, 2011, **11**, 875-886.
12. P. M. Bhatt, Y. Azim, T. S. Thakur and G. R. Desiraju, *Cryst. Growth Des.*, 2009, **9**, 951-957.
13. L. Jiang, Y. Huang, Q. Zhang, H. He, Y. Xu and X. Mei, *Cryst. Growth Des.*, 2014, **14**, 4562-4573.
14. Y. Ma, S. Wu, E. G. J. Macaringue, T. Zhang, J. Gong and J. Wang, *Org. Process Res. Dev.*, 2020, DOI: 10.1021/acs.oprd.9b00362.
15. Y. L. Shi, M. P. Zhuo, X. D. Wang and L. S. Liao, *ACS Appli. Nano Mater.*, 2020, **3**, 1080-1097.
16. M. Mohan, T. Maris and A. Duong, *CrystEngComm*, 2020, **22**, 441-447.
17. L. Wang, J. K. Pratt, T. Soltwedel, G. S. Sheppard, S. D. Fidanze, D. Liu, L. A. Hasvold, R. A. Mantei, J. H. Holms, W. J. McClellan, M. D. Wendt, C. Wada, R. Frey, T. M. Hansen, R. Hubbard, C. H. Park, L. Li, T. J. Magoc, D. H. Albert, X. Lin, S. E. Warder, P. Kovar, X. Huang, D. Wilcox, R. Wang, G. Rajaraman, A. M. Petros, C. W. Hutchins, S. C. Panchal, C. Sun, S. W. Elmore, Y. Shen, W. M. Kati and K. F. McDaniel, *J. Med. Chem.*, 2017, **60**, 3828-3850.

18. S. Mata, V. Cortijo, W. Caminati, J. L. Alonso, M. E. Sanz, J. C. López and S. Blanco, *J. Phys. Chem. A*, 2010, **114**, 11393-11398.
19. A. Z. Michelson, A. Petronico and J. K. Lee, *J. Org. Chem.*, 2012, **77**, 1623-1631.
20. C. S. Peng and A. Tokmakoff, *J. Phys. Chem. Lett.*, 2012, **3**, 3302-3306.
21. J. Almlöf, Å. Kvick and I. Olovsson, *Acta Crystallogr. B*, 1971, **27**, 1201-1208.
22. C. B. Aakeröy and K. R. Seddon, *Chem. Soc. Rev.*, 1993, **22**, 397-407.
23. A. M. Moragues-Bartolome, W. Jones and A. J. Cruz-Cabeza, *CrystEngComm*, 2012, **14**, 2552-2559.
24. Q. Zhang, L. Lu, W. Dai and X. Mei, *CrystEngComm*, 2014, **16**, 1919-1926.
25. A. n. F. Crespi, D. Vega, A. K. Chattah, G. A. Monti, G. Y. Buldain and J. M. Lázaro-Martínez, *J. Phys. Chem. A*, 2016, **120**, 7778-7785.
26. P. Devendar, R. Y. Qu, W. M. Kang, B. He and G. F. Yang, *J. Agric. Food Chem.*, 2018, **66**, 8914-8934.
27. W. K. Chow, O. Y. Yuen, P. Y. Choy, C. M. So, C. P. Lau, W. T. Wong and F. Y. Kwong, *RSC Adv.*, 2013, **3**, 12518-12539.

For Table of Contents Only

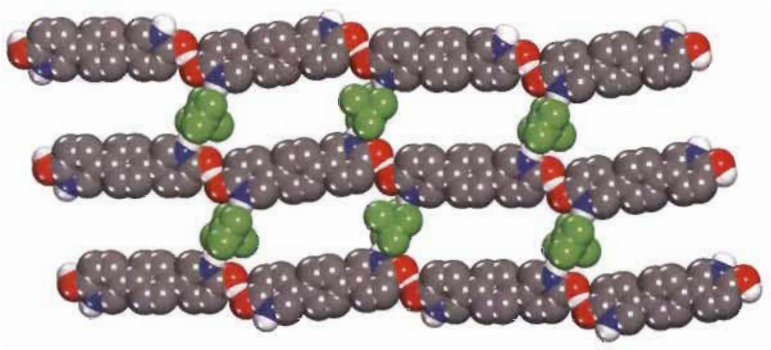

3.5 Conclusion

Hydrogen bonding has played a key role in the rational design of materials through intermolecular interactions which were well established mostly in supramolecular chemistry. Understanding the molecular organization has led us to determine the properties and activities of the materials produced by self-assembly. 2-Pyridone motifs have been extensively used in supramolecular self-assembly. Nevertheless, ditopic pyridonyl functionalities are seldom used. This chapter focussed on developing a series of novel ditopic pyridone-based organic ligands. The synthesized ligands, **2-4** were crystallized in different conditions such as TFA/$CHCl_3$, DMSO/EtOH and TFA/H_2O, respectively. The acidic conditions for co-crystallizing dipyridone compounds were investigated in this work. This work can motivate the researchers in developing a new class of ditopic organic ligands which can well serve as promising candidates for supramolecular chemistry. Coordination modes of 2-pyridone also drive considerable attention to these class of materials for the development of novel coordination polymers such as porous MOFs with improved stability and characteristic properties.

CHAPTER 4: Intercalated Co-Crystallization of Pyridone Functionality

4.1 Introduction

Co-crystallization is the supramolecular formation of two or more different components in a single-phase crystalline solid material with distinctive properties through non-covalent interactions. It contributes to the understanding of interactions between multi-component crystalline solids as well as their design which has been reflected in the literature through their applications mainly in the pharmaceuticals and hybrid explosives. It brings new perspectives to pre-formulation and initial steps towards crystal engineering. Co-crystallization comprises of solvates, solid solutions, eutectics, salts, ionic liquids, solid dispersions, supramolecular gelators and so on whose formation can be controlled by the nature of the components and the conditions such as temperature, pressure, solvent, pH, etc. Due to the versatility in the controlling parameters, physicochemical properties are varied and can be altered to address distinct applications in diverse fields. The interesting prospects of the previous chapter inspired us to incorporate the bidentate pyridonyl functionality for developing solid solutions. In this chapter, we have developed dipyridone ligand to co-crystallize with hydrated cobalt salt. Characterization of the synthesized ligand and co-crystal structure of ligand with cobalt salts was conducted using various methods. This work facilitates and strengthens the impression of using multidentate pyridone ligands for the formation of coordination and other non-covalent interactions.

4.2 Objectives

- Study and synthesis of co-crystallization process of dipyridone and cobalt salt.

- Characterization of synthesized co-crystals to identify the existence of intercalated hydrogen-bonded sheets of dipyridone and hydrated cobalt units with counter-ions.
- A detailed investigation on the supramolecular organization through hydrogen bonds of both organic and metallic 2D sheets.
- Understanding the variation in properties due to the co-crystallization process.

4.3 Authors' Contribution

Midhun Mohan. Conceptualization of the project, visualization and investigation of experiments, all synthesis and experiments conducted, validation of methodology and curation of data, drafting the original manuscript.

Love Karan Rana. Structure description.

Thierry Maris. Investigation and curation of X-ray diffraction experiments.

Adam Duong. Project administration, supervision, funding acquisition and editing of the manuscript.

4.4 Article 2

Intercalated 2D + 2D Hydrogen-Bonded Sheets in Co-Crystals of Cobalt Salt with 1H,1'H-[3,3']bipyridinyl-6,6'-dione

Intercalated 2D+2D hydrogen-bonded sheets in co-crystals of cobalt salt with 1H,1'H-[3,3']bipyridinyl-6,6'-dione

Midhun Mohan,[a] Love Karan Rana,[a] Thierry Maris[b] and Adam Duong[a]*

[a]Département de Chimie, Biochimie et physique and Institut de Recherche sur l'Hydrogène, Université du Québec à Trois-Rivières, Trois-Rivières, Québec, G9A 5H7, Canada.

[b]Département de Chimie, Université de Montréal, Montréal, Québec, H3C 3J7, Canada.

*To whom correspondence should be addressed. E-mail: adam.duong@uqtr.ca

ABSTRACT

Co-crystals of Co(II) salt and 1H,1'H-[3,3']Bipyridinyl-6,6'-dione **1** with the composition **1**•$Co(CHOO)_2(H_2O)_4$ were obtained by mixing both reactants. The single-crystal structure reveals that metal salt and organic ratio is 1:1. The supramolecular organization of the two components in the co-crystal was mainly dictated by hydrogen bonds between **1** and Co(II) complex. Infrared and powder X-ray diffraction were used to confirm the homogeneity and the phase purity of the bulk crystalline sample of **1**•$Co(CHOO)_2(H_2O)_4$. TGA/DTA was recorded to evaluate the thermal stability of the co-crystals.

Keywords: tecton, hydrogen bonds, co-crystals, self-assembly

INTRODUCTION

Co-crystals are the single-phase crystalline solid materials with distinctive properties involving stoichiometric ratio of at least two or more different molecular compounds which are neither solvates/or salts.[1] There are many synthetic strategies that are reported to prepare co-crystals.[2] However, it is still difficult to predict if a mixture of compounds has co-crystallized or not owing to the difficulty in obtaining single-crystals suitable for X-ray diffraction. Co-crystals are typically produced by slow evaporation of a mixture of solution components.[3,4] Generally, this approach works well for the molecules with complementary hydrogen bonding properties. Several other methods exist to generate co-crystals such as crystallization of the slurry, phase change in sublimation, neat and liquid-assisted grinding, and so forth.[3] In the crystallization process, solvent plays a key role to guide the molecular organizations through solute-solvent intermolecular interactions.[5-7] Up to date, the role of the solvent in the nucleation of co-crystals remains poorly understood. It may seem facile to prepare co-crystals when the experimental conditions are well determined but on the contrary, this is far from routine. Co-crystal engineering is interesting because the co-crystal solid obtained has enhanced physical properties than both the reactants due to which these solids find applications in energetic materials, agrochemicals and predominantly in pharmaceuticals.[8-13]

As part of our ongoing work on crystal engineering, we have synthesized and investigated the co-crystals of bipyridone **1** and cobalt salt (Scheme 1a). Pyridone and related compounds are known to form well-defined self-assembly by hydrogen bonding according to motifs **I** and **II** (scheme 1b).[14-17] Such compounds also known as "tectons" utilize specific attractive interactions during geometrically controlled aggregation process (because hydrogen bonds are highly directional in nature) and are often used to design and prepare molecular networks in crystalline phase.[18] Design and preparation of complex molecular networks using coordination bonding and various non-covalent interactions can be often foreseen by knowing the structure of tectons.[19] However, the molecular assembly of multi-component systems is relatively difficult to predict.

In this work, we synthesized the co-crystals by mixing **1** and cobalt salt and characterized it with single-crystal and powder X-ray diffractions, and infrared spectroscopy to elucidate the molecular structure. Thermogravimetric analysis was employed to evaluate the thermal stability of the molecularly ordered materials.

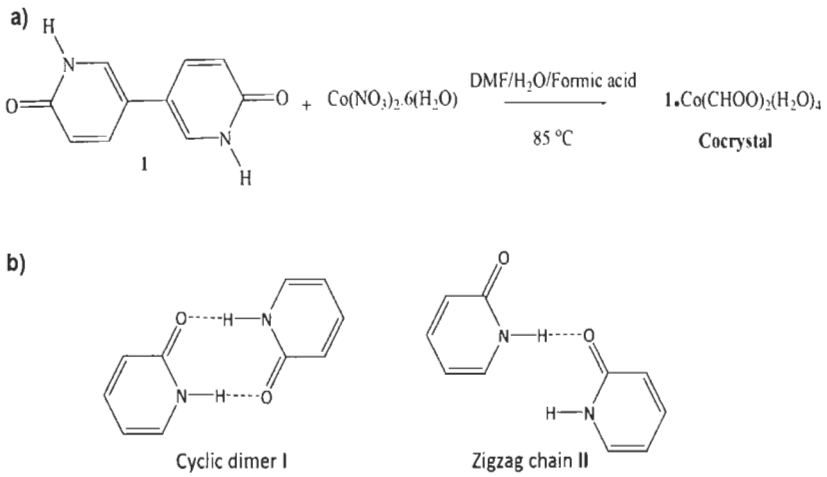

Scheme 1. a) Co-crystallization of **1** and cobalt complex to produce **1**•$Co(COO)_2(H_2O)_4$. b) Characteristic hydrogen bonding motifs **I** and **II** of 2-pyridone.

EXPERIMENTAL SECTION

All reagents were purchased from Alfa Aesar and were dried and degassed in Argon atmosphere prior to use. All solvents were purchased from Fischer Scientific and were used without further purification. 1H,1'H-[3,3']Bipyridinyl-6,6'-dione **1** was according to report method.[20] Co-crystals of both metal salt and ligand were obtained by mixing 0.2 mmol of $Co(NO_3)_2$. $6H_2O$ dissolved in 6 mL of water and 0.1 mmol of dipyridone **1** dissolved in 6 mL of DMF. Following this step few drops of 0.1N formic acid were added with constant stirring and the mixture was sealed in a 10 mL glass vial. The solution was kept in an oven at 85 ^{0}C for 48 h and then cooled to room temperature to produce the co-crystals. **1**•$Co(CHOO)_2(H_2O)_4$: yield 70 %. Pink crystals. FT-IR v 3176, 2852, 1641, 1566, 1462, 1415, 1355, 1237, 1163, 985, 955, 885, 846, 711 cm^{-1}.

Analytical Techniques

Single-crystal X-ray diffraction data were collected using a Bruker Venture Metaljet diffractometer with Ga Kα radiation. The structures were solved by direct methods using *SHELXT* [21], and non-hydrogen atoms were refined anisotropically with Least Squares minimization using *SHELXL-2018*.[22] Powder X-ray diffraction data was collected on a Bruker D8 Advance diffractometer equipped with a LYNXEYE linear position sensitive detector (Bruker AXS, Madison, WI). Neat samples were smeared directly onto the silicon wafer of a proprietary low-background sample holder. Data was collected using a continuous coupled θ/2θ scan with Ni-filtered CuKα (λ = 1.54178 Å) radiation operated at 40 kV and 40 mA. The IR(ATR) spectra were observed with a Nicolet iS 10 Smart FT-IR Spectrometer within 600–4000 cm^{-1}. The thermogravimetry analysis was performed using a Diamond Pyris TGA/DTA apparatus from Perkin-Elmer.

RESULTS AND DISCUSSION

Co-crystals with the formula of **1**•$Co(CHOO)_2(H_2O)_4$ were prepared by mixing **1** (1 equiv) and $Co(NO_3)_2$. $6H_2O$ (2 equiv) in DMF/H_2O followed by addition of 0.1 N formic acid. FT-IR was recorded to detect the main functional groups existing in the co-crystals. The infrared spectrum of

the co-crystals **1**•$Co(CHOO)_2(H_2O)_4$ shows the C=O of the pyridone groups at 1566 cm^{-1} (Figure 1). The bands in the range 2900-2800 cm^{-1} are attributed to the =CH bonds of the compound **1**. Although, we have used $Co(NO_3)_2 \cdot 6H_2O$ salt, the characteristic peak corresponding to nitrate counter ions was not observed in the FT-IR spectrum of the co-crystals, however, absorption bands at 1641 and 1415 cm^{-1} indicated the presence of C=O bonds corresponding to formate anions ($CHOO^-$). The band at 711 cm^{-1} can be attributed to Co–O vibration in octahedral coordination site. The presence of water molecules is diagnosed with the broad band in the range 3200-3000 cm^{-1}.

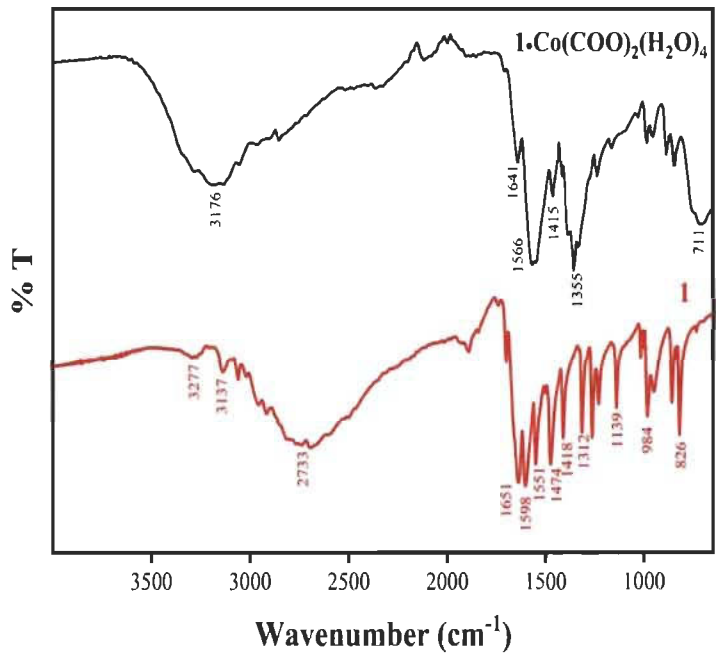

Figure 1. Comparison FT-IR spectra of compound **1** and **1**•$Co(CHOO)_2(H_2O)_4$.

Crystal structure and phase purity

Co-crystals of both organic and inorganic components were crystallized in monoclinic space group *C2/c* with the composition **1**•$Co(CHOO)_2(H_2O)_4$. Perspective view of the structure is shown in Figure 2, and crystallographic data are given in Table S1. The octahedral coordination geometry

around cobalt(II) ion is granted by four water molecules in a square planar arrangement and two formate groups in the axial position. The Co-O distances of the cobalt complex are normal (average Co-O distance = 2.085).[22-23] In the cocrystal, compound **1** forms self-assemblies by hydrogen bonded $R_2^2(6)$ ring synthons[24-25] according to motif **I** (Figure 2a) to produce 1D chains propagating along the *c* axis (average N-H···O distance = 2.807 Å). These organic chains are linked to $Co(CHOO)_2(H_2O)_4$ units by D(1) catemer synthons (average O_{water}-H···$O_{pyridone}$ distance = 2.707 Å) to generate a 2D sheet parallel to the *ac*- plane (Figure 2a). In another 2D sheet running parallel to the *bc*- plane, adjacent metal units are linked together by hydrogen bonds (average O_{water}-H···$O_{formate}$ distance = 2.718 Å) between coordinated formate anions and adjacent water molecules generating three cyclic ring synthons *viz*. $R_2^2(8)$, $R_2^2(12)$, and $R_3^2(8)$ synthons (Figure 2b). These 2D sheets are arranged perpendicular to each other and interlinked to form three-dimensional hydrogen bonded grid network (Figure 2c, and 2d). Moderate and weak π···π interactions of magnitude 3.708 Å and 4.037 Å between pyridine rings reinforce the structure. Details of the hydrogen bonds and their angles are summarized in Table S2.

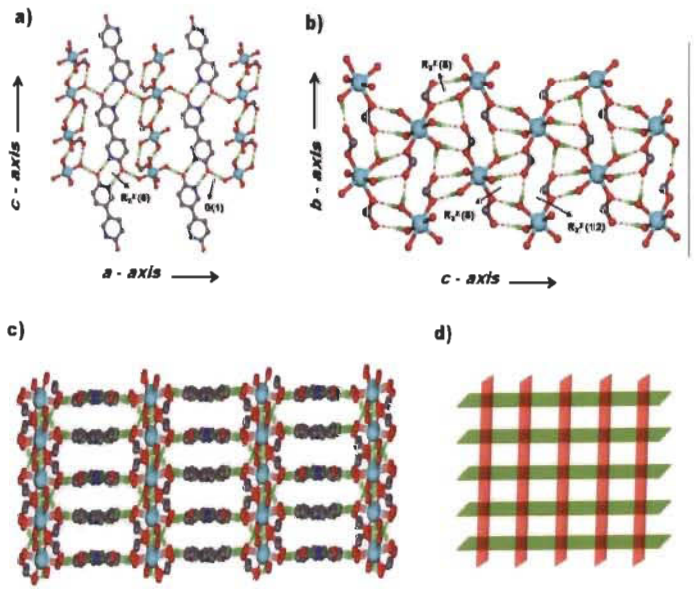

Figure 2. Structure of the cocrystal **1**•$Co(CHOO)_2(H_2O)_4$. (a) View of a hydrogen bonded 2D sheet running parallel to *ac*- plane built by alternating chains of organic tecton **1** and inorganic $Co(CHOO)_2(H_2O)_4$ units, (b) View of a sheet comprised of $Co(CHOO)_2(H_2O)_4$ units running parallel to *bc*- plane by hydrogen bonds, (c) 3D hydrogen bonded framework, d) 3D grid type arrangement. Note carbon atoms are shown in gray, hydrogen atoms in green, oxygen atoms in red, nitrogen atoms in blue and cobalt atoms in cyan.

In the crystal structure the dipyridone based molecular *tectons* are self-assembled according to classical cyclic dimer motif *viz.* $R_2^2(6)$ ring synthons (homosynthons) to form 1D chains in the crystal lattice. Conversely, metallic units with coordinated water molecules and counter anions can potentially form different supramolecular synthons (hetero- and catemer synthons) to direct structural organization in the crystal structure. The rationale is that oxygen atoms (water molecules and formate anions) slightly get electron deficient after the donation of lone pair of electrons to metal atom which makes O-H bonds more polar and shorter because of the electrostatic component introduced in the same. Moreover, coordination to metal ions introduces anisotropic character in oxygen atoms of formate anions and water molecules resulting in flexible O-H···O angles and in fact more directional preference in the angle of approach of hydrogen bond donors. Thus, in the current structure we have different O-H···O bonds varying in strength due to flexibility in O-H···O angles which is apparent from moderate to strong hydrogen bonds observed (average D-A distance in (D) O-H···O (A) ~ 2.732 Å), bond angles ~ 120° for moderate and >170° for strong) in the synthons ($R_2^2(8)$, $R_2^2(12)$ and $R_3^2(8)$ synthons). So the metallic unit co-crystallized in the lattice can also play an important role in molecular organization and thus important from crystal engineering point of view.

As the co-crystallization process might result in a blend of several crystalline phases, the bulk sample was examined by powder X-ray diffraction (PXRD). Crystals of **1**•$Co(CHOO)_2(H_2O)_4$ were stable outside of the mother liquors and were suitable for PXRD analysis. All peaks of measured PXRD (in black) match well with the simulated (in red) patterns confirming the phase purity of the crystalline sample (Figure 3). The predominant peaks at 7.4° and 14.7° in the pattern

belong to the [400] plane. Due to the preferential orientation of the pattern in [400] plane, peak at 18.1° is reduced in the simulated pattern, which belongs to the [20-2] plane.

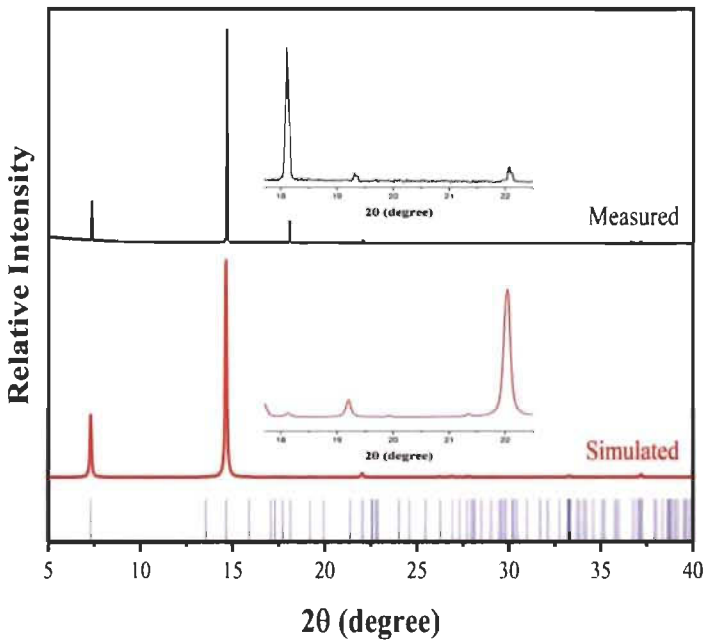

Figure 3. Comparison of the observed PXRD (red) of the bulk crystalline sample with the simulated pattern (black) calculated from the XRD data **1**•$Co(CHOO)_2(H_2O)_4$ (insets are zooms in the respective region). The vertical bars (blue) denotes the calculated positions of the diffraction peaks.

Thermal analysis

Thermal stability of the co-crystals **1**•$Co(CHOO)_2(H_2O)_4$ was investigated by thermogravimetric analysis and differential thermal analysis simultaneously (Figure 4). The TGA/DTA curves of co-crystal sample display an exothermic peak with a weight loss of 18 wt% at 146 ^{0}C which can be attributed to the loss of four water molecules. The two last decomposition steps with weight losses of 32 wt% and 19 wt% accompanied with a sharp exothermic peak at 292 ^{0}C and a weaker peak

at 591 ^{0}C respectively. These two mass losses are characteristic of the decomposition of organic components to give the final residue. A comparison of TGA curves of 1•$Co(CHOO)_2(H_2O)_4$ and free ligand show a faster decomposition for the co-crystals (Figure S2).

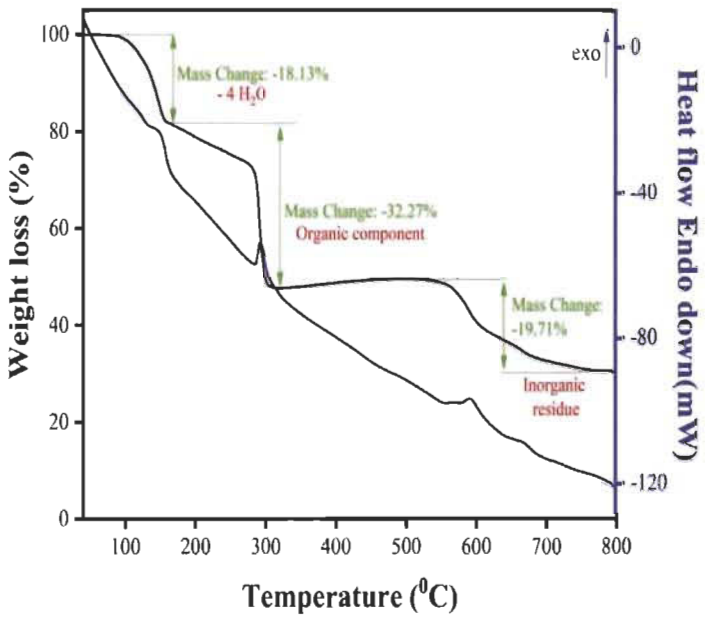

Figure 4. TGA (black) and DTA (blue) curves of 1•$Co(CHOO)_2(H_2O)_4$.

CONCLUSIONS

Pyridone and their derivatives are a family of compounds that self-assemble by hydrogen bonding with well-known motifs. Nevertheless, these hydrogen bond patterns can be interrupted by the intercalation of the co-compound that is added in the solution mixture. In this work, we demonstrated that bipyridone **1** is disposed to form strong intermolecular interaction by hydrogen bonds with a predictable pattern. The crystal structure shows that tecton **1** undergoes self-assembly by hydrogen bonds to form chains according to motif **I** and these chains are linked to hydrogen bonded 2D sheets of $Co(CHOO)_2(H_2O)_4$ units to generate a 3D framework. The IR spectrum of the co-crystal sample demonstrate the absence of the nitrate counter ions and indicates the presence

of formate ($CHOO^-$) which is in good correlation with the single-crystal X-ray diffraction. The phase purity of the bulk products was checked by comparing its observed and simulated PXRD patterns. The TG curves show that the thermal stability of **1** is drastically modified by the presence of $Co(CHOO)_2(H_2O)_4$.

Supporting Information

Additional crystallographic details (including thermal atomic displacement ellipsoid plots), ORTEP diagrams and other crystallographic data and Thermogravimetry analysis are available with the article through the journal web site at http://nrcresearchpress.com/doi/suppl/xxxxxx.

Accession Codes

CCDC 1959446 contain the supplementary crystallographic data for this paper. These data can be obtained free of charge via www.ccdc.cam.ac.uk/data_request/cif, of by email data_request@ccdc.cam.ac.uk, or by contacting The Cambridge Crystallographic Data Centre, 12 Union Road Cambridge CB2 1EZ, UK; fax: +44 1223 336033.

Author Information

Corresponding Author

*E-mail: adam.duong@uqtr.ca.

ORCID

Adam Duong : 0000-0002-4927-3603

CONFLICTS OF INTEREST

There are no conflicts to declare.

ACKNOWLEDGMENT

We are grateful to the Natural Sciences and Engineering Research Council of Canada (RGPIN-2015-06425), the Fonds de Recherche du Québec – Nature et Technologies, the Canada

Foundation for Innovation, the Canadian Queen Elizabeth II Diamond Jubilee Scholarships and the Université du Québec à Trois-Rivières for financial supports.

REFERENCES

1. Aitipamula, S.; Banerjee, R.; Bansal, A. K.; Biradha, K.; Cheney, M. L.; Choudhury, A. R.; Desiraju, G. R.; Dikundwar, A. G.; Dubey, R.; Duggirala, N.; Ghogale, P. P.; Ghosh, S.; Goswami, P. K.; Goud, N. R.; Jetti, R. R. K. R.; Karpinski, P.; Kaushik, P.; Kumar, D.; Kumar, V.; Moulton, B.; Mukherjee, A.; Mukherjee, G.; Myerson, A. S.; Puri, V.; Ramanan, A.; Rajamannar, T.; Reddy, C. M.; Rodriguez- Hornedo, N.; Rogers, R. D.; Row, T. N. G.; Sanphui, P.; Shan, N.; Shete, G.; Singh, A.; Sun, C. C.; Swift, J. A.; Thaimattam, R.; Thakur, T. S.; Kumar Thaper, R.; Thomas, S. P.; Tothadi, S.; Vangala, V. R.; Variankaval, N.; Vishweshwar, P.; Weyna, D. R.; Zaworotko, M. J. Crystal Growth & Design 2012, 12, 2147-2152.

2. Jafari, M. K.; Padrela, L.; Walker, G. M.; Croker, D. M. Cryst. Growth Des. 2018, 18, 6370-6387.

3. Basavoju, S.; Boström, D.; Velaga, S. P. Cryst. Growth Des. 2006, 6, 2699–2708.

4. Wittering, K.; King, J.; Thomas, L.; Wilson, C. Crystals, 2014, 4, 123.

5. Khamar, D. k.; Zeglinski, J.; Mealey, D.; Rasmuson, A. C. J. Am. Chem. Soc. 2014, 136, 11664-11673.

6. Jia, L.; Svard, M.; Rasmuson, A. C. Cryst. Growth Des. 2017, 17, 2964-2974.

7. Zeglinski, J.; Kuhs, M.; Devi, K. R.; Khamar, D. k.; Hegarty, A. C.; Thompson, D.; Rasmuson, A. C. Cryst. Growth Des. 2019, 194, 2037-2049.

8. Bolton, O.; Simke, L. R.; Pagoria, P. F.; Matzger, A. J. Crystal Growth & Design 2012, 12, 4311-4314.

9. Sekhon, B. S. International Journal of Agrochemicals and Plant Protection 2014, 2, 44-47.

10. Aitipamula, S.; Wong, A. B. H.; Chow, P. S.; Tan, R. B. H. Crystal Growth & Design 2014, 14, 2542-2556.

11. Aitipamula, S.; Chow, P. S.; Tan, R. B. H. CrystEngComm, 2009, 11, 1823-1827.

12. Basavoju, S.; Bostrom, D.; Velaga, S. P. Crystal Growth & Design 2006, 6, 2699-2708.

13. Banerjee, R.; Bhatt, P. M.; Ravindra, N. V.; Desiraju, G. R., Crystal Growth & Design 2005, 5, 2299-2309.

14. Munakata, M.; Wu, L. P.; Yamamoto, M.; Sowa, T. K.; Maekawa, M. J. Am. Chem. Soc. 1996, 118, 3117-3124.

15. Wu, L. P.; Yamamoto, M.; Sowa, T. K.; Maekawa, M.; Suenaga Y.; Munakata, M. J. Chem. Soc., Dalton Trans. 1996, 203I-2037.

16. Rawson, J. M.; Winpenny, R. E. P.; Coord. Chem.Rev., 1995, 139, 313-374.

17. Simard, M.; Su, D.; Wuest, J. D. J. Am. Chem. SOC. 1991, 113, 4696-4698

18. Brunet, P.; Simard, M.; Wuest, J. D. J. Am. Chem. Soc. 1997, 119, 2737-2738.

19. Hosseini, M.W. Acc. Chem. Res. 2005, 38, 313-323.

20. Mohan, M.; Maris, T.; Duong, A., CrystEngComm., 2020, DOI: 10.1039/C9CE01725A.

21. Sheldrick, G. M. Acta Crystallogr., Sect. A 2015, 71, 3-8.

22. Sheldrick, G. M. Acta Crystallogr., Sect. C 2015, 71, 3-8.

23. Mohan, M.; Rajak, S.; Tremblay, A. A.; Maris T.; Duong A.; Dalton Trans. 2019, 48, 7006-7014.

24. Ibrahim, S.; Shehzadi, K.; Iqbal, B.; Abbas, S.; Turner, D. R.; Nadeem, M. A. Journal of Colloid and Interface Science, 2019, 545, 269-275.

25. Desiraju, G.R. Angew. Chem., Int. Ed. Engl. 1995, 34, 2311-2327.

26. Bernstein, J.; Davis, R.E.; Shimoni, L.; Chang, N.L. Angew. Chem., Int. Ed. Engl. 1995, 34, 1555-1573

Figure 2. Comparison FT-IR spectra of compound **1** and **1**•$Co(CHOO)_2(H_2O)_4$.

Figure 2. Structure of the cocrystal **1**•$Co(CHOO)_2(H_2O)_4$. (a) View of a hydrogen bonded 2D sheet running parallel to *ac*- plane built by alternating chains of organic tecton **1** and inorganic $Co(CHOO)_2(H_2O)_4$ units, (b) View of a sheet comprised of $Co(CHOO)_2(H_2O)_4$ units running parallel to *bc*- plane by hydrogen bonds, (c) 3D hydrogen bonded framework, d) 3D grid type arrangement. Note carbon atoms are shown in gray, hydrogen atoms in green, oxygen atoms in red, nitrogen atoms in blue and cobalt atoms in cyan.

Figure 3. Comparison of the observed PXRD (red) of the bulk crystalline sample with the simulated pattern (black) calculated from the XRD data **1**•$Co(CHOO)_2(H_2O)_4$ (insets are zooms in

the respective region). The vertical bars (blue) denotes the calculated positions of the diffraction peaks.

Figure 4. TGA (black) and DTA (blue) curves of **1**•$Co(CHOO)_2(H_2O)_4$.

Table of Contents Graphic

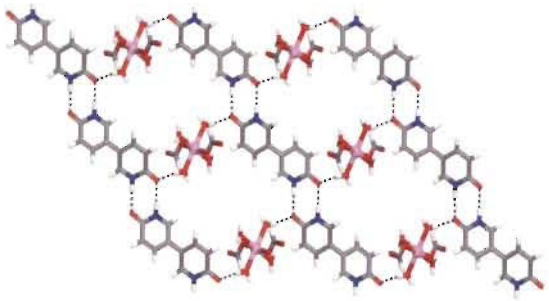

Table of Contents Synopsis

Co-crystals of composition **1**•$Co(CHOO)_2(H_2O)_4$ were obtained by mixing organic and inorganic components. The hydrogen bonded supramolecular associations resulted from co-assembly of dipyridone and cobalt complex.

4.5 Conclusions

The supramolecular self-assembly of pyridonyl functional compounds has motivated us to investigate the co-crystallization of the dipyridone with cobalt salts. Hydrogen bond motifs of pyridone can result in the formation of new moieties which can interest the material science community to develop a new class of supramolecular architectures. In this chapter, a detailed understanding has been provided on the formation of a strong intermolecular hydrogen bonding pattern of dipyridone which are intercalated with the hydrogen bonded 2D sheets of cobalt salt forming a 3D network. The crystal analysis of the synthesized co-crystal reveals the self-assembly of the molecular tectons of dipyridone according to the cyclic dimer motif forming a homosynthon of 1D chains whereas metallic unit with counter ions and coordinated water molecules forms a different supramolecular synthon. The materials synthesized were characterized using various techniques. As predicted, the development of co-crystals has altered the stability and other properties of the parent organic ligand. This work can be regarded as a forecast to enlighten the possibility of exploring co-crystallization as a powerful tool to understand the supramolecular chemistry and building materials with special physical and chemical properties.

CHAPTER 5: Coordination Chemistry of Bidentate Pyridone Based Organic Ligand

5.1 Introduction

The significance of designing novel organic ligands and their molecular self-assemblies has had been discussed in the previous chapter. These synthesized organic moieties have been proposed as the potential alternates for carboxylate ligands as they comprise of numerous coordination modes than the latter as well as restrict the free rotation of the coordinated sphere along the plane of the ligand. This can greatly increase the stability of the constructed coordination polymers. These studies motivated us to use bidentate pyridonyl ligand for the coordination chemistry which has been highlighted in this chapter that focuses on the use of pyridonyl based ligands for the synthesis of Metal-Organic Frameworks and other coordination polymers. Similar strategies for the synthesis of ligand were adopted. Furthermore, the self-assembly of the bipyridone compounds through hydrogen bonds was also investigated in different conditions. This work can also lead to the use of other bidentate as well as multidentate pyridonyl functional compounds for constructing a novel class of coordination polymers.

5.2 Objectives

- A detailed investigation on the coordination modes of pyridonyl functional groups and the possibility to utilize these motifs to obtain extended frameworks.
- Design novel coordination polymers by taking advantage of the versatility of the coordination mode of 2-pyridone ligating group.
- Synthesis of dipyridone by Suzuki coupling.

- Crystallization of the synthesized dipyridone in different solvent and temperature conditions to investigate the self-assembly.
- Characterization of the dipyridone using various techniques.
- Coordination of the dipyridone by solvothermal conditions to form organic-inorganic hybrid crystalline extended two-dimensional structure and its characterization.

5.3 Authors' Contribution

Midhun Mohan. Visualization and investigation of experiments, synthesis of all compounds, validation of the concept and curation of data, drafting the original manuscript.

Thierry Maris. Investigation and curation of X-ray diffraction experiments.

Adam Duong. Conceptualization of the project, project administration, supervision, funding acquisition, crystallization of compound **1b**, editing of the manuscript and design of the art cover.

5.4 Article 3

Building Coordination Polymers Using Dipyridone Ligands

CrystEngComm

ROYAL SOCIETY OF CHEMISTRY

PAPER

View Article Online
View Journal

Cite this: DOI: 10.1039/c9ce01725a

Building coordination polymers using dipyridone ligands†

Midhun Mohan,[a] Thierry Maris[b] and Adam Duong*[a]

Received 30th October 2019,
Accepted 15th November 2019

DOI: 10.1039/c9ce01725a

rsc.li/crystengcomm

By examining the crystal structures of the self-assemblies of 1*H*,1'*H*-[3,3']bipyridinyl-6,6'-dione **1** and its coordination structure with Co(II), to form novel **CP-671**, our study demonstrates the tendency of dipyridones to generate predictable patterns by hydrogen bonding depending on the crystallization conditions and the potential of pyridone ligating groups to design novel coordination polymers with structural diversity. The two structures of **1** elucidated by single-crystal X-ray diffraction show a cyclic dimer and zigzag chain to generate fascinating hydrogen bond frameworks. A two-dimensional coordination polymer structure (**CP-671**) is obtained by the linkage of **1** with a cobalt cation according to a known coordination mode of the 2-pyridone ligating group.

Introduction

Coordination polymers (CPs) are organometallic compounds containing metal cation centres linked by ligands with a repeating unit extending in 1-, 2- and 3-dimensions. They are relevant to many fields such as organic and inorganic chemistry, biochemistry, materials science and so forth.[1–6] This interdisciplinary nature of CPs has led to extensive studies in the past few decades. Coordination polymers by virtue of their unique properties such as porosity, structural diversity and functional tunability have been claimed to be mainstream candidates for applications such as gas storage, catalysis, drug delivery, photoluminescence, molecular machines, magnetism, and optoelectronics.[11–15] Their properties are mainly facilitated by the diverse assembly of metal ions and organic moieties resulting mainly in 2D and 3D frameworks. The most commonly used ligands to prepare CPs include polypyridines and polycarboxylates, which limit their structural diversity.[7–10]

For the past few decades, 2-pyridone and its derivatives have been studied for their rich coordination chemistry and ability to self-assemble by hydrogen bonding.[16–19] The dynamics involved in forming and breaking hydrogen bonds along with the structural possibility for tautomerism allow these materials to be used in biological and electronic applications.[20–22] Their structural similarity to carboxylic acids makes it easy for these compounds to produce self-assembled hydrogen bond networks according to motifs **I** and **II** (Scheme 1a)[23–26] along with their numerous ligating coordination modes **III–IX** (Scheme 1b).[27–34] Due to the presence of two different donor atoms (O and N atoms), they have been used to prepare heteroatomic complexes. Although there have been extensive reports on the molecular aggregation behaviour of 2-pyridone and related compounds, there remain some curious omissions. For instance, although the number of single-crystal structures of dipyridones and related heterocycles have been reported, only a few display self-assembly by hydrogen bonds with motif **II**.[25,26] Moreover,

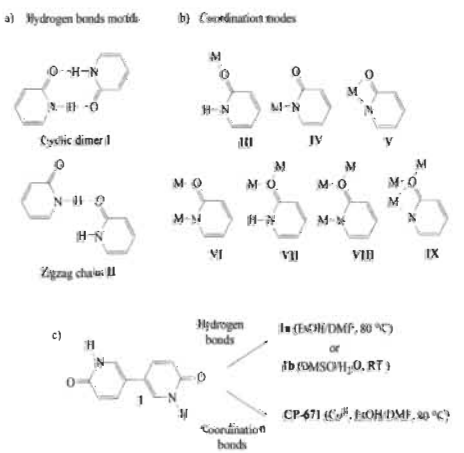

Scheme 1 (a) Representation of the hydrogen-bonded structures, (b) the coordination modes of 2-pyridone, and (c) schematic illustration of the preparation of crystals of **1a**, **1b** and **CP-671**.

[a] Département de Chimie, Biochimie et physique and Institut de Recherche sur l'Hydrogène, Université du Québec à Trois-Rivières, Trois-Rivières, Québec, G9A 5H7, Canada. E-mail: adam.duong@uqtr.ca
[b] Département de Chimie, Université de Montréal, Montréal, Québec, H3C 3J7, Canada

† Electronic supplementary information (ESI) available: Synthesis of **1**, **1'** and **CP-671**; NMR, IR, SEM, and XRD data. CCDC 1908861–1908865a contain the supplementary crystallographic data for this paper. For ESI and crystallographic data in CIF or other electronic format see DOI: 10.1039/c9ce01725a

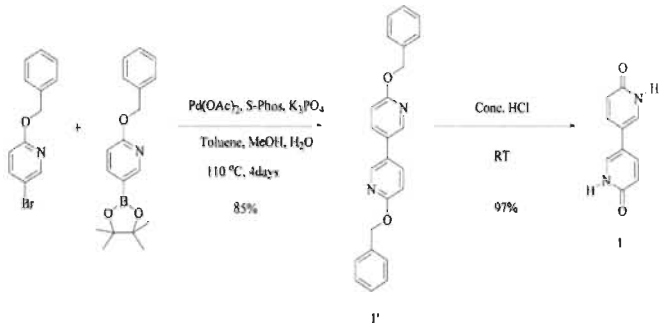

Scheme 2 Synthetic route of intermediate 1' and dipyridone 1.

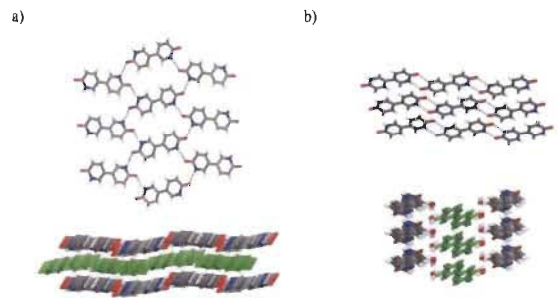

Fig. 1 (a) View of the 2D self-assembly by hydrogen bonding according to motif II (top) and the stacked three layers (bottom) of 1a. (b) View showing how N-H···O hydrogen bonds of motif I link molecules into chains along the c-axis (top) and view along the a-axis showing the alternating layers composed of compound 1 and water molecules. For clarity, one layer is marked in green. Hydrogen bonds are represented by broken lines. C, gray; O, red; N, blue; H, white.

coordination chemists tend to restrict their interest only in the formation of molecular complexes.[35-37] Noelle R. C. *et al.*, reported the synthesis of a metal-organic framework (MOF-910) made from a heterotritopic linker, with the pyridone group being one of the ligating groups, which remains the only known example of a constructed crystalline extended framework structure containing a pyridone group.[38]

Our main focus is to design novel CPs by taking advantage of the versatility of the coordination mode of the 2-pyridone ligating group. 2-Pyridone can bind metal ions in its neutral (mode III and VII) or deprotonated (mode IV–VI and VIII–IX) forms which can be adjusted according to the conditions used, thereafter providing structural diversities in CPs. In this work, as a second focus, we also investigated the crystallization conditions to control the association motif of 1 by hydrogen bonding. In the solid state, the predominant form is 2-pyridone, which has been confirmed with X-ray crystallographic data.[39] In principle, dipyridone 1 should be perfect to design chains and 2D networks by hydrogen bonding according to motifs I and II.

Herein, we report a new synthetic strategy for 1, the investigation of its self-assembly processes to create organic supramolecular crystals (1a and 1b) and the synthesis of an organic–inorganic hybrid crystalline extended structure (CP-671). This work demonstrates that dipyridone can bind with metal ions to produce two-dimensional CPs. From our knowledge, this is the first example of an extended structure built using a polypyridone ligand. This study also illustrates that depending on the conditions of crystallization, 1 can self-assemble to associate in particular ways.

Experimental

Materials

Most reagents were purchased from Alfa Aesar and were dried and degassed in an argon atmosphere prior to use. 2,5-Dibromopyridine was purchased from TCI and silica for column chromatography was purchased from SiliCycle. Freshly distilled benzyl alcohol was used. All solvents were purchased from Fisher Scientific and were used without further purification.

Single crystal X-ray diffraction

Single-crystal X-ray diffraction data were collected using a Bruker Venture Metaljet diffractometer with Ga Kα radiation for compounds 1a and CP-671 and a Bruker Smart APEX 2

Table 1 Crystallographic data of compound 1 and CP-671

Compound	1a (EtOH/DMF)	1b (DMSO/H_2O)	CP-671
Formula	$C_{10}H_8N_2O_2$	$C_{10}H_8N_2O_2 \cdot 2H_2O$	$C_{20}H_{20}CoN_6O_{12}$
Mr	188.18	224.22	595.35
Crystal system	Monoclinic	Monoclinic	Orthorhombic
Space group	$P2_1/n$	$P2_1/n$	$Pbca$
a (Å)	6.9152(3)	8.9683(15)	7.6304(5)
b (Å)	18.3958(8)	3.8091(7)	17.6827(13)
c (Å)	7.2525(3)	14.749(3)	17.7371(11)
α (deg)	90	90	90
β (deg)	115.199(2)	91.476(13)	90
γ (deg)	90	90	90
V (Å^3)	834.80(6)	503.68(16)	2393.2(3)
Z	4	2	4
ρ_{calcd} (g cm^{-3})	1.497	1.478	1.652
T (K)	150	100	100
Radiation	GaKα	CuKα	GaKα
λ (Å)	1.34139	1.54178	1.34139
μ (mm^{-1})	0.567	0.980	4.390
F (000)	392	236	1220
No. of measured reflections	12 285	4085	20 193
No. of independent reflections	1912	915	2735
No. of obsd. reflections $I > 2\sigma(I)$	1637	606	1718
Nb params	160	85	180
R_1, $I > 2\sigma$ (%)	0.0450	0.0696	0.0730
R_1, all data (%)	0.0518	0.1055	0.1301
ωR_2, $I > 2\sigma(I)$ (%)	0.1215	0.2046	0.1376
ωR_2, all data (%)	0.1289	0.2483	0.1607
GoF	1.056	1.099	1.111

diffractometer with Cu Kα radiation for compound **1b**. The structures were solved by direct methods using SHELXT-2018,[40] and non-hydrogen atoms were refined anisotropically with least squares minimization using SHELXL-2018.[11] Hydrogen atoms were treated by first locating them from difference Fourier maps and were fully refined for **1a**. For **1b**, hydrogen atoms attached to carbon were refined using a riding model (C–H distances of 0.95 Å) while those attached to O and N were fully refined. For **CP-671**, all H atoms were refined using the riding model (C–H distances of 0.95 Å and N–H & O–H distances of 0.88 Å).

Powder X-ray diffraction

Powder X-ray diffraction data were collected on a Bruker D8 Advance diffractometer equipped with a LYNXEYE linear position sensitive detector (Bruker AXS, Madison, WI). Neat samples were smeared directly onto the silicon wafer of a proprietary low-background sample holder. Data were collected using a continuous coupled $\theta/2\theta$ scan with Ni-filtered CuKα (λ = 1.54178 Å) radiation operating at 40 kV and 40 mA.

Other analysis techniques

The IR(ATR) spectra were observed with a Nicolet iS 10 Smart FT-IR spectrometer within 600–4000 cm^{-1}. Thermogravimetry analysis was performed using Diamond Pyris TGA/DTA apparatus from Perkin-Elmer and Mettler Toledo TGA/DSC1. Scanning electron microscopy was performed using a JEOL model 5500. EDS was performed using an X-Max 20 mm^2 model. XPS was carried out with an Axis Ultra model. *In situ* thermal microscopy was performed using a combination of a Nikon Eclipse E200 microscope and Mettler Toledo FP82 hot stage microscopy system. ^{1}H and ^{13}C NMR spectra were recorded with Bruker 400 MHz and 100 MHz spectrometers, respectively.

Synthesis of 1′

Dried and degassed $Pd(OAc)_2$ (0.101 g, 0.15 mmol) and SPhos (0.118 g, 0.288 mmol) were placed into a dried Schlenk flask and degassed for 2 hours. To this mixture, degassed toluene (20 mL) was added followed by adding 5-benzyloxy-2-(4,4,5,5-tetramethyl-[1,3,2]dioxaborolan-2-yl) pyridine (1 g, 3.21 mmol) and 5-benzyloxy-2-bromo-pyridine (0.8451 g, 3.21 mmol). The solution was bubbled with argon gas for 1 hour. In a 2-neck flask, K_3PO_4 was dried, solubilized with degassed MeOH/H_2O (6 mL each) solution, and degassed for an hour. This K_3PO_4 solution was added into a reaction flask dropwise with a rate of 1 mL min^{-1}. The reaction flask was sealed with a cold finger and refluxed at 110 °C for 4 days, after which the mixture was cooled to room temperature and the solvent was evaporated under reduced pressure. The solution was then diluted with DCM (30 mL), and washed with water and the organic layer was extracted followed by drying using magnesium sulphate, filtering and solvent evaporation. The crude product was purified using column chromatography (silica gel, eluent: $CHCl_3$: hexane, 1 : 2). Compound **1′** was obtained as a colourless solid and dried under vacuum, and

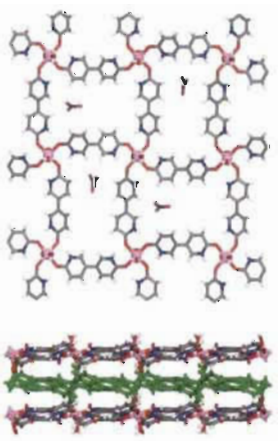

Fig. 2 View of a layer of **CP-671** showing the linkage of **1** with Co ions according to mode III (top) and the packing of the 2D layers to form the three-dimensional structure (bottom). For clarity, one layer is marked in green. Co, pink; C, gray; O, red; N, blue; H, white.

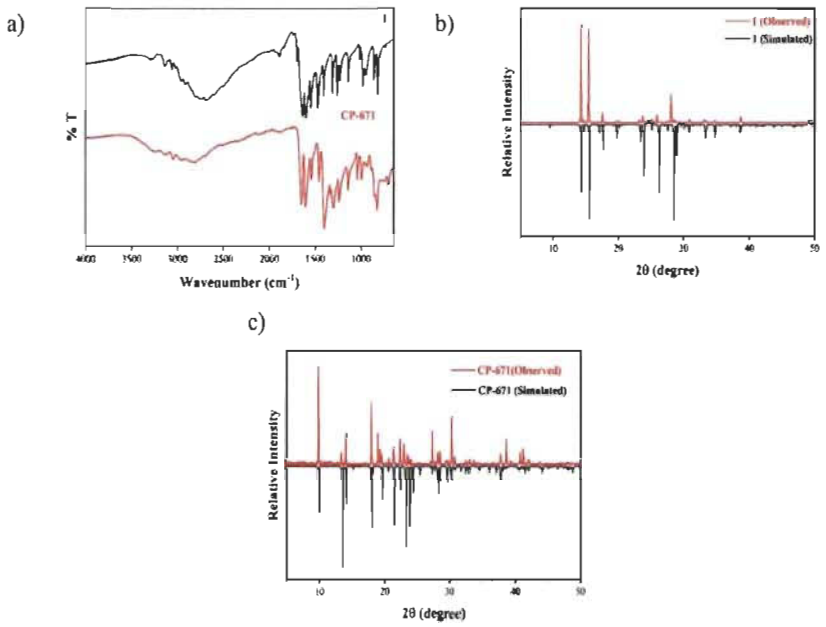

Fig. 3 (a) Comparison of the FTIR spectra of **1** (black) and **CP-671** (red). (b) and (c) Comparison of the observed PXRD (red) with the simulated pattern (black) calculated from the XRD data for **1a** and **CP-671**, respectively.

the yield was noted (0.946 g, yield 85%). ^{1}H-NMR (700 MHz, DMSO-d_6) δ 8.49 (d, J = 2.5 Hz, 2H), 8.06 (dd, J = 8.6, 2.6 Hz, 2H), 7.47 (d, J = 7.5 Hz, 4H), 7.39 (t, J = 7.5 Hz, 4H), 7.33 (t, J = 7.4 Hz, 2H), 6.99 (d, J = 8.69 Hz, 2H), 5.41 (s, 4H). ^{13}C-NMR (175 MHz, DMSO-d_6) δ 162.9, 144.7, 137.9, 137.7, 128.8, 128.3, 128.2, 127.0, 111.4, 67.5. FT-IR ν 3063, 3039, 2951, 2888, 1598, 1560, 1496, 1477, 1463, 1453 1354, 1307, 1279, 1243, 1144, 1047, 999, 991, 917, 870, 822, 740, 724, 697 cm^{-1}. HRMS (ESI) (M + H)$^+$ calc. 369.1598, found 369.1604.

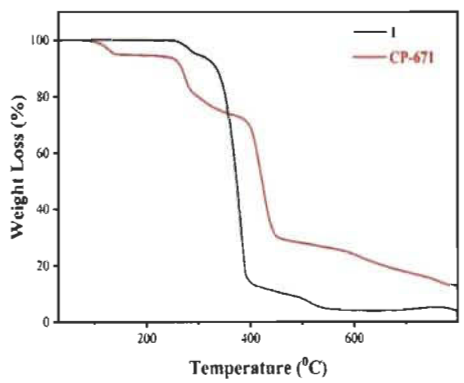

Fig. 4 TG curves of **1** (black) and **CP-671** (red).

Synthesis of 1

Compound **1'** (0.871 g, 2.37 mmol) was placed into a round bottom flask and diluted with methanol (45 mL). The solution was stirred and heated at 65 °C for a while. Concentrated HCl (15 mL) was added to the above solution dropwise. The solution was refluxed overnight. The resulting mixture was cooled, and the pH was neutralized by adding a saturated $NaHCO_3$ solution. Ligand **1** started to precipitate which was then filtered, washed with water followed by cold ethanol and dried in a vacuum. Compound **1** was obtained as a colourless solid (0.433 g, yield 97%).

^{1}H-NMR (700 MHz, DMSO-d_6) δ 11.75 (s, 2H), 7.70 (dd, J = 9.5, 2.8 Hz, 2H), 7.57 (d, J = 2.5 Hz, 2H), 6.38 (d, J = 9.5 Hz, 2H). ^{13}C-NMR (175 MHz, DMSO-d_6) δ 162.0, 139.8, 131.8, 120.5, 114.8. FT-IR ν 3268, 3137, 3054, 2827, 1711, 1651, 1611, 1551, 1474, 1418, 1337, 1273, 1242, 1162, 992, 954, 888, 826 cm^{-1}. HRMS (ESI) (M + H)$^+$ calc. 189.0659, found 189.066.

Crystallization of 1a

0.04 g of compound **1** was dissolved with a mixture of 6 mL of DMF and 6 mL of ethanol solution in a scintillation vial. The solution was slowly heated to obtain a clear solution. The resulting solution was kept in an oven at 80 °C for 24 h. The solution was cooled slowly to room temperature and pale-yellow coloured crystals were washed using cold ethanol (0.034 g, yield 85%).

Crystallization of 1b

Crystals of **1b** were grown by allowing vapors of H_2O to diffuse into solutions of 1 dissolved in DMSO (~5 mg mL^{-1}) in closed vessels (~4 mg, yield 80%).

Synthesis of CP-671

0.058 g (0.2 mmol) of $Co(NO_3)_2{\cdot}6H_2O$ was dissolved in 6 mL of water and 0.188 g (0.1 mmol) of dipyridone was dissolved in 6 mL of DMF. Both solutions were mixed, placed into a scintillated vial and kept in an oven at 85 °C for 48 h. The mixture was cooled and the crystals were washed with MeOH. FTIR ν 3242, 3140, 3047, 2809, 1652, 1606, 1541, 1458, 1402, 1305, 1241, 1144, 1042, 996, 824, 568, 510 cm^{-1} (0.052 g, yield 87%).

Results and discussion

To assess the novel CPs, we tested the ability of **1** to form a periodic structure by coordination to transition metal ions. Most significantly, we demonstrated that crystalline extended structures (**CP-671**) can be obtained by linking **1** with cobalt(II) according to the well-established coordination mode **III**. The synthesis of compound **1** was previously reported by Edwin *et al.* with a 70% yield.[42] Here, we present a new synthetic approach for **1** with an improvement in the yield (see Scheme 2). Compound **1** was prepared by the Suzuki–Miyaura reaction of 5-benzyloxy-2-bromopyridine[13] and 5-benzyloxy-2-(4,4,5,5-tetramethyl-[1,3,2]dioxaborolan-2-yl)-pyridine[17] to form intermediate **1'** followed by deprotection with conc. HCl. The structure and the purity of **1** were confirmed by MS, IR, ^{1}H-NMR and ^{13}C-NMR as well as by single-crystal X-ray diffraction (XRD).

Crystal structure

Compound 1a. Crystals of **1a** were grown under solvothermal conditions at 80 °C in an EtOH/DMF solvent mixture. They were found to belong to the monoclinic $P2_1/n$ space group. The crystals are composed of molecule **1** only. Fig. 1a shows the views of the structure of **1a** and Table 1 contains other crystallographic data. In the solid state, the two N–H groups are *trans*-oriented. The planes of the two rings of pyridone are twisted with a torsional angle of 18.9°. Each pyridonyl group forms two hydrogen bonds with adjacent neighbours according to motif **II** producing a 2D network (average distance of N–H···O = 2.717 Å). The details of the hydrogen bonds and angles are provided in Table S1, ESI.† The three-dimensional structure consists of the packing of layers of **1**.

Compound 1b. To evaluate the influence of solvent and temperature in the self-assembly by hydrogen bonding, we crystallized **1** under other conditions. Crystallization by slow diffusion at room temperature in DMSO/H_2O gave single crystals of **1b**. The structure determined by XRD proved to belong to the monoclinic space group $P2_1/n$ and to have the composition $1{\cdot}2H_2O$. The views of the structure of **1b** are shown in Fig. 1b, and other crystallographic data are summarized in Table 1. Characteristic self-assembly of 2-pyridone according to motif **I** is observed in the crystals (N–H···O = 2.782 Å). The selected hydrogen bonds and angles are given in Table S2, ESI.† The two pyridones in **1** are nearly coplanar and the N–H groups are again *trans*-oriented. Each molecule participates in four hydrogen bonds forming tapes, which further stack to produce layers. The layers are joined by hydrogen bonding involving the bridging of water molecules to form the three-dimensional structure of alternating layers composed of **1** and water.

The structures determined for **1a** and **1b** have two major differences: (i) the twist angle of the pyridone rings are 18.9° and ~0°, respectively and (ii) the presence of solvate molecules in **1b**. These differences explain the variation of the supramolecular association. The results show the effect of temperature and solvent in the crystallization process. The two structures of **1** demonstrate that as temperature increases in the DMF–EtOH solvent system, the extended motif **II** becomes favoured rather than the cyclic dimer of motif **I**.

CP-671. In order to create a coordination polymer with metallic bonds of mode **III** or **VII**, we performed the synthesis in polar solvents such as ethanol and *N*,*N*-dimethylformamide. This avoids the deprotonation of the pyridonyl coordinating group, which may lead to producing other motifs involving 1,3-bridging with O and N atoms such as motifs **V**, **VI**, **VIII** and **IX**. Solvothermal synthesis of **1** with $Co(NO_3)_2{\cdot}6H_2O$ yielded the crystals of **CP-671**. Structural elucidation by single-crystal XRD reveals that **CP-671** belongs to the orthorhombic space group *Pbca* with lattice parameters of a = 7.630(4) Å, b = 17.682(7) Å and c = 17.737(1) Å and have the composition $1_2Co(H_2O)_2{\cdot}2(NO_3)$ per unit cell. The views of the structure are shown in Fig. 2, and other crystallographic data are summarized in Table 1. As anticipated, the ligands in **CP-671** are neutral, with each cobalt atom linked in an equatorial position with four ligands according to mode **III** and two water molecules in an apical position. Hydrogen bonds involving the N–H group and adjacent oxygen atom reinforce the octahedral coordination geometry of the cobalt atom. Because **1** is a ditopic ligand, the coordination mode is repeated along the (b, c) plane and thereafter forming the 2D CP. The two N–H groups of each ligand are *cis*-oriented and the average planes of the two pyridone rings form an angle of 30.2°. Remarkably, each $[Co(1)_4]^{2+}$ unit has left handed or right handed helical chirality (M or P, respectively) and they alternate within the CP layers. Nitrate counter ions are located in the cavities near to the metal ion centre. The three-dimensional structure consists of a packing of layers to produce **CP-671**. The details of the hydrogen bonds and other bond angles and lengths are given in Tables S3–S5 respectively, ESI.†

Fourier transform infrared spectroscopy, powder X-ray diffraction and scanning electron microscopy

FTIR spectra were recorded for the free ligand **1** and **CP-671** (Fig. 3a). In the spectrum of **1**, two characteristic absorption

bands at 1601 and 1636 cm^{-1} are attributed to the N–H in plane bending and C=O stretching modes, respectively. The absorption bands at 3138 cm^{-1} can be attributed to the N–H stretching. The band at 820 cm^{-1} corresponds to the C–H out of plane bending mode. Comparison of the spectra of **1** and **CP-671** allows to correlate the absorption bands from one to another. In the spectrum of **CP-671**, the N–H in plane bending and C=O stretching modes are shifted at 1606 and 1650 cm^{-1}, respectively. The C–H out of plane bending mode is also shifted at 824 cm^{-1}. As expected, the characteristic band of the NO_3^- group is observed at 1403 cm^{-1}. Two other additional bands are also detected in the spectrum of **CP-671** at 511 and 569 cm^{-1}. These can be attributed to the metal-ligand bonds.

The powder X-ray diffraction (PXRD) patterns of **1a** and **CP-671** were collected and compared with their respective simulated patterns generated from XRD, which confirm the phase purity of the crystalline samples (Fig. 3b and c). Subsequent analysis by scanning electron microscopy (SEM) was performed to confirm the absence of any amorphous phase (Fig. S9†). As can be seen, a homogeneous morphology was observed for the samples of **1a** and **CP-671**.

Thermal analysis

To evaluate the thermal stability of the free ligand and **CP-671**, their thermal behaviours were investigated by thermogravimetric analysis (TGA) (Fig. 4). All the samples were studied from 25 °C to 800 °C with a heating rate of 10 °C min^{-1} under a N_2 atmosphere. The TG curve of **1** shows three main decomposition steps between 240–650 °C with mass losses of ~6%, ~82% and ~7%, respectively. The TG curve of **CP-671** demonstrates that upon heating, the as-synthesized sample showed the first weight loss of about 5% up to 173 °C which was ascribed to the loss of two coordinated water molecules of the CP material. The second weight loss of about ~21% at 260 °C can be attributed to the loss of free solvents in the channels. The third weight loss of 66% between 400–800 °C was attributed to the complete collapse of the **CP-671** framework. The thermal stability of **CP-671** is comparable with other known coordination polymers.[44]

Conclusions

In summary, **1** was prepared in good yields and its structure was confirmed by XRD, IR, MS, ^{1}H-NMR and ^{13}C-NMR techniques. The structure of unbound ligand **1** provides valuable information about the ability of 2-pyridone to direct molecular association by forming hydrogen bonds to produce chains and 2D networks depending on the crystallization conditions. Novel **CP-671** was synthesized by coordinating **1** with Co(II) without a basic reactant in polar solvents by linkage according to mode **III**. Our results show that under adequate conditions, a pyridonyl ligating group can produce a specific linkage with metal ions according to modes **III–IX**, which makes polypyridone ligands a promising candidate for CP synthesis. We foresee a new class of pyridone-based CPs with intriguing architectures to be developed in the near future.

Conflicts of interest

There are no conflicts to declare.

Acknowledgements

We are grateful to the Natural Sciences and Engineering Research Council of Canada (RGPIN-2015-06425), the Canada Foundation for Innovation, the Fonds de Recherche du Québec – Nature et Technologies, the Canadian Queen Elizabeth II Diamond Jubilee Scholarships and the Université du Québec à Trois-Rivières for the financial support.

References

1 X. Huang, P. Sheng, Z. Tu, F. Zhang, J. Wang, H. Geng, Y. Zou, C.-a. Di, Y. Yi and Y. Sun, *Nat. Commun.*, 2015, **6**, 7408.
2 P.-P. Liu, L. Sheng, X.-Q. Song, W.-Y. Xu and Y.-A. Liu, *Inorg. Chim. Acta*, 2015, **434**, 252–257.
3 M. L. Foo, R. Matsuda, Y. Hijikata, R. Krishna, H. Sato, S. Horike, A. Hori, J. Duan, Y. Sato and Y. Kubota, *J. Am. Chem. Soc.*, 2016, **138**, 3022–3030.
4 A. Lytvynenko and S. Kolotilov, *Theor. Exp. Chem.*, 2016, **52**, 197–211.
5 Y. Yang, W. Zhu, Z. Dong, Y. Chao, L. Xu, M. Chen and Z. Liu, *Adv. Mater.*, 2017, **29**, 1703588.
6 J. Deng, F. Wu, P. Yu and L. Mao, *Appl. Mater. Today*, 2018, **11**, 338–351.
7 H.-N. Li, H.-Y. Li, L.-K. Li, L. Xu, K. Hou, S.-Q. Zang and T. C. Mak, *Cryst. Growth Des.*, 2015, **15**, 4331–4340.
8 J.-W. Zhang, X.-M. Kan, X.-L. Li, J. Luan and X.-L. Wang, *CrystEngComm*, 2015, **17**, 3887–3907.
9 C. Pettinari, A. Tăbăcaru and S. Galli, *Coord. Chem. Rev.*, 2016, **307**, 1–31.
10 A. Tăbăcaru, C. Pettinari and S. Galli, *Coord. Chem. Rev.*, 2018, **372**, 1–30.
11 S. Ma and H.-C. Zhou, *Chem. Commun.*, 2010, **46**, 44–53.
12 C. Y. Lee, O. K. Farha, B. J. Hong, A. A. Sarjeant, S. T. Nguyen and J. T. Hupp, *J. Am. Chem. Soc.*, 2011, **133**, 15858–15861.
13 C.-Y. Sun, C. Qin, X.-L. Wang and Z.-M. Su, *Expert Opin. Drug Delivery*, 2013, **10**, 89–101.
14 G. Calleja, R. Sanz, G. Orcajo, D. Briones, P. Leo and F. Martínez, *Catal. Today*, 2014, **227**, 130–137.
15 H.-R. Fu, F. Wang and J. Zhang, *Dalton Trans.*, 2014, **43**, 4668–4673.
16 M. Simard, D. Su and J. D. Wuest, *J. Am. Chem. Soc.*, 1991, **113**, 4696–4698.
17 E. Boucher, M. Simard and J. D. Wuest, *J. Org. Chem.*, 1995, **60**, 1408–1412.
18 T. Heinz, D. M. Rudkevich and J. Rebek Jr., *Angew. Chem., Int. Ed.*, 1999, **38**, 1136–1139.

19 D. R. Borst, J. R. Roscioli, D. W. Pratt, G. M. Florio, T. S. Zwier, A. Müller and S. Leutwyler, *Chem. Phys.*, 2002, **283**, 341–354.
20 G. G. Hammes and H. O. Spivey, *J. Am. Chem. Soc.*, 1966, **88**, 1621–1625.
21 A. Fujimoto, K. Inuzuka and R. Shiba, *Bull. Chem. Soc. Jpn.*, 1981, **54**, 2802–2806.
22 P.-T. Chou, C.-Y. Wei and F.-T. Hung, *J. Phys. Chem. B*, 1997, **101**, 9119–9126.
23 C. B. Aakeröy and K. R. Seddon, *Chem. Soc. Rev.*, 1993, **22**, 397–407.
24 A. M. Moragues-Bartolome, W. Jones and A. J. Cruz-Cabeza, *CrystEngComm*, 2012, **14**, 2552–2559.
25 Q. Zhang, L. Lu, W. Dai and X. Mei, *CrystEngComm*, 2014, **16**, 1919–1926.
26 A. n. F. Crespi, D. Vega, A. K. Chattah, G. A. Monti, G. Y. Buldain and J. M. Lázaro-Martínez, *J. Phys. Chem. A*, 2016, **120**, 7778–7785.
27 B. Dojer, A. Pevec, Z. Jagličić and M. Kristl, *J. Mol. Struct.*, 2017, **1128**, 724–729.
28 T. P. Brewster, T. H. Nguyen, Z. Li, W. T. Eckenhoff, N. D. Schley and N. J. DeYonker, *Inorg. Chem.*, 2018, **57**, 1148–1157.
29 C. S. Letko, Z. M. Heiden, T. B. Rauchfuss and S. R. Wilson, *Inorg. Chem.*, 2011, **50**, 5558–5566.
30 S. J. Forrest, S. Manojveer and M. T. Johnson, *Eur. J. Inorg. Chem.*, 2017, **2017**, 3239–3243.
31 D. Chen, A. Ahrens-Botzong, V. Schünemann, R. Scopelliti and X. Hu, *Inorg. Chem.*, 2011, **50**, 5249–5257.
32 L. S. Hollis, M. M. Roberts and S. J. Lippard, *Inorg. Chem.*, 1983, **22**, 3637–3644.
33 N. Ghavale, A. Wadawale, S. Dey and V. K. Jain, *J. Organomet. Chem.*, 2010, **695**, 1237–1245.
34 G. A. Bowmaker, M. Nitiatmodjo, B. W. Skelton and A. H. White, *Inorg. Chim. Acta*, 2005, **358**, 4327–4341.
35 F. A. Cotton, P. E. Fanwick, R. H. Niswander and J. C. Sekutowski, *J. Am. Chem. Soc.*, 1978, **100**, 4725–4732.
36 M. H. Chisholm, K. Folting, J. C. Huffman and I. P. Rothwell, *Inorg. Chem.*, 1981, **20**, 2215–2218.
37 C. Benelli, A. J. Blake, P. E. Milne, J. M. Rawson and R. E. Winpenny, *Chem. – Eur. J.*, 1995, **1**, 614–618.
38 N. R. Catarineu, A. Schoedel, P. Urban, M. B. Morla, C. A. Trickett and O. M. Yaghi, *J. Am. Chem. Soc.*, 2016, **138**, 10826–10829.
39 J. Almlof, A. Kvick and I. Olovsson, *Acta Crystallogr., Sect. B: Struct. Crystallogr. Cryst. Chem.*, 1971, **27**, 1201–1208.
40 G. M. Sheldrick, *Acta Crystallogr., Sect. A: Found. Adv.*, 2015, **71**, 1–8.
41 G. M. Sheldrick, *Acta Crystallogr., Sect. C: Struct. Chem.*, 2015, **71**, 1–8.
42 E. C. Constable, D. Morris and S. Carr, *New J. Chem.*, 1998, **22**, 287–294.
43 Q. Zhou, F. Du, X. Liang, W. Liu, T. Fang and G. Chen, *Molecules*, 2018, **23**, 1784.
44 E. A. Tomic, *J. Appl. Polym. Sci.*, 1965, **9**, 3745–3752.

5.5 Conclusions

Inspired from the works of chapters 3 and 4, we designed and synthesized the dipyridone ligand which was further used to coordinate cobalt ion to form a novel class of coordination polymers CP-**671**. This work gives an insight into the ability of pyridonyl groups to facilitate the molecular self-assembly through hydrogen bonds. With a difference in the crystallization conditions, dipyridone was observed to form a molecular organization in extended zigzag and cyclic dimer motifs. The major structural differences being the epicentre of hydrogen bonds, twisted angles of the pyridone rings and the presence of solvate molecules which together result in the variation in supramolecular association. As a proof of concept in the construction of pyridonyl based infinite frameworks, CP-**671** has been prepared using the solvothermal conditions by mixing the dipyridone and the cobalt salt to obtain a crystalline material that was characterized using various techniques to determine the structure and confirm the purity and homogeneity of the sample. This chapter forms the first example in literature on the use of pyridonyl based multidentate organic ligand for the construction of organic-inorganic hybrid extended frameworks. The success of this approach highlights the potentials of using it as a fundamental tool in designing and engineering novel crystalline materials. The work also opens wider access for developing a new class of coordination polymers.

CHAPTER 6: Preparation of Chromic Materials Using Coordination Chemistry

6.1 Introduction

During the last few decades, one of the key roles for the tremendous achievements in the field of material science was largely contributed to the exponential growth in the areas of coordination chemistry. A wide range of materials is known to exhibit properties that interest the current requirements such as porosity and find applications in catalysis, gas storage and sequestration, sensor applications, electronic applications, molecular sieves, photovoltaics, molecular machines, optoelectronics, photoluminescence, biomimetic and pharmaceuticals. Even though most of these materials have advanced applications, their uses are limited because most of them are not stable and their synthetic routes are not economical. In this chapter, we focus on the preparation of chromic materials through the economic and eco-friendly synthetic approach. Through the course of the research, we intended to develop isostructural coordination polymers (MOPs) using polyaromatic nitrogen-rich potassium cyamelurate as the organic ligand and various transition metal ions connected through coordination bonds and Coulombic interactions. The addition of new properties can be done by adding different metals in the frameworks. As MOPs were isostructural, replacing a metal from one site with another metal can be possible without changing the structure. This can lead to the development of solid solutions of mixed metallic systems (MMOPs) which are coordination polymers consisting of at least two different metal ions connected by organic ligands. Our study has led to determine various properties of MOPs and MMOPs such as the reversible chromic effect and potential applications in moisture and temperature sensors.

6.2 Objectives

- Design and synthesis of nitrogen-rich, rigid and polyaromatic organic ligand capable of having multiple coordination sites.
- Syntheses of isostructural coordination polymers by mixing potassium cyamelurate and transition metals.
- Syntheses of mixed metallic coordination polymers.
- Characterization of coordination polymers by X-ray diffractions (SCXRD and PXRD), spectroscopies (FTIR, UV-Vis and EDS), microscopy (Thermal optical microscopy and SEM), elemental analysis (EA) and thermogravimetry (TGA) to determine the structure, purity, homogeneity and thermal stability of materials.
- Study of the chromic properties of the coordination polymers and elucidation of the mechanism using a combination of characterization techniques including TOM, UV-Vis, FTIR, PXRD and TGA.

6.3 Authors' Contribution

Midhun Mohan. Conceptualization of the project, visualization and investigation of experiments, all synthesis and experiments conducted, validation of methodology and curation of data, drafting the original manuscript.

Sanil Rajak. Review the manuscript.

Alexandre A. Tremblay. Helping in preparation of the cyamelurate linker and review the manuscript.

Thierry Maris. Investigation and curation of X-ray diffraction experiments.

Adam Duong. Project administration, supervision, funding acquisition and editing of the manuscript.

6.4 Article 4

Syntheses of Mono and Bimetallic Cyamelurate Polymers with Reversible Chromic Behaviour

Dalton Transactions

PAPER

View Article Online
View Journal | View Issue

Cite this: Dalton Trans., 2019, 48, 7006

Syntheses of mono and bimetallic cyamelurate polymers with reversible chromic behaviour†

Midhun Mohan, [a] Sanil Rajak, [a] Alexandre A. Tremblay,[a] Thierry Maris [b] and Adam Duong *[a]

Received 25th March 2019,
Accepted 15th April 2019

DOI: 10.1039/c9dt01278h

rsc.li/dalton

Ordered coordination polymers (CPs) have been an interesting class of materials for scientific and industrial research for the last few decades. However, their availability as well as certain economic and environmental limitations could slow down their use in many applications. Herein, we present room temperature synthesis in water of a series of CPs (four metal–organic polymers MOPs-(**1–4**) and three mixed metal–organic polymers MMOPs-(**5–7**)). All MMOPs were found to be isostructural to MOPs as determined by XRD. Remarkably, MOPs-(**2** and **3**) and MMOPs-(**5–7**) exhibit switchable chromic behaviour associated with reversible structural transformation which was facilitated by dehydration/rehydration or solvent exchange ($MeOH/H_2O$) processes. Chromic behaviour and its mechanism were investigated using IR, solid-state UV-Vis, XRD, PXRD and TGA indicating the coordination/de-coordination of water molecules to be the key factor that influences the colour changes. These results render the potential application of MOPs and MMOPs as sensor materials.

Introduction

Intense research has been focused on developing advanced materials that can be applied for the enhancement of technologies. One of the most promising classes of materials highlighted is coordination polymers (CPs) which are widely studied for their vast varieties of novel structures and properties. Coordination polymers are one-, two- or three-dimensional materials containing metal ions (or clusters) linked by coordinated organic ligands into an infinite array.[1–5] CPs have the advantage of combining the properties derived from organic and inorganic components as well as the structural features into a single material.[1,5] The addition of diverse properties into coordination polymers can be achieved by either linking organic ligands to multiple metals or coordinating multiple ligands to the same metals, thereby enhancing the properties in the same system.[6–9] Hence, a judicious combination of building units allows the preparation of hybrid materials with well-defined structures and tailored properties for various potential applications such as gas storage, gas separation, catalysis, biomedicine, sensor technology and so forth.[10–19] Currently, chromism is emerging as a key area for developing sensor technology.[20] A colour change may be caused, either chemically or physically, which involves various external stimuli such as photo-irradiation, heating or solvent treatments called photochromism, thermochromism and solvatochromism, respectively.[21–26] Chromic materials offer several potential technological applications, for instance, temperature and moisture sensors, thermometers (fever indicators, devices, design applications), chromic glass, security markers, government documents and colour filters.[27–30] Generally, chromism can be caused by changes of the coordination geometry around the metal center, tautomerism in the organic component or any other phenomena that can alter the electron density of substances.[31,32] Earlier studies on chromic CPs have been carried out with carboxylate and related ligands linked to various transition metals.[33] However, chromic CPs involving cyamelurate ligands seldom have been described so far. Furthermore, the synthesis of crystalline CPs requires solvothermal conditions, making the process more expensive and non-environment friendly. In addition to the issues, most of the reported CPs are chemically and/or thermally unstable limiting their applications.[34–37] Herein, we report two novel series of chromic CP materials called metal–organic polymers (MOPs) and mixed metal–organic polymers (MMOPs) synthesized in water as the only solvent and at room temperature. Despite the fact that water is the cheapest, safest and non-toxic solvent, its use in the synthesis of coordination polymers is not common due to the poor water solubility of organic

[a]Département de Chimie, Biochimie et physique and Institut de Recherche sur l'Hydrogène, Université du Québec à Trois-Rivières, Trois-Rivières, Québec, G9A 5H7, Canada. E-mail: adam.duong@uqtr.ca
[b]Département de Chimie, Université de Montréal, Montréal, Québec, H3C 3J7, Canada

†Electronic supplementary information (ESI) available. CCDC 1866130–1866133 and 1867180–1867182. For ESI and crystallographic data in CIF or other electronic format see DOI: 10.1039/c9dt01278h

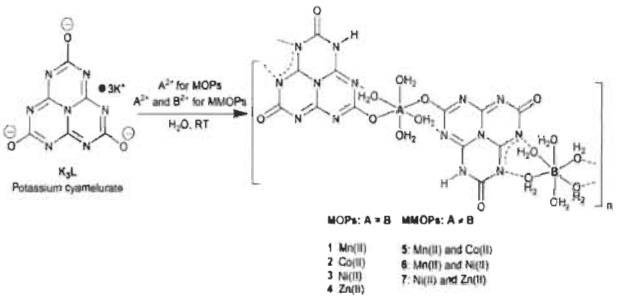

Scheme 1 Coordination modes of the ligand $(HL)^{2-}$ in metal–organic polymers (1–4) and mixed metal–organic polymers (5–7).

ligands. MOPs and MMOPs are coordination polymers consisting of metal ions linked with organic ligands by coordination bonds, coulombic interactions and hydrogen bonds. Our approach to ensuring the chromic properties in MOPs and MMOPs is to combine planar organic ligands and inorganic moieties that potentially exhibit chromic properties. In many studies, the planarity of molecules has been invoked to explain the chromism of several organic compounds that made possible the modification of electron density by the mesomeric effect or tautomerization possible with a small energy requirement. In this study, we elected to use the potassium cyamelurate ligand (K_3L) which is a water soluble, flat, rigid, *N*-heteroaromatic, thermally stable, polyconjugate ligand. It possesses multiple potential coordination sites, including N and O atoms which give more opportunities to construct various framework structures. Moreover, studies of CP materials involving cyamelurate and related ligands are quite rare and the only known examples of studies regarding these kinds of compounds do not explore their chromic properties.[38–40]

Four crystalline isostructural MOPs-(1–4) with Mn(II), Co(II), Ni(II) and Zn(II) metal ions, respectively, have been synthesized in water and at room temperature starting from the potassium cyamelurate ligand (Scheme 1). MOPs-(2 and 3) exhibit a remarkable reversible chromic behaviour associated with solid-state reversible transformation for more than 15 cycles. The isostructurality of MOPs-(1–4) opens a synthesis avenue to design chromic MMOPs with precise control of the chemical composition, crystal structure and topology. Addition of various metals into a substance modifies and improves the material's properties.[6–9] The combination of diverse metal ions can lead to an infinite array of new materials with interesting properties for many applications. Although, many strategies to prepare coordination polymers exist, only a few of them involve mixed metal compositions with single-crystal X-ray diffraction studies.[41,42] Additionally, bimetallic coordination polymers usually differ significantly from the parental CPs. By taking advantage of a modular building principle and the isostructurality of MOPs-(1–4), we incorporated two different metals within one structure to produce MMOPs-(5–7) with compositions of (Mn^{II}/Co^{II}), (Mn^{II}/Ni^{II}) and (Ni^{II}/Zn^{II}), respectively, with molar ratios of the metal cations to form solid solutions chosen arbitrarily. Crystal structures, solid-state reversible chromic phenomena and structural transformations, and metal concentrations in structures of MOPs and MMOPs were determined by experimental methods.

Experimental section

Potassium cyamelurate (K_3L) was synthesized according to the method described in the literature.[13,16] MOPs were obtained by reactions of metal salts with K_3L in water at room temperature, whereas MMOPs were prepared by following the same synthesis approach except that various ratios of two different metal salts in an aqueous solution of K_3L were added. All MOPs and MMOPs prepared were extremely stable at high temperature and insoluble in water and common organic solvents.

Crystallographic data were collected using a Bruker Venture Metaljet diffractometer with Ga Kα radiation. The structures were solved by direct methods using ShelxT, and non-hydrogen atoms were refined anisotropically with least squares minimization.[59,60] Hydrogen atoms were treated by first locating them from difference Fourier maps, recalculating their positions using standard values for distances and angles, and then refining them as riding atoms. Microcrystalline powders were analyzed in transmission-mode geometry using a Bruker D8-Discover instrument (*θ–θ* geometry) equipped with an XYZ platform and a HI-STAR gas detector. X-rays were generated using a conventional sealed-tube source with a copper anode producing Cu Kα radiation (λ = 1.54178 Å). The samples were gently ground and then mounted on a flat Kapton sample holder. The data collection involved the acquisition of two different sections with increasing angular position, giving two differenr 2D frames. These frames were integrated and combined to produce the final 1D X-ray diffraction powder pattern. Calculated X-ray powder diffraction patterns were generated from the structural data in the corresponding CIFs resulting from single-crystal analyses. The calculation was performed using Mercury software of the Cambridge Crystallographic Data Centre.[61] A unique value of the FWHM for the diffraction peaks was adjusted in order to obtain a better match between

the resolution of the experimental and the calculated patterns. The determination of the total carbon, hydrogen, nitrogen, and sulphur (C, H, N, S) content in the compounds was performed using a EA 1108 Fisons CHNS Element analyzer by the quantitative 'dynamic flash combustion' method. The solid-state UV-visible spectra were recorded on a Cary 5000. The IR (ATR) spectra were recorded with a Nicolet iS 10 Smart FT-IR Spectrometer within 600–4000 cm^{-1}. The thermogravimetry analysis was performed using a Diamond Pyris TGA/DTA apparatus from PerkinElmer and Mettler Toledo TGA/DSC1. Scanning electron microscopy was performed using a JEOL model 5500. EDS was performed using a model X-Max 20 mm^2. XPS was performed with a model Axis Ultra. *In situ* thermal microscopy was performed using a combination of a microscope Nikon Eclipse E200 and hot stage microscopy system Mettler Toledo FP82.

Results and discussion

Single-crystal X-ray diffraction (XRD) analysis revealed that MOPs-(**1–4**) are isomorphous crystallizing in the space group $P\bar{1}$ with only slight differences in their unit-cell dimensions. Therefore, only the structure of MOP-**1** is described in detail as a representative example. Views of the structures of MOP-**1** and MOPs-(**2–4**) are provided in Fig. 1 and Fig. S1–S4† respectively. Crystallographic data are summarized in Table S1.† MOP-**1** was prepared as amber crystals by the coordination of cyamelurate and Mn(II) in aqueous solution. The crystal structure of MOP-**1** proved to belong to the triclinic space group $P\bar{1}$. The coordination reaction of potassium cyamelurate with $Mn(SO_4)$ at room temperature in water resulted in zwitterionic 1D polymeric chains of alternating species of $[Mn(HL)_2(H_2O)_4]^{2-}$ and $[Mn(H_2O)_6]^{2+}$. In the anionic complex, each Mn(II) centre is six-coordinate, associated with a pair of *trans* located O atoms from two different ligands (average distance $Mn–O_L$ = 2.131 Å is normal as compared to those reported for other similar Mn complexes) and four water molecules at equatorial positions to complete the octahedral coordination sphere (average distance $Mn–O_{aqua}$ = 2.052 Å is normal).[47–49] It is important to note that the complex is stabilized by the formation of intramolecular hydrogen bonding O–H···N involving nitrogen atoms of the ligand and adjacent water molecules (average distance O–H···N = 2.771 Å). The 1D infinite chain is then obtained by coulombic interaction between cationic hexaaquamaganese(II) and the anionic complex strengthened by hydrogen bonds O–H···N involving water molecules of the $[Mn(H_2O)_6]^{2+}$ cation (average distance O–H···N = 2.755 Å). The chains are further interlinked *via* hydrogen bonding N–H···O involving neighbours of anionic complexes to form 2D networks (average distance O–H···N = 2.724 Å). Furthermore, multiple hydrogen bonds involving the hexaaquamanganese(II) cation reinforce the corrugated 2D layer (average distances O–H···N = 2.766 Å and O–H···O_L = 2.724 Å). The stacking of layers is then controlled by multiple hydrogen bonding involving the coordinated water molecules out of plane and π–π interactions between the aromatic rings of heptazine (3.365 Å) to form the 3D structure. The details of the hydrogen bonds and angles of each crystal structures of MOPs are summarized in Tables S3–S6.† The most remarkable feature of the structure is that zwitterionic 1D polymeric chains in each layer and interlayer are disposed in the same orientation. It is noted that in a layer, anionic complexes face each other instead of being shifted to minimize electrostatic repulsions between identical charges. This arrangement can be explained by the formation of multiple hydrogen bonds. Isostructurality of the MOPs-(**1–4**) indicates that manganese(II), cobalt(II), nickel(II) and zinc(II) atoms adopt equivalent structural roles. Similar interatomic distances, bond angles, entity charge balances and coordination modes of the metal ions are noted for MOPs-(**1–4**).

The isostructural nature of MOPs-(**1–4**) suggests that one type of metal can be substituted by another without alteration of the lattice, so that these same structures would be preserved while forming solid solutions containing two different metal ions. Mixed metal ions in a single-crystal are known to exhibit rich chemistry, properties and can be considered as a molecular alloy. MMOPs-(**5–7**) are prepared by mixing two different transition metal salts (MMOP-**5** with Mn and Co), (MMOP-**6** with Mn and Ni) and (MMOP-**7** with Ni and Zn) in a one-pot reaction with the potassium cyamelurate ligand. The as-synthesized MMOP-**5** and MMOPs-(**6–7**) are prepared as pink and cyan solids respectively. Single-crystal structures of MMOPs-(**5–7**) proved to be isostructural to MOPs-(**1–4**) (Fig. S5–S7†). Crystallographic data of MMOPs-(**5–7**) are summarized in

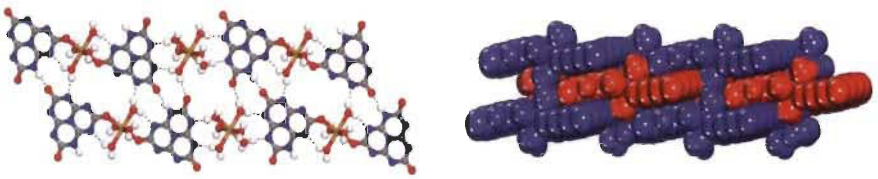

Fig. 1 Views of the structure of MOP-**1**, (a) View of the 2D sheet in MOP-**1** crystals, constructed from 1D infinite chains, cross-linked *via* multiple hydrogen bonding represented by broken lines and (b) packing of 2D layers to form the three-dimensional structure. For more clarity, layers are marked in red and blue. Carbon atoms are shown in gray, hydrogen atoms in white, oxygen atoms in red, nitrogen atoms in blue and manganese atoms in orange.

Table S2.† Selected hydrogen bonds and angles of MMOPs are provided in Tables S7–S9.† For the solid solution crystal structures, the two metal ions were assumed to be statistically distributed on the two metal centres of the asymmetric unit and the occupancy factors were refined on these two shared sites.

The crystallinity and phase purity of all the samples were confirmed by comparing the simulated diffraction patterns generated from XRD data with powder X-ray diffraction (PXRD) patterns collected in the transmission mode (Fig. 2 and Fig. S8†). As such, the observed PXRD at room temperature (in red) of the as-synthesized samples match well with the simulated patterns (in black) calculated from the single-crystal structures, confirming that all MOPs and MMOPs synthesized are free of secondary phases. Furthermore, the proof of the phase purity of MOPs and MMOPs was reinforced by exhaustive scanning electron microscopy (SEM) which confirms that all samples have an identical morphology of crystals and no contamination by an amorphous phase can be observed (see insert SEM images in Fig. 2 and Fig. S8†). Repeatable elemental analysis (EA) of all samples also confirms the homogeneity and the purity of MOPs and MMOPs. The compositions found by EA with the general formula $A_xB_{(2-x)}C_{12}H_{22}N_{14}O_{16}$ ($x = 0$ in the case of MOPs and $0 < x < 2$ in the case of MMOPs) were consistent with those as refined in the single-crystal structures. In the case of MMOPs, EA was performed on different batches to ensure the consistency in composition from batch to batch and within the same batch. Together, the PXRD, SEM and EA confirm that the structures determined by XRD are representative of the MOP and MMOP bulk crystalline samples.

To examine the distribution and ratios of the metal ions, energy dispersive spectroscopy (EDS) analyses were carried out on each MMOPs-(5–7) (Fig. 3 and Fig. S12–S14†). We first determined the ratios of the two metal ions by EDS element-point analysis on a single-crystal for each sample followed by EDS element-mapping to prove the uniformity of the bulk crystalline samples. The results confirm the presence and the uniform distribution of the two metal ions within the area of the crystalline sample and that the bulk crystalline sample is not a physical mixture of parental MOPs. Comparison of EDS element-point analysis and element-mapping is in good agreement, indicating that each single-crystal of a bulk crystalline sample of a MMOP has the same metal ion ratios. Together, the SEM images and EDS analyses confirm that all MMOPs synthesized were reasonably homogeneous and are solid solutions containing two different metal ions. The fine-tuning of metal ion ratios was also investigated for MMOPs. An illustrative study on adjusting metal ion ratios in MMOP-5 was conducted with Mn : Co ranging from 20 : 80 to 80 : 20 mol% (Table S12†). EDS element-point and mapping analyses measured on different batches of these series of MMOP-5 confirm the consistency in the metal ratios (Fig. S15–S18†). The difference in the values of metal ratios by EDS and reaction stoichiometry could be explained by the tendency of Co atoms to occupy both metal sites compared to Mn atoms which mostly occupy the anionic site. This explanation is supported by the XRD data. This trend in variation of metal ratios can also be observed in other MMOPs. These results demonstrate the potential of the synthesis method to prepare ordered materials with diverse metal compositions and thereby can lead to materials with tunable properties.

X-ray photoelectron spectroscopy (XPS) was employed to further investigate the elemental composition and chemical state of metal ions of MMOPs. Fig. 4 shows the XPS spectra of MMOPs along with their corresponding parent MOPs. The narrow survey XPS of metal ions in each MOP and MMOP is provided in the ESI (Fig. S19–S25†). XPS patterns confirm the presence of the two metal ions for each sample of MMOPs. Comparison of XPS patterns of MMOPs with their parental MOPs did not show any detectable shifts of the peaks of the binding energy values of C, N, O and metal ions indicating that the electronic states and the structural configuration of each metal ion in MMOPs are identical to those of the parent MOPs. The binding energies of metal ions in each MOPs and MMOPs are within the literature value ranges for a six-coordinated metal ion(II).[50–55] These results are in good agreement with the crystal structures of MMOPs. A summary of binding energy values of XPS peaks for MOPs-(1–4) and MMOPs-(5–7) is provided in Table S13.†

An interesting chromic behaviour is observed for MOPs-(2 and 3) and MMOPs-(5–7). At room temperature, MOP-2 and MMOP-5 are pink solids, and MOP-3, MMOP-6 and MMOP-7 are cyan solids. A rapid, visible colour change to purple solids

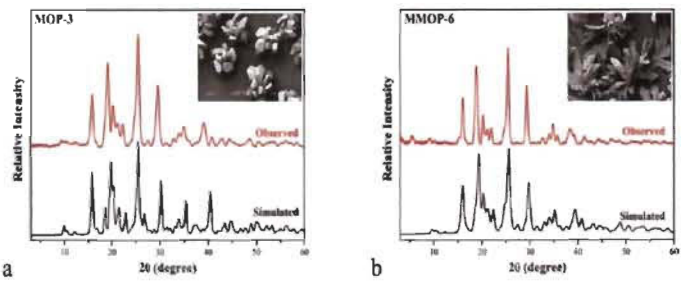

Fig. 2 PXRD and SEM of the MOP-3 and MMOP-6 bulk crystalline samples. Scale bar 100 μm. (a) and (b) Comparison of the observed PXRD (red) with the simulated pattern (black) calculated from the XRD data and the insert SEM images for MOP-3 and MMOP-6 respectively.

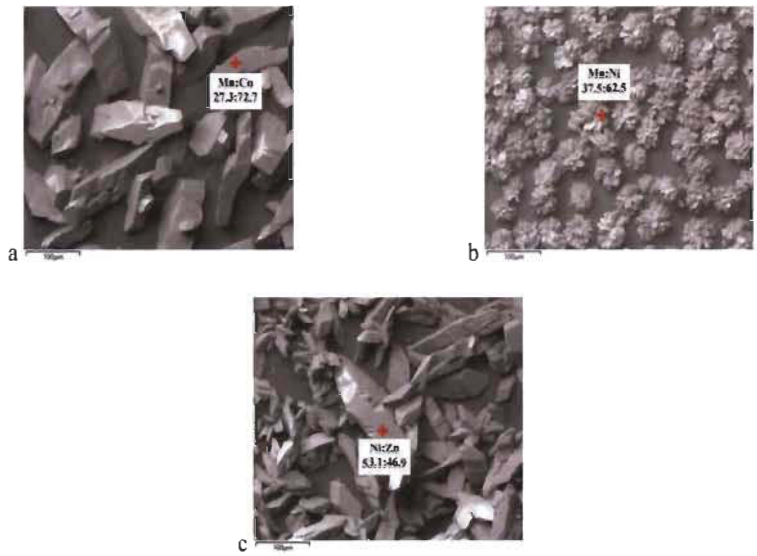

Fig. 3 EDS analyses of MMOP-(5–7). (a)–(c) EDS element-point analysis images of crystals of MMOPs-(5–7) respectively, showing the location and the results of measurements in percentage of the two metal ions (scale bar, 100 μm).

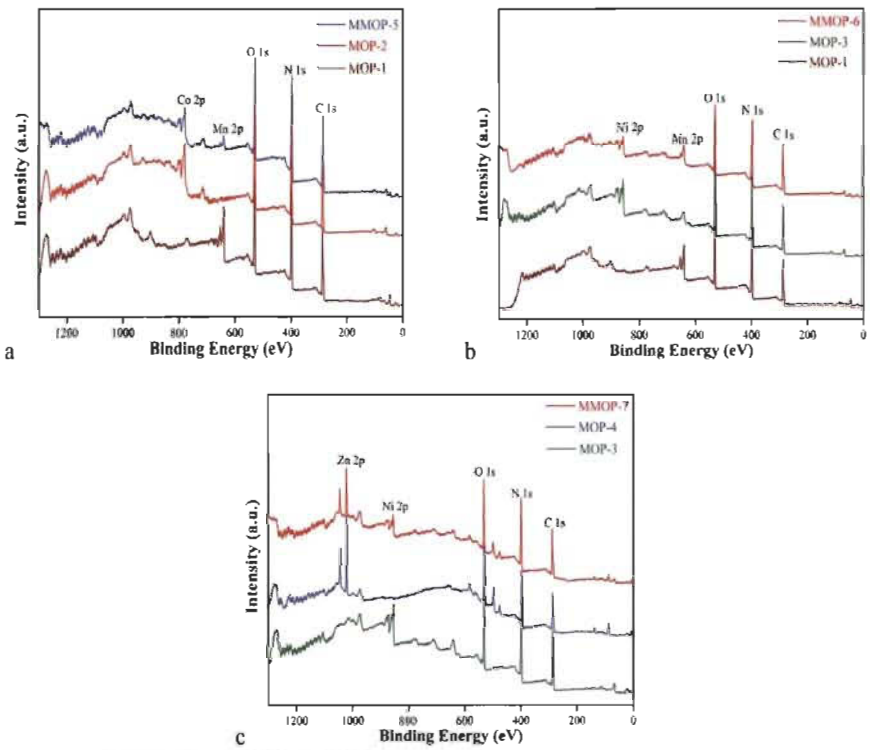

Fig. 4 Comparison of wide survey XPS spectra of (a) MOP-1, MOP-2 and MMOP-5, (b) MOP-1, MOP-3 and MMOP-6 and (c) MOP-3, MOP-4 and MMOP-7.

after being heated at 130 °C is observed for MOP-2 and MMOP-5, and to yellow solids for MOP-3, MMOP-6 and MMOP-7. These can be restored to the original colour when subjected to water. The reversible chromic process of MOPs-(2 and 3) and MMOPs-(5–7) can be achieved *via* dehydration/rehydration or solvent exchange with MeOH/H_2O. It is noteworthy that the colour change by solvent exchange occurs only when the as-synthesized species were heated at 130 °C to initiate the chromic behaviour after which the chromism can be monitored by solvent exchange. The chromic behaviour of MOPs-(2 and 3) and MMOPs-(5–7) was observed by *in situ* thermal microscopy images at different temperatures. As an illustrative example, Fig. S27 and S31† show the *in situ* thermal microscopy images of the colour change of MOP-2 and MMOP-6 upon heating between 25–250 °C. *In situ* thermal microscopy images for MOP-3, MMOP-5 and MMOP-7 are provided in the ESI (Fig. S28a, S30a and S32a in ESI†). As can be seen, the samples were fully converted to purple or to yellow species at 130 °C.

The switchable chromic behaviour was confirmed using solid-state UV-Vis by recording several cycles of colour change in MOPs-(2 and 3) and MMOPs-(5–7). The absorption curves of the restored species for MOPs-(2 and 3) and MMOPs-(5–7) were of close resemblance to the spectra of the as-synthesized compounds (Fig. 5 and Fig. S28b, S30b and S32b in the ESI†). In MOP-2, the as-synthesized spectrum (solid red line curve) exhibits a major peak at λ_{max} = 505 nm and a discernible shoulder around 465 nm (Fig. 5a) which are attributed to $^4A_2(F) \leftarrow {}^4T_1(F)$ and $^4T_1(P) \leftarrow {}^4T_1(F)$, respectively, typical of an octahedral coordination geometry. Upon heat treatment at 130 °C (solid blue line curve), the UV-Vis spectrum of the purple species displays optical bands at 595 and 537 nm. After exposure to water, a comparable UV-Vis spectrum of the original species was investigated again. Similar variation trends of the UV-Vis spectrum can be observed in MOP-3 and MMOPs-(5–7).

To investigate the origin of the chromism, IR, PXRD and TGA were performed for each species of MOPs-(2 and 3) and MMOPs-(5–7) (Fig. 6 and Fig. S28, S30, S31 and S32 in the ESI†). The IR spectra of the as-synthesized MOPs and MMOPs show recognizable broad bands in the 3900–2400 cm^{-1} region that are attributed to the O–H stretch from the presence of H_2O and the N–H at around 3400 cm^{-1} from the protonated cyameluric core. The main absorption bands characteristic of the cyameluric nucleus appear in the fingerprint region.[56–58] When MOPs-(2 and 3) and MMOPs-(5–7) were heated to 130 °C, the absorption band corresponding to N–H disappeared and a broad band covered the entire region from 3900–2400 cm^{-1}. These changes were attributed to the tautomerization between two forms between keto-amine and enol-imine achieved by proton migration on the cyameluric core. In fact, it is well known that the planarity of molecules makes it possible for the proton transfer. Interestingly, the comparison of the vibration spectra of different cycles of dehydration/rehydration confirms that the structures of MOPs-(2 and 3) (MMOPs-(5–7) respectively) remained identical.

To determine the structural changes in depth, each species of several cycles of MOPs-(2 and 3) and MMOPs-(5–7) were recorded by PXRD to observe the phase transitions occurring with the chromic phenomena. The PXRD pattern of the simulated, as-synthesized MOPs-(2 and 3) and MMOPs-(5–7), heated at 130 °C, exposed to water and methanol, is shown in Fig. 6b and Fig. S28d, S30d, S31d and S32d in the ESI.† It is noteworthy that the positions of the diffraction peaks for the regenerate species are in accordance with those of the as-synthesized compounds which confirms that the returned crystal structure remains essentially unchanged and the structural transformation is reversible. For the dehydrated species, either by heating at 130 °C or by solvent exchange, the crystals were no longer birefringent, therefore XRD patterns were not collected.

The usual trends of chromism in coordination complexes are exhibited either due to the change in the coordination geometry of the metal centre and/or by tautomerization in ligands. To elucidate the mechanism of the chromism, TGA was performed for each species of MOPs-(1–4) and MMOPs-(5–7) (Fig. 6c and Fig. S26e, S28e–S32e†). As a representative example, TG curves of each species of MOP-2 were compared to each other to prove the de-coordination of water molecules

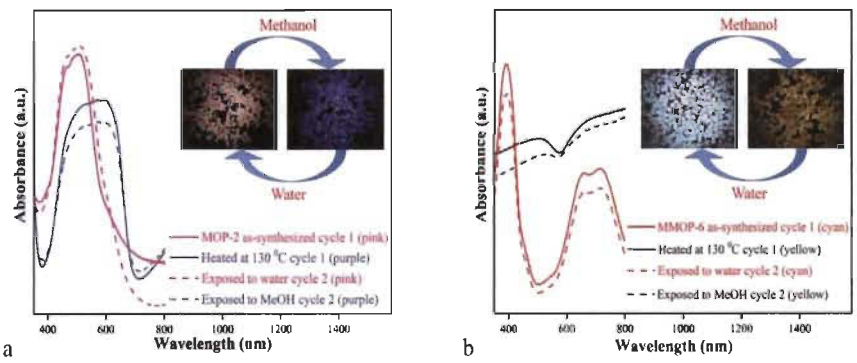

Fig. 5 Chromic behaviour of (a) MOP-2 and (b) MMOP-6 species using solid-state UV-Vis (inset chromism images).

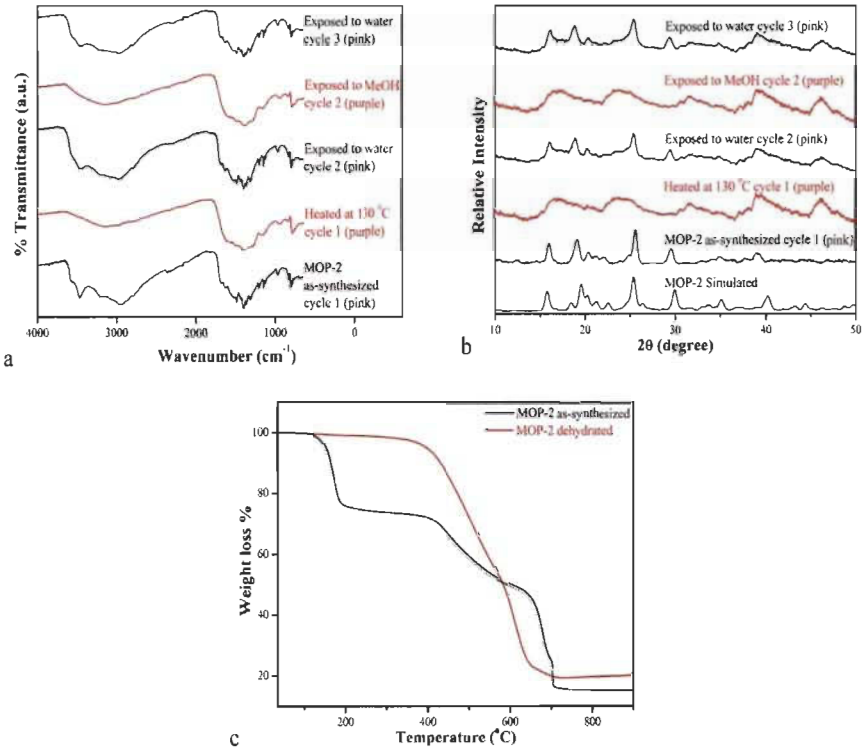

Fig. 6 Analysis of MOP-2 species using (a) FTIR, (b) PXRD and (c) TGA.

from the metal ions (Fig. 6c) when heated or exposed to methanol. The TG curve of the as-synthesized MOP-2 (pink species) shows three main weight losses. The first weight loss corresponds to the removal of ten water molecules starting at T = 101 °C while the two other steps are likely the decomposition of the associated organic moiety which are similar to the TG curve of the potassium cyamelurate (see Fig. S11†). As anticipated, the TG curve of dehydrated MOP-2 (purple species) displays similar decomposition of the ligand K_3L. Together, the TGA of the as-synthesized and dehydrated species of MOP-2 suggests a change in the coordination geometry of the metal centre that could explain the chromism. The de-coordination of water molecules from the metal ions is also observed for MOP-3 and MMOPs-(5–7) (see the ESI†).

MOPs-(1 and 4) were examined by the same characterization techniques used to study the chromic behaviour of MOPs-(2 and 3) and MMOPs-(5–7) (Fig. S26 and S29†). The previous results confirm that during the colour change in MOPs-(2 and 3) and MMOPs-(5–7), the coordination environment of metal centres as well as tautomerization were observed. In contrast, no significant chromism was observed for MOP-1 and MOP-4 by *in situ* thermal microscopy and solid-state UV-Vis. This can be explained by the half-filled and fully filled electronic configuration of Mn(II) (d^5) and Zn(II) (d^{10}) of MOP-1 and MOP-4 respectively, which are known to be stable and, therefore, no electron transition happened. However, their IR, PXRD and TGA show a similar structural transformation mechanism to that of MOPs-(2 and 3) and MMOPs-(5–7) (Fig. S26 and S29†). The vibration spectra of MOP-1 and MOP-4 display also a proton migration between keto-amine and enol-imine. Together, *in situ* thermal microscopy, solid-state UV-Vis and IR of MOPs-(1 and 4) demonstrate that the tautomerization is not the factor that influences the chromism in MOPs-(2 and 3) and MMOPs-(5–7) but rather the coordination geometry of the metal centres.

Conclusions

We have developed an eco-friendly method to prepare a series of novel coordination polymers (MOPs-(1–4) and MMOPs-(5–7)) using water as the only solvent at room temperature. The crystal structures of MOPs-(1–4) and MMOPs-(5–7) studied by XRD are isostructural showing 1D zwitterionic chains held together by multiple hydrogen bonds to produce 2D layers. This study provides a suitable method to prepare novel unime-

tallic and bimetallic coordination polymers with a well-defined structure, compositions and suitable properties. The existence of mixed metalation in MMOPs-(5–7) was characterized by various techniques including XRD, SEM, EDS and XPS to confirm the presence and the uniform distribution of the bimetallic systems. Interestingly, MOPs-(2 and 3) and MMOPs-(5–7) exhibit switchable chromic behaviour associated with proton migration and reversible solid-state structural transformation occurring by dehydration/hydration or solvent exchange with MeOH/H_2O. The mechanism of the chromic behaviour studied by *in situ* thermal microscopy, solid-state UV-Vis, FT-IR, PXRD and TGA provides the information that the change in the coordination geometry of metal ions is the key factor that influences the colour change. Proton migration was excluded to explain the chromic behaviour due to the absence of the colour change of MOP-1 and MOP-4 although their IR spectra display proton transfer in the cyameluric core. The chromic behaviour exhibited by MOPs and MMOPs favours their potential applications in sensor technology. The synthesis methods for developing multi-metallic CPs are interesting to modify and tune the properties of materials for desired applications. We expect that our approach to the synthesis of MOPs and MMOPs will be useful in the context of crystal engineering regarding the design and the development of ordered CP materials for new technologies.

Conflicts of interest

There are no conflicts to declare.

Acknowledgements

We are grateful to the Natural Sciences and Engineering Research Council of Canada, the Canadian Queen Elizabeth II Diamond Jubilee Scholarships and the Université du Québec à Trois-Rivières for their financial support.

Notes and references

1 A. Y. Robin and K. M. Fromm, *Coord. Chem. Rev.*, 2006, **250**, 2127–2157.
2 A. M. Spokoyny, D. Kim, A. Sumrein and C. A. Mirkin, *Chem. Soc. Rev.*, 2009, **38**, 1218–1227.
3 S. Diring, S. Furukawa, Y. Takashima, T. Tsuruoka and S. Kitagawa, *Chem. Mater.*, 2010, **22**, 4531–4538.
4 J.-B. Lin, J.-P. Zhang and X.-M. Chen, *J. Am. Chem. Soc.*, 2010, **132**, 6654–6656.
5 H. Wu, J. Yang, Z.-M. Su, S. R. Batten and J.-F. Ma, *J. Am. Chem. Soc.*, 2011, **133**, 11406–11409.
6 L. Qin, J. Hu, M. Zhang, Y. Li and H. Zheng, *Cryst. Growth Des.*, 2012, **12**, 4911–1918.
7 L. J. Wang, H. Deng, H. Furukawa, F. Gándara, K. E. Cordova, D. Peri and O. M. Yaghi, *Inorg. Chem.*, 2014, **53**, 5881–5883.
8 C.-C. Wang, S.-Y. Ke, C.-W. Cheng, Y.-W. Wang, H.-S. Chiu, Y.-C. Ko, N.-K. Sun, M.-L. Ho, C.-K. Chang and Y.-C. Chuang, *Polymers*, 2017, **9**, 644.
9 S. Yuan, J.-S. Qin, J. Li, L. Huang, L. Feng, Y. Fang, C. Lollar, J. Pang, L. Zhang and D. Sun, *Nat. Commun.*, 2018, **9**, 808.
10 S. I. Noro, S. Kitagawa, M. Kondo and K. Seki, *Angew. Chem., Int. Ed.*, 2000, **39**, 2081–2084.
11 B. Xing, M. F. Choi and B. Xu, *Chem. – Eur. J.*, 2002, **8**, 5028–5032.
12 S. Kitagawa, R. Kitaura and S. I. Noro, *Angew. Chem., Int. Ed.*, 2004, **43**, 2334–2375.
13 D. N. Dybtsev, H. Chun, S. H. Yoon, D. Kim and K. Kim, *J. Am. Chem. Soc.*, 2004, **126**, 32–33.
14 S. Hasegawa, S. Horike, R. Matsuda, S. Furukawa, K. Mochizuki, Y. Kinoshita and S. Kitagawa, *J. Am. Chem. Soc.*, 2007, **129**, 2607–2614.
15 C. Yang, X. Wang and M. A. Omary, *J. Am. Chem. Soc.*, 2007, **129**, 15454–15455.
16 G. Givaja, P. Amo-Ochoa, C. J. Gómez-García and F. Zamora, *Chem. Soc. Rev.*, 2012, **41**, 115–147.
17 H. Furukawa, K. E. Cordova, M. O'Keeffe and O. M. Yaghi, *Science*, 2013, **341**, 1230444.
18 T.-Y. Gu, M. Dai, D. J. Young, Z.-G. Ren and J.-P. Lang, *Inorg. Chem.*, 2017, **56**, 4668–4678.
19 J.-W. Ye, J.-M. Lin, Z.-W. Mo, C.-T. He, H.-L. Zhou, J.-P. Zhang and X.-M. Chen, *Inorg. Chem.*, 2017, **56**, 4238–4243.
20 B. F. Spencer, M. E. Ruiz-Sandoval and N. Kurata, *Struct. Control Health Monit.*, 2004, **11**, 349–368.
21 S. Kawata and Y. Kawata, *Chem. Rev.*, 2000, **100**, 1777–1788.
22 S. Lam Po Tang and G. Stylios, *Int. J. Cloth Sci. Tech.*, 2006, **18**, 108–128.
23 C. Shen, T. Sheng, Q. Zhu, S. Hu and X. Wu, *CrystEngComm*, 2012, **14**, 3189–3198.
24 U. R. Lakmali and C. V. Hettiarachchi, *CrystEngComm*, 2015, **17**, 8607–8611.
25 O. Toma, N. Mercier, M. Allain, A. A. Kassiba, J.-P. Bellat, G. Weber and I. Bezverkhyy, *Inorg. Chem.*, 2015, **54**, 8923–8930.
26 J. He and J. S. Chen, *Mater. Sci. Forum*, 2018, **914**, 182–192.
27 X.-C. Shan, F.-L. Jiang, D.-Q. Yuan, H.-B. Zhang, M.-Y. Wu, L. Chen, J. Wei, S.-Q. Zhang, J. Pan and M.-C. Hong, *Chem. Sci.*, 2013, **4**, 1484–1489.
28 S. Z. Zhan, M. Li, S. W. Ng and D. Li, *Chem. – Eur. J.*, 2013, **19**, 10217–10225.
29 P.-C. Guo, T.-Y. Chen, X.-M. Ren, Z. Chu and W. Jin, *J. Mater. Chem. A*, 2014, **2**, 13698–13704.
30 A. Yadav, A. K. Srivastava, A. Balamurugan and R. Boomishankar, *Dalton Trans.*, 2014, **43**, 8166–8169.
31 T. C. N. Dzesse, E. N. Nfor and S. A. Bourne, *Cryst. Growth Des.*, 2017, **18**, 416–423.
32 M. Yoshida and M. Kato, *Coord. Chem. Rev.*, 2017, **355**, 101–115.
33 J. Troyano, O. Castillo, J. I. Martínez, V. Fernández-Moreira, Y. Ballesteros, D. Maspoch, F. Zamora and S. Delgado, *Adv. Funct. Mater.*, 2018, **28**, 1704040.

34 A. Dhakshinamoorthy, M. Alvaro, P. Concepcion and H. Garcia, *Catal. Commun.*, 2011, **12**, 1018–1021.
35 H. S. Lee, J. Choi, J. Jin, J. Chun, S. M. Lee, H. J. Kim and S. U. Son, *Chem. Commun.*, 2012, **48**, 94–96.
36 J. E. Mondloch, M. J. Katz, N. Planas, D. Semrouni, L. Gagliardi, J. T. Hupp and O. K. Farha, *Chem. Commun.*, 2014, **50**, 8944–8946.
37 J. R. Karra, H. Jasuja, Y.-G. Huang and K. S. Walton, *J. Mater. Chem. A*, 2015, **3**, 1624–1631.
38 N. E. El-Gamel, L. Seyfarth, J. Wagler, H. Ehrenberg, M. Schwarz, J. Senker and E. Kroke, *Chem. – Eur. J.*, 2007, **13**, 1158–1173.
39 J. Gracia and P. Kroll, *J. Mater. Chem.*, 2009, **19**, 3020–3026.
40 A. Sattler, M. R. Budde and W. Schnick, *Z. Anorg. Allg. Chem.*, 2009, **635**, 1933–1939.
41 D. Vujovic, H. G. Raubenheimer and L. R. Nassimbeni, *Eur. J. Inorg. Chem.*, 2004, **2004**, 2943–2949.
42 M.-H. Zeng, B. Wang, X.-Y. Wang, W.-X. Zhang, X.-M. Chen and S. Gao, *Inorg. Chem.*, 2006, **45**, 7069–7076.
43 E. Kroke, M. Schwarz, E. Horath-Bordon, P. Kroll, B. Noll and A. D. Norman, *New J. Chem.*, 2002, **26**, 508–512.
44 E. Horvath-Bordon, E. Kroke, I. Svoboda, H. Fueß, R. Riedel, S. Neeraj and A. K. Cheetham, *Dalton Trans.*, 2004, 3900–3908.
45 J. R. Holst and E. G. Gillan, *J. Am. Chem. Soc.*, 2008, **130**, 7373–7379.
46 J. R. Holst, *Synthesis of inorganic heptazine-based materials*, The University of Iowa, 2009.
47 E. Pardo, C. Train, G. Gontard, K. Boubekeur, O. Fabelo, H. Liu, B. Dkhil, F. Lloret, K. Nakagawa and H. Tokoro, *J. Am. Chem. Soc.*, 2011, **133**, 15328–15331.
48 A. Grundmeier and H. Dau, *Biochim. Biophys. Acta, Bioenerg.*, 2012, **1817**, 88–105.
49 N. Cox and J. Messinger, *Biochim. Biophys. Acta, Bioenerg.*, 2013, **1827**, 1020–1030.
50 T. Akitsu and Y. Einaga, *Inorg. Chim. Acta*, 2007, **360**, 497–505.
51 M. C. Biesinger, L. W. Lau, A. R. Gerson and R. S. C. Smart, *Appl. Surf. Sci.*, 2010, **257**, 887–898.
52 Y. Gorlin and T. F. Jaramillo, *J. Am. Chem. Soc.*, 2010, **132**, 13612–13614.
53 D. Hong, J. Jung, J. Park, Y. Yamada, T. Suenobu, Y.-M. Lee, W. Nam and S. Fukuzumi, *Energy Environ. Sci.*, 2012, **5**, 7606–7616.
54 Y. Li, W. Zhou, H. Wang, L. Xie, Y. Liang, F. Wei, J.-C. Idrobo, S. J. Pennycook and H. Dai, *Nat. Nanotechnol.*, 2012, **7**, 394.
55 J. Chen, R. Liu, H. Gao, L. Chen and D. Ye, *J. Mater. Chem.*, 2014, **2**, 7205–7213.
56 H. Schroeder and E. Kober, *J. Org. Chem.*, 1962, **27**, 4262–4266.
57 A. I. Finkel'shtein and N. y. V. Spiridonova, *Russ. Chem. Rev.*, 1964, **33**, 400–405.
58 B. Jürgens, E. Irran, J. Senker, P. Kroll, H. Müller and W. Schnick, *J. Am. Chem. Soc.*, 2003, **125**, 10288–10300.
59 G. Sheldrick, *Acta Crystallogr., Sect. A: Found. Adv.*, 2015, **71**, 3–8.
60 G. Sheldrick, *Acta Crystallogr., Sect. C: Struct. Chem.*, 2015, **71**, 3–8.
61 C. F. Macrae, P. R. Edgington, P. McCabe, E. Pidcock, G. P. Shields, R. Taylor, M. Towler and J. van de Streek, *J. Appl. Crystallogr.*, 2006, **39**, 453–457.

6.5 Conclusions

In this chapter, we have synthesized an inexpensive, eco-friendly, nitrogen-rich, rigid and polyaromatic organic ligand (potassium cyamelurate) that incorporates multiple coordination sites. Due to the water solubility of the organic moiety, we adopted an eco-friendly method at room temperature and water solvent reaction conditions to synthesize a series of novel two-dimensional coordination polymers that were isostructural. Motivated by the isostructural nature of the MOPs, we designed and developed a series of bimetallic coordination polymers MMOPs. Most of the materials synthesized exhibited reversible chromic behaviour as well as reversible structural transformation. All the materials were characterized using various techniques to determine the structure, purity, homogeneity and thermal stability. The existence of bimetallic systems and their uniform distribution throughout the material was also determined using XRD, SEM, EDS and XPS. The reversible chromic behaviour in most of the MOPs and MMOPs was determined and analysed using *in-situ* thermal optical microscopy, FTIR, solid-state UV-Vis spectroscopy and TGA. The chromic behaviour of these materials is attributed to the change in the coordination geometry of the metal ions. This reversible phenomenon occurred by the variation of temperature (thermochromic) or *via* solvent exchanged (solvochromic). Our materials can potentially be used for moisture and thermal sensor applications.

CHAPTER 7: 3D Lanthanide Based Metal-Organic Frameworks for Gas Separation

7.1 Introduction

Lanthanum-based MOFs have appealed to utmost interest due to their higher geometries and accessibilities. Due to the versatility in the selection of the two counterparts, these porous systems can vary, claiming unusual diversities in their properties such as porosity, functionalisation and structure, which makes them potential candidates for various applications. One of the important areas of MOF application has been focussed on gas storage and separation with high selectivity, mainly CO_2 due to its adverse effects on the ecosystem associated with climate change. In this work, Lanthanide based Metal-Organic Frameworks (namely IRHs) were prepared during a solvothermal condition by mixing lanthanide metal salts and cyamelurate linker. All the porous solids (IRHs) were characterized by XRD, PXRD, EA, TGA, FTIR, SEM and EDS to determine the structure, phase purity and homogeneity of the bulk samples and their thermal stability. The porous materials were activated by solvent exchange and heating for the surface area determination. Adsorption isotherm was conducted on each sample which shows the exceptional selectivity for CO_2 over CH_4 in comparison with other MOFs.

7.2 Objective

- Detailed investigation of various coordination modes of cyamelurate linker.
- Design and synthesis of nitrogen-rich, rigid and polyaromatic organic ligand capable of having multiple coordination sites.
- Syntheses of isostructural porous 3D lanthanum-based MOFs by potassium cyamelurate and lanthanide salts.

- Characterization of the porous MOFs using various techniques to elucidate the structure and determine the phase purity and homogeneity of each bulk sample and their thermal stability.
- Activation of the pores of the MOFs by solvent exchange method and heating process to determine the surface area using a BET instrument.
- Optimization of synthesis and activation conditions.
- Understanding the pore properties using theoretical studies.
- Study of the gas separation behaviour of the MOFs.

7.3 Authors' Contribution

Midhun Mohan. Conceptualization of the project, visualization and investigation of experiments, all synthesis and experiments conducted, validation of methodology and curation of data, adsorption studies, drafting the original manuscript.

Mohamed Essalhi. Structural study and review of the manuscript.

David Durette. Theoretical studies.

Love Karan Rana. Structure description.

Follivi Kloutse Ayevide. Adsorption studies.

Thierry Maris. Investigation and curation of X-ray diffraction experiments.

Adam Duong. Project administration, supervision, funding acquisition and editing of the manuscript.

7.4 Article 5

A Rational Design of Microporous Nitrogen-Rich Lanthanide Metal-Organic Frameworks for CO_2/CH_4 Separation

ACS APPLIED MATERIALS & INTERFACES

www.acsami.org Research Article

A Rational Design of Microporous Nitrogen-Rich Lanthanide Metal–Organic Frameworks for CO_2/CH_4 Separation

Midhun Mohan, Mohamed Essalhi, David Durette, Love Karan Rana, Follivi Kloutse Ayevide, Thierry Maris, and Adam Duong*

Cite This: ACS Appl. Mater. Interfaces 2020, 12, 50619–50627 Read Online

ACCESS | Metrics & More | Article Recommendations | Supporting Information

ABSTRACT: Three new lanthanide metal–organic frameworks IRHs-(1–3) supported by cyamelurate linkers have been synthesized and structurally characterized. The incorporation of numerous heteroatoms (N and O) into the pore walls and the relatively small microchannels of these porous solids enhance bonding force of the host–guest interactions, thus promoting the adsorption of carbon dioxide (CO_2) over methane (CH_4). The nonpolar covalent bonds in methane also favor the less uptake due to the hydrophilic walls of these frameworks. Grand canonical Monte Carlo simulations were performed to determine the origin of the adsorption. The density isocontour surfaces show that CO_2 is mainly adsorbed on the walls composed of organic linkers and around the metal sites, whereas no specific adsorption site is observed for CH_4, which indicates weak interactions between the framework and the adsorbed gas. As expected, the simulations show that CH_4 is not observed around the metal center due to the presence of H_2O molecules. The excellent selectivity of CO_2/CH_4 binary mixture was predicted by the ideal adsorbed solution theory (IAST) *via* correlating pure component adsorption isotherms with the Toth model. At 25 °C and 1 bar, the CO_2 and CH_4 uptakes for IRH-3 were 2.7 and 0.07 mol/kg, respectively, and the IAST predicated selectivity for CO_2/CH_4 (1:1) reached 27, which is among the best value for MOF materials.

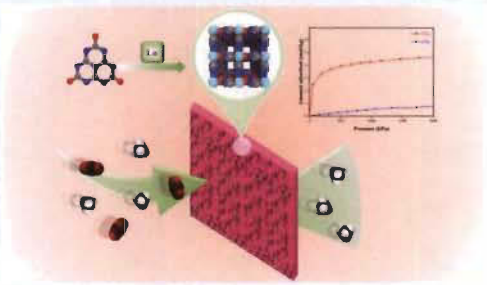

KEYWORDS: *metal–organic frameworks, CO_2/CH_4 separation, adsorption, IRHs-(1–3), selectivity, molecular simulation*

INTRODUCTION

Porous metal–organic frameworks (MOFs) are a class of crystalline materials that have shown highly promising applications in gas storage, molecular recognition and separation, heterogeneous catalysis, and so forth.[1,2] They can be readily synthesized from diverse polytopic organic linkers and metal ions under solvothermal conditions, which facilitates systematic tailoring of their architectures and chemistry.[3,4] Among the synthetic porous materials, MOFs have the record performance for post-combustion CO_2 capture and great separations for some specific gas such as O_2/N_2, CO/H_2, CO_2/N_2, CO_2/C_2H_2, CO_2/CH_4, etc.[5−10] Although, many MOFs have shown high gas uptake, the performance of most of them is not yet reaching the industrial demands for CO_2 capture and gas separation.[11] Therefore, designing of porous MOFs with functionalized internal surfaces is a great challenge. Ideal porous solids for gas separation are those which have not only high adsorption capacity but also significant high selectivity. An approach to enhance the MOF's affinity and selectivity toward CO_2 is to adjust the pore sizes, pore volumes, and pore surface functions.[12−14] These characteristics of MOFs can be easily tuned by changing either the organic and/or the metallic ions. Previous works indicate that the incorporation of accessible Lewis basic nitrogen into the pore walls of porous solids can drastically influence the gas adsorption capacity and selectivity of MOFs, particularly for CO_2 capture.[15−18] The past decades have seen impressive developments of MOFs using multitopic carboxylates (as anionic linker) and *d*-block metal ions (Co(II), Ni(II), Cu(II), Zn(II), etc.).[19,20] However, the analogous chemistry with lanthanide ions is still lacking in scope, although several advantages have been reported such as (i) higher coordination numbers than *d*-block metal ions and (ii) ancillary ligands can be eliminated to form unsaturated lanthanide ions (Lewis acidic site) that potentially enhance the physical adsorption capacity and/or the catalytic activity of MOFs.[21−24]

Received: August 27, 2020
Accepted: October 12, 2020
Published: October 26, 2020

https://dx.doi.org/10.1021/acsami.0c15395
ACS Appl. Mater. Interfaces 2020, 12, 50619–50627

All these considerations motivated us to design, synthesize, and characterize an original novel series of lanthanide MOFs 1−3 with La(III), Ce(III), and Pr(III), respectively (termed IRHs-(1−3); IRH, Institut de Recherche sur l'Hydrogène) supported by cyamelurate linkers (Cy) that have never been utilized to produce porous materials.[25] Because Cy contains a large number of heteroatoms (O and N atoms) and consists of three fused aromatic rings, it should give particularly interesting coordination motifs and enhance the framework−guest interactions, which is mainly dependent on the pore size, the functional surface of MOFs materials, and the electronic structural of target adsorbates. Theoretically, the small size of the Cy linker and its chemical structure should feature IRHs-(1−3) with a relatively small pore aperture and a bulk amount of accessible nitrogen-donor groups (Lewis basic site) into the pore walls, which could enhance the gas uptake and selectivity of CO_2 over CH_4. Both organic (Cy) and inorganic (lanthanide metal ion) components are judiciously chosen not only to support on the construction of stable porous MOFs but also to fairly balance the selectivity efficiency and adsorption capacity, so-called trade-off.

Herein, we report the unique example of IRHs-(1−3) built from the cyamelurate linker and carried out their adsorption studies. IRHs have been synthesized through solvothermal reaction and structurally characterized by single-crystal X-ray diffractions (SCXRD). They have been activated and used to investigate on CO_2 capture and gas separation from a binary mixture of CO_2 and CH_4 at the pressure range of interest. Grand canonical Monte Carlo simulations (GCMC) have been also performed to determine the origin of adsorption for these two gases.

RESULTS AND DISCUSSION

Cyamelurate linker (Cy) was prepared according to the reported method.[26] It based on three fused rings of six C=N bonds, which surround a central sp^2-hydribized N-atom and three oxygen atoms negatively charged in the external to form a flat cross-conjugated aromatic system. This compound is known to be thermally very stable and possess interesting chemical properties.[27,28] Up to date, it has not yet been employed to generate porous solids. The main reason is due to the low solubility of this molecule (Cy) in organic solvents, which results in the difficulty to develop a rich chemistry. We became interested in tri-*s*-triazine compounds whilst searching for an organic building block to design extended frameworks. Considering that the Cy linker has never been used to form porous materials and has a high number of possible coordination modes, we designed and synthesized a series of lanthanide MOFs. Solvothermal synthesis with Cy and lanthanide salt (Ln = La(III), Ce(III), and Pr(III)) yielded octahedral crystals of IRHs (Scheme 1). The bulk single crystals produced are insoluble in water and common organic solvents.

Scheme 1. Synthetic Approach to Prepare IRHs-(1−3)

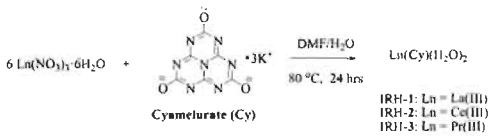

Structural Characterization. Structural elucidation by single-crystal X-ray diffraction (SCXRD) revealed that IRHs-(1−3) are isostructural as well as isomorphous compounds crystallizing in the tetragonal space group $P4_322$, having the framework formula of $[Ln(Cy)(H_2O)_2]_n$ (Figure 1 and Figures S1−S5). Thus, only the structure of IRH-1 is described as an illustrative example. Crystallographic data of all IRHs are summarized in Table S1. Views of the structure of IRHs are shown in Figure 1 and Figures S2 and S4. In the asymmetric unit of IRH-1, a half linker molecule and a unique water molecule are coordinated to La(III) (Figure 1). The coordination number of La(III) ion is 10, provided by four symmetry related Cy and two H_2O molecules (Figure 1a). Each Cy acts as a 4-c linker displaying μ_4-bridging mode (Figure 1b) while each metal node acts as a 10-c node (Figure 1c) to form a rigid three-dimensional porous framework with regular square 1D tubular channels running along the *c* direction (Figure 1d). It is worth mentioning that the channel is equipped with the bound water molecules pointing to the internal space. Selected coordination bonds and angles are provided in Tables S2−S4. IRHs-(1−3) have an effective pore aperture of about 4.19 Å (regardless of the van der Waals radii), and the potential solvent-accessible volume estimated by PLATON[29] is equal to ~41−42% of the cell volume.

As the pore size (4.19 Å) is smaller than the kinetic diameters of DMF (5.5 Å) the Q peaks observed from the SCXRD data are assigned to water molecules (2.6 Å). To validate the hypothesis, FT-IR, TGA, and EA were employed to precise on the solvent content. As expected, FT-IR spectra of as-synthesized IRHs do not show any characteristic absorption bands of DMF (Figures S7−S9). However, several absorption bands can be attributed to H_2O molecules. As an illustrative example, IRH-1 display characteristic bands of free and coordinated H_2O molecules at ~3350, 2127, 1643, and 1639 cm^{-1}. The nature of the solvent in the pores was also confirmed by thermogravimetric analysis (TGA) (Figures S10−S12). All IRHs show similar TG curves. The first weight losses starting at ~110 °C is assigned to the release of unbound H_2O molecules from the pores. The second loss of mass beginning at ~140 °C is attributed to the departure of coordinated H_2O. The decomposition of the frameworks is observed at ~245 °C. Furthermore, the elemental analysis also indicates the presence of water molecules in the general formula (see the Experimental Section). FT-IR, TGA, and EA analysis gave consistent information on the solvent content entrapped in the pores of IRHs. Energy dispersive X-ray spectroscopy (EDS) was also performed to confirm on the elemental compositions of the frameworks of IRHs (Figures S13−S15). A comparison of the PXRD patterns obtained for IRH-3 samples exposed to humid air as well as those heated at various temperatures from RT to 160 °C with the as-synthesized samples indicate the atmospheric and thermal stability of the materials (Figure S23).

The phase purity of the bulk products of as-synthesized IRHs-(1−3) were determined by a comparison of the simulated and experimental PXRD patterns (Figure 2). This result was strengthened by scanning electron microscopy (SEM), which substantiate the identical morphology of crystals with an average size of 50−150 μm, and no contamination by any amorphous phase was observed for each sample (see insert SEM images in Figure 2).

Gas Adsorption Measurements. Prior to gas adsorption measurement, uncoordinated water from the pores of the as-

https://dx.doi.org/10.1021/acsami.0c15395
ACS Appl. Mater. Interfaces 2020, 12, 50619−50627

ACS Applied Materials & Interfaces www.acsami.org Research Article

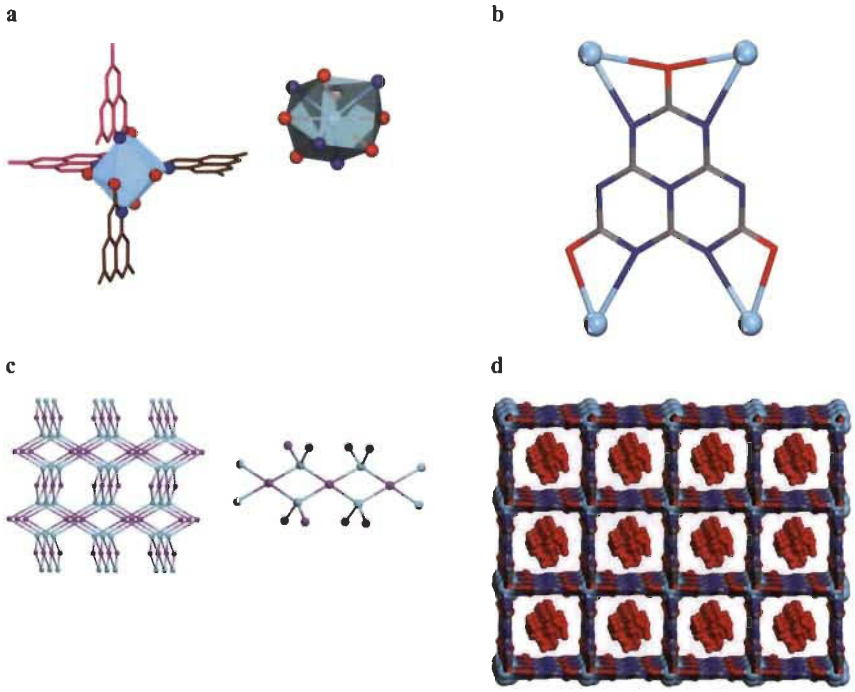

Figure 1. As an illustrative example, the view of the structure of IRH-1. (a) Bicapped square antiprismatic geometry around the La(III) ion provided by symmetry related Cy linkers and H_2O molecules. (b) Bridging mode of the Cy linker. (c) 10-c net formed by metal nodes. (d) 3D porous framework filled with disordered water molecules. Carbon atoms are shown in gray, oxygen atoms in red, nitrogen atoms in blue, and La(III) ions in cyan.

synthesized IRHs were exchanged with dry MeOH several times followed by thermal heating under dynamic vacuum to yield guest-free phases (called activated IRHs). This is evident from the TGA measurements conducted after activation, which shows the emptied pores (Figures S10–S12). The PXRD of the activated IRHs confirmed that the frameworks did not collapse after removal of free solvents in the pores (Figures S16–S18). Optimal activation temperature was found at 398 K with maximum amount of CO_2 gas of ~2.5 mol/kg at 1 bar (Figure S19). Beyond 398 K, the adsorption capacity decreases drastically for all IRHs. Details about the experimental procedures are given in the Supporting Information. It is worth mentioning that at 398 K, the internal oriented coordinated water molecular cannot be removed from the framework as shown by the TGA experiments. Generally, measurement of the surface area by isotherm sorption is performed using N_2 at 77 K or Ar at 87 K. Brunauer–Emmett–Teller surface area (S_{BET}) measurement with these two adsorbates gave low adsorption although the SCXRD shows pores for IRHs (Figures S20,S21). However, the CO_2 adsorption isotherm experiment at 273 K show fully reversible type-I behavior of the three analogues porous materials. S_{BET} of 742.9, 594.5, and 525.4 $m^2.g^{-1}$ are recorded for IRHs-(**1**–**3**), respectively (Figure 3). The sorption isotherms found by CO_2-S_{BET} confirm the presence of a permanent porosity and that the pores are free of solvents. After the sorption study, all IRHs again were analyzed by PXRD to confirm that the structures are remained identical to the as-synthesized samples (see Figures S16–S18, red patterns). The calculated pore size distribution demonstrated a single pore width that matches the van der Waals pore diameter as determined by SCXRD. The total pore volumes derived from the CO_2 adsorption isotherm are 0.15 $cm^3.g^{-1}$, 0.14 $cm^3.g^{-1}$, and 0.13 $cm^3.g^{-1}$ for IRHs-(**1**–3), respectively.

The structure of IRHs prompted us to investigate on the gas sorption of CO_2 and CH_4. The microchannel environment with a relatively small pore aperture and particularly large number of accessible nitrogen atoms on the wall surfaces suggests that IRHs should exhibit a good affinity and selectivity for CO_2 over CH_4. Indeed, it is well known that porous materials with narrow micropores (<1 nm) and basicity of a surface should enhance the bonding force with acidic CO_2 molecules.[30] In most of the reported study on adsorption involving MOFs, coordinated water molecules are constantly removed to generate open metal sites for the enhancement of the gas uptake. However, we believed that these H_2O molecules could be useful to get a high selectivity because they can act as a barrier to reduce the sorption affinity of IRHs to CH_4, which is hydrophobic. Single-component sorption isotherms for CO_2 and CH_4 were collected at 298 K for all activated IRHs (Figure 4). As illustrated, IRHs-(**1**–3) manifest a rapid increase adsorption capacity at very low pressure, reaching 2.6, 3.1, and 2.8 mol/kg for CO_2 at 298 K and 1 bar, respectively, while the CH_4 uptake is negligible except for IRH-

https://dx.doi.org/10.1021/acsami.0c15395
ACS Appl. Mater. Interfaces 2020, 12, 50619–50627

ACS Applied Materials & Interfaces www.acsami.org Research Article

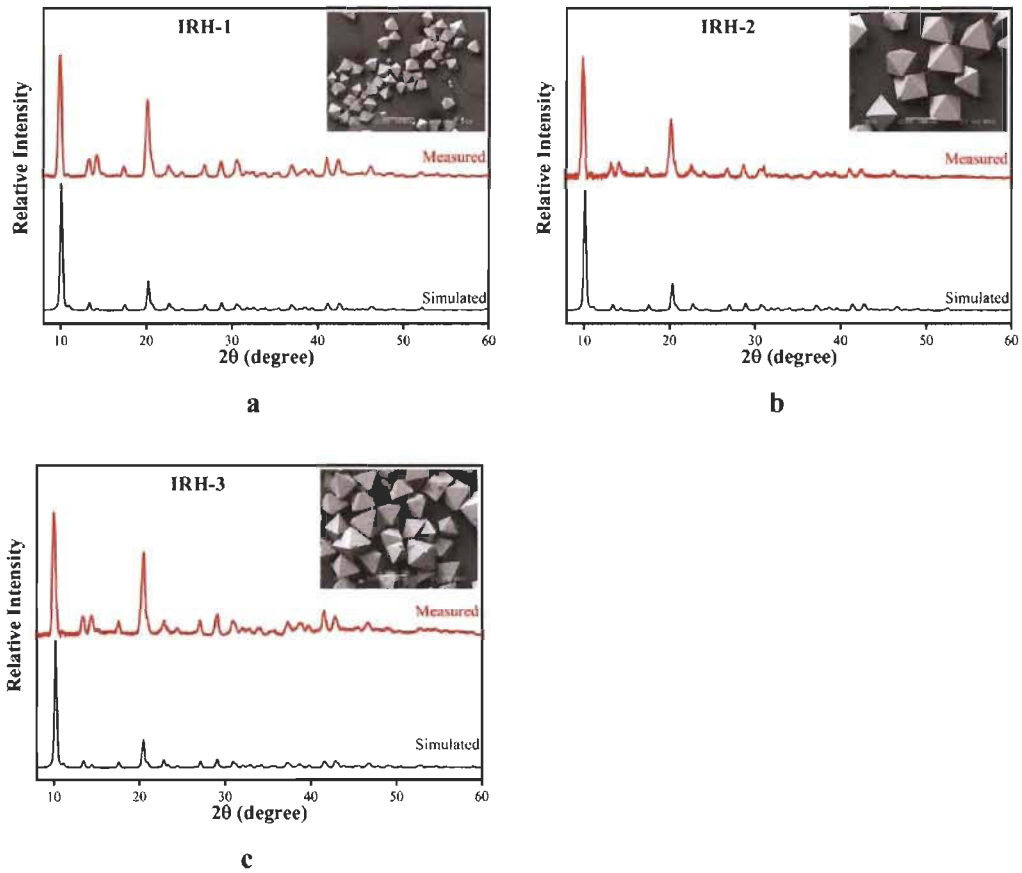

Figure 2. Comparison of the observed PXRD (red) with the simulated patterns (black) calculated from the SCXRD data and the inset SEM images (scale bar, 100 μm). (a–c) as-synthesized IRHs-(1–3), respectively.

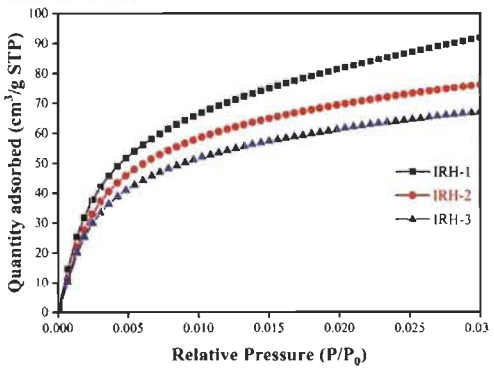

Figure 3. BET measurement curves for CO_2 adsorption at 273 K for IRHs-(1–3).

1 under the same condition. This indicates a very strong interaction between the CO_2 and the framework. For pressure above 1 bar, the adsorption of CO_2 remains almost constant, approaching saturation. The quick saturation of CO_2 is likely due to the small volume of the pore network. The uptake difference between these two adsorbates can be explained because of the higher polarizability and the presence of quadrupole moment of CO_2 compared to CH_4 that it does not possess.[31−33] The framework–gas interactions are exclusively between CO_2 and organic surfaces of the channels since the metal sites are not directly accessible. The systemic higher adsorption of CO_2 compared to CH_4 highlights the potential of the IRH materials for the separation of these two gases. The significant difference uptakes offer a strong potential for the separation of these two gases at 1 bar and 298 K. Adsorption and desorption cycles show no hysteresis, confirming the complete removal of gas molecules from the pores at low pressures and 298 K (Figure S24). The repeatability in data also signifies the stability of the framework after each adsorption and desorption cycles.

https://dx.doi.org/10.1021/acsami.0c15395
ACS Appl. Mater. Interfaces 2020, 12, 50619−50627

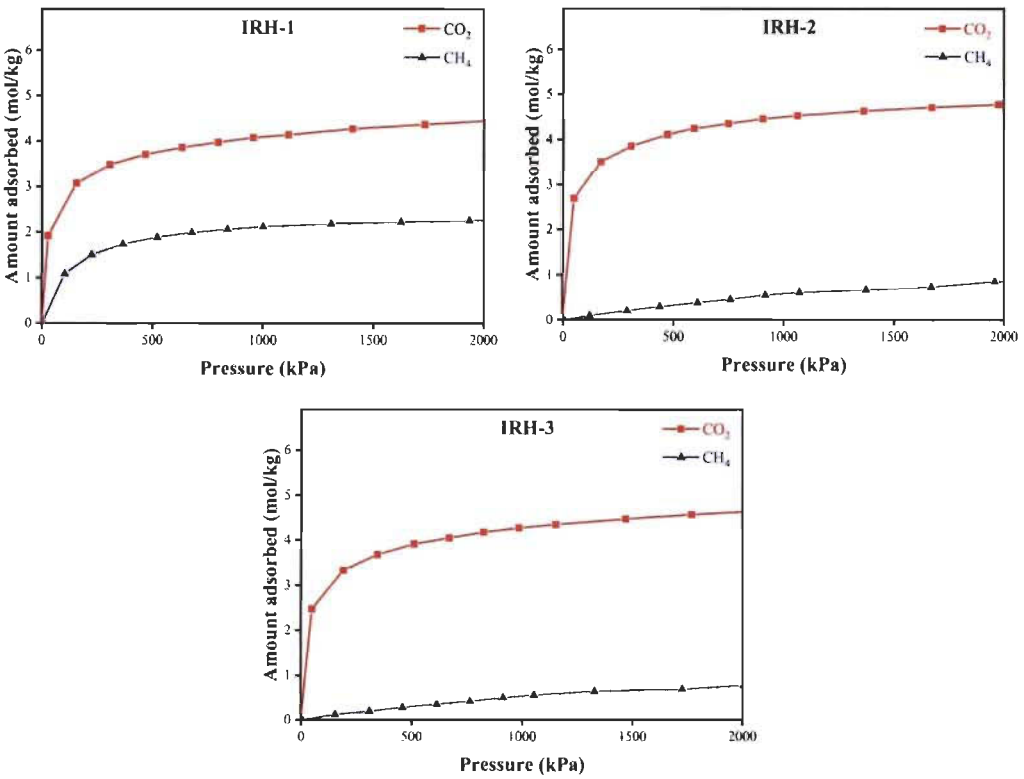

Figure 4. Adsorption isotherms of CO_2 and CH_4 on IRHs-(1−3) at 298 K.

Molecular Simulation. To understand the origin of the adsorption, grand canonical Monte Carlo simulations (GCMC) were performed to evaluate the maximum CO_2 and CH_4 uptakes on rigid IRH-3 at 298 K. Monte Carlo (MC) steps are applied to calculate the average number of molecules that can be filled in the pores and to evaluate the preferential adsorption sites.[34,35] The calculation were run using Lennard-Jones (LJ) 6−12 potential for the gas−gas and the framework−gas interactions.[36,37] Quadrupole moments contribution for the CO_2−CO_2 interactions was accounted with a Coulomb potential. The maximum adsorptions found by GCMC for CO_2 (5.4 mol/kg) and CH_4 (3.6 mol/kg) are consistent with the experimental values obtained at the same temperature (Figure S22). From the density isocontour surfaces (Figure 5), we can see how the adsorbed molecules are accommodated within the IRH-3 framework. The CO_2 molecules fill the MOF channels by interacting with the walls that contain organic linkers and coordinated water molecules (Figure 5a,b) while no specific adsorption sites are detected for CH_4 due to its weak van der Waals interactions with the framework (Figure 5c,d). Moreover, the hydrophobic nature of CH_4 favors its very low concentration near the metallic sites due to the bounded water molecules.

Calculation of the Selectivity. Based on the adsorption isotherms and the simulation studies, it is clear that all IRHs exhibited preferential adsorption of CO_2 over CH_4. Ideal adsorption selectivity (IAST) calculation has been widely employed to examine the binary gas mixture selective adsorption behavior from single component isotherms.[38] To investigate the potential in separation of CO_2/CH_4 binary mixture, the Toth model was combined with IAST to predict the selectivity of IRH-3. As shown in Figure 6, the simulated adsorption selectivity (S_{ads}) for the CO_2/CH_4 binary equimolar mixture at 298 K is above 27 at low pressure, even far more than few of the best MOFs previously reported, but with increase of pressure it gradually decreases to 17 at 1 bar. However, the S_{ads} still fairly surpasses those observed in other MOFs and inorganic porous solids such as HKUST-1 (7 at 1 bar), MOF-5 (2 at 1 bar), ZIF-8 (2 at 1 bar), MOF-505 (4 at 1 bar), and zeolite 5A (6 at 1 bar).[39−43] The decay of the selectivity behavior is typical for several adsorbents and can be attributed to the increase of the permeability at higher pressure due to the swelling of the MOF framework. These results demonstrate the high potential of IRH-3 for selective CO_2/CH_4 separation.

■ CONCLUSIONS

In summary, we have synthesized a new series of nitrogen-rich lanthanide metal−organic frameworks IRHs-(1−3) from the cyamelurate organic linker that has never been used to form porous materials. Gas adsorption studies show that these porous MOF materials present a higher adsorption of CO_2

https://dx.doi.org/10.1021/acsami.0c15395
ACS Appl. Mater. Interfaces 2020, 12, 50619−50627

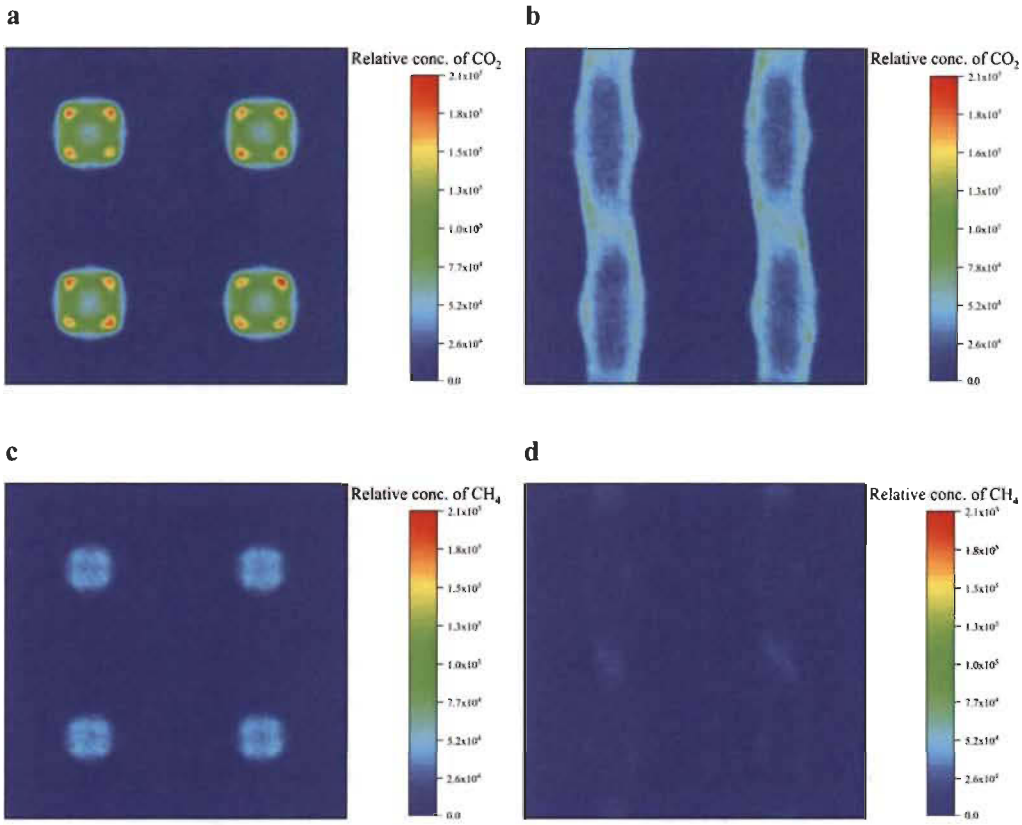

Figure 5. Front and side views of the density isocontour surfaces simulated for relative concentrations of (a, b) CO_2 and (c, d) CH_4 for IRH-3.

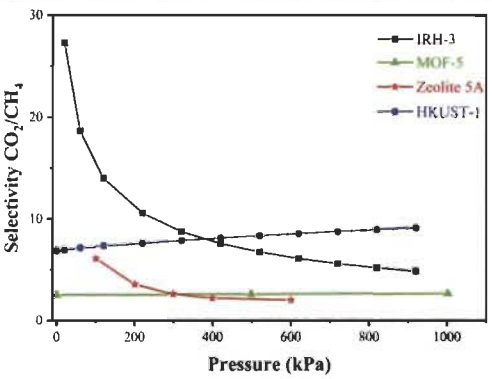

Figure 6. Comparison of selectivity of binary mixture (CO_2/CH_4) for four different adsorbants: IRH-3, HKUST-1, MOF-5, and zeolite 5A.

than CH_4. The density isocontour surfaces obtained from GCMC simulations indicate a strong affinity of the framework for CO_2 molecules. These results can be rationalized by the following features: (i) the limiting pore size of 4.19 Å, (ii) the functionalized interior surfaces with high densities of accessible nitrogen-donor sites, and (iii) the presence of coordinated water molecules. The prediction equimolar binary mixture CO_2/CH_4 selectivity using IAST calculation for IRH-3 indicates that at 298 K, the selectivity coefficient is above 27 at low pressure, which is much higher than several MOFs identified for this gas mixture separation. From a structure point of view, we have made some progress to design new MOFs that could be used to develop ideal porous materials for gas separation/purification. We expected that more Cy-MOFs will be emerging in the near future for their variety of applications.

EXPERIMENTAL SECTION

Materials and General Methods. All chemical reagents were purchased from commercial sources and used as received without further purification. Melamine and all metal salts were obtained from Sigma Aldrich. Elemental analysis for C, H, and N were carried out by EA 1108 Fisons CHNS Element analyzer using the quantitative dynamic flash combustion method. Infrared spectra were performed in the range of 4000 to 400 cm^{-1} using a Nicolet iS 10 Smart FT-IR spectrometer. Thermogravimetric analyses were conducted using a Diamond Pyris 6000 TGA/DTA apparatus from Perkin-Elmer from room temperature to 900 °C under N_2 flow at a heating rate of 10 °C/min. The scanning electron microscopy was performed using a

https://dx.doi.org/10.1021/acsami.0c15395
ACS Appl. Mater. Interfaces 2020, 12, 50619−50627

JEOL model 5500 coupled with an X-Max 20 mm^2 EDS analyzer. Crystallographic data were collected using a Bruker Venture Metaljet diffractometer with Ga Kα radiation. The structures were solved by dual-space algorithm using ShelxT,[44] and non-hydrogen atoms were refined anisotropically with least-squares minimization.[45] Hydrogen atoms were treated by first locating them from different Fourier maps, recalculating their positions using standard values for distances and angles, and then refining them as riding atoms. Powder X-ray diffraction was performed in transmission-mode geometry using a Bruker D8-Discover instrument (θ–θ geometry) equipped with an XYZ platform and a HI-STAR gas detector. X-rays were generated using a conventional sealed-tube source with a copper anode producing Cu Kα radiation (λ = 1.54178 Å). The samples were gently ground and then mounted on a flat Kapton sample holder. The data collection involved acquisition of two different sections with increasing angular position, giving two different 2D frames. These frames were integrated and combined to produce the final 1D X-ray diffraction powder pattern. Calculated X-ray powder diffraction patterns were generated from the structural data in corresponding CIFs, resulting from single-crystal analyses. The calculation was performed using Mercury software of the Cambridge Crystallographic Data Centre.[46] A unique value of the FWHM for the diffraction peaks was adjusted to obtain a better match between the resolution of the experimental and the calculated patterns.

Synthesis of IRHs-(1–3). Potassium cyamelurate (Cy) was synthesized according to the method described in the literature.[26] A mixture of Cy (0.05 mmol), $Ln(NO_3)_3{\cdot}6H_2O$ (0.15 mmol), DMF (6 mL), and H_2O (6 mL) were stirred thoroughly followed by sonication for 10 min. The resulting solution were sealed in a scintillation vial, which was heated at 80 °C for 24 h, and then cooled slowly to room temperature at a rate of 10 °C/h. Colorless octahedral crystals were collected by filtration and washed by DMF/H_2O (1:1). All IRHs are obtained with a yield of 90% based on the cyamelurate linker.

IRH-1. Anal. Calcd for $LaC_9H_8N_8O_7$ (%): C, 22.56; H, 1.68; N, 23.39. Found: C, 22.74; H, 2.31; N, 23.54. IR: 3330, 3205, 1674, 1648, 1555, 1502, 1478, 1445, 1411, 1158, 1085, 846, 814, 768, 728, 709, 616 cm^{-1}.

IRH-2. Anal. Calcd for $CeC_9H_8N_8O_7$ (%): C, 22.50; H, 1.68; N, 23.33. Found: C, 23.44; H, 2.38; N 23.30. IR: 3330, 3189, 1678, 1650, 1555, 1502, 1478, 1446, 1412, 1159, 1085, 848, 815, 771, 729, 711, 620 cm^{-1}.

IRH-3. Anal. Calcd for $PrC_9H_8N_8O_7$ (%): C, 22.50; H, 1.68; N, 23.28. Found: C, 23.03; H, 2.23; N, 22.50. IR: 3336, 3189, 1677, 1652, 1554, 1503, 1480, 1444, 1411, 1160, 1085, 848, 815, 771, 729, 712, 620 cm^{-1}.

Theoretical Calculation. GCMC simulation consists of three different types of steps: moving, creating, and suppressing molecule of the adsorbate inside the system. These steps, combined with probabilities formula derived from statistical physics, allow us to study a system at thermodynamic equilibrium by minimizing the partition function define by eq (1).[47]

$$Z(\mu, V, T) = \sum_{i}^{N} \exp(\beta\mu N) Q(N, V, T) \tag{1}$$

where $Q(N, V, T)$ is the canonical partition function defined by eq (2), μ is the chemical potential and $\beta = 1/k_B T$.

$$Q(N, V, T) = \frac{1}{N!}\left(\frac{m}{2\pi\beta\hbar}\right)^{3N/2} \int d\mathbf{r}_1 \ldots d\mathbf{r}_N \exp(\beta U(\mathbf{r}_1, \ldots, \mathbf{r}_N)) \tag{2}$$

where $U(r_1, \ldots r_N)$ is the total energy of the system, and r_i is the position of the i^{th} particle in the system.

Different methods exist in the literature to calculate the chemical potential μ of the system. Widom's test has been chosen because the simulation model becomes self-sufficient. The chemical potential is calculated in the canonical ensemble of the bulk phase and used in the adsorbed phase of the grand canonical ensemble since they have the same value in both phases.[47,47] Both Canonical Monte Carlo (CMC) and GCMC are performed, as follows: 5 million steps are achieved to reach equilibrium and 25 million steps for the measurement. At each 5000 steps, thermodynamics properties (energy, number of molecules, pressure, etc.) are conserved with the current configurations of the adsorbate. In GCMC simulation, the probability of attempting to move a molecule was set at 34% and attempting creation and suppression was set at 33%. Since CO_2 is simulated using a three bodies approach, it can also rotate. Probabilities of attempting moving CO_2 were therefore set at 50% to move the molecule in the same orientation and 50% to rotate it. Using the pore volume, excess adsorption of the adsorbate was calculated with the average number of molecules in the measurement phase. Finally, the potential of interaction consisted of a combination of a Lennard-Jones (6-12) (LJ) and a Coulombic interaction for the non-bonded interaction of CO_2 and only LJ for CH_4. In this study, the porous solid is defined as a rigid structure of a 4 × 4 × 2 unit cell (box) with no partial charge. Dimension of a one-unit cell of IRH-3 is 8.68 Å by 8.68 Å by 20.15 Å. All the cross-interaction parameters were determined using the Lorentz-Berthelot combining rules. Cutoff of LJ interaction was set at 16 Å while cutoff of the Coulombic interaction was set at a maximum of 1 box of simulation. Parameters for CO_2 and CH_4 were taken from the TraPPe force field while parameters for the adsorbent were taken from the universal force field (UFF).[48–50]

Gas Adsorption Measurement. Pure gas adsorption isotherms were measured using a homemade closed-loop volumetric apparatus at 298 K and pressures up to 2 kPa. The description of the apparatus is documented in the literature.[51–53] Prior to the measurements, the sample cell containing the pre-activated sample (~300 mg) was heated (activated) under vacuum at 298 K for 16 h. This activation temperature was chosen from several trials in the range 373 to 420 K. As shown from Figure S19, the activation at 398 K yielded to the highest adsorbed amount. The single-gas adsorption isotherms were measured *via* the standard volumetric approach. In this technique, a known amount of gas, initially stored in the reference volume, is expanded into the measurement volume. A simple mass balance between the initial and final conditions is used to calculate the adsorbed amount. The process is continued repeatedly until the final equilibrium pressure is reached. Afterward, the reverse procedure was used to determine the desorption isotherm.[54–56]

For predicting equimolar gas mixture selectivity, we employed Ideal Adsorbed Solution Tbeory (IAST).[57] IAST is widely used to predict gas mixture selectivity in zeolites and MOFs. In this work, the adsorption isotherm of pure CO_2 and CH_4 gas were fitted with the Toth model.[58] The fit parameters were then used to predict the adsorption mixture. Adsorption selectivity was calculated by the equilibrium selectivity defined as follows

$$S_{i,j} = \frac{q_i p_j}{p_i q_j} \tag{3}$$

where q_i and p_i are respectively the adsorbed phase and gas phase mole fractions of component (i), $S_{i,j}$ is the selectivity of the adsorbent for component (i) with respect to component (j).

■ ASSOCIATED CONTENT

Supporting Information

The Supporting Information is available free of charge at https://pubs.acs.org/doi/10.1021/acsami.0c15395.

Additional crystallographic details (including thermal atomic displacement ellipsoid plots), mass spectrum, ORTEP diagrams and other crystallographic data, powder X-ray diffraction, infrared, thermogravimetric analysis, and photographs of the crystalline samples (PDF)

Supplementary crystallographic data of IRH-1 (CIF)

Supplementary crystallographic data of IRH-2 (CIF)

Supplementary crystallographic data of IRH-3 (CIF)

https://dx.doi.org/10.1021/acsami.0c15395
ACS Appl. Mater. Interfaces 2020, 12, 50619–50627

AUTHOR INFORMATION

Corresponding Author

Adam Duong – *Département de Chimie, Biochimie et physique and Institut de Recherche sur l'Hydrogène, Université du Québec à Trois-Rivières, Trois-Rivières, Québec G9A 5H7, Canada;* Email: adam.duong@uqtr.ca

Authors

Midhun Mohan – *Département de Chimie, Biochimie et physique and Institut de Recherche sur l'Hydrogène, Université du Québec à Trois-Rivières, Trois-Rivières, Québec G9A 5H7, Canada*

Mohamed Essalhi – *Département de Chimie, Biochimie et physique and Institut de Recherche sur l'Hydrogène, Université du Québec à Trois-Rivières, Trois-Rivières, Québec G9A 5H7, Canada*

David Durette – *Département de Chimie, Biochimie et physique and Institut de Recherche sur l'Hydrogène, Université du Québec à Trois-Rivières, Trois-Rivières, Québec G9A 5H7, Canada*

Love Karan Rana – *Département de Chimie, Biochimie et physique and Institut de Recherche sur l'Hydrogène, Université du Québec à Trois-Rivières, Trois-Rivières, Québec G9A 5H7, Canada*

Follivi Kloutse Ayevide – *Département de Chimie, Biochimie et physique and Institut de Recherche sur l'Hydrogène, Université du Québec à Trois-Rivières, Trois-Rivières, Québec G9A 5H7, Canada*

Thierry Maris – *Département de Chimie, Université de Montréal, Montréal, Québec H3C 3J7, Canada;* orcid.org/0000-0001-9731-4046

Complete contact information is available at: https://pubs.acs.org/10.1021/acsami.0c15395

Notes

The authors declare no competing financial interest.

ACKNOWLEDGMENTS

We are grateful to the Natural Sciences and Engineering Research Council of Canada (RGPIN-2015-06425), the Canadian Queen Elizabeth II Diamond Jubilee Scholarships, the Fonds de recherche du Québec–Nature et technologies, the Canadian Foundation for Innovation, and Mitacs and the Université du Québec à Trois-Rivières. We also thank the ATS-Scientific Inc. and Micromeritics Instrument Corp., Norcross, USA for the measurement of the BET surface areas.

REFERENCES

(1) Wang, C.; Liu, D.; Lin, W. Metal–Organic Frameworks as a tunable platform for designing functional molecular materials. *J. Am. Chem. Soc.* **2013**, *135*, 13222–13234.

(2) Biradha, K.; Ramanan, A.; Vittal, J. J. Coordination polymers versus Metal–Organic Frameworks. *Cryst. Growth Des.* **2009**, *9*, 2969–2970.

(3) Guillerm, V.; Maspoch, D. Geometry Mismatch and Reticular Chemistry: Strategies To Assemble Metal–Organic Frameworks with Non-default Topologies. *J. Am. Chem. Soc.* **2019**, *141*, 16517–16538.

(4) Howarth, A. J.; Peters, A. W.; Vermeulen, N. A.; Wang, T. C.; Hupp, J. T.; Farha, O. K. Best practices for the synthesis, activation, and characterization of Metal–Organic Frameworks. *Chem. Mater.* **2017**, *29*, 26–39.

(5) Daglar, H.; Keskin, S. Computational Screening of Metal–Organic Frameworks for Membrane-Based $CO_2/N_2/H_2O$ Separations: Best Materials for Flue Gas Separation. *J. Phys. Chem. C* **2018**, *122*, 17347–17357.

(6) Fan, W.; Yuan, S.; Wang, W.; Feng, L.; Liu, X.; Zhang, X.; Wang, X.; Kang, Z.; Dai, F.; Yuan, D.; Sun, D.; Zhou, H.-C. Optimizing Multivariate Metal–Organic Frameworks for Efficient C_2H_2/CO_2 Separation. *J. Am. Chem. Soc.* **2020**, *142*, 8728–8737.

(7) Bloch, E. D.; Hudson, M. R.; Mason, J. A.; Chavan, S.; Crocellà, V.; Howe, J. D.; Lee, K.; Dzubak, A. L.; Queen, W. L.; Zadrozny, J. M.; Geler, S. J.; Lin, L.-C.; Gagliardi, L.; Smit, B.; Neaton, J. B.; Bordiga, S.; Brown, C. M.; Long, J. R. Reversible CO binding enables tunable CO/H_2 and CO/N_2 separations in Metal–Organic Frameworks with exposed divalent metal cations. *J. Am. Chem. Soc.* **2014**, *136*, 10752–10761.

(8) Xiao, D. J.; Gonzalez, M. I.; Darago, L. E.; Vogiatzis, K. D.; Haldoupis, E.; Gagliardi, L.; Long, J. R. Selective, tunable O_2 binding in cobalt (II)–triazolate/pyrazolate Metal–Organic Frameworks. *J. Am. Chem. Soc.* **2016**, *138*, 7161–7170.

(9) Herm, Z. R.; Swisher, J. A.; Smit, B.; Krishna, R.; Long, J. R. Metal–Organic Frameworks as adsorbents for hydrogen purification and precombustion carbon dioxide capture. *J. Am. Chem. Soc.* **2011**, *133*, 5664–5667.

(10) Bao, Z.; Yu, L.; Ren, Q.; Lu, X.; Deng, S. Adsorption of CO_2 and CH_4 on a Magnesium-Based Metal Organic Framework. *J. Colloid Interface Sci.* **2011**, *353*, 549–556.

(11) Yu, J.; Xie, L.-H.; Li, J.-R.; Ma, Y.; Seminario, J. M.; Balbuena, P. B. CO_2 capture and separations using MOFs: computational and experimental studies. *Chem. Rev.* **2017**, *117*, 9674–9754.

(12) Poloni, R.; Smit, B.; Neaton, J. B. CO_2 capture by Metal–Organic Frameworks with van der Waals density functionals. *J. Phys. Chem. A* **2012**, *116*, 4957–4964.

(13) Song, X.; Zhang, M.; Chen, C.; Duan, J.; Zhang, W.; Pan, Y.; Bai, J. Pure-Supramolecular-Linker Approach to Highly Connected Metal–Organic Frameworks for CO_2 Capture. *J. Am. Chem. Soc.* **2019**, *141*, 14539–14543.

(14) Jiang, J.; Lo, Z.; Zhang, M.; Duan, J.; Zhang, W.; Pan, Y.; Bai, J. Higher symmetry multinuclear clusters of Metal–Organic Frameworks for highly selective CO_2 capture. *J. Am. Chem. Soc.* **2018**, *140*, 17825–17829.

(15) Wang, K.; Huang, H.; Liu, D.; Wang, C.; Li, J.; Zhong, C. Covalent triazine-based frameworks with ultramicropores and high nitrogen contents for highly selective CO_2 capture. *Environ. Sci. Technol.* **2016**, *50*, 4869–4876.

(16) Wen, H.-M.; Wang, H.; Li, B.; Cui, Y.; Wang, H.; Qian, G.; Chen, B. A Microporous Metal–Organic Framework with Lewis Basic Nitrogen Sites for High C_2H_2 Storage and Significantly Enhanced C_2H_2/CO_2 Separation at Ambient Conditions. *Inorg. Chem.* **2016**, *55*, 7214–7218.

(17) Li, X.-Y.; Ma, L.-N.; Liu, Y.; Hou, L.; Wang, Y.-Y.; Zhu, Z. Honeycomb Metal–Organic Framework with Lewis Acidic and Basic Bifunctional Sites: Selective Adsorption and CO_2 Catalytic Fixation. *ACS Appl. Mater. Interfaces* **2018**, *10*, 10965–10973.

(18) Ye, Y.; Zhang, H.; Chen, L.; Chen, S.; Lin, Q.; Wei, F.; Zhang, Z.; Xiang, S. Metal–Organic Framework with Rich Accessible Nitrogen Sites for Highly Efficient CO_2 Capture and Separation. *Inorg. Chem.* **2019**, *58*, 7754–7759.

(19) Zhu, Q.-L.; Xu, Q. Metal–Organic Framework composites. *Chem. Soc. Rev.* **2014**, *43*, 5468–5512.

(20) Lu, W.; Wei, Z.; Gu, Z.-Y.; Liu, T.-F.; Park, J.; Park, J.; Tian, J.; Zhang, M.; Zhang, Q.; Gentle, T., III; Bosch, M.; Zhou, H.-C. Tuning the structure and function of metal–organic frameworks via linker design. *Chem. Soc. Rev.* **2014**, *43*, 5561–5593.

(21) Yu, M.; Xie, Y.; Wang, X.; Li, Y.; Li, G. Highly water-stable dye@Ln-MOFs for sensitive and selective detection toward antibiotics in water. *ACS Appl. Mater. Inter.* **2019**, *11*, 21201–21210.

(22) Chen, H.-J.; Zheng, X.-Y.; Zhao, Y.-R.; Yuan, D.-Q.; Kong, X.-J.; Long, L.-S.; Zheng, L.-S. A Record-Breaking Loading Capacity for Single-Molecule Magnet Mn_{12} Clusters Achieved in a Mesoporous Ln-MOF. *ACS Appl. Electron. Mater.* **2019**, *1*, 804–809.

(23) Gao, M.-L.; Wang, W.-J.; Liu, L.; Han, Z.-B.; Wei, N.; Cao, X.-M.; Yuan, D.-Q. Microporous Hexanuclear Ln(III) Cluster-Based Metal–Organic Frameworks: Color Tunability For Barcode Applica-

https://dx.doi.org/10.1021/acsami.0c15395
ACS Appl. Mater. Interfaces 2020, 12, 50619–50627

tion and Selective Removal of Methylene Blue. *Inorg. Chem.* **2017**, *56*, 511−517.
(24) Pagis, C.; Ferbinteanu, M.; Rothenberg, G.; Tanase, S. Lanthanide-Based Metal Organic Frameworks: Synthetic Strategies and Catalytic Applications. *ACS Catal.* **2016**, *6*, 6063−6072.
(25) Mohan, M.; Rajak, S.; Tremblay, A. A.; Maris, T.; Duong, A. Syntheses of mono and bimetallic cyamelurate polymers with reversible chromic behaviour. *Dalton Trans.* **2019**, *48*, 7006−7014.
(26) Holst, J. R., *Synthesis of inorganic heptazine-based materials*. Theses and Dissertations 2009, *242*.
(27) Horvath-Bordon, E.; Kroke, E.; Svoboda, I.; Fueß, H.; Riedel, R.; Neeraj, S.; Cheetham, A. K. Alkalicyamelurates, $M_3[C_6N_7O_3]\cdot xH_2O$, M = Li, Na, K, Rb, Cs: UV-luminescent and thermally very stable ionic tri-s-triazine derivatives. *Dalton Trans.* **2004**, *22*, 3900−3908.
(28) Holst, J. R.; Gillan, E. G. From triazines to heptazines: deciphering the local structure of amorphous nitrogen-rich carbon nitride materials. *J. Am. Chem. Soc.* **2008**, *130*, 7373−7379.
(29) Spek, A. L. Single-crystal structure validation with the program PLATON. *J. Appl. Crystallogr.* **2003**, *36*, 7−13.
(30) Oschatz, M.; Antonietti, M. A search for selectivity to enable CO_2 capture with porous adsorbents. *Energy Environ. Sci.* **2018**, *11*, 57−70.
(31) Graham, C.; Pierrus, J.; Raab, R. E. Measurement of the electric quadrupole moments of CO_2, CO and N_2. *Mol. Phys.* **1989**, *67*, 939−955.
(32) Torii, H. The role of atomic quadrupoles in intermolecular electrostatic interactions of polar and nonpolar molecules. *J. Chem. Phys.* **2003**, *119*, 2192−2198.
(33) Pal, A.; Chand, S.; Madden, D. G.; Franz, D.; Ritter, L.; Johnson, A.; Space, B.; Curtin, T.; Das, M. C. A Microporous Co-MOF for Highly Selective CO_2 Sorption in High Loadings Involving Aryl C−H···O═C═O Interactions: Combined Simulation and Breakthrough Studies. *Inorg. Chem.* **2019**, *58*, 11553−11560.
(34) Kim, J.; Smit, B. Efficient Monte Carlo Simulations of Gas Molecules Inside Porous Materials. *J. Chem. Theory Comput.* **2012**, *8*, 2336−2343.
(35) Sirjoosingh, A.; Alavi, S.; Woo, T. K. Grand-Canonical Monte Carlo and Molecular-Dynamics Simulations of Carbon-Dioxide and Carbon-Monoxide Adsorption in Zeolitic Imidazolate Framework Materials. *J. Phys. Chem. C* **2010**, *114*, 2171−2178.
(36) Sharma, A.; Huang, R.; Malani, A.; Babarao, R. Computational materials chemistry for carbon capture using porous materials. *J. Phys. D: Appl. Phys.* **2017**, *50*, 463002.
(37) Gurdal, Y.; Keskin, S. A new approach for predicting gas separation performances of MOF membranes. *J. Membrane Sci.* **2016**, *519*, 45−54.
(38) Simon, C. M.; Smit, B.; Haranczyk, M. pyIAST: Ideal adsorbed solution theory (IAST) Python package. *Comput. Phys. Commun.* **2016**, *200*, 364−380.
(39) Yan, X.; Komarneni, S.; Zhang, Z.; Yan, Z. Extremely enhanced CO2 uptake by HKUST-1 metal−organic framework via a simple chemical treatment. *Microporous Mesoporous Mater.* **2014**, *183*, 69−73.
(40) Saha, D.; Bao, Z.; Jia, F.; Deng, S. Adsorption of CO_2, CH_4, N_2O, and N_2 on MOF-5, MOF-177, and Zeolite 5A. *Environ. Sci. Technol.* **2010**, *44*, 1820−1826.
(41) Kloutse, F. A.; Hourri, A.; Natarajan, S.; Benard, P.; Chahine, R. Experimental benchmark data of CH_4, CO_2 and N_2 binary and ternary mixtures adsorption on MOF-5. *Sep. Purif. Technol.* **2018**, *197*, 228−236.
(42) Mofarahi, M.; Gholipour, F. Gas adsorption separation of CO_2/CH_4 system using Zeolite 5A. *Microporous Mesoporous Mater.* **2014**, *200*, 1−10.
(43) Huang, H.; Zhang, W.; Liu, D.; Zhong, C. Understanding the effect of trace amount of water on CO_2 capture in natural gas upgrading in metal−organic frameworks: a molecular simulation study. *Ind. Eng. Chem. Res.* **2012**, *51*, 10031−10038.
(44) Sheldrick, G. M. SHELXT−Integrated space-group and crystal-structure determination. *Acta Crystallogr., Sect. A: Found. Adv.* **2015**, *71*, 3−8.
(45) Sheldrick, G. M. Crystal structure refinement with SHELXL. *Acta Crystallogr., Sect. C: Struct. Chem.* **2015**, *71*, 3−8.
(46) Macrae, C. F.; Bruno, I. J.; Chisholm, J. A.; Edgington, P. R.; McCabe, P.; Pidcock, E.; Rodriguez-Monge, L.; Taylor, R.; van de Streek, J.; Wood, P. A. Mercury CSD 2.0−new features for the visualization and investigation of crystal structures. *J. Appl. Crystallogr.* **2008**, *41*, 466−470.
(47) Samios, S.; Stubos, A. K.; Kanellopoulos, N. K.; Cracknell, R. F.; Papadopoulos, G. K.; Nicholson, D. Determination of Micropore Size Distribution from Grand Canonical Monte Carlo Simulations and Experimental CO_2 Isotherm Data. *Langmuir* **1997**, *13*, 2795−2802.
(48) Eggimann, B. L.; Sunnarborg, A. J.; Stern, H. D.; Bliss, A. P.; Siepmann, J. I. An online parameter and property database for the TraPPE force field. *Mol. Simul.* **2014**, *40*, 101−105.
(49) Addicoat, M. A.; Vankova, N.; Akter, I. F.; Heine, T. Extension of the Universal Force Field to Metal−Organic Frameworks. *J. Chem. Theory Comput.* **2014**, *10*, 880−891.
(50) Casewit, C. J.; Colwell, K. S.; Rappe, A. K. Application of a universal force field to organic molecules. *J. Am. Chem. Soc.* **1992**, *114*, 10035−10046.
(51) Hamon, L.; Llewellyn, P. L.; Devic, T.; Ghoufi, A.; Clet, G.; Guillerm, V.; Pirngruber, G. D.; Maurin, G.; Serre, C.; Driver, G.; van Beek, W.; Jolimaitre, E.; Vimont, A.; Daturi, M.; Férey, G. Co-adsorption and Separation of CO_2−CH_4 Mixtures in the Highly Flexible MIL-53(Cr) MOF. *J. Am. Chem. Soc.* **2009**, *131*, 17490−17499.
(52) Bastin, L.; Bárcia, P. S.; Hurtado, E. J.; Silva, J. A. C.; Rodrigues, A. E.; Chen, B. A Microporous Metal− Organic Framework for Separation of CO_2/N_2 and CO_2/CH_4 by Fixed-Bed Adsorption. *J. Phys. Chem. C* **2008**, *112*, 1575−1581.
(53) Rios, R. B.; Stragliotto, F. M.; Peixoto, H. R.; Torres, A. E. B.; Bastos-Neto, M.; Azevedo, D. C. S.; Cavalcante, C. L., Jr. Studies on the adsorption behavior of CO_2-CH_4 mixtures using activated carbon. *Braz. J. Chem. Eng.* **2013**, *30*, 939−951.
(54) Zheng, J.-J.; Kusaka, S.; Matsuda, R.; Kitagawa, S.; Sakaki, S. Theoretical Insight into Gate-Opening Adsorption Mechanism and Sigmoidal Adsorption Isotherm into Porous Coordination Polymer. *J. Am. Chem. Soc.* **2018**, *140*, 13958−13969.
(55) Alezi, D.; Belmabkhout, Y.; Suyetin, M.; Bhatt, P. M.; Weseliński, L. J.; Solovyeva, V.; Adil, K.; Spanopoulos, I.; Trikalitis, P. N.; Emwas, A.-H. MOF Crystal Chemistry Paving the Way to Gas Storage Needs: Aluminum-Based soc-MOF for CH_4, O_2, and CO_2 Storage. *J. Am. Chem. Soc.* **2015**, *137*, 13308−13318.
(56) Li, Y.; Yang, R. T. Gas Adsorption and Storage in Metal−Organic Framework MOF-177. *Langmuir* **2007**, *23*, 12937−12944.
(57) Zhou, L.; Wu, J.; Li, M.; Wu, Q.; Zhou, Y. Prediction of multicomponent adsorption equilibrium of gas mixtures including supercritical components. *Chem. Eng. Sci.* **2005**, *60*, 2833−2844.

https://dx.doi.org/10.1021/acsami.0c15395
ACS Appl. Mater. Interfaces 2020, 12, 50619−50627

7.5 Conclusion

In this chapter, a series of novel lanthanide-based MOFs [IRH-(**1-3**)] were synthesized. These versatile porous structures exemplify the incorporation of the flat and rigid organic ligand as the building block to target specific net. Also, the higher coordination numbers of lanthanide SBU serves in the construction of 3D frameworks forming the one-directional architecture. Structural characterizations were conducted using XRD revealing the formation of the desired assembly. Other characterizations such as PXRD, FTIR, EA, SEM, EDS and TGA were also conducted to determine material purity, homogeneity and stability. The synthesized IRHs were activated using solvent exchange process after which the surface area of the activated MOFs was measured using BET as 742.9, 594.5 and 525.4 m^2/g for IRH-(**1-3**), respectively. Theoretical studies were conducted to understand the pore properties and adsorption behaviour which was assisted through the density isocontour surface measurements using GCMC simulation showing a strong affinity of CO_2 over CH_4 in the pores. The single-component sorption isotherms for CO_2 and CH_4 were collected at 298 K for activated IRHs. In the case of CO_2 isotherm, the adsorption capacities of IRHs-(**1-3**) were noted to be 2.6, 3.1 and 2.8 mol/kg at 298 k and 1 bar pressure while negligible amounts of CH_4 were adsorbed. This shows the very high gas selectivity for CO_2 over CH_4. The simulated adsorption selectivity for CO_2/CH_4 binary equimolar mixtures at 298 K and atmospheric pressures is Above 27 which is higher than any reported MOFs and even higher than other adsorbents used for CO_2/CH_4 separation. This work enlightens the design of novel porous MOFs with high selectivity for gas separation applications.

CHAPTER 8: Conclusions and Future Outlooks

8.1 Conclusions

8.1.1 Frame of Thesis

Intense research has been focused on the development of smart materials for the advancements in technology. This steep rise in demands can be perceived due to the exponential growth in global population and shortage of availability of current energy sources. Energy crisis being the most affected sector, new materials need to be developed to harvest and store energies efficiently. Among the various classes of materials used, coordination chemistry is one of the perfect materials to address these issues due to the versatility in structural engineering. In the thesis, this approach has been used to develop various novel coordination polymers with intrinsic properties. The primary focus in this thesis is the design, synthesis, characterization and properties analysis of novel coordination polymers including Metal-Organic Frameworks by implementing exclusive approaches on rational construction like molecular building blocks that introduce the desired properties in the synthons before coordination to the metal ions.

Chapters 1and 2 give an idea on the objectives that are focused on the various projects undertaken in this thesis. These include (i) design an approach on addressing the issues such as gas storage and separation and moisture sensing applications, (ii) synthesis of novel and known pyridone based ligands, (iii) construction of coordination polymers to prove the concept of forming frameworks using multi-dentate pyridonyl functionality, (iv) development of 2D coordination polymers using bidentate dipyridone to understand the coordination modes which make polypyridone ligands promising candidates for the synthesis of a new class of extended frameworks, (v) synthesis of a rigid and flat potassium cyamelurate ligand which consists of multiple coordination sites and nitrogen-

rich system, (vi) development of 2D coordination polymers based on cyamelurate ligand with various transition metals and mixed metallic systems for sensing applications and, (vii) design, synthesis and adsorption properties of 3D MOFs for gas separation applications.

To fulfil these objectives, adequate strategies were implemented to construct materials with specific properties desired. For the synthesis of polypyridonyl systems, coupling reactions were employed due to their high yield. Traditional methods were adopted to synthesize potassium cyamelurate. Metal ions were judiciously selected depending on the desired properties. Solvothermal synthesis was performed to link the organic ligands with the metal species and to crystallize the materials simultaneously.

Understanding the molecular arrangement is considered as an optimal method to correlate with the properties exhibited by the materials. All synthesized materials underwent various characterization techniques to comprehend the molecular attainability. Single-crystal X-ray diffraction (SCXRD) technique was used to investigate the atomic level arrangement. Powder X-ray diffraction (PXRD) was performed to confirm the phase purity by comparing the measured patterns with those generated from SCXRD. The presence of functionalities was determined by infrared spectroscopy. The stability of the materials was investigated using gravimetric analysis techniques.

8.1.2 Bidentate Pyridonyl Systems

Most of the coordination polymers known till date have been mainly made with carboxylate ligands. To investigate the potential of pyridonyl functionality as a coordination site, a series of novel bidentate organic ligands were synthesized as

described in chapter 3. This article mainly focuses on the synthesis and characterization of novel dipyridone ligands. All ligands were synthesized by Suzuki coupling reactions followed by deprotection reactions. Each stage of the synthesis was monitored using various characterization techniques. Slow diffusion and solvothermal methods were performed to produce single crystals of all the ligands suitable for analysis by single crystal X-ray diffraction. ^{1}H and ^{13}C NMR spectroscopy, FTIR spectroscopy and Mass spectroscopy were also used to confirm the structural and the purity of the samples. Thermal analyses were also performed on all the ligands synthesized. High yield of all the ligands eases the possibility of using them to build various coordination polymers. This chapter gives an insight to the scientific community on building organic ligands based on polypyridonyl functionality which can be used to prepare a new class of coordination polymers.

Chapters 4 and 5 examined the potential of polypyridonyl organic ligands in chapter 3 as candidates for the construction of periodic and ordered framework structures. As a proof of the concept, dipyridone ligand was coordinated with cobalt salt. Co-crystals of $Co(CHOO)_2$ $(H_2O)_4$ made from cobalt (II) salts with one of the dipyridone **1** were obtained and presented in chapter 4. In this work, dipyridone self-assembles through strong intermolecular interaction by hydrogen bonds which are linked with the 2D hydrogen bonded sheets of $Co(CHOO)_2(H_2O)_4$ creating the 3D framework. In chapter 5, we focus on designing novel coordination polymer using dipyridone ligand linked with cobalt ions through solvothermal method forming CP-**671**. It also dealt on the investigation of the self-assembly of dipyridone **1** in slow diffusion and solvothermal conditions forming hydrogen bonding polymers with zigzag **1a** and cyclic dimer **1b** motifs. The novel CP-**671** was characterized using X-ray diffraction and other techniques. This study has opened a new door for the research on coordination and supramolecular

chemistry based on polypyridone ligands making it a promising candidate for the construction of coordination polymers. Abundant ligating modes in pyridonyl groups with metal systems ease the formation of novel coordination polymers.

8.1.3 Potassium Cyamelurate Systems

Next objective of the thesis was to focus on constructing rigid and stable novel coordination polymers. For this, potassium cyamelurate was selected as the organic ligand with pyridonyl functionality due to the intrinsic properties exhibited. Points to be mentioned here are their aromaticity, N-rich system, rigid, polyconjugative and multiple coordination sites. From the knowledge gained regarding the numerous coordination modes of pyridonyl functional groups, potassium cyamelurate was coordinated with various transition and lanthanide metal ions. In chapter 6, a series of novel unimetallic (MOPs-(**1-4**)) and bimetallic (MMOPs-(**5-7**)) compounds were designed and developed under room temperature conditions using water as the only solvent forming isostructural coordination polymers linked by multiple hydrogen bonds to produce 2D framework structures. The isostructurality of MOPs motivated us to develop mixed metallic systems MMOPs which can be interesting for applications involving metal ions. MOPs-(**2** and **3**) and MMOPs-(**5-7**) were seen to exhibit thermo and solvo-chromic behaviour and the mechanism of this phenomena was attributed to the change in the metal coordination geometry. These results encouraged us to investigate coordination using other metal species with similar properties which can give an array of materials with different detection ranges. The incorporation of coordination polymers in sensing application can improve the lifetime of the devices designed as the materials are quite stable in adverse conditions. This also has a direct influence on the research community to develop smart

materials *via* eco-friendly and cheap methods and to have a deeper insight on crystal engineering of ordered materials.

The supramolecular architecture of cyamelurate based coordination polymers (MOPs and MMOPs) has given an understanding on the utility of this organic ligand for the construction of extended porous frameworks. Lanthanide metals have higher coordination numbers and can be employed to build MOFs through solvothermal synthesis techniques. This was achieved in chapter 7 where potassium cyamelurate was coordinated with a series of lanthanide metal salts forming infinite frameworks IRH-(**1-3**) consisting of one-directional pores. This has been the first report on synthesis of one-directional Lanthanide based MOFs. The MOFs were characterized using various techniques to understand the structure, purity, homogeneity and thermal stability. The higher surface area with smaller pore size facilitates the materials to be used for selective gas separation. As expected, all MOFs synthesized showed exceptionally high selectivity on CO_2-CH_4 gas separation at room temperatures and pressures. Theoretical studies showed that the adsorption behaviour was different with CO_2 and CH_4 which has resulted in the increased selectivity. Adsorption sites were influenced by the nitrogen-rich ligand walls in the pores which were determined using the computational studies. The study has been a breakthrough in the field of MOF synthesis whereby using new coordination moieties such as cyamelurate ligand has resulted in rigid and stable frameworks monitoring the molecular structural arrangement. It has motivated the research community on forecasting the structural integrity using the proper selection of precursors. New lanthanide MOFs can be developed inspired from this work for other applications including photoluminescence and magnetism.

8.2 Future Outlooks

The research dealt with has focused on various aspects such as the development of a novel class of materials addressing the issues regarding gas storage and separation and for sensing applications. Although the research poses many exciting potential applications, the primary goal was focused on developing new smart materials with intrinsic properties. A few of the areas where the research can point out future perspectives are listed below.

- Inspired by the novel bidentate pyridone ligands, synthesis of novel extended bipyridone and polypyridone based organic ligands can be accomplished. These new ligands can be an asset for the replacement of all MOF architectures known thereby improving the desired properties of the material developed. The coordination modes can be monitored through the reaction conditions which can also be employed to generate polypyridone based multi-metallic systems.

- The MMOPs developed in chapter 6 can be further investigated for their other properties depending on the secondary metals used for coordination. The work highlights that the structural arrangement is seldom controlled by the secondary metal thereby ensuring the similar molecular arrangement with other transition metals too. Thus, an effort on developing new MMOPs based on other mixed transition metals can also be focused upon to attain various other interesting properties.

- As an outbreak of the research carried on MMOPs, one of the major areas to be focused would be on the study of the change in properties depending on the change in the ratios of metals in MMOPs. A periodical increase of the parental MOPs to an equilibrium ratio of two metals in the system with different

combinations of metals can enlarge this field of solid solutions thereby generating an array of new class of smart materials. A series of chromic materials in this fashion can be employed in any desired range of sensing devices.

- During the course of the research some other interesting systems were also developed. One such promising material was Cu-MOP seen to have interesting magnetic and electrochemical properties. Due to the unique formation of one-dimensional MOF, along with the trapped potassium ions within the frameworks, it can show great interest in the replacement of Li-ion batteries where the charge-discharge issue can be addressed conveniently. Other interesting materials developed during the course of the research were Pd and Pt-cyamelurate 2D frameworks which can have interesting applications in photocatalysis and cancer therapy studies. These materials can be developed in future to focus on some promising outcomes.

- Persuaded by the research in chapter 7, a series of 3D MOFs can be designed similar to IRHs with exceptional gas selectivity and improved gas storage capacity. Other elements in the lanthanide series can be employed for achieving this, thereby generating a series of isostructural 3D MOFs with similar pore sizes and adsorption capacities but varying properties and adsorption selectivity. By varying the size of precursors, the pore size can be reformed which can monitor the adsorption capacity of the material designed. The larger lanthanides can also affect the topology of the molecular arrangements which has been evident from the Tb-IRH synthesized using a different approach generating 3D MOF with interconnected pores in x- and y-planes. This finding paves a new path towards developing novel frameworks with interesting properties.

- Along 3D MOFs, an investigation on developing 1D MOFs based on cyamelurates coordinated with lanthanide metals were also conducted during the course of the research synthesizing a full spectrum of 1D-IRHs. Further studies on these materials can be highlighted on the photoluminescence properties that can arise due to the lanthanide metals present. In this series, the most promising materials are expected to be Eu, Dy, Tb and Sm-IRHs. The synthesis methods are slightly different from the 3D forms with higher yields.

- Another interesting class of material that can be developed is based on the 3D one-directional channelled IRHs. As these MOFs are isostructural, mixed metallic lanthanide based MMOFs can be designed. As a proof of study, four MMOFs were developed during the research which include MOF-(La-Ce), MOF-(La-Pr), MOF-(Ce-Pr) and MOF-(La-Ce-Pr). Other lanthanide metals can also be incorporated to generate multi-metallic solid solutions as these improve the multi-functionality of the final materials which is dependent on the metals added. As an extended form of the idea, a new class of lanthanide-transition metal combination can also be designed and synthesized to address multiple applications. Finally, as the studies also lead to increasing the pore sizes, incorporation of nanoparticles within the pores can also be investigated for catalytic properties.

Appendix 1: Supplementary Information of Article 1

Hydrogen Bonds Patterns in Co-Crystals of Dipyridone

Midhun Mohan,[a] Mohamed Essalhi,[a] Sarah Zaye,[a] Love Karan Rana,[a] Thierry Maris[b] and Adam Duong[a]*

[a]*Département de Chimie, Biochimie et physique and Institut de Recherche sur l'Hydrogène, Université du Québec à Trois-Rivières, Trois-Rivières, Québec, G9A 5H7, Canada.*

[b]*Département de chimie, Université de Montréal, Montréal, Québec, H3T 1J4, Canada*

*To whom correspondence should be addressed. E-mail : adam.duong@uqtr.ca

Table of Contents

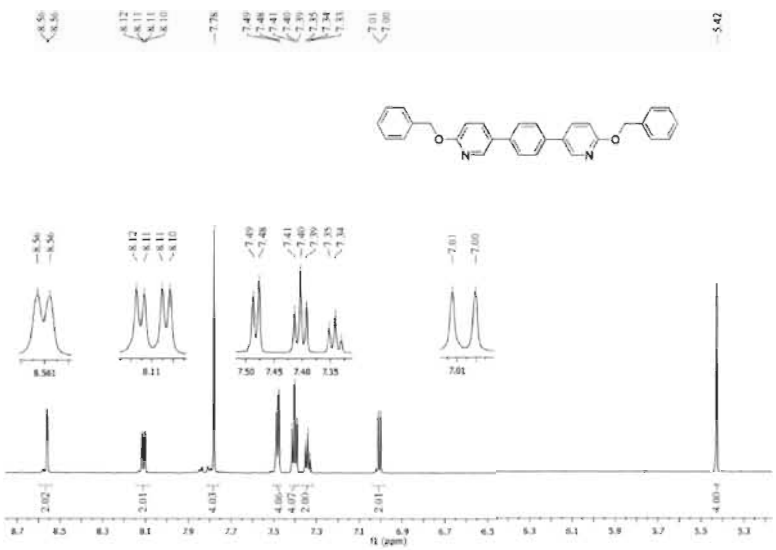

Fig. S1 ^{1}H-NMR spectrum of **2'** recorded in DMSO-d_6 solution.

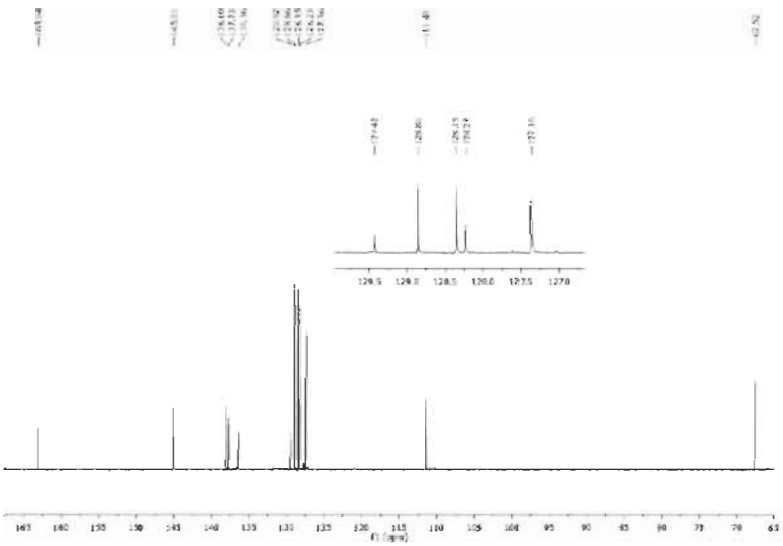

Fig. S2 ^{13}C-NMR spectrum of **2'**, recorded in DMSO-d_6 solution.

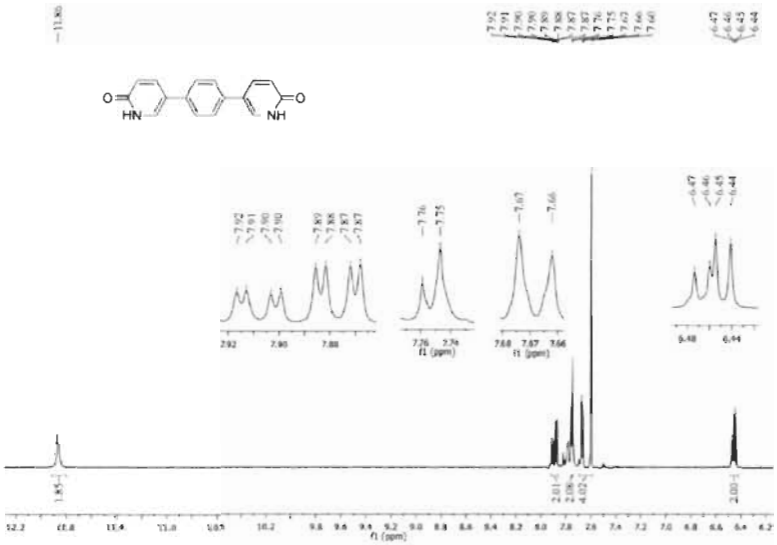

Fig. S3 ^{1}H-NMR spectrum of **2** recorded in DMSO-d_6 solution.

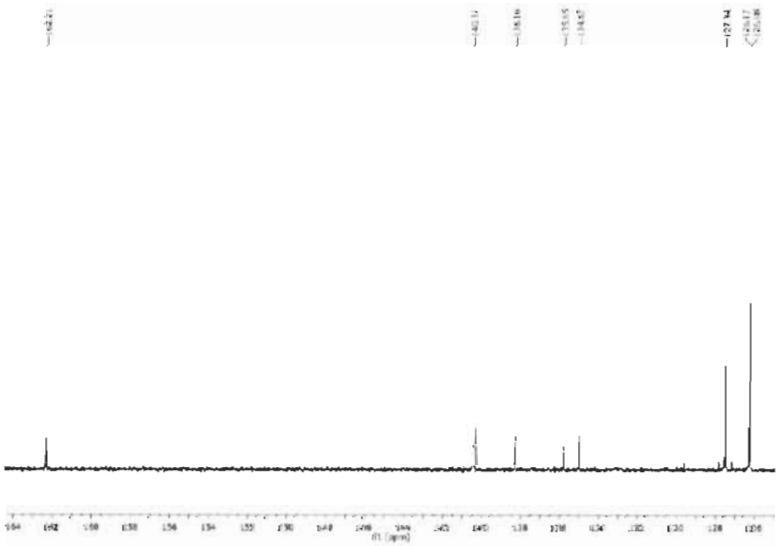

Fig. S4 ^{13}C-NMR spectrum of **2** recorded in DMSO-d_6 solution.

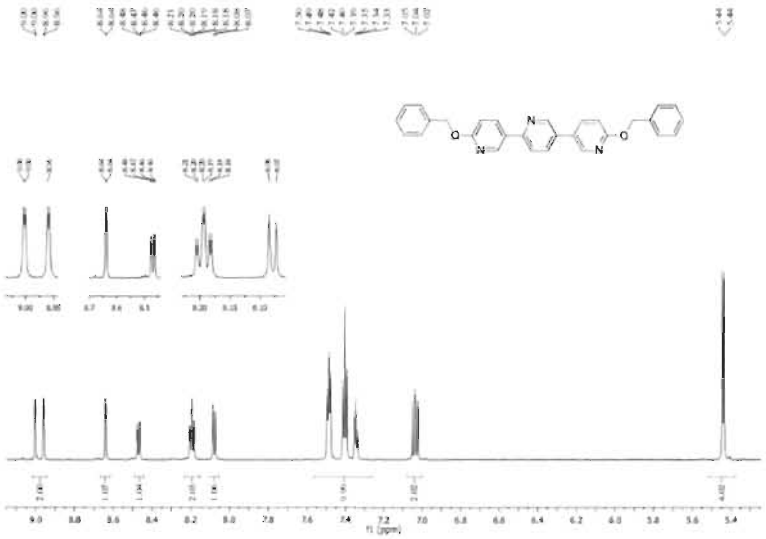

Fig. S5 ^{1}H-NMR spectrum of **3'** recorded in DMSO-d_6 solution.

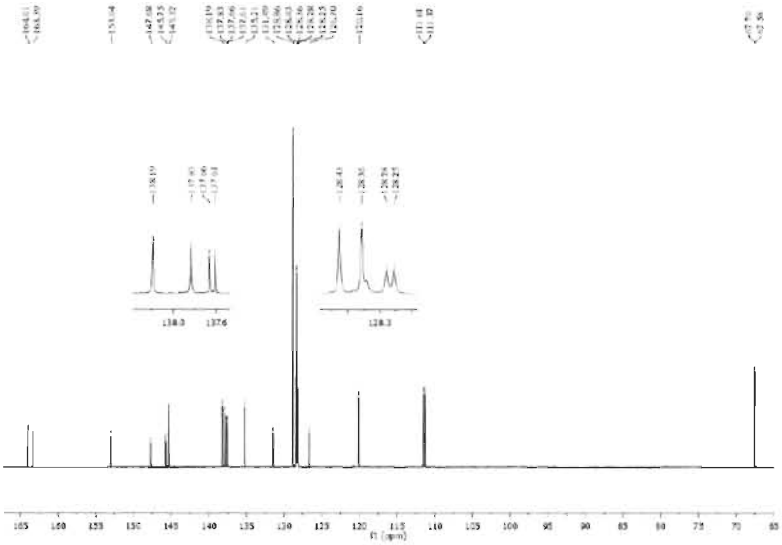

Fig. S6 ^{13}C-NMR spectrum of **3'** recorded in DMSO-d_6 solution.

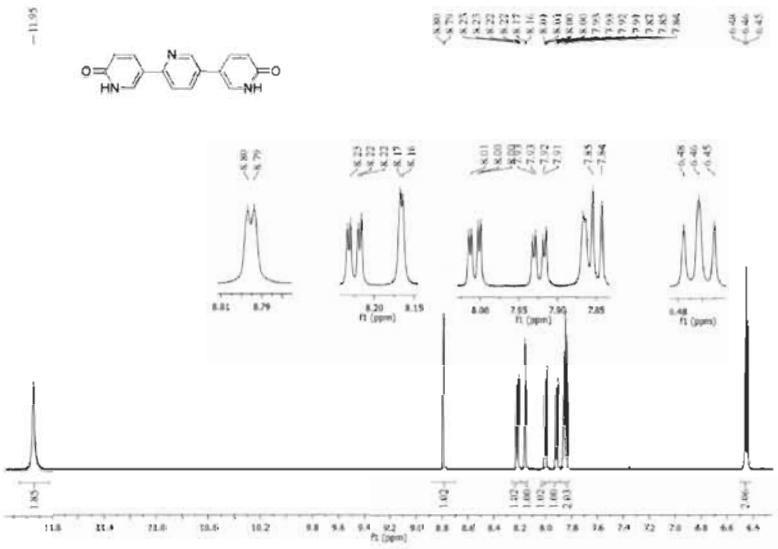

Fig. S7 ^{1}H-NMR spectrum of **3** recorded in DMSO-d_6 solution.

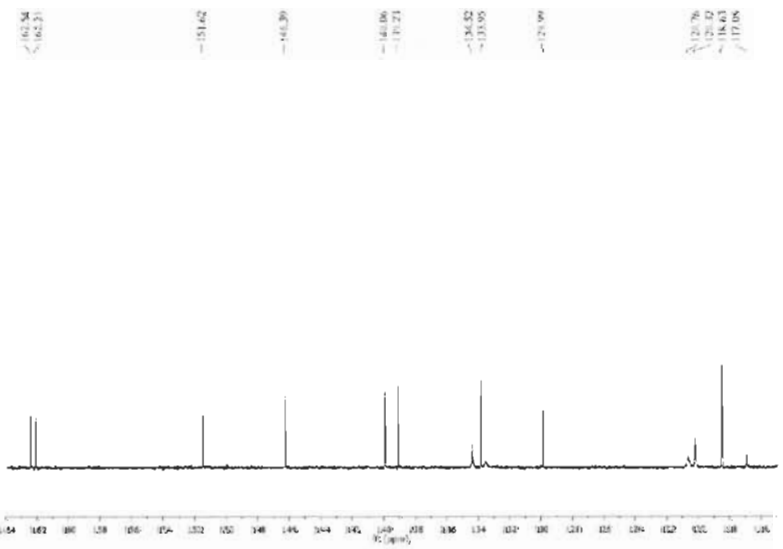

Fig. S8 ^{13}C-NMR spectrum of **3** recorded in DMSO-d_6 solution.

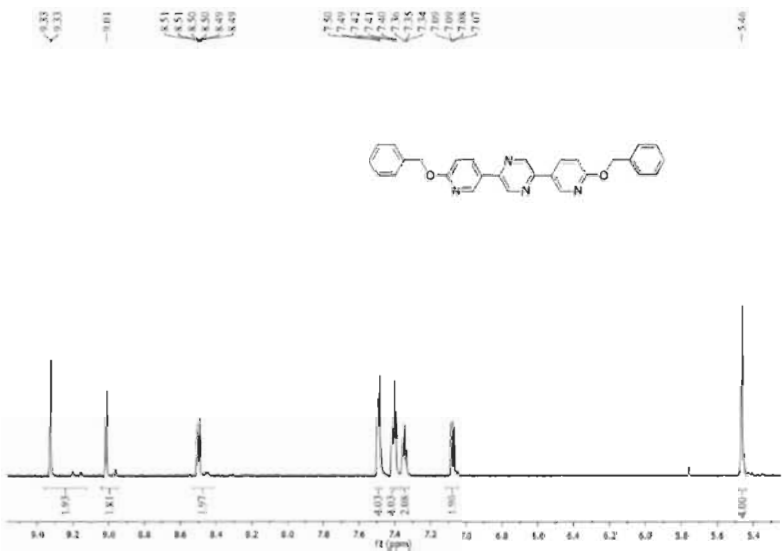

Fig. S ^{1}H-NMR spectrum of **4'** recorded in DMSO-d_6 solution.

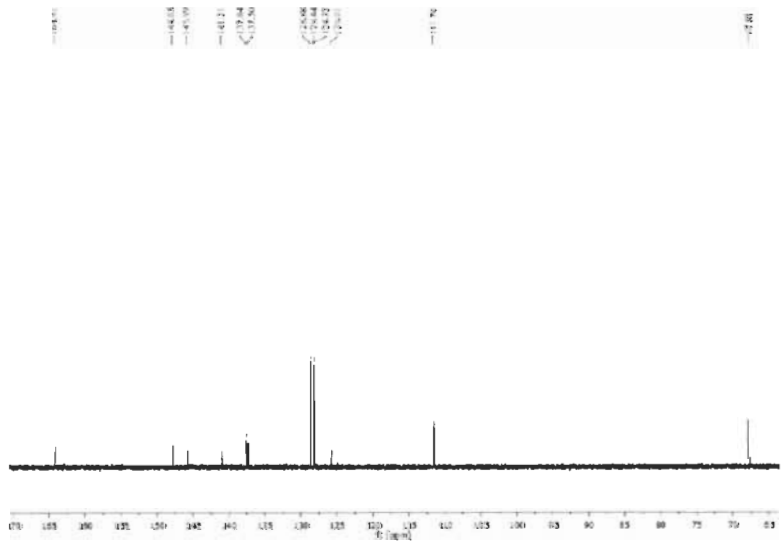

Fig. S10 ^{13}C-NMR spectrum of **4'** recorded in DMSO-d_6 solution.

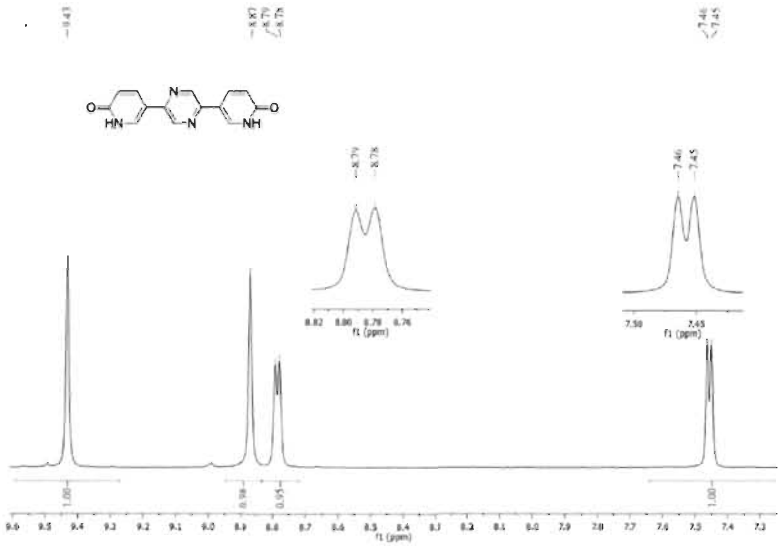

Fig. S11 ^{1}H-NMR spectrum of **4** recorded in TFA-*d* solution.

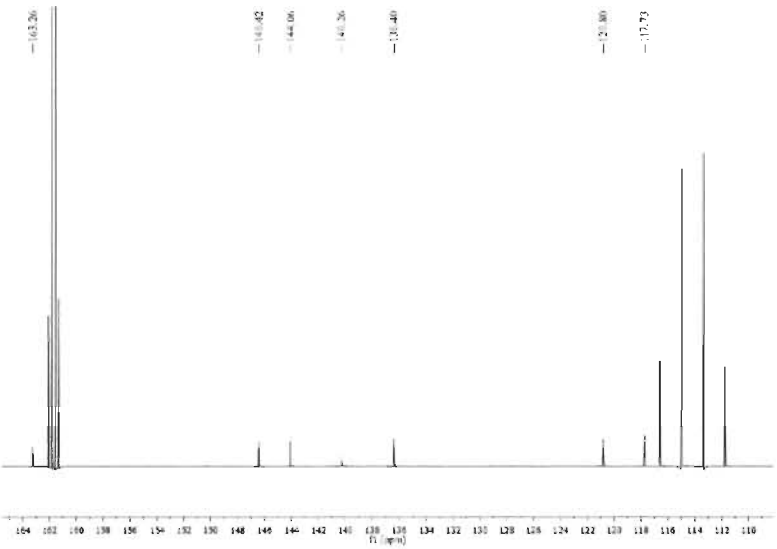

Fig. S12 ^{13}C-NMR spectrum of **4** recorded in TFA-*d* solution.

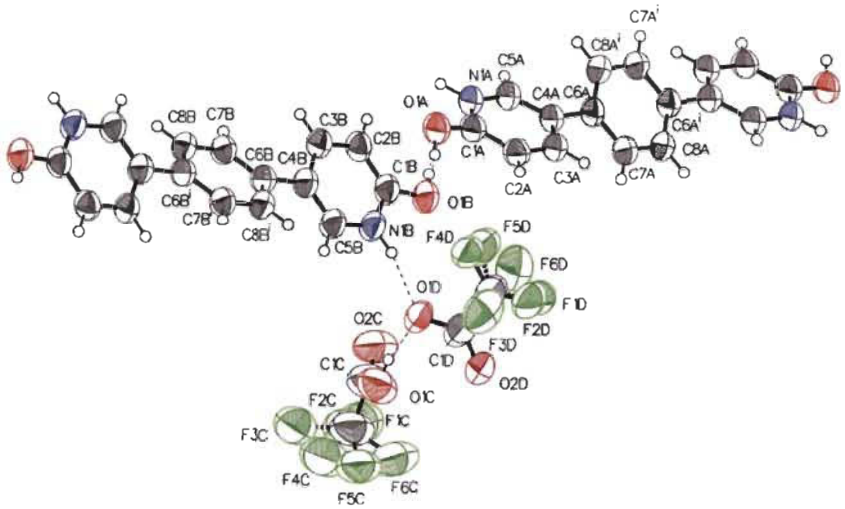

Fig. S13 Thermal atomic displacement ellipsoid plot of **2**. Thermal atomic displacement ellipsoid plot of 2. The ellipsoids of non-hydrogen atoms are drawn at 50% probability level, hydrogen atoms are represented by a sphere of arbitrary size, and hydrogen bonds are represented by dotted lines.

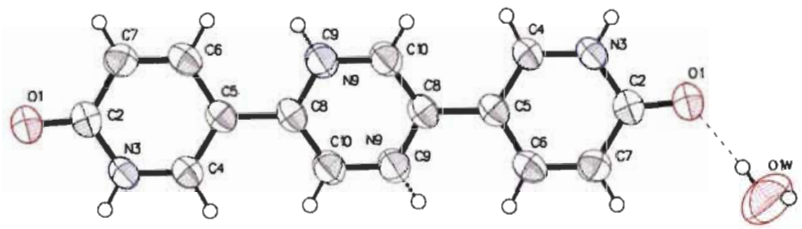

Fig. S14 Thermal atomic displacement ellipsoid plot of **3**. The ellipsoids of non-hydrogen atoms are drawn at 50% probability level, hydrogen atoms are represented by a sphere of arbitrary size, and hydrogen bonds are represented by dotted lines.

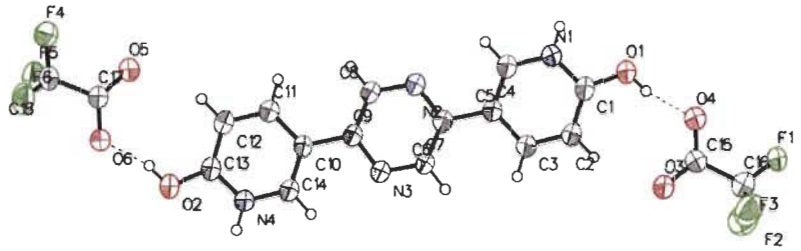

Fig. S15 Thermal atomic displacement ellipsoid plot of **4**. The ellipsoids of non-hydrogen atoms are drawn at 50% probability level, hydrogen atoms are represented by a sphere of arbitrary size, and hydrogen bonds are represented by dotted lines.

Table S1. Hydrogen bond geometry (Å) observed in **2**.

D—*H*···*A*	*D*—*H*	*H*···*A*	*D*···*A*	*D*—*H*···*A*
O1C–H1C···O1D	0.84	1.65	2.474(4)	167.1
O1B–H1B···O1A	0.84	1.59	2.431(3)	175.1
N1B–H1BA···F4D	0.91(3)	2.44(3)	3.011(12)	120.8(19)
N1B–H1BA···O1D	0.91(3)	1.90(3)	2.789(3)	167(2)
O1A–H1A···O1B	0.84	1.61	2.431(3)	164.0
N1A–H1AA···O2D^{i}	0.95(3)	1.84(3)	2.784(3)	173(2)

Symmetry codes: (i) +x, 1+y, +z.

Table S2. Bond angle (°) observed in **2**.

Atom	Atom	Atom	Angle/°
O1C	C1C	C2C	113.7(5)
O2C	C1C	O1C	129.2(5)
O2C	C1C	C2C	117.0(6)
F2C	C2C	F3C	93.6(6)
F2C	C2C	F5C	129.5(8)
F2C	C2C	C1C	117.0(6)
F4C	C2C	F1C	127.2(8)
F4C	C2C	F6C	101.6(7)
F4C	C2C	C1C	121.2(9)
F5C	C2C	F3C	90.0(8)
F5C	C2C	C1C	112.7(6)
F6C	C2C	F1C	80.1(8)
F6C	C2C	C1C	106.9(6)
C1C	C2C	F1C	107.9(7)
C1C	C2C	F3C	95.6(6)
O1D	C1D	C2D	114.7(3)
O2D	C1D	O1D	129.2(4)
O2D	C1D	C2D	116.0(4)

F1D	C2D	F3D	98.9(12)
F1D	C2D	C1D	115.9(11)
F2D	C2D	F4D	121.8(13)
F2D	C2D	C1D	123.1(12)
F2D	C2D	F6D	88.4(13)
F4D	C2D	C1D	114.9(6)
F4D	C2D	F6D	93.7(6)
F5D	C2D	F1D	108.7(13)
F5D	C2D	F3D	104.4(9)
F5D	C2D	C1D	122.7(8)
C1D	C2D	F3D	102.3(4)
C1D	C2D	F6D	92.7(4)
C1B	N1B	C5B	123.6(2)
O1B	C1B	N1B	116.8(2)
O1B	C1B	C2B	126.0(2)
N1B	C1B	C2B	117.1(2)
C3B	C2B	C1B	119.8(2)
C2B	C3B	C4B	121.8(2)
C3B	C4B	C6B	122.0(2)
C5B	C4B	C3B	117.0(2)
C5B	C4B	C6B	121.0(2)
N1B	C5B	C4B	120.6(2)
C7B	C6B	C4B	121.2(2)
C7B	C6B	C8B'	117.9(2)
C8B'	C6B	C4B	120.9(2)
C8B	C7B	C6B	121.2(2)
C7B	C8B	C6B'	120.9(2)
C5A	N1A	C1A	123.1(2)
O1A	C1A	N1A	117.1(2)
O1A	C1A	C2A	126.4(2)
N1A	C1A	C2A	116.5(2)
C3A	C2A	C1A	120.7(2)
C2A	C3A	C4A	121.4(2)
C3A	C4A	C6A	122.1(2)
C5A	C4A	C3A	116.6(2)
C5A	C4A	C6A	121.3(2)
N1A	C5A	C4A	121.8(2)
C7A	C6A	C4A	120.6(2)
C7A	C6A	C8A"	118.4(2)
C8A"	C6A	C4A	121.0(2)
C8A	C7A	C6A	121.3(2)
C7A	C8A	C6A"	120.3(2)

Symmetry codes: (i) -x+3, -y+2, -z+1; (ii) -x, -y+2, -z.

Table S3. Bond length (Å) observed in **2**.

Atom–Atom	Length [Å]	Atom–Atom	Length [Å]
F1C–C2C	1.622(16)	C3B–C4B	1.414(3)
F2C–C2C	1.216(11)	C4B–C5B	1.368(3)
F3C–C2C	1.647(11)	C4B–C6B	1.485(3)
F4C–C2C	1.216(10)	C5B–H5B	0.9500
F5C–C2C	1.265(10)	C6B–C7B	1.395(4)
F6C–C2C	1.428(12)	C6B–C8B^{i}	1.399(4)
O1C–H1C	0.8400	C7B–H7B	0.9500
O1C–C1C	1.309(7)	C7B–C8B	1.379(3)
O2C–C1C	1.184(6)	C8B–H8B	0.9500
C1C–C2C	1.548(8)	O1A–H1A	0.8400
F1D–C2D	1.31(2)	O1A–C1A	1.264(3)
F2D–C2D	1.135(19)	N1A–H1AA	0.95(3)
F3D–C2D	1.739(6)	N1A–C1A	1.365(4)
F4D–C2D	1.315(13)	N1A–C5A	1.354(3)
F5D–C2D	1.266(18)	C1A–C2A	1.412(4)
O1D–C1D	1.252(4)	C2A–H2A	0.9500
O2D–C1D	1.208(4)	C2A–C3A	1.367(3)
C1D–C2D	1.503(7)	C3A–H3A	0.9500
C2D–F6D	1.740(7)	C3A–C4A	1.410(4)
O1B–H1B	0.8400	C4A–C5A	1.372(3)
O1B–C1B	1.289(3)	C4A–C6A	1.485(3)
N1B–H1BA	0.91(3)	C5A–H5A	0.9500
N1B–C1B	1.352(3)	C6A–C7A	1.398(3)
N1B–C5B	1.362(3)	C6A–C8A^{ii}	1.409(3)
C1B–C2B	1.412(4)	C7A–H7A	0.9500
C2B–H2B	0.9500	C7A–C8A	1.387(3)
C2B–C3B	1.361(3)	C8A–H8A	0.9500
C3B–H3B	0.9500		

Symmetry codes: (i) -x+3, -y+2, -z+1; (ii) -x, -y+2, -z.

Table S4. Torsion angles (^{0}) for **2**.

A	B	C	D	Angle/°
O1C	C1C	C2C	F1C	-162.6(7)
O1C	C1C	C2C	F2C	174.8(6)
O1C	C1C	C2C	F3C	77.8(6)
O1C	C1C	C2C	F4C	37.6(11)
O1C	C1C	C2C	F5C	-14.6(12)
O1C	C1C	C2C	F6C	-77.8(9)
O2C	C1C	C2C	F1C	14.9(10)
O2C	C1C	C2C	F2C	-7.7(11)
O2C	C1C	C2C	F3C	-104.6(7)
O2C	C1C	C2C	F4C	-144.8(9)

O2C	C1C	C2C	F5C	163.0(10)
O2C	C1C	C2C	F6C	99.7(8)
O1D	C1D	C2D	F1D	-160.5(14)
O1D	C1D	C2D	F2D	175.2(16)
O1D	C1D	C2D	F3D	93.2(6)
O1D	C1D	C2D	F4D	0.3(10)
O1D	C1D	C2D	F5D	-23.1(13)
O1D	C1D	C2D	F6D	-95.0(6)
O2D	C1D	C2D	F1D	23.8(15)
O2D	C1D	C2D	F2D	-0.5(18)
O2D	C1D	C2D	F3D	-82.6(6)
O2D	C1D	C2D	F4D	-175.4(7)
O2D	C1D	C2D	F5D	161.2(10)
O2D	C1D	C2D	F6D	89.3(6)
O1B	C1B	C2B	C3B	-178.7(2)
N1B	C1B	C2B	C3B	0.0(4)
C1B	N1B	C5B	C4B	-1.0(4)
C1B	C2B	C3B	C4B	0.5(4)
C2B	C3B	C4B	C5B	-1.1(4)
C2B	C3B	C4B	C6B	178.3(2)
C3B	C4B	C5B	N1B	1.4(4)
C3B	C4B	C6B	C7B	29.5(4)
C3B	C4B	C6B	C8B^{i}	-150.3(2)
C4B	C6B	C7B	C8B	179.9(2)
C5B	N1B	C1B	O1B	179.1(2)
C5B	N1B	C1B	C2B	0.3(4)
C5B	C4B	C6B	C7B	-151.1(3)
C5B	C4B	C6B	C8B^{i}	29.1(4)
C6B	C4B	C5B	N1B	-178.0(2)
C6B	C7B	C8B	C6B^{i}	0.3(4)
C8B^{i}	C6B	C7B	C8B	-0.3(4)
O1A	C1A	C2A	C3A	-178.1(2)
N1A	C1A	C2A	C3A	1.5(3)
C1A	N1A	C5A	C4A	-0.7(4)
C1A	C2A	C3A	C4A	-1.0(4)
C2A	C3A	C4A	C5A	-0.4(4)
C2A	C3A	C4A	C6A	-179.0(2)
C3A	C4A	C5A	N1A	1.3(4)
C3A	C4A	C6A	C7A	32.0(3)
C3A	C4A	C6A	C8A^{ii}	-149.9(2)
C4A	C6A	C7A	C8A	178.1(2)
C5A	N1A	C1A	O1A	179.0(2)
C5A	N1A	C1A	C2A	-0.7(3)
C5A	C4A	C6A	C7A	-146.6(3)
C5A	C4A	C6A	C8A^{ii}	31.5(4)
C6A	C4A	C5A	N1A	179.9(2)

13

C6A	C7A	C8A	C6A"	0.0(4)
C8A"	C6A	C7A	C8A	0.0(4)

Symmetry codes: (i) -x+3, -y+2, -z+1; (ii) -x, -y+2, -z.

Table S5. Bond angle (°) observed in **3**.

Atom	Atom	Atom	Angle/°
C9	C10	C8^{i}	122.0(2)
N9	C10	C8^{i}	122.0(2)
O1	C2	N3	119.8(2)
O1	C2	C7	125.4(2)
N3	C2	C7	114.9(2)
C4	N3	C2	124.49(18)
N3	C4	C5	121.3(2)
C4	C5	C6	116.5(2)
C4	C5	C8	121.7(2)
C6	C5	C8	121.79(19)
C7	C6	C5	121.9(2)
C6	C7	C2	121.0(2)
N9	C8	C10^{i}	118.7(2)
C9	C8	C5	118.8(2)
N9	C8	C5	118.8(2)
C10^{i}	C8	C5	122.44(19)
C8	N9	C10	119.3(2)
C8	C9	C10	119.3(2)

Symmetry codes: (i) -x, -y+1, -z+1.

Table S6. Bond length (Å) observed in **3**.

Atom	Atom	Length/Å
O1	C2	1.253(3)
C10	C9	1.361(3)
C10	N9	1.361(3)
C10	C8^{i}	1.383(3)
C2	N3	1.368(3)
C2	C7	1.424(3)
C4	C5	1.364(3)
C5	C6	1.413(3)
C5	C8	1.485(3)
C6	C7	1.357(3)
C8	C9	1.359(3)
C8	N9	1.359(3)

Symmetry codes: (i) -x, -y+1, -z+1.

Table S7. Hydrogen bond geometry (Å,^{0}) observed in **4**.

D—*H*···*A*	*D*—*H*	*H*···*A*	*D*···*A*	*D*—*H*···*A*
O1—H1···O4	0.830(2)	1.669(11)	2.481(3)	165(4)
O2—H2···O6	0.830(2)	1.645(13)	2.454(3)	164(5)
N1—H1A···O3^{i}	0.88	1.83	2.698(3)	170.5
N4—H4···O5^{ii}	0.88	1.94	2.798(3)	163.9

Symmetry codes: (i) -x-1/2, y+1/2, -z+1/2; (ii) -x+3/2, y-1/2, -z+3/2.

Table S8. Bond angle (^{0}) observed in **4**.

Atom	Atom	Atom	Angle/°
C1	N1	C5	123.2(2)
C8	N2	C6	117.0(2)
C7	N3	C9	117.1(2)
C13	N4	C14	123.2(2)
O1	C1	N1	114.7(2)
O1	C1	C2	127.2(2)
N1	C1	C2	118.1(2)
C3	C2	C1	119.6(2)
C2	C3	C4	120.8(3)
C3	C4	C6	123.4(2)
C5	C4	C3	117.2(2)
C5	C4	C6	119.3(2)
N1	C5	C4	121.0(2)
N2	C6	C4	115.9(2)
N2	C6	C7	120.4(2)
C7	C6	C4	123.6(2)
N3	C7	C6	122.7(2)
N2	C8	C9	122.4(2)
N3	C9	C8	120.5(2)
N3	C9	C10	116.0(2)
C8	C9	C10	123.5(2)
C11	C10	C9	123.8(2)
C14	C10	C9	119.0(2)
C14	C10	C11	117.1(2)
C12	C11	C10	121.0(3)
C11	C12	C13	120.0(3)
O2	C13	N4	115.0(2)
O2	C13	C12	127.4(2)
N4	C13	C12	117.6(2)
N4	C14	C10	121.1(2)
O3	C15	O4	128.3(3)
O3	C15	C16	115.2(3)
O4	C15	C16	116.5(3)
F1	C16	C15	117.0(3)
F1	C16	F2	109.3(4)

F1	C16	F3	110.6(4)
F2	C16	C15	108.7(3)
F3	C16	C15	110.1(3)
F3	C16	F2	99.7(4)
F1A	C16	C15	106.9(5)
F2A	C16	C15	107.8(5)
F2A	C16	F1A	97.9(8)
F3A	C16	C15	120.9(5)
F3A	C16	F1A	108.5(9)
F3A	C16	F2A	112.3(9)
O5	C17	O6	129.1(3)
O5	C17	C18	118.0(3)
O6	C17	C18	113.0(2)
F4	C18	C17	112.2(13)
F5	C18	C17	114.7(9)
F5	C18	F4	103.8(15)
F5	C18	F6	109.3(16)
F6	C18	C17	112.0(16)
F6	C18	F4	104.1(17)
F4A	C18	C17	109.8(5)
F5A	C18	C17	111.8(4)
F5A	C18	F4A	109.7(6)
F5A	C18	F6A	109.1(5)
F6A	C18	C17	111.4(3)
F6A	C18	F4A	104.7(4)

Table S9. Bond length (Å) observed in **4**.

Atom	Atom	Length/Å
O1	C1	1.308(3)
O2	C13	1.298(3)
O3	C15	1.215(4)
O4	C15	1.239(3)
O5	C17	1.228(3)
O6	C17	1.254(4)
N1	C1	1.342(3)
N1	C5	1.354(3)
N2	C6	1.341(3)
N2	C8	1.337(3)
N3	C7	1.331(3)
N3	C9	1.340(3)
N4	C13	1.351(3)
N4	C14	1.353(3)
C1	C2	1.388(4)
C2	C3	1.380(4)
C3	C4	1.409(3)
C4	C5	1.359(4)

C4	C6	1.484(3)
C6	C7	1.377(4)
C8	C9	1.380(4)
C9	C10	1.483(3)
C10	C11	1.416(3)
C10	C14	1.363(4)
C11	C12	1.370(4)
C12	C13	1.400(4)
C15	C16	1.535(4)
C16	F1	1.247(4)
C16	F2	1.366(5)
C16	F3	1.344(5)
C16	F1A	1.427(10)
C16	F2A	1.355(10)
C16	F3A	1.119(8)
C17	C18	1.544(4)
C18	F4	1.34(3)
C18	F5	1.164(19)
C18	F6	1.19(3)
C18	F4A	1.396(10)
C18	F5A	1.301(9)
C18	F6A	1.359(8)

Table S10. Torsion Angles (°) observed in **4**.

A	B	C	D	Angle/°
O1	C1	C2	C3	-178.9(3)
O3	C15	C16	F1	-176.4(5)
O3	C15	C16	F2	-52.1(5)
O3	C15	C16	F3	56.2(5)
O3	C15	C16	F1A	127.9(7)
O3	C15	C16	F2A	-127.7(7)
O3	C15	C16	F3A	3.3(12)
O4	C15	C16	F1	2.5(6)
O4	C15	C16	F2	126.8(4)
O4	C15	C16	F3	-124.9(4)
O4	C15	C16	F1A	-53.2(7)
O4	C15	C16	F2A	51.2(8)
O4	C15	C16	F3A	-177.8(11)
O5	C17	C18	F4	-10.2(11)
O5	C17	C18	F5	107.9(13)
O5	C17	C18	F6	-126.8(14)
O5	C17	C18	F4A	-112.2(5)
O5	C17	C18	F5A	9.8(8)
O5	C17	C18	F6A	132.3(5)
O6	C17	C18	F4	168.9(10)
O6	C17	C18	F5	-73.0(13)

O6	C17	C18	F6	52.3(15)
O6	C17	C18	F4A	66.9(5)
O6	C17	C18	F5A	-171.1(8)
O6	C17	C18	F6A	-48.6(6)
N1	C1	C2	C3	0.1(5)
N2	C6	C7	N3	0.7(5)
N2	C8	C9	N3	-1.2(5)
N2	C8	C9	C10	179.1(3)
N3	C9	C10	C11	-176.3(3)
N3	C9	C10	C14	5.5(4)
C1	N1	C5	C4	0.9(5)
C1	C2	C3	C4	0.5(5)
C2	C3	C4	C5	-0.4(4)
C2	C3	C4	C6	177.2(3)
C3	C4	C5	N1	-0.3(4)
C3	C4	C6	N2	174.1(3)
C3	C4	C6	C7	-8.1(5)
C4	C6	C7	N3	-177.0(3)
C5	N1	C1	O1	178.3(3)
C5	N1	C1	C2	-0.8(5)
C5	C4	C6	N2	-8.3(4)
C5	C4	C6	C7	169.5(3)
C6	N2	C8	C9	0.5(4)
C6	C4	C5	N1	-178.0(3)
C7	N3	C9	C8	1.6(4)
C7	N3	C9	C10	-178.7(3)
C8	N2	C6	C4	177.7(2)
C8	N2	C6	C7	-0.2(4)
C8	C9	C10	C11	3.4(5)
C8	C9	C10	C14	-174.7(3)
C9	N3	C7	C6	-1.4(5)
C9	C10	C11	C12	-179.2(3)
C9	C10	C14	N4	179.4(2)
C10	C11	C12	C13	1.0(5)
C11	C10	C14	N4	1.1(4)
C11	C12	C13	O2	178.9(3)
C11	C12	C13	N4	-1.0(5)
C13	N4	C14	C10	-1.3(4)
C14	N4	C13	O2	-178.8(3)
C14	N4	C13	C12	1.2(4)
C14	C10	C11	C12	-1.0(4)

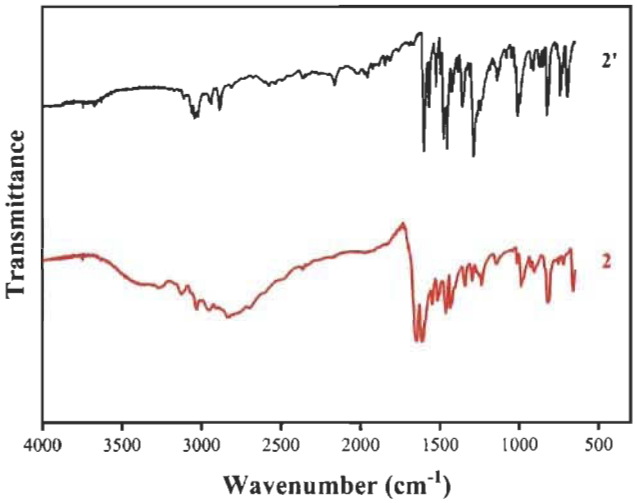

Fig. S16 FTIR of compounds **2'** (black) and **2** (red).

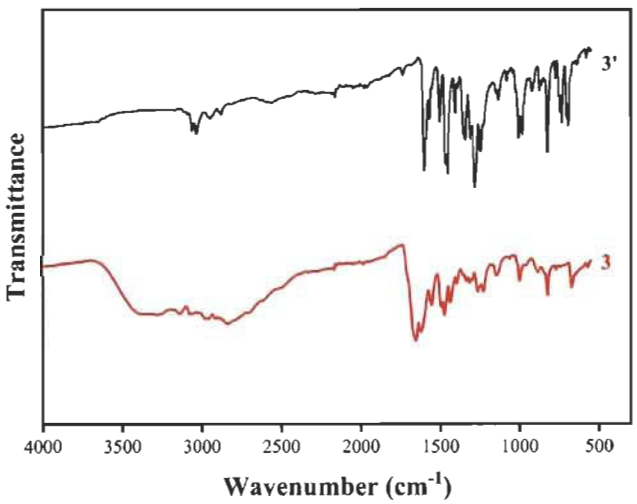

Fig. S17 FTIR of compounds **3'** (black) and **3** (red).

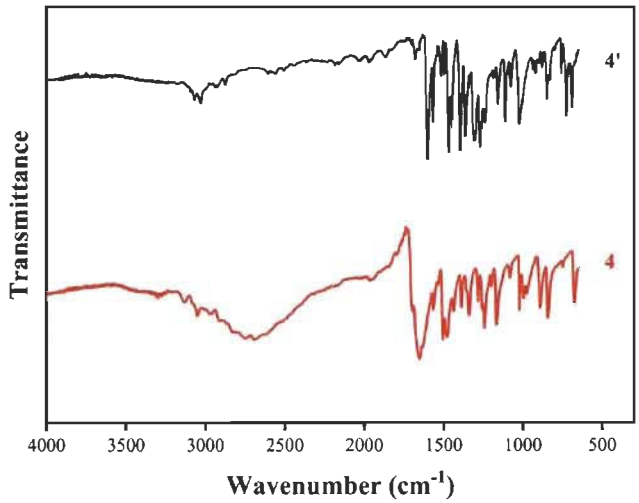

Fig. S18 FTIR of compounds **4'** (black) and **4** (red).

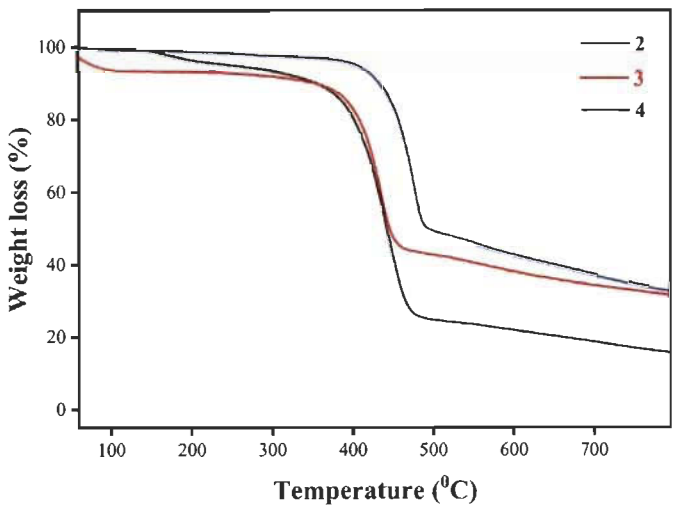

Fig. S19 TGA of compounds **2-4**.

Appendix 2: Supplementary Information for Article 2

Supplementary Information

Intercalated 2D+2D hydrogen-bonded sheets in co-crystals of cobalt salt with 1*H*,1'*H*-[3,3']bipyridinyl-6,6'-dione

Midhun Mohan,[a] Love Karan Rana,[a] Thierry Maris[b] and Adam Duong[*,a]*

[a]Département de Chimie, Biochimie et physique and Institut de Recherche sur l'Hydrogène, Université du Québec à Trois-Rivières, Trois-Rivières, Québec, G9A 5H7, Canada.

[b]Département de Chimie, Université de Montréal, Montréal, Québec, H3C 3J7, Canada.

Supplementary Information

*To whom correspondence should be addressed. E-mail: adam.duong@uqtr.ca

Contents **Pages**

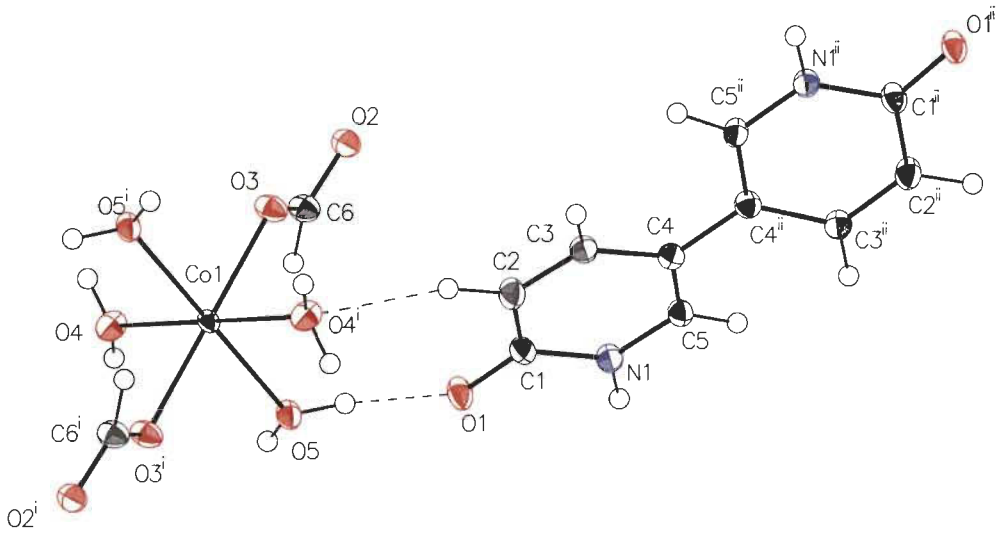

Figure S1. Thermal atomic displacement ellipsoid plot of **1**•$Co(CHOO)_2(H_2O)_4$ crystallized in EtOH/DMF at 80 °C. The ellipsoids of non-hydrogen atoms are drawn at 50% probability level, hydrogen atoms are represented by a sphere of arbitrary size.

Table S1. Crsytallographic data of **1**•$Co(CHOO)_2(H_2O)_4$

	1•$Co(CHOO)_2(H_2O)_4$
Formula	$Co_4C_{48}H_{72}N_8O_{40}$
Crystal System	Monoclinic
Mr	409.21
T (K)	100
Radiation	CuKα
λ (Å)	1.54178
F (000)	844
Space group	C2/c
a (Å)	25.6206(5)
b (Å)	6.78540(10)
c (Å)	9.7945(2)
α (deg)	90
β (deg)	109.4190(10)
γ (deg)	90
V (Å^3)	1605.87()
Z	4
ρ_{calcd} (g cm^{-3})	1.693
μ (mm^{-1})	8.936
No. measured reflections	10162
No. independent reflections	1559
No. obsd. reflections I>2σ(I)	1559
Nb Params	151
R_1, I>2σ (%)	0.0253
R_1, all data (%)	0.0287
ωR_2, I>2σ(I) (%)	0.0684
ωR_2, all data (%)	0.0712
GoF	1.091

Table S2. Hydrogen bond geometry (Å, °) of **1**•$Co(CHOO)_2(H_2O)_4$

D—H···*A*	*D*—H	H···*A*	*D*···*A*	*D*—H···*A*
O4—H4*A*···O2^{i}	0.81 (3)	1.96 (3)	2.7617 (17)	170 (2)
O4—H4*B*···O3^{ii}	0.83 (3)	1.87 (3)	2.6945 (16)	175 (2)
O5—H5*A*···O1	0.88 (3)	1.83 (3)	2.7065 (18)	172 (2)
O5—H5*B*···O2^{ii}	0.79 (3)	1.97 (3)	2.7515 (18)	172 (2)
C5—H5···O2^{iii}	0.97 (2)	2.39 (2)	3.353 (2)	172.2 (14)
C2—H2···O4^{iv}	1.01 (2)	2.51 (2)	3.486 (2)	161.9 (16)
N1—H1···O1^{v}	0.95 (3)	1.86 (3)	2.807 (2)	174 (2)

Symmetry codes: (i) $-x+3/2, -y+1/2, -z+1$; (ii) $x, -y+1, z-1/2$; (iii) $-x+1, -y+1, -z+1$; (iv) $-x+3/2, -y+3/2, -z+1$; (v) $-x+1, y, -z+1/2$.

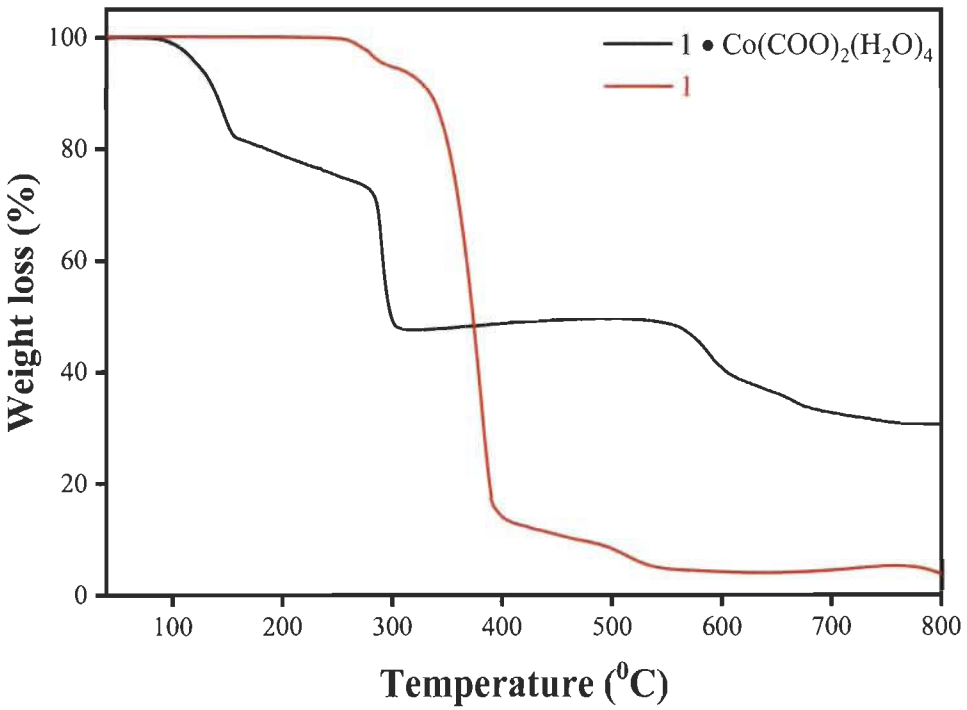

Figure S2. Comparison of TG curves of compound 1 (red) and **1**•$Co(CHOO)_2(H_2O)_4$ (black).

Appendix 3: Supplementary Information for Article 3

Electronic Supplementary Material (ESI) for CrystEngComm.

Electronic Supplementary Information (ESI†)

Building Coordination Polymers using Dipyridone Ligands

Midhun Mohan,[a] Thierry Maris[b] and Adam Duong*[,a]

[a]*Département de Chimie, Biochimie et physique* and *Institut de Recherche sur l'Hydrogène,* Université du Québec à Trois-Rivières, Trois-Rivières, Québec, G9A 5H7, Canada
[b]*Département de Chimie,* Université de Montréal, Montréal, Québec, H3C 3J7, Canada

Supplementary Information

*To whom correspondence should be addressed. E-mail: adam.duong@uqtr.ca

Contents **Pages**

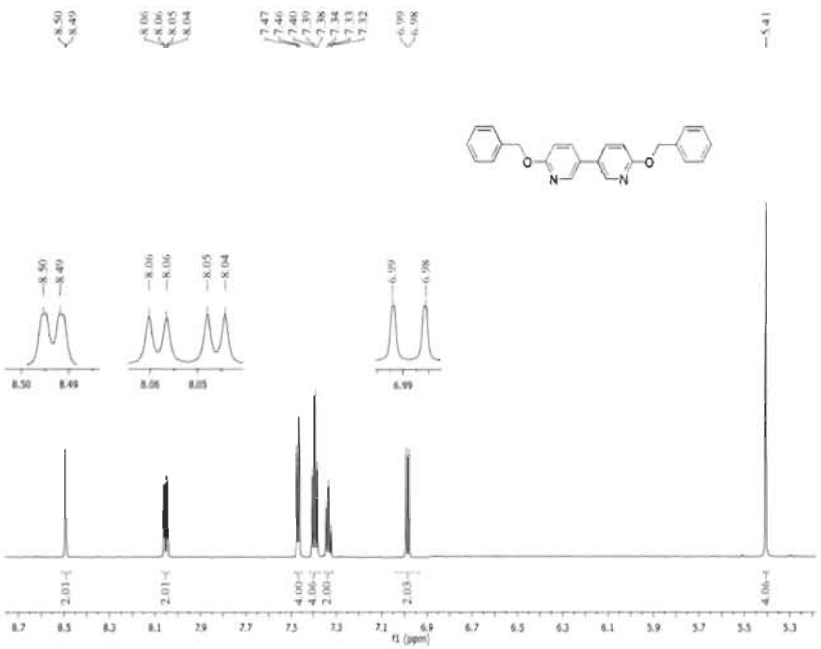

Fig. S1. ^{1}H-NMR spectrum of **2** recorded in DMSO-d_6 solution.

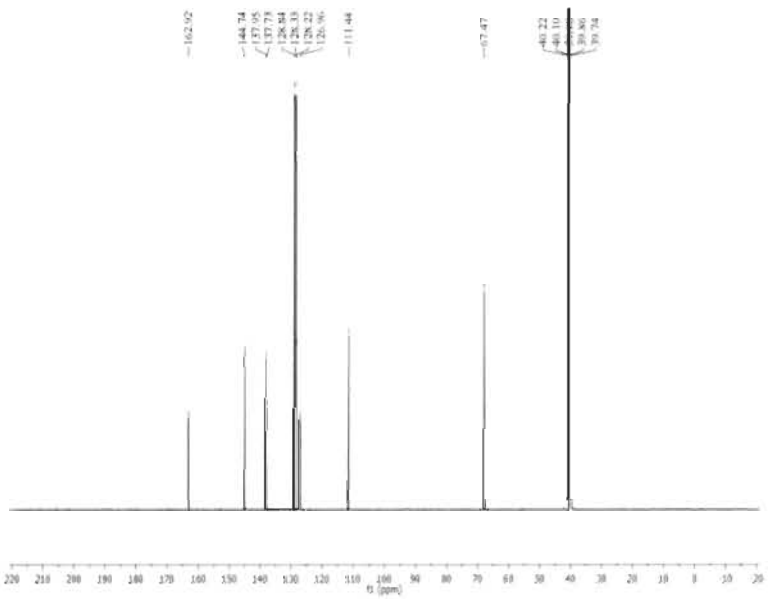

Fig. S2. ^{13}C-NMR spectrum of **2** recorded in DMSO-d_6 solution.

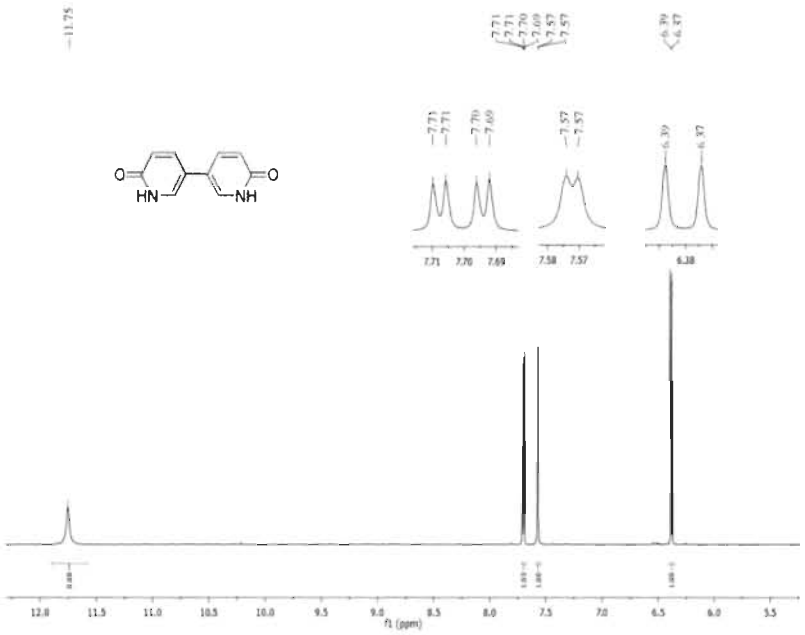

Fig. S3. ^{1}H-NMR spectrum of **1** recorded in DMSO-d_6 solution.

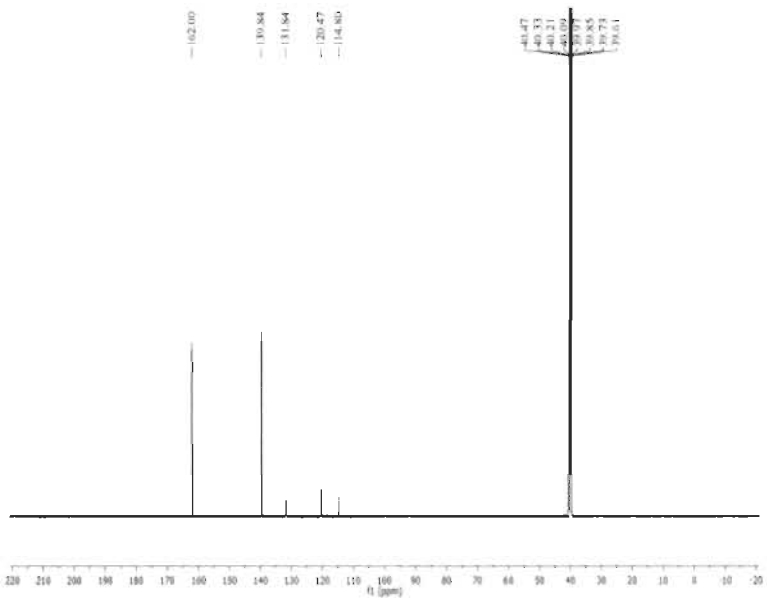

Fig. S4. ^{13}C-NMR spectrum of **1** recorded in DMSO-d_6 solution.

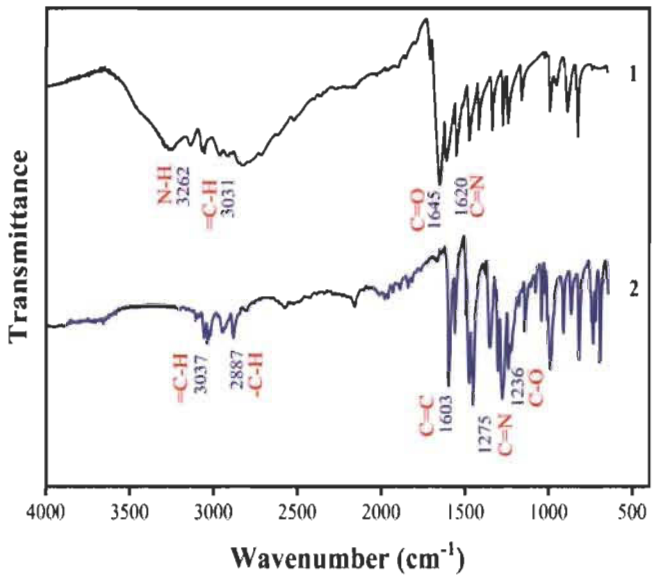

Fig S5. FTIR of compounds **1** (black) and **2** (blue).

Crystallographic data

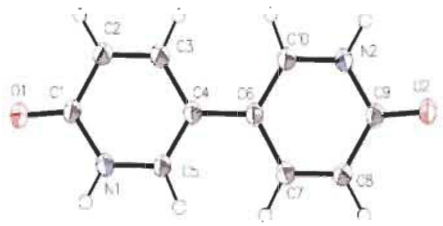

Fig. S6 Thermal atomic displacement ellipsoid plot of **1a** crystallized at 80 °C in EtOH/DMF. The ellipsoids of non-hydrogen atoms are drawn at 50% probability level, hydrogen atoms are represented by a sphere of arbitrary size.

Table S1. Hydrogen bond geometry (Å, °) of **1a** crystallized in EtOH/DMF

D—H···*A*	*D*—H	H···*A*	*D*···*A*	*D*—H···*A*
N1—H1···O2^{i}	0.941 (19)	1.800 (19)	2.7287 (14)	168.6 (17)
N2—H2···O1^{ii}	0.963 (19)	1.764 (19)	2.7053 (14)	164.7 (16)

Symmetry codes: (i) −*x*+3/2, *y*+1/2, −*z*+3/2; (ii) −*x*+3/2, *y*−1/2, −*z*+1/2.

a

Fig. S7 Thermal atomic displacement ellipsoid plot of **1b** crystallized in DMSO/H_2O. The ellipsoids of non-hydrogen atoms are drawn at 50% probability level, hydrogen atoms are represented by a sphere of arbitrary size.

Table S2. Hydrogen bond geometry (Å, °) of **1b** crystallized in DMSO/H_2O

D—H···*A*	*D*—H	H···*A*	*D*···*A*	*D*—H···*A*
N1—H1···O1^{i}	0.79 (5)	2.00 (5)	2.782 (5)	174 (4)
O2—H2*A*···O2^{ii}	0.87 (1)	1.94 (1)	2.788 (5)	166 (5)
O2—H2*B*···O1	0.87 (1)	1.91 (2)	2.753 (4)	164 (6)

Symmetry codes: (i) −x+1, −y, −z+1; (ii) −x+1/2, y+1/2, −z+1/2.

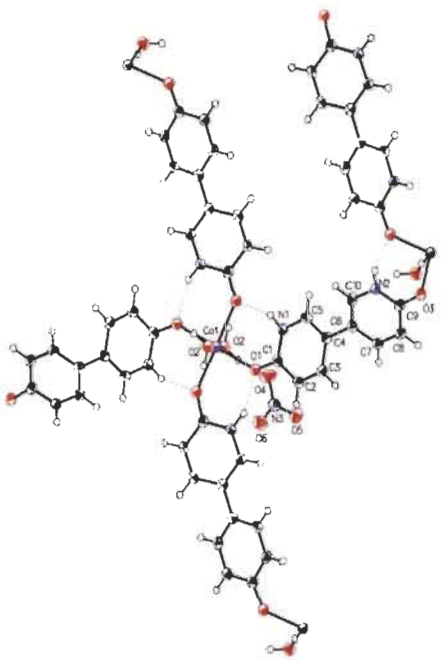

Fig. S8 Thermal atomic displacement ellipsoid plot of **CP-671** crystallized at 80 °C in EtOH/DMF. The ellipsoids of non-hydrogen atoms are drawn at 50% probability level, hydrogen atoms are represented by a sphere of arbitrary size, and hydrogen bonds are represented by dotted lines.

Table S3. Hydrogen bond geometry (Å, °) observed in **CP-671**

D—H···*A*	*D*—H	H···*A*	*D*···*A*	*D*—H···*A*
N1—H1···O3^{i}	0.88	1.89	2.720 (4)	157
C2—H2···O5^{ii}	0.95	2.38	3.278 (6)	158
O2—H2*A*···O4	0.89	1.85	2.690 (5)	158
O2—H2*B*···O4^{iii}	0.88	1.85	2.692 (5)	159
N2—H2*C*···O1^{iv}	0.88	1.94	2.759 (5)	154
C5—H5···O6^{v}	0.95	2.36	3.295 (6)	167
C8—H8···O6^{vi}	0.95	2.54	3.309 (6)	138
C10—H10···O5^{v}	0.95	2.39	3.304 (6)	162

Symmetry codes: (i) *x*, −*y*+3/2, *z*+1/2; (ii) *x*+1/2, *y*, −*z*+1/2; (iii) −*x*+1, −*y*+1, −*z*+1; (iv) −*x*+2, *y*+1/2, −*z*+1/2; (v) −*x*+3/2, *y*+1/2, *z*; (vi) −*x*+3/2, −*y*+1, *z*−1/2.

Table S4. Bond angles (°) observed in **CP-671**

Atoms	Angle (°)	Atoms	Angle (°)
O1^{i} Co1 O1	180.0	C3 C2 C1	120.4 (5)
O2 Co1 O1^{i}	89.51 (12)	C10 N2 C9	124.7 (4)
O2^{i} Co1 O1	89.51 (12)	C4 C3 C2	122.1 (5)
O2 Co1 O1	90.49 (12)	C9 O3 Co1^{iv}	137.5 (3)
O2^{i} Co1 O1^{i}	90.49 (12)	C5 C4 C3	116.4 (4)
O2^{i} Co1 O2	180.0	C6 C4 C3	121.3 (4)
O3^{ii} Co1 O1	90.49 (12)	C6 C4 C5	122.3 (4)
O3^{ii} Co1 O1^{i}	89.51 (12)	C4 C5 N1	121.3 (4)
O3^{iii} Co1 O1^{i}	90.49 (12)	C7 C6 C4	1208 (4)
O3^{iii} Co1 O1	89.51 (12)	C10 C6 C4	122.1 (4)
O3^{ii} Co1 O2^{i}	90.44 (13)	C10 C6 C7	117.1 (4)
O3^{ii} Co1 O2	89.56 (13)	C8 C7 C6	120.9 (4)
O3^{iii} Co1 O2^{i}	89.56 (13)	C9 C8 C7	120.7 (4)
O3^{iii} Co1 O2	90.44 (13)	O3 C9 N2	120.0 (4)
O3^{ii} Co1 O3^{iii}	180.0	C8 C9 N2	116.0 (4)
N1 C1 O1	119.8 (4)	C8 C9 O3	124.0 (4)
C2 C1 O1	124.5 (5)	C6 C10 N2	120.6 (4)
C2 C1 N1	115.7 (4)	O5 N3 O4	119.2 (4)
C1 O1 Co1^{i}	133.6 (3)	O6 N3 O4	118.7 (4)
C5 N1 C1	124.1 (4)	O6 N3 O5	122.1 (4)

Symmetry codes: (i) -x+2, −y+1, -z+1; (ii) x, -y+3/2, z+1/2; (iii) −x+2, y-1/2, −z+1/2; (iv) −x+2, y+1/2, −z+1/2.

Table S5. Bond lengths (Å) observed in **CP-671**

Atoms	Bond Lengths (Å)	Atoms	Bond Lengths (Å)
Co1 O1	2.109 (3)	N2 C10	1.354 (6)
Co1 O1^{i}	2.109 (3)	C3 C4	1.408 (7)
Co1 O2	2.044 (3)	O3 C9	1.278 (5)
Co1 O2^{i}	2.044 (3)	C4 C5	1.367 (6)
Co1 O3^{ii}	2.118 (3)	C4 C6	1.481 (6)
Co1 O3^{iii}	2.118 (3)	C6 C7	1.425 (6)
C1 O1	1.270 (5)	C6 C10	1.360 (6)
C1 N1	1.368 (6)	C7 C8	1.363 (7)
C1 C2	1.413 (7)	C8 C9	1.411 (7)
N1 C5	1.357 (6)	N3 O4	1.263 (5)
C2 C3	1.370 (7)	N3 O5	1.240 (5)
N2 C9	1.352 (6)	N3 O6	1.235 (5)

Symmetry codes: (i) -x+2, -y+1, -z+1; (ii) x, -y+3/2, z+1/2; (iii) -x+2, y-1/2, -z+1/2.

Additional SEM images

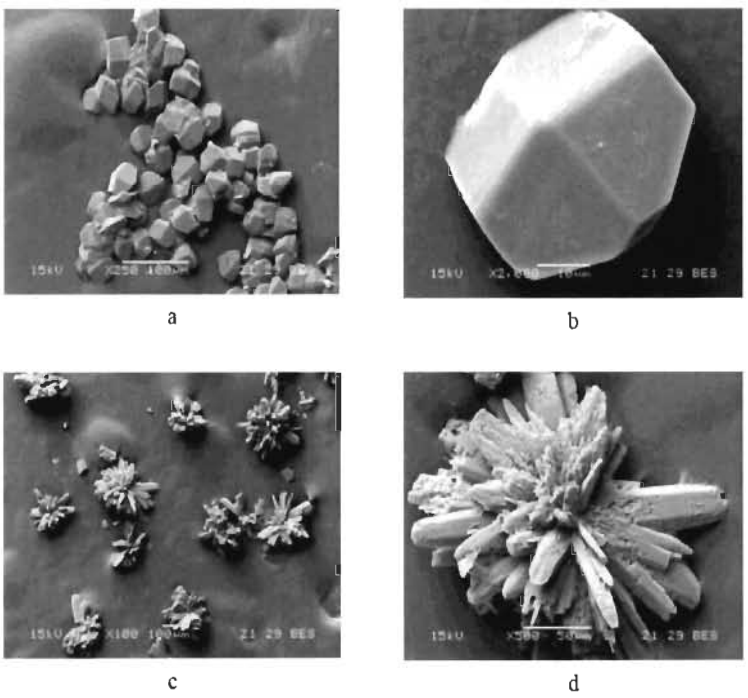

a b c d

Fig. S9 (a), (c) SEM images of **1a** and **CP-671** respectively and (b), (d) Crystal morphologies of **1a** and **CP-671** respectively.

Appendix 4: Supplementary Information for Article 4

Electronic Supplementary Material (ESI) for Dalton Transactions.

Syntheses of Mono and Bimetallic Cyamelurate Polymers with Reversible Chromic Behaviour

Midhun Mohan,[a] Sanil Rajak,[a] Alexandre A. Tremblay,[a] Thierry Maris[b] and Adam Duong*[,a]

[a] *Département de Chimie, Biochimie et physique* and *Institut de Recherche sur l'Hydrogène,* Université du Québec à Trois-Rivières, Trois-Rivières, Québec, G9A 5H7, Canada
[b] *Département de Chimie,* Université de Montréal, Montréal, Québec, H3C 3J7, Canada

*To whom correspondence should be addressed. E-mail : adam.duong@uqtr.ca

Contents **Pages**

Experimental Section

General notes. Potassium cyamelurate K_3L was synthesized by known reported methods. All chemicals and solvents were purchased from commercial sources and were used without further purification.

General procedure for preparing MOPs-(1-4). Aqueous solutions of 0.1 mmol of potassium cyamelurate (6 mL) and 0.6 mmol of metal salt ($MnSO_4$, $Co(NO_3)_2.6H_2O$, $Ni(NO_3)_2.6H_2O$ or $Zn(NO_3)_2.6H_2O$) (6 mL) were mixed together at room temperature. The mixture was stirred for 2 h and then kept at room temperature for 12 h. Crystalline samples of MOPs-(**1-4**) were collected by filtration.

MOP-1. Amber crystal, yield 91 %. IR(ATR) 3546, 3348, 3240, 2970, 2797, 1678, 1637, 1454, 1439, 1401, 1369, 1331, 1316, 1198, 1148, 1124, 978, 963, 832, 798, 760 cm^{-1}. Anal. Calcd for $Mn_2(C_6N_7O_3H)_2.10H_2O$: C, 19.71; H, 2.95; N, 26.28. Found: C, 19.74; H, 3.31, N, 26.85.

MOP-2. Pink crystal, yield 82 %. IR(ATR) 3566, 3462, 3190, 2946, 2797, 1681, 1621, 1487, 1439, 1401, 1369, 1331, 1313, 1204, 1148, 1129, 978, 963, 832, 798, 957, 707, 692 cm^{-1}. Anal. Calcd for $Co_2(C_6N_7O_3H)_2.10H_2O$: C, 19.53; H, 2.97; N, 26.03. Found: C, 19.52; H, 3.28; N, 26.56.

MOP-3. Cyan crystal, yield 80 %. IR(ATR) 3573, 3472, 3198, 2946, 2797, 1681, 1487, 1436, 1403, 1369, 1331, 1315, 1205, 1169, 1148, 1124, 978, 965, 832, 799, 789, 757, 710, 695 cm^{-1}. Anal. Calcd for $Ni_2(C_6N_7O_3H)_2.10H_2O$: C, 19.22; H, 2.79; N, 25.76. Found: C, 19.12; H, 3.21; N, 26.01.

MOP-4. Colourless crystal, yield 80 % based on metal salt. IR(ATR) 3390, 3147, 2958, 2797, 1681, 1597, 1516, 1487, 1455, 1403, 1369, 1329, 1315, 1201, 1194, 1161, 1148, 1124, 978, 965,849, 832, 799, 762, 716, 692 cm^{-1}: Anal. Calcd for $Zn_2(C_6N_7O_3H)_2.10H_2O$: C, 20.28; H, 2.66; N, 25.26. Found: C, 19.24, H 2.96, N 26.17.

General procedure for preparing MMOPs-(5-7). Aqueous solutions of 0.1 mmol of potassium cyamelurate (6 mL) and 0.3 mmol equimolar ratio of the two metals salts (A/B =

$Mn(SO_4)/Co(NO_3)_2.6H_2O$, $Mn(SO_4)/Ni(NO_3)_2.6H_2O$, or $Ni(NO_3)_2.6H_2O/Zn(NO_3)_2.6H_2O$) (6 mL) were mixed together at room temperature. The mixture was stirred for 2 h and then kept at room temperature for 12 h. Crystalline samples of MMOPs-(**5**-**7**) were collected by filtration.

MMOP-5. Pink crystal, yield 89 %. IR(ATR) 3567, 3459, 3216, 2964, 2749, 1699, 1682, 1634, 1488, 1455, 1435, 1404, 1369, 1331, 1315, 1201, 1161, 1148, 1125, 1125, 977, 964, 832, 799, 788, 761, 709, 691 cm^{-1}. Anal. Calcd for $Mn_{0.26}Co_{1.74}(C_6N_7O_3H)_2.10H_2O$: C, 19.83; H, 3.11; N, 26.32. Found: C, 19.68; H, 3.03, N, 26.78.

MMOP-6. Cyan crystal, yield 90 %. IR(ATR) 3565, 3462, 3207, 2958, 2793, 1682, 1635, 1489, 1454, 1438, 1403, 1369, 1329, 1316, 1202, 1163, 1148, 1126, 978, 964, 833, 799, 787, 760, 709, 693 cm^{-1}. Anal. Calcd for $Mn_{0.32}Ni_{1.68}(C_6N_7O_3H)_2.10H_2O$: C, 19.64; H, 2.99; N, 26.52. Found: C, 19.69; H, 3.03, N, 26.79.

MMOP-7. Cyan crystal, yield 80 %. IR(ATR) 3564, 3463, 3192, 2934, 2790, 1682, 1633, 1489, 1455, 1438, 1402, 1368, 1330, 1315, 1204, 1163, 1148, 1126, 979, 966, 833, 800, 788, 767, 759, 708, 694 cm^{-1}. Anal. Calcd for $Ni_{1.41}Zn_{0.59}(C_6N_7O_3H)_2.10H_2O$: C, 19.43; H, 2.96; N, 26.06. Found: C, 19.41; H, 2.99, N, 26.41.

Studies of Single-Crystal Structures of Metal-Organic Polymers (1-4) and Mixed Metal-Organic Polymers (5-7)

The position of hydrogen atoms in the structures of MOPs-(**1**-**4**) are fully refined and determined using the difference Fourier map. For MOP-**1**, MOP-**2** and MOP-**4**, the first 11 Q peaks with electron density maxima appearing in the map correspond exactly to the position of the 11 hydrogen atoms in the asymmetric unit. For MOP-**3**, due to residual electron density around the Ni atom from absorption the Q peaks of all hydrogen atoms are not all in the first 11. For each difference Fourier map of MOPs-(**1**-**4**), notice that one of the Q peak is closer to the nitrogen atom of the heptazine confirming the presence of N-H group in the structures.

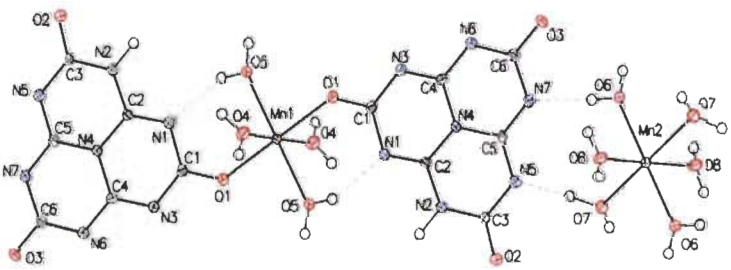

Figure S1. Thermal atomic displacement ellipsoid plot of MOP-**1**. The ellipsoids of non-hydrogen atoms are drawn at 50% probability level, hydrogen atoms are represented by a sphere of arbitrary size, and hydrogen bonds are represented by dotted lines.

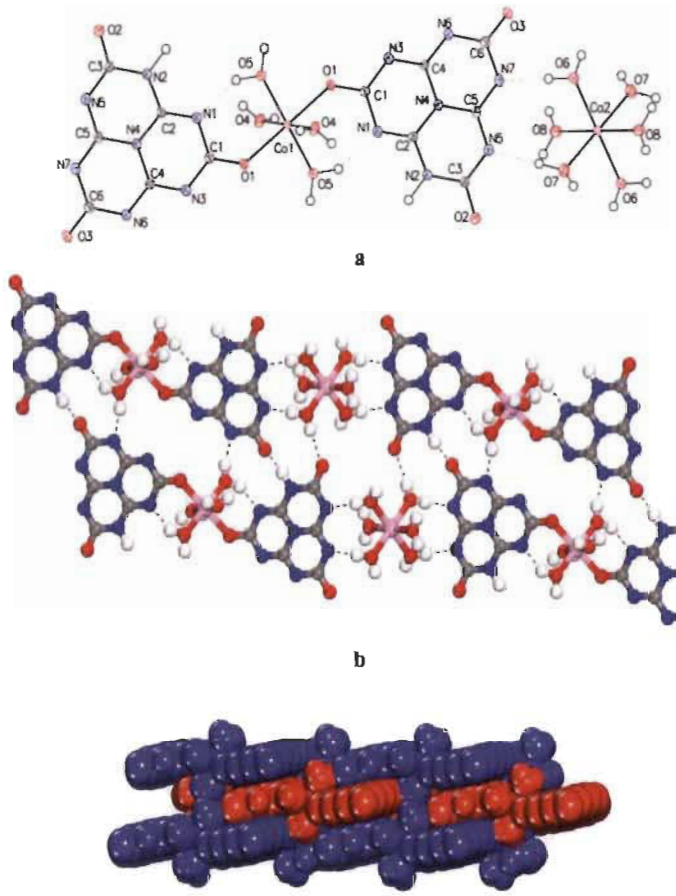

Figure S2. Crystal structure of MOP-2. a) Thermal atomic displacement ellipsoid plot of MOP-2. The ellipsoids of non-hydrogen atoms are drawn at 50% probability level, hydrogen atoms are represented by a sphere of arbitrary size, and hydrogen bonds are represented by dotted lines. b) View of the 2D sheets connected by coordination bonds and hydrogen bonds. Hydrogen bonds are represented in dotted lines, and cobalt atoms are shown in pink, carbon atoms in grey, hydrogen atoms in white, nitrogen atoms in blue, and oxygen atoms in red. c) Packing of the 2D sheets to form the three-dimensional structure. For more clarity layers marked in red and blue.

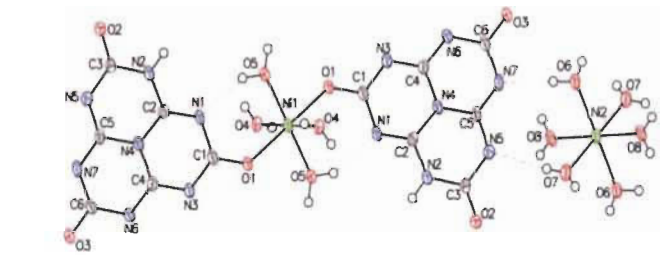

a

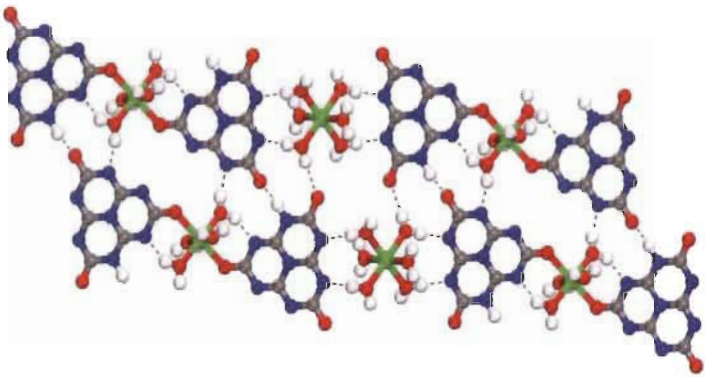

b

c

Figure S3. Crystal structure of MOP-**3**. a) Thermal atomic displacement ellipsoid plot of MOP-**3**. The ellipsoids of non-hydrogen atoms are drawn at 50% probability level, hydrogen atoms are represented by a sphere of arbitrary size, and hydrogen bonds are represented by dotted lines. b) View of the 2D sheets connected by coordination bonds and hydrogen bonds. Hydrogen bonds are represented in dotted lines, and nickel atoms are shown in green, carbon atoms in grey, hydrogen atoms in white, nitrogen atoms in blue, and oxygen atoms in red. c) Packing of the 2D sheets to form the three-dimensional structure. For more clarity layers marked in red and blue.

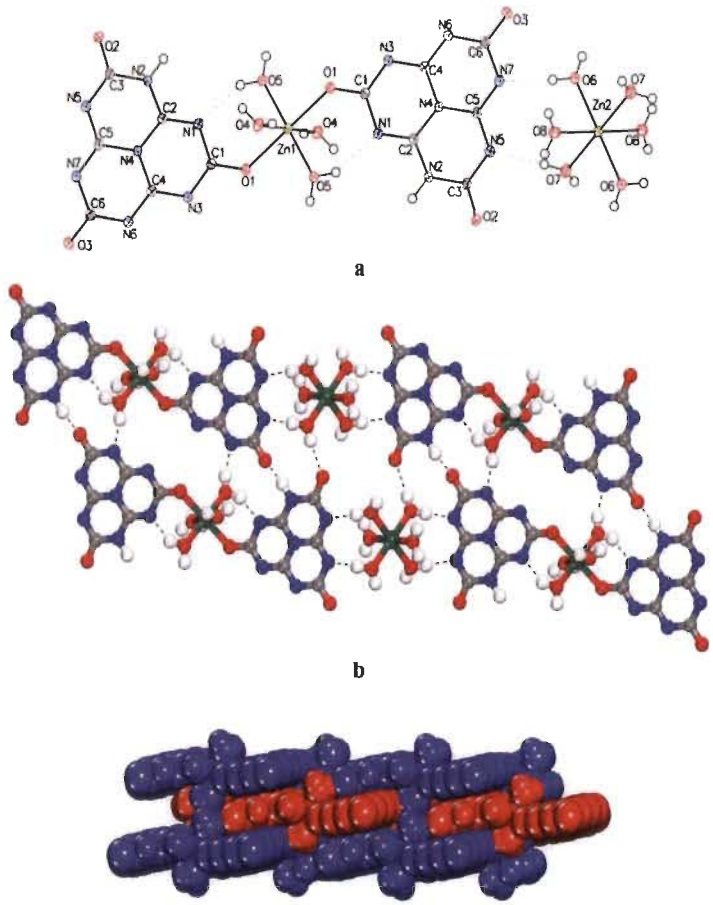

a

b

c

Figure S4. Crystal structure of MOP-**4**. a) Thermal atomic displacement ellipsoid plot of MOP-**4**. The ellipsoids of non-hydrogen atoms are drawn at 50% probability level, hydrogen atoms are represented by a sphere of arbitrary size, and hydrogen bonds are represented by dotted lines. b) View of the 2D sheets connected by coordination bonds and hydrogen bonds. Hydrogen bonds are represented in dotted lines, and zinc atoms are shown in olive-drab, carbon atoms in grey, hydrogen atoms in white, nitrogen atoms in blue, and oxygen atoms in red. c) Packing of the 2D sheets to form the three-dimensional structure. For more clarity layers marked in red and blue.

Table S1. Crystallographic Data of Metal-Organic Polymers (**1-4**).

	MOP-1	**MOP-2**	**MOP-3**	**MOP-4**
Formula	$Mn_2C_{12}H_{22}N_{14}O_{16}$	$Co_2C_{12}H_{22}N_{14}O_{16}$	$Ni_2C_{12}H_{22}N_{14}O_{16}$	$Zn_2C_{12}H_{22}N_{14}O_{16}$
Crystal System	Triclinic	Triclinic	Triclinic	Triclinic
Mr	728.31	736.29	735.82	749.17
T (K)	100	120	100	100
Radiation	GaKα	GaKα	GaKα	GaKα
λ (Å)	1.34139	1.34139	1.34139	1.34139
F (000)	370	374	376	380
Space group	$P\bar{1}$	$P\bar{1}$	$P\bar{1}$	$P\bar{1}$
a (Å)	6.9844(4)	7.3633(3)	7.3698(3)	7.4188(3)
b (Å)	8.7175(5)	8.6464(3)	8.6190(3)	8.6369(4)
c (Å)	10.0198(6)	9.2763(3)	9.1796(3)	9.2126(4)
α (deg)	79.079(2)	77.947(2)	78.027(2)	77.798(2)
β (deg)	81.581(2)	84.247(2)	84.389(2)	84.443(2)
γ (deg)	84.507(2)	87.228(2)	86.957(2)	87.127(2)
V (Å^3)	591.11(6)	574.43(4)	567.36(4)	573.99(4)
Z	1	1	1	1
ρ_{calcd} (g cm^{-3})	2.046	2.128	2.154	2.167
μ (mm^{-1})	6.655	8.627	9.766	2.388
No. measured reflections	32337	30851	18351	23186
No. independent reflections	2698	2633	2490	2636
No. obsd. reflections I>2σ(I)	2632	2457	2599	2454
Nb Params	246	246	246	246
R_1, I>2σ (%)	0.0215	0.0287	0.0742	0.0264
R_1, all data (%)	0.0219	0.0307	0.1017	0.0284
ωR_2, I>2σ(I) (%)	0.0633	0.0764	0.1723	0.0705
ωR_2, all data (%)	0.0639	0.0783	0.1909	0.0719
GoF	1.116	1.093	1.101	1.067

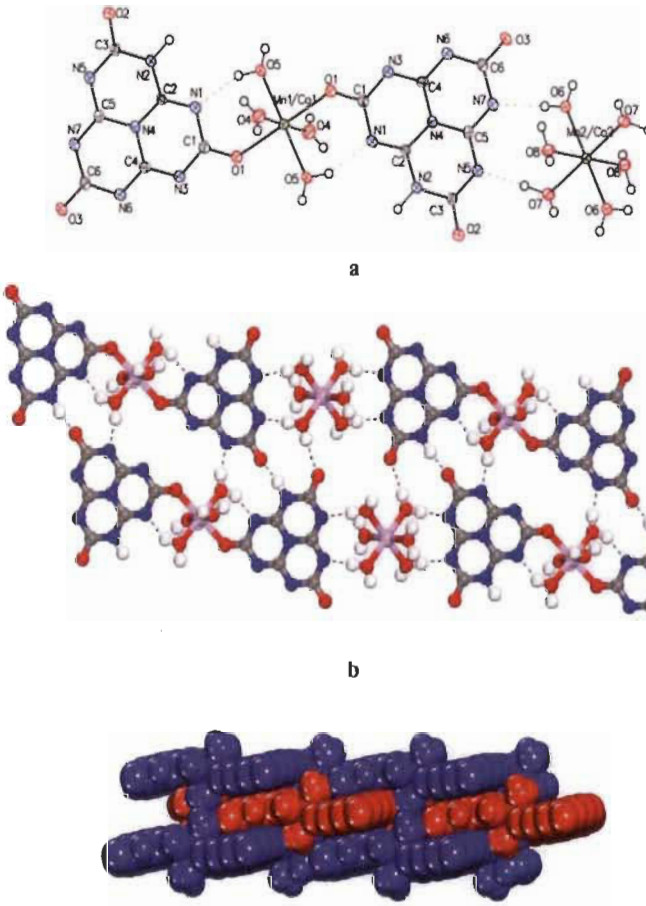

Figure S5. Crystal structure of MMOP-**5**. a) Thermal atomic displacement ellipsoid plot of MMOP-**5**. The ellipsoids of non-hydrogen atoms are drawn at 50% probability level, hydrogen atoms are represented by a sphere of arbitrary size, and hydrogen bonds are represented by dotted lines. b) View of the 2D sheets connected by coordination bonds and hydrogen bonds. Hydrogen bonds are represented in dotted lines, and manganese and cobalt atoms are shown in dark green, carbon atoms in grey, hydrogen atoms in white, nitrogen atoms in blue, and oxygen atoms in red. c) Packing of the 2D sheets to form the three-dimensional structure. For more clarity layers marked in red and blue.

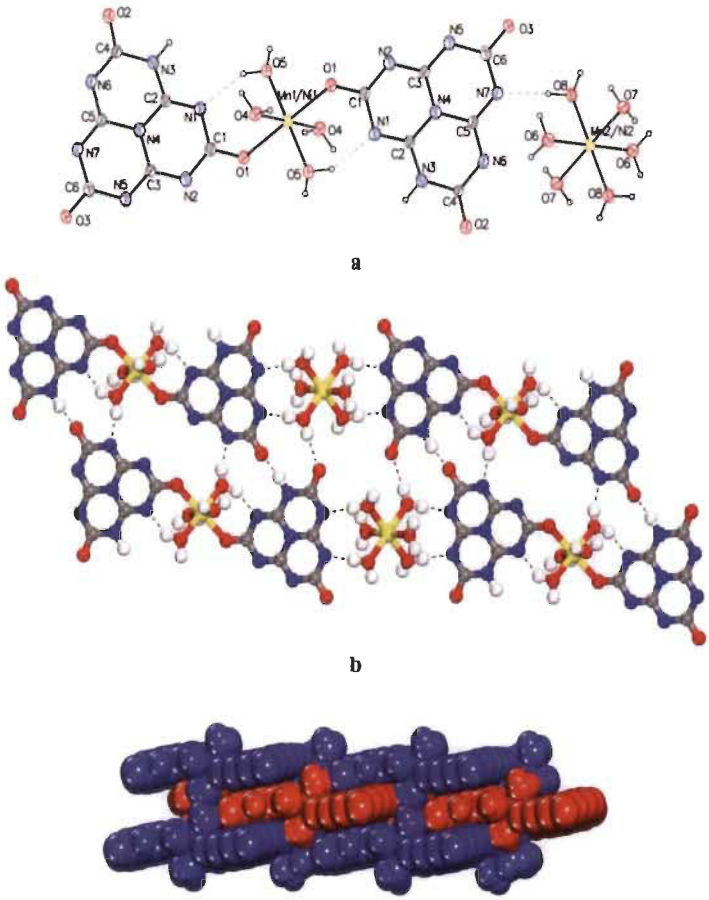

Figure S6. Crystal structure of MMOP-**6**. a) Thermal atomic displacement ellipsoid plot of MMOP-**6**. The ellipsoids of non-hydrogen atoms are drawn at 50% probability level, hydrogen atoms are represented by a sphere of arbitrary size, and hydrogen bonds are represented by dotted lines. b) View of the 2D sheets connected by coordination bonds and hydrogen bonds. Hydrogen bonds are represented in dotted lines, and manganese and nickel atoms are shown in yellow, carbon atoms in grey, hydrogen atoms in white, nitrogen atoms in blue, and oxygen atoms in red. c) Packing of the 2D sheets to form the three-dimensional structure. For more clarity layers marked in red and blue.

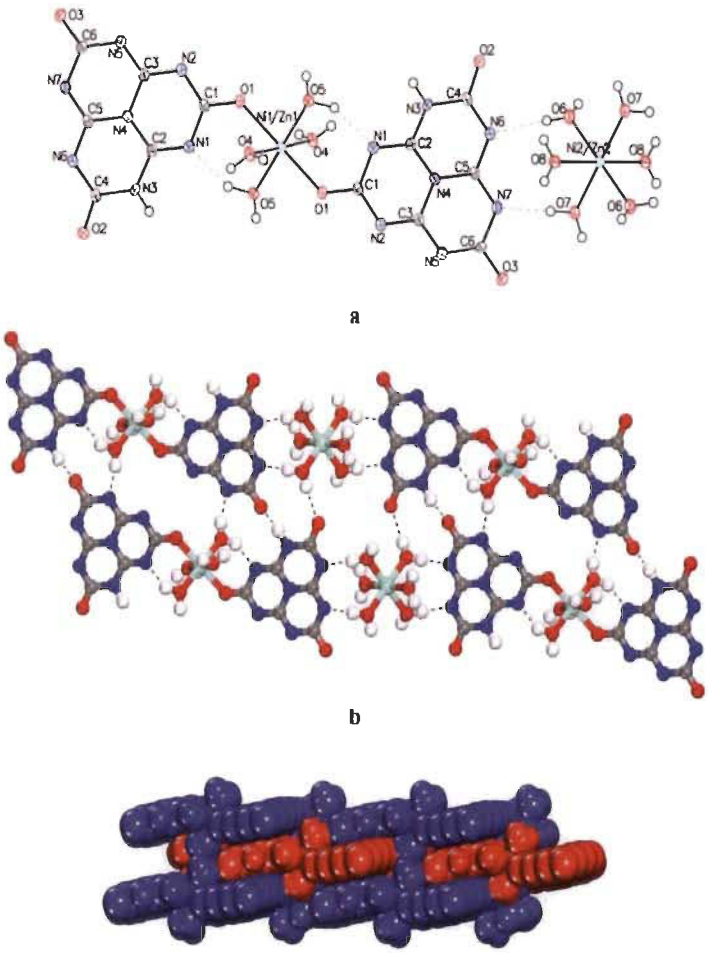

Figure S7. Crystal structure of MMOP-7. a) Thermal atomic displacement ellipsoid plot of MMOP-7. The ellipsoids of non-hydrogen atoms are drawn at 50% probability level, hydrogen atoms are represented by a sphere of arbitrary size, and hydrogen bonds are represented by dotted lines. b) View of the 2D sheets connected by coordination bonds and hydrogen bonds. Hydrogen bonds are represented in dotted lines, and nickel and zinc atoms are shown in light blue, carbon atoms in grey, hydrogen atoms in white, nitrogen atoms in blue, and oxygen atoms in red. c) Packing of the 2D sheets to form the three-dimensional structure. For more clarity layers marked in red and blue.

Table S2. Crystallographic Data of Mixed Metal-Organic Polymers (**5**-7).

	MMOP-5	**MMOP-6**	**MMOP-7**
Formula	$Mn_{0.3}Co_{1.7}C_{12}H_{22}N_{14}O_{16}$	$Mn_{0.84}Ni_{1.16}C_{12}H_{22}N_{14}O_{16}$	$Ni_{1.41}Zn_{0.59}C_{12}H_{22}N_{14}O_{16}$
Crystal System	Triclinic	Triclinic	Triclinic
Mr	735.10	732.69	739.78
T (K)	120	100	100
Radiation	GaKα	GaKα	GaKα
λ (Å)	1.34139	1.34139	1.34139
F (000)	373	373	377
Space group	$P\bar{1}$	$P\bar{1}$	$P\bar{1}$
a (Å)	6.999(2)	7.2816(16)	7.3891(3)
b (Å)	8.6955(2)	8.6497(19)	8.6307(3)
c (Å)	9.8777(3)	9.4431(19)	9.1887(4)
α (deg)	78.7700(10)	78.648(13)	77.928(2)
β (deg)	81.6070(10)	83.519(13)	84.470(2)
γ (deg)	85.0940(10)	87.455(14)	87.086(2)
V (Å^3)	582.39(3)	579.2(2)	570.08(4)
Z	1	1	1
ρ_{calcd} (g cm^{-3})	2.096	2.100	2.155
μ (mm^{-1})	8.245	8.405	7.566
No. measured reflections	27640	6859	16725
No. independent reflections	2658	2018	2583
No. obsd. reflections I>2σ(I)	2678	2208	2613
Nb Params	247	209	248
R_1, I>2σ (%)	0.0508	0.1045	0.0499
R_1, all data (%)	0.0586	0.1325	0.0572
ωR_2, I>2σ(I) (%)	0.0962	0.2826	0.1096
ωR_2, all data (%)	0.0988	0.3137	0.1148
GoF	1.217	1.071	1.158

Table S3. Hydrogen bond geometry (Å, °) of MOP-**1**.

D—H···*A*	*D*—H	H···*A*	*D*···*A*	*D*—H···*A*
O4—H4b···O2i	0.84 (3)	1.86 (3)	2.6845 (15)	170 (3)
O5—H5a···N6ii	0.82 (3)	1.97 (3)	2.7717 (16)	166 (3)
O5—H5b···N1	0.79 (3)	2.04 (3)	2.7709 (16)	154 (3)
O6—H6a···O2iii	0.80 (3)	2.12 (3)	2.8919 (15)	163 (2)
O6—H6b···N7	0.79 (3)	1.96 (3)	2.7554 (16)	177 (3)
O7—H7a···N5	0.99 (3)	1.77 (3)	2.7533 (16)	170 (2)
O8—H8b···N3iv	0.85 (3)	1.86 (3)	2.7055 (15)	176 (2)
N2—H2···O3ii	1.00 (2)	1.73 (2)	2.7243 (14)	176.7 (19)

Symmetry codes: (i) *x*−1, *y*, *z*+1; (ii) *x*, *y*+1, *z*; (iii) *x*, *y*−1, *z*; (iv) *x*+1, *y*, *z*−1.

Table S4. Hydrogen bond geometry (Å, °) of MOP-**2**.

D—H···*A*	*D*—H	H···*A*	*D*···*A*	*D*—H···*A*
O4—H4*A*···O2^{i}	0.79 (3)	1.94 (3)	2.7180 (18)	167 (3)
O4—H4*B*···O2^{ii}	0.92 (4)	2.07 (4)	2.9800 (19)	170 (3)
O5—H5*A*···O3^{iii}	0.92 (3)	2.51 (3)	2.9905 (18)	113 (2)
O5—H5*A*···N1	0.92 (3)	1.89 (3)	2.716 (2)	148 (3)
O5—H5*B*···N6^{iii}	0.90 (3)	1.80 (3)	2.682 (2)	167 (3)
O6—H6*A*···O2^{iv}	0.82 (3)	2.12 (3)	2.9220 (19)	166 (3)
O6—H6*B*···N7	0.92 (3)	1.81 (3)	2.730 (2)	178 (3)
O7—H7*A*···N5	0.93 (3)	1.92 (3)	2.835 (2)	171 (2)
O7—H7*B*···O1^{v}	0.94 (3)	2.00 (4)	2.8868 (18)	157 (3)
O8—H8*A*···N3^{v}	0.85 (3)	1.95 (3)	2.785 (2)	168 (3)
O8—H8*B*···O1^{vi}	0.90 (4)	2.55 (4)	3.0698 (18)	117 (3)
O8—H8*B*···O4^{vii}	0.90 (4)	2.19 (4)	3.0311 (19)	155 (3)
O8—H8*B*···O5^{vii}	0.90 (4)	2.63 (4)	3.3098 (19)	133 (3)
N2—H2···O3^{iii}	1.07 (3)	1.66 (3)	2.7200 (18)	171 (2)

Symmetry codes: (i) x+1, y, z−1; (ii) −*x*+*1*, −*y*, −*z*+*1*; (iii) x, y−1, z; (iv) x, y+1, z; (v) x−1, y, z+1; (vi) −x, −*y*+*1*, −*z*+*1*; (vii) x−1, y+1, z+1.

Table S5. Hydrogen bond geometry (Å, °) of MOP-**3**.

D—H···*A*	*D*—H	H···*A*	*D*···*A*	*D*—H···*A*
O4—H4*A*···O2^{i}	0.97 (8)	2.00 (8)	2.965 (7)	177 (7)
O4—H4*B*···O2^{ii}	0.71 (10)	2.08 (10)	2.719 (6)	151 (11)
O5—H5*A*···N6^{iii}	0.85 (7)	1.85 (8)	2.687 (7)	166 (6)
O5—H5*B*···O3^{iii}	0.81 (8)	2.54 (8)	2.982 (6)	116 (6)
O5—H5*B*···N1	0.81 (8)	1.99 (8)	2.707 (7)	148 (7)
N2—H2···O3^{iii}	0.84 (8)	1.88 (8)	2.714 (7)	170 (8)
O6—H6*A*···O2^{iv}	0.75 (9)	2.23 (9)	2.957 (7)	163 (9)
O6—H6*B*···N7	0.80 (9)	1.94 (9)	2.736 (6)	170 (8)
O7—H7*A*···O1^{v}	0.84 (9)	2.08 (10)	2.895 (6)	161 (8)
O7—H7*B*···N5	0.71 (8)	2.13 (8)	2.837 (7)	175 (8)

Symmetry codes: (i) x, y, z−1; (ii) −x+1, −y, −z+1; (iii) x, y−1, z; (iv) x, y+1, z; (v) x−1, y, z+1.

Table S6. Hydrogen bond geometry (Å, °) of MOP-**4**.

D—H···*A*	*D*—H	H···*A*	*D*···*A*	*D*—H···*A*
O4—H4*A*···O2^{i}	0.79 (2)	1.97 (2)	2.7198 (14)	158 (3)
O4—H4*B*···O2^{ii}	0.81 (2)	2.17 (2)	2.9835 (15)	175 (2)
O5—H5*A*···N6^{iii}	0.81 (2)	1.90 (2)	2.6828 (15)	164 (3)
O5—H5*B*···O3^{iii}	0.81 (2)	2.57 (2)	2.9903 (14)	114 (2)
O5—H5*B*···N1	0.81 (2)	1.98 (2)	2.7173 (15)	151 (2)
N2—H2···O3^{iii}	0.91 (2)	1.82 (2)	2.7176 (14)	171 (2)
O6—H6*A*···O2^{iv}	0.78 (1)	2.17 (2)	2.9303 (14)	164 (2)
O6—H6*B*···N7	0.80 (2)	1.94 (2)	2.7346 (15)	176 (2)
O7—H7*A*···N5	0.81 (1)	2.04 (1)	2.8367 (15)	172 (2)
O7—H7*B*···O1^{v}	0.81 (2)	2.15 (2)	2.8920 (14)	153 (3)
O8—H8*A*···N3^{v}	0.78 (1)	2.01 (2)	2.7839 (15)	175 (2)
O8—H8*B*···O1^{vi}	0.79 (2)	2.60 (2)	3.0714 (15)	120 (2)
O8—H8*B*···O4^{vii}	0.79 (2)	2.28 (2)	3.0240 (15)	158 (2)

Symmetry codes: (i) x−1, y, z+1; (ii) −x+1, −y+2, −z+1; (iii) x, y+1, z; (iv) x, y−1, z; (v) x+1, y, z−1; (vi) −x+2, −y−1, −z+1; (vii) x+1, y−1, z−1.

Table S7. Hydrogen bond geometry (Å, °) of MMOP-**5**.

D—H···*A*	*D*—H	H···*A*	*D*···*A*	*D*—H···*A*
O4—H4*A*···O7^{i}	0.75 (6)	2.31 (6)	3.008 (4)	154 (6)
O4—H4*B*···O2^{ii}	0.76 (5)	1.93 (5)	2.679 (4)	174 (5)
O5—H5*A*···N6^{iii}	0.78 (5)	2.01 (5)	2.760 (4)	162 (5)
O5—H5*B*···N1	0.85 (5)	1.95 (5)	2.750 (4)	157 (4)
N2—H2···O3^{iii}	0.99 (3)	1.72 (4)	2.716 (3)	178 (3)
O6—H6*A*···O2^{iv}	0.78 (5)	2.13 (5)	2.892 (3)	165 (4)
O6—H6*B*···N7	0.80 (5)	1.95 (5)	2.746 (4)	177 (5)
O7—H7*A*···N5	0.96 (5)	1.84 (5)	2.784 (4)	170 (4)
O7—H7*B*···O1^{v}	0.78 (5)	2.24 (5)	2.991 (3)	163 (4)
O8—H8*A*···O1^{vi}	0.75 (5)	2.21 (5)	2.940 (4)	165 (5)
O8—H8*B*···N3^{vii}	0.86 (5)	1.85 (5)	2.715 (4)	176 (4)

Symmetry codes: (i) −x+1, −y+2, −z+1; (ii) x−1, y, z+1; (iii) x, y+1, z; (iv) x, y−1, z; (v) x+1, y, z−1; (vi) x, y, z−1; (vii) −x+1, −y+1, −z+1.

Table S8. Hydrogen bond geometry (Å, °) of MMOP-**6**.

D—H···*A*	*D*—H	H···*A*	*D*···*A*	*D*—H···*A*
N3—H3···O3^{i}	0.88	1.85	2.725 (10)	171
O4—H4*A*···O2^{ii}	0.87	1.91	2.695 (11)	150
O4—H4*B*···O2^{iii}	0.87	2.25	3.106 (12)	169
O5—H5*A*···N5^{iv}	0.87	2.05	2.709 (11)	132
O5—H5*B*···N1^{v}	0.87	1.97	2.740 (11)	147
O5—H5*B*···O3^{iv}	0.87	2.62	3.077 (9)	114
O6—H6*A*···O4^{iii}	0.86	2.33	3.037 (11)	140
O6—H6*B*···N2^{vi}	0.86	1.99	2.766 (12)	150
O7—H7*A*···N5^{vii}	0.87	2.66	3.458 (12)	152
O7—H7*B*···O1^{vi}	0.87	2.06	2.932 (11)	177
O8—H8*A*···O2^{viii}	0.88	2.12	2.923 (10)	153
O8—H8*B*···N7	0.87	1.87	2.741 (11)	177

Symmetry codes: (i) x, y+1, z; (ii) x−1, y, z+1; (iii) −x+1, −y+2, −z+1; (iv) −x+1, −y+1, −z+2; (v) −x+1, −y+2, −z+2; (vi) −x−1, −y−1, −z+1; (vii) x, y, z−1; (viii) x, y−1, z.

Table S9. Hydrogen bond geometry (Å, °) of MMOP-7.

D—H···*A*	*D*—H	H···*A*	*D*···*A*	*D*—H···*A*
N3—H3···O3^{i}	0.84 (5)	1.88 (5)	2.715 (4)	171 (4)
O4—H4*A*···O2^{ii}	0.80 (6)	1.93 (6)	2.717 (4)	168 (5)
O4—H4*B*···O2^{iii}	0.88 (6)	2.11 (6)	2.977 (4)	168 (5)
O5—H5*A*···N1^{iv}	0.92 (6)	1.89 (6)	2.706 (4)	148 (5)
O5—H5*B*···O3^{v}	0.77 (7)	2.65 (6)	2.989 (3)	108 (5)
O5—H5*B*···N5^{v}	0.77 (7)	1.94 (7)	2.689 (4)	164 (6)
O6—H6*A*···N6	0.82 (5)	2.03 (5)	2.831 (4)	165 (4)
O6—H6*B*···O1^{vi}	0.82 (5)	2.16 (6)	2.900 (4)	150 (5)
O7—H7*A*···N7	0.85 (5)	1.88 (6)	2.731 (4)	177 (5)
O7—H7*B*···O2^{vii}	0.82 (6)	2.14 (6)	2.943 (4)	169 (5)
O8—H8*A*···N2^{vi}	0.81 (5)	1.99 (6)	2.790 (4)	169 (5)
O8—H8*B*···O1^{viii}	0.81 (5)	2.58 (5)	3.067 (3)	120 (4)
O8—H8*B*···O4^{viii}	0.81 (5)	2.27 (6)	3.030 (4)	156 (5)
O8—H8*B*···O5^{viii}	0.81 (5)	2.68 (5)	3.293 (4)	134 (4)

Symmetry codes: (i) x, y−1, z; (ii) −x+1, −y, −z+1; (iii) x, y, z−1; (iv) −x+2, −y, −z; (v) −x+2, −y+1, −z; (vi) x−1, y, z+1; (vii) x, y+1, z; (viii) −x+1, −y+1, −z+1.

Studies of Crystallinity, Purity and Homogeneity of the Bulk Samples of Metal-Organic Polymers (1-4) and Mixed Metal-Organic Polymers (5-7)

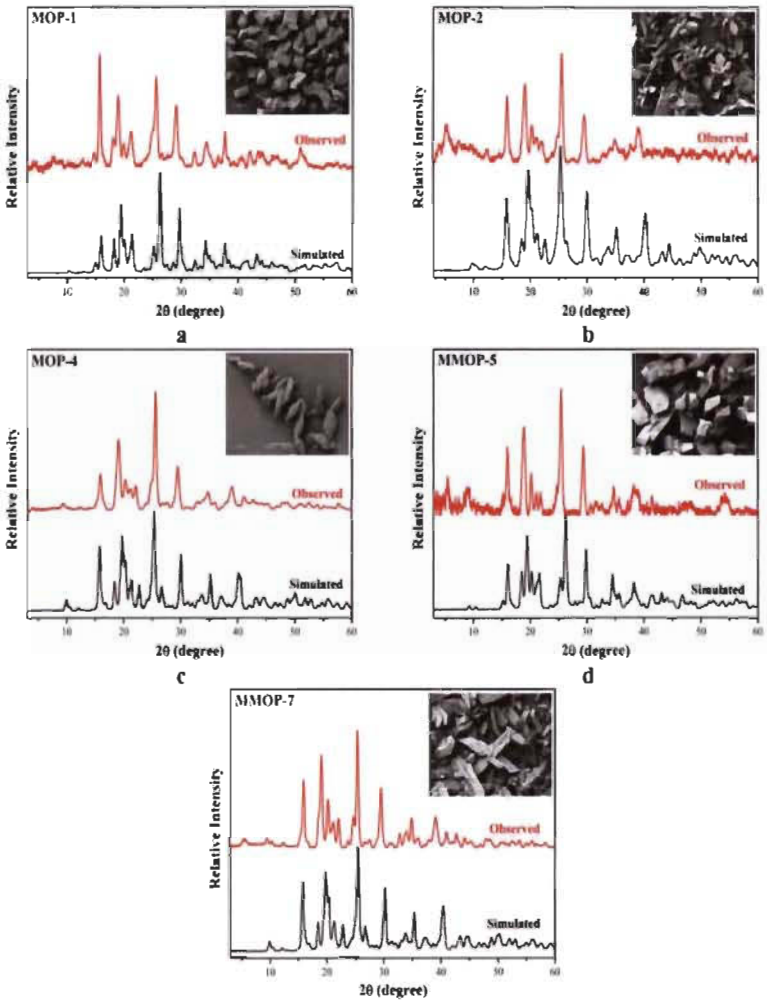

Figure S8. Characterization of MOP-**1**, MOP-**2**, MOP-**4**, MMOP-**5** and MMOP-**7** by PXRD and SEM images of the bulk crystalline samples. Scale bar 100 μm for Figure 2a-b and 2d-e, and 50 μm for Figure 2b. (a)-(e) Comparison of the observed powder X-ray diffraction with the simulated pattern calculated from the single-crystal X-ray diffraction data and the insert SEM images for each sample. Observed PXRD and simulated patterns are shown in red and black respectively.

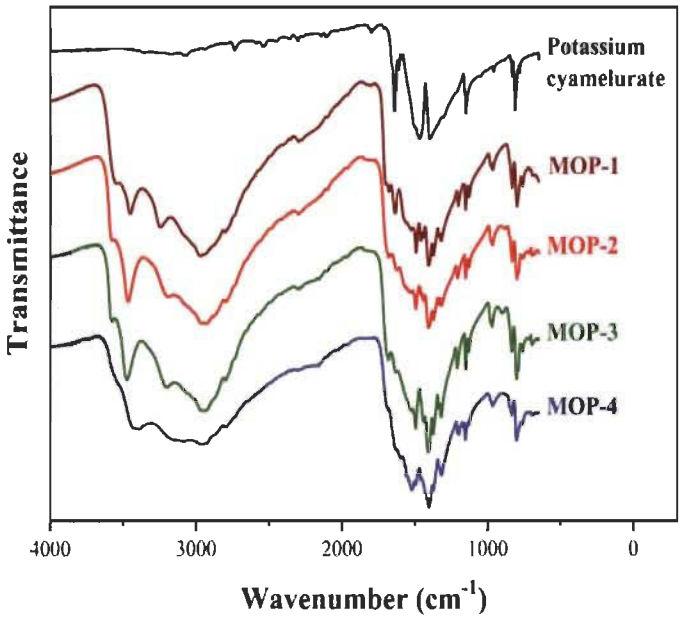

Figure S9. FT-IR spectra of MOPs-(1-4) compared to ligand.

Table S10. Assignment of FT-IR spectra peaks of MOPs-(**1-4**).

$\tilde{\nu}$/cm^{-1}					Assignment
Potassium cyamelurate	**MOP-1**	**MOP-2**	**MOP-3**	**MOP-4**	
	693sh 709sh	692sh 709sh	695sh 708sh	694sh	Ring breathing, τ(OH)
	760w	755sh	760sh	762sh	τ(OH)
782w 814m	777w 798w	787w 799w	768w 788w 800w	 801w	γ(CN)-Linker, Ring Breathing for all, τ(NH), ω(OH)-MOPs
834w	832w	831w	833w	833w 848sh	Ring Breathing for all, ν(CN) saturated N atom-linker, ω(OH)-MOPs
961w	963w	966w	967w	964w	(Ring Breathing, ν(CN) in ring-linker), (ρ(OH) hydrogen-bonded, γ(CN), ω(NH)-MOPs)
  1150m	1121w 1149w 1162w	1126w 1148w	1127w 1149w 1165w	1127w 1149w 1161w	ν(CN) in ring for all, ρ(OH)-MOPs
	1199w	1204w	1205w	1195w 1203w	Ring Breathing, ρ(OH)
1310sh	1317w 1333w	1313w 1333w	1316w 1331w	1313w 1330w	ν(CN) in ring for all, ρ(NH)-MOPs
	1370m	1368m	1369m	1369w	Ring breathing, δ(OH)
1399s	1402s 1438w	1402s 1436vw	1404s 1436w	1404s	ν(CN)-linker, δ(OH)-MOPs
1470s	1455w 1487m	1488m	1489	1454w 1486w	δ(OH)-MOPs, ν(CN)-Linker
1503s					ν(CN) in ring-linker
1586vw					ν(CN) in ring for all, ρ(NH)
	1636w		1635sh	1634sh	ω(NH), Ring Breathing
1642m				1635sh	ν(CO) single bond type-linker
	1677sh 1701sh	1680sh	1683sh		ν(CO) double bond type-MOPs
1801w					ν(CO) double bond type-linker (due to resonance)
	2793sh 2965s	2790sh 2930s	2796sh 2957s	2797sh 2957m	ν(OH) (hydrogen-bonded)
	3240w 3450w 3547w	3193m 3463m 3579sh	3201w 3473w 3576sh	3085w 3390w 3430m	ν(NH) (characteristic amide)

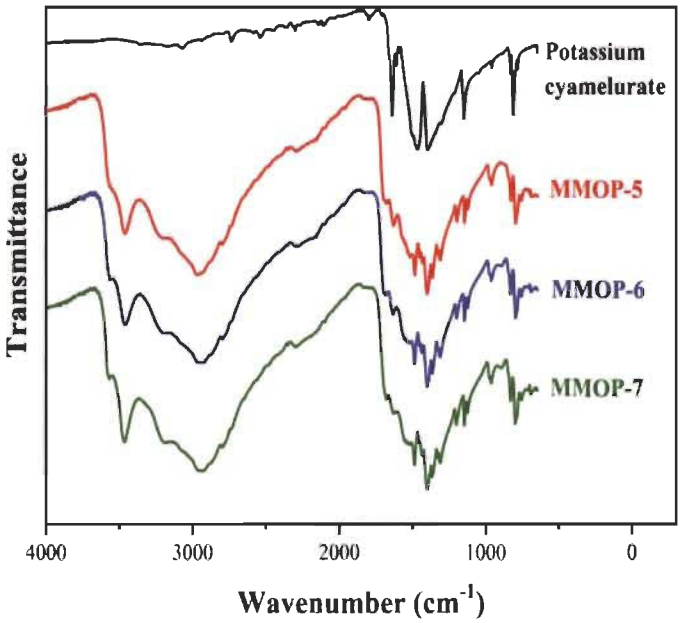

Figure S10. FT-IR spectra of MMOPs-(**5**-7) compared to ligand.

Table S11. Assignment of FT-IR spectra peaks of MMOPs-(5-7).

$\tilde{\nu}$/cm^{-1}				Assignment
Potassium cyamelurate	**MMOP-5**	**MMOP-6**	**MMOP-7**	
	691sh	693sh	694sh	
	709sh	709sh	708sh	Ring breathing, τ(OH)
	761sh	760sh	759sh	τ(OH)
782w	788sh	787sh	767sh	
814m	799w	799sh	788w	γ(CN)-Linker, Ring Breathing for all.
			800w	τ(NH), ω(OH)-MMOPs
834w	832w	833w	833w	Ring Breathing for all, ν(CN) saturated N atom-linker, ω(OH)-MMOPs
961w	964w	964w	966w	(Ring Breathing, ν(CN) in ring-linker).
1051sh	977w	978w	979w	(ρ(OH) hydrogen-bonded, γ(CN), ω(NH)-MMOPs)
	1125w	1126w	1126w	ν(CN) in ring for all, ρ(OH)-MOPs
	1148w	1148w	1148w	
1150m	1161sh	1163sh	1163sh	
	1201w	1202w	1204w	Ring Breathing, ρ(OH)
1310sh	1315w	1316w	1315w	
	1331w	1329w	1330w	
	1369w	1369m	1368m	ν(CN) in ring for all, ρ(NH)-MOPs
1399s	1404s	1403s	1402s	Ring breathing, δ(OH)
	1435w	1438w	1438w	
1470s	1455w	1454w	1455w	ν(CN)-linker, δ(OH)-MOPs
	1488w	1489w	1489w	
1503s				δ(OH)-MOPs, ν(CN)-Linker
1586vw				ν(CN) in ring-linker
1613w				ν(CN) in ring for all, ρ(NH)
	1634w	1635w	1633w	
1642m				ω(NH), Ring Breathing
	1682w	1682w	1682w	ν(CO) single bond type-linker
	1699sh			
1801w				ν(CO) double bond type-MOPs
	2794sh	2793sh	2790sh	ν(CO) double bond type-linker (due to resonance)
	2964m	2958s	2934s	ν(OH) (hydrogen-bonded)
	3216m	3207m	3192m	
	3459m	3462m	3463m	ν(NH) (characteristic amide)
	3567sh	3565sh	3564sh	

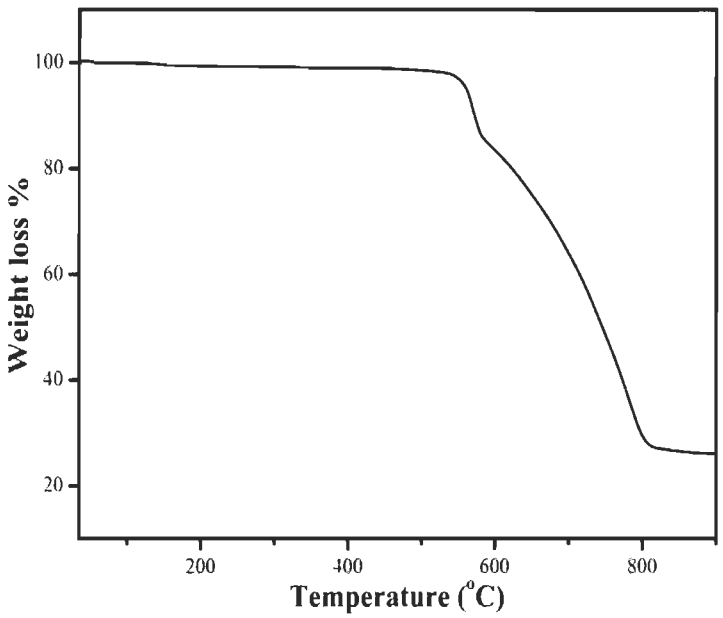

Figure S11. Thermogravimetric analysis curve of cyamelurate.

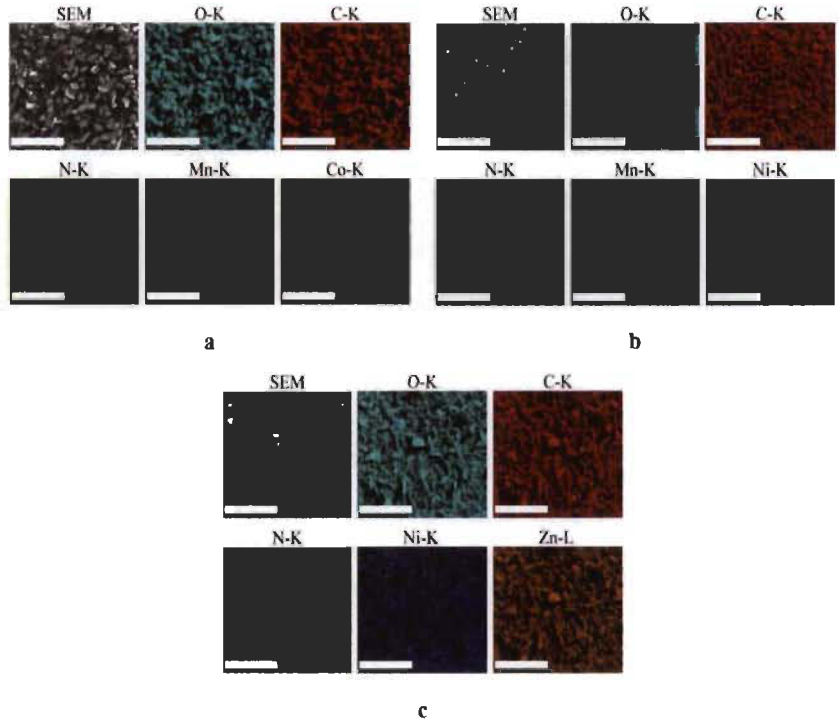

Figure S12. Energy Dispersive X-ray Diffraction analyses of MMOP-(**5**-**7**). (a)-(c) EDS element-mapping images of MMOPs-(**5**-**7**) respectively, showing the distribution of carbon (red), nitrogen (green), oxygen (cyan) and metal ions (Mn in purple, Co in yellow, Ni in blue and Zn in orange) in the area of the crystalline samples (scale bar, 500 μm).

***In-situ* Energy Dispersive Spectroscopy/Scanning Electron Microscopy**

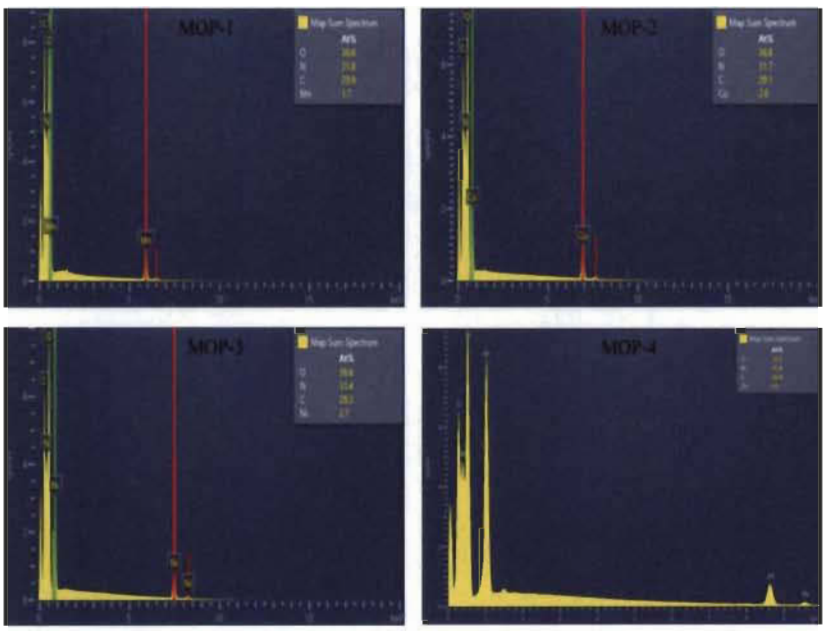

Figure S13. Energy Dispersive X-ray Diffraction plot analysis of MOPs-(**1-4**) representing the percentage of elements.

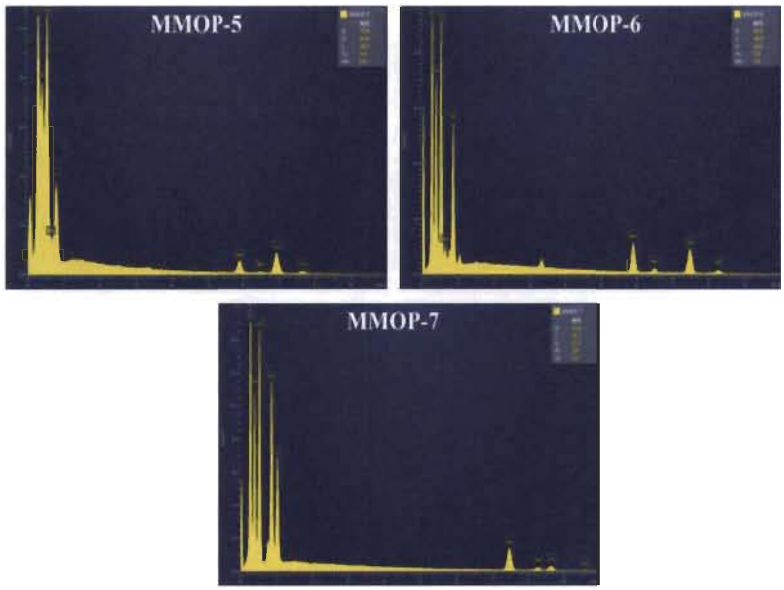

a

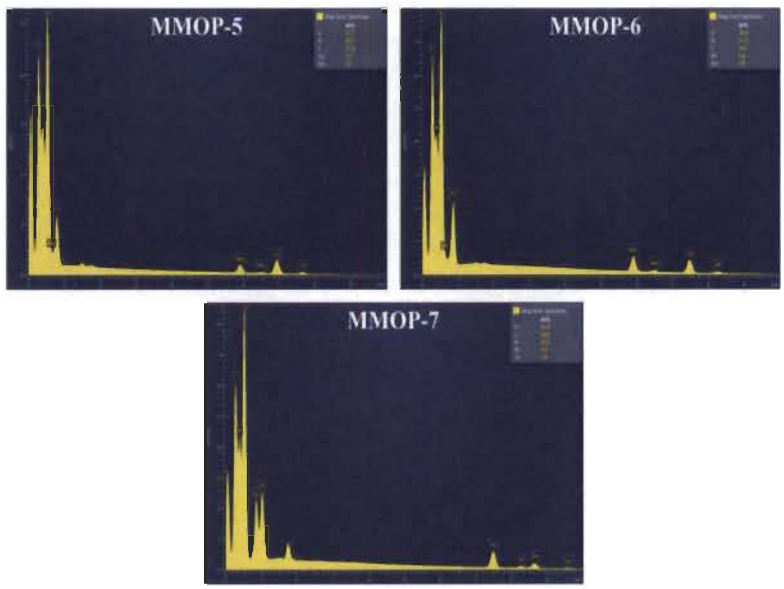

b

Figure S14. Energy Dispersive X-ray Diffraction plot analysis of MMOPs-(5-7) representing the percentage of elements. a) Point, b) Mapping analysis.

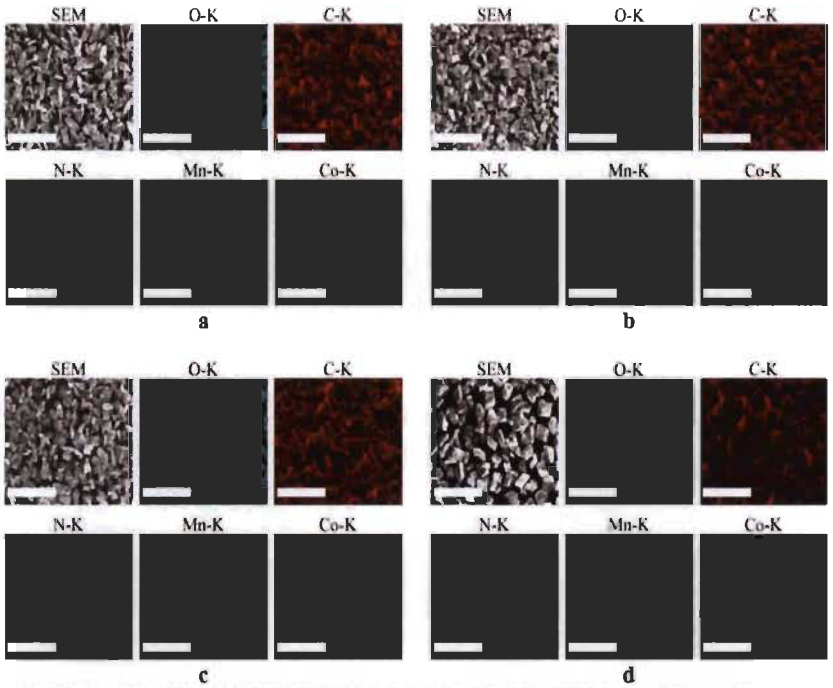

Figure S15. Energy Dispersive X-ray Diffraction mapping analysis of MMOP-5 metal ratios study. a)20-80, b) 40-60, c) 60-40, d) 80-20 (Scale bar, 500 μm).

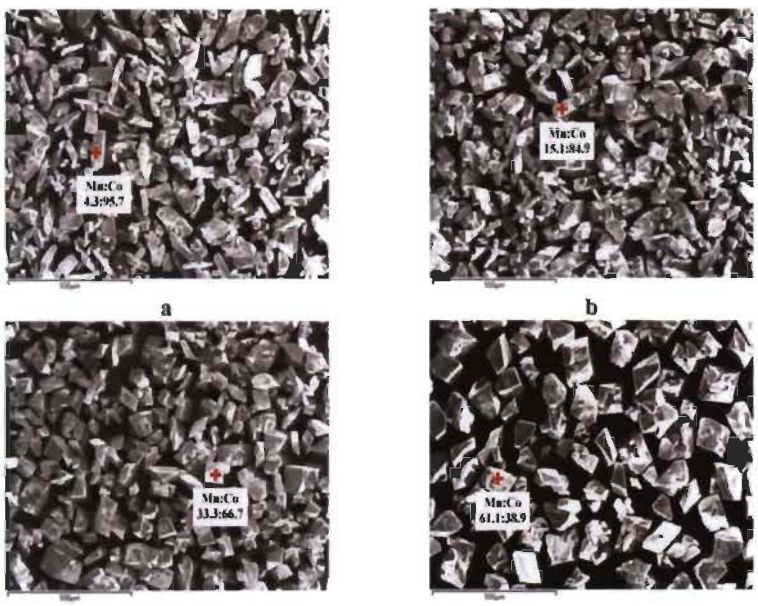

Figure S16. Energy Dispersive X-ray Diffraction point analysis of MMOP-5 metal ratios study. a) 20-80, b) 40-60, c) 60-40, d) 80-20.

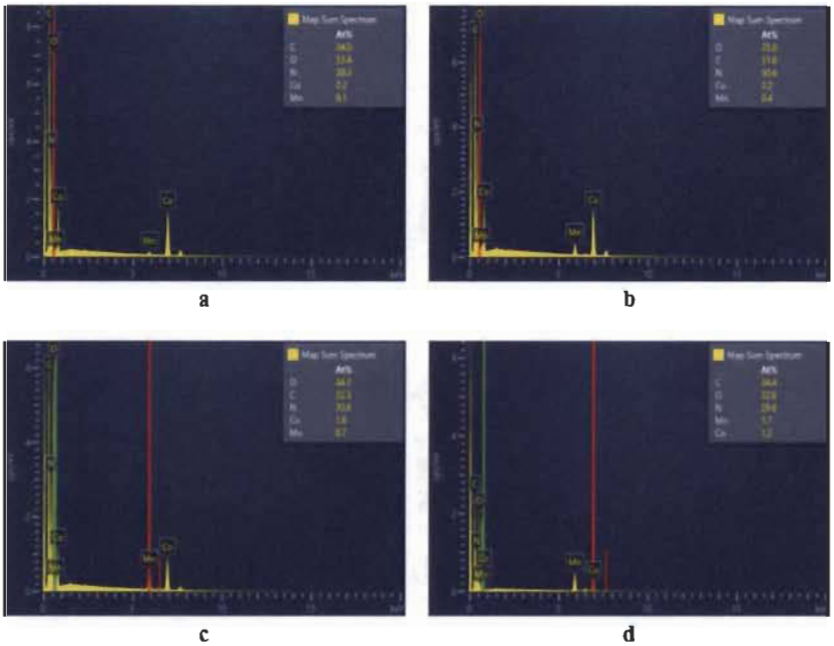

Figure S17. Energy Dispersive X-ray Diffraction plot of mapping analysis of MMOP-5 metal ratio study a) 20-80, b) 40-60, c) 60-40, d) 80-20.

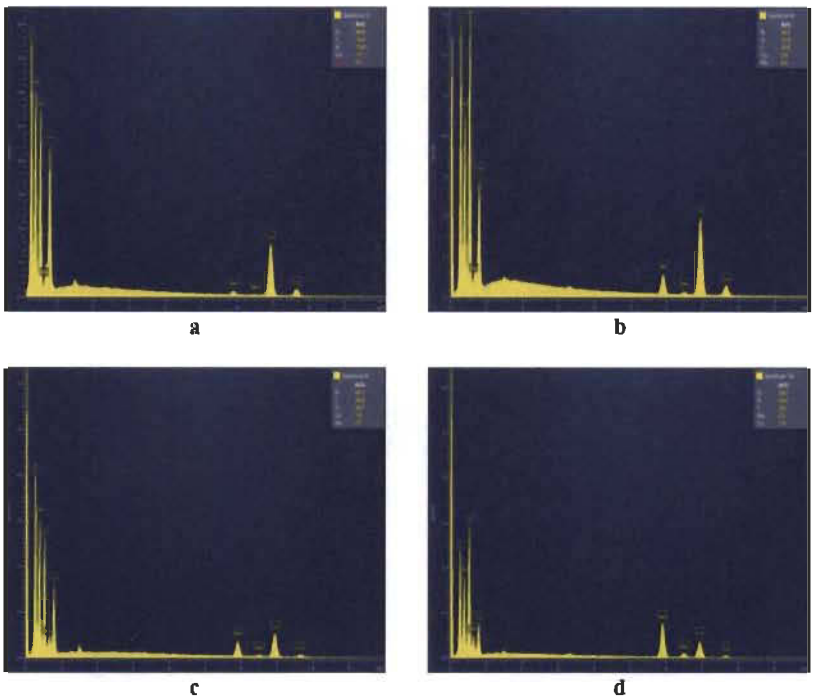

Figure S18. Energy Dispersive X-ray Diffraction plot of point analysis of MMOP-5 metal ratio study a) 20-80, b) 40-60, c) 60-40, d) 80-20.

Table S12. Summary of Energy Dispersive X-ray Diffraction analysis of MMOP-5 prepared with different metal ratios.

Ratios	Ratios seen in EDS (Mn:Co)	
	Mole %	
	Mapping	Point
20:80	4.3:95.7	4.3:95.7
40:60	15.4:84.6	15.1:84.9
50:50	28:72	28:72
60:40	30.4:69.6	33.3:66.7
80:20	58.6:41.4	61.1:38.9

X-ray photoelectron spectroscopy

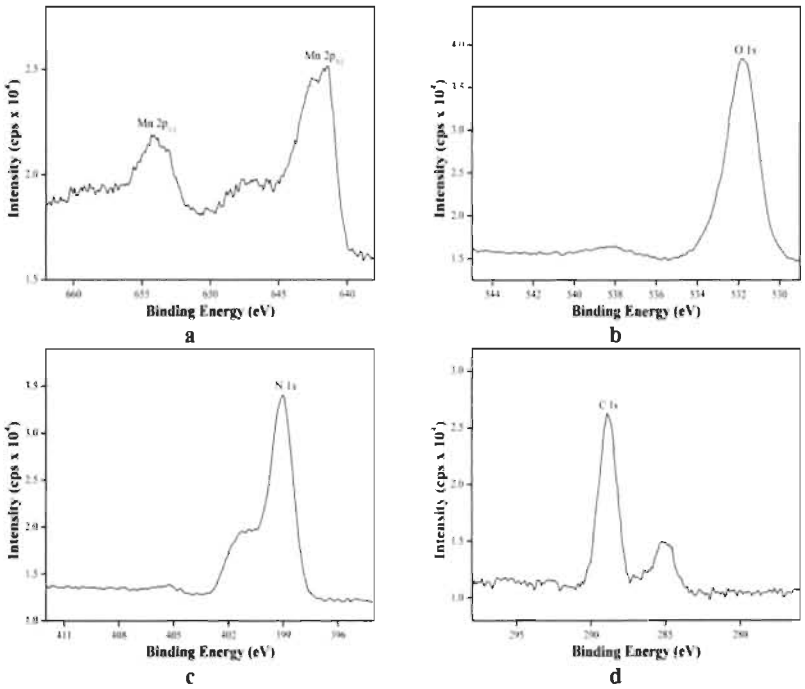

Figure S19. XPS patterns of MOP-**1**. a)-d) Narrow survey XPS in MOP-**1** of Mn $2p_{3/2}$ and $2p_{1/2}$; O 1s; N 1s; C 1s.

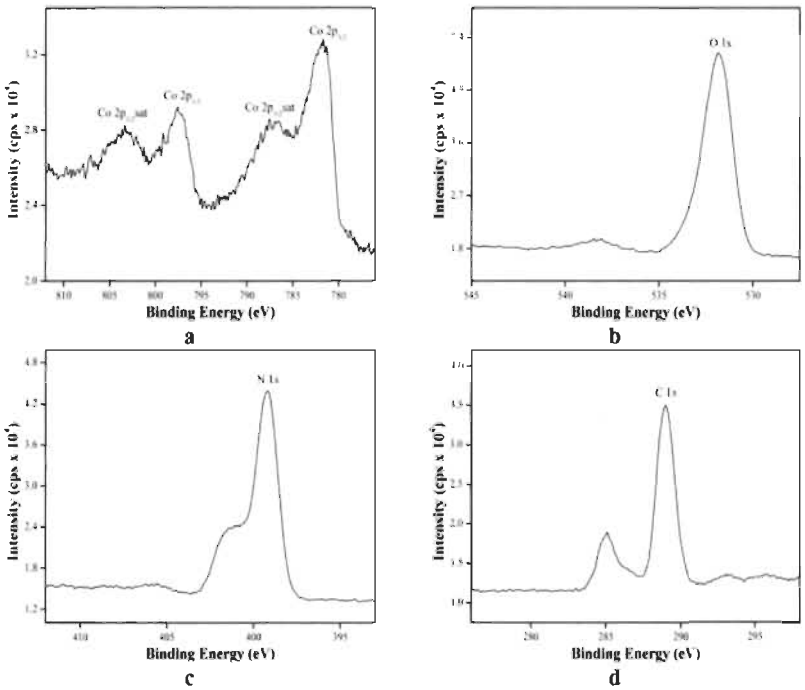

Figure S20. XPS patterns of MOP-2. a)-d) Narrow survey XPS in MOP-2 of Co $2p_{3/2}$, $2p_{3/2}$sat, $2p_{1/2}$ and $2p_{1/2}$sat; O 1s; N 1s; C 1s.

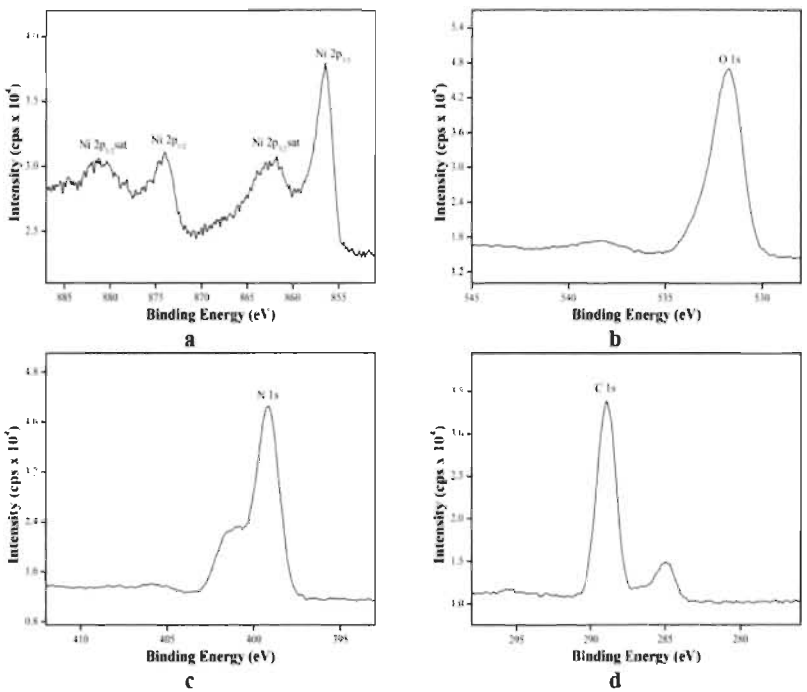

Figure S21. XPS patterns of MOP-**3**. a)-d) Narrow survey XPS in MOP-**3** of Ni $2p_{3/2}$, $2p_{3/2}$sat, $2p_{1/2}$ and $2p_{1/2}$sat; O 1s; N 1s; C 1s.

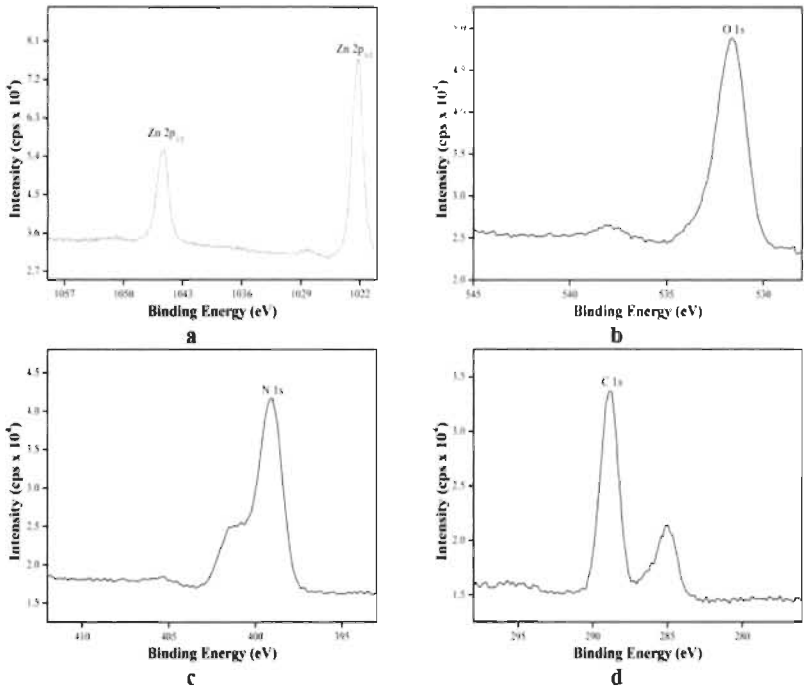

Figure S22. XPS patterns of MOP-4. a)-d) Narrow survey XPS in MOP-4 of Zn $2p_{3/2}$ and $2p_{1/2}$; O 1s; N 1s; C 1s.

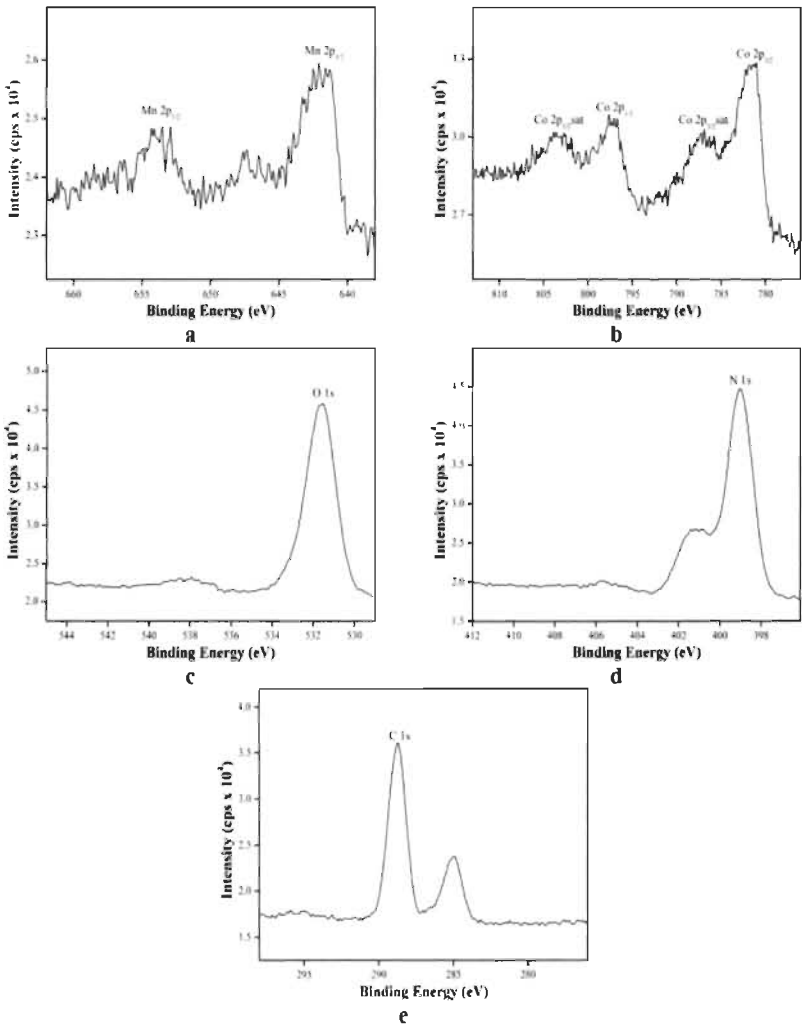

Figure S23. XPS patterns of MMOP-**5**. a)-e) Narrow survey XPS in MMOP-**5** of Mn $2p_{3/2}$ and $2p_{1/2}$; Co $2p_{3/2}$, $2p_{3/2}$sat, $2p_{1/2}$ and $2p_{1/2}$sat; O 1s; N1s; C 1s.

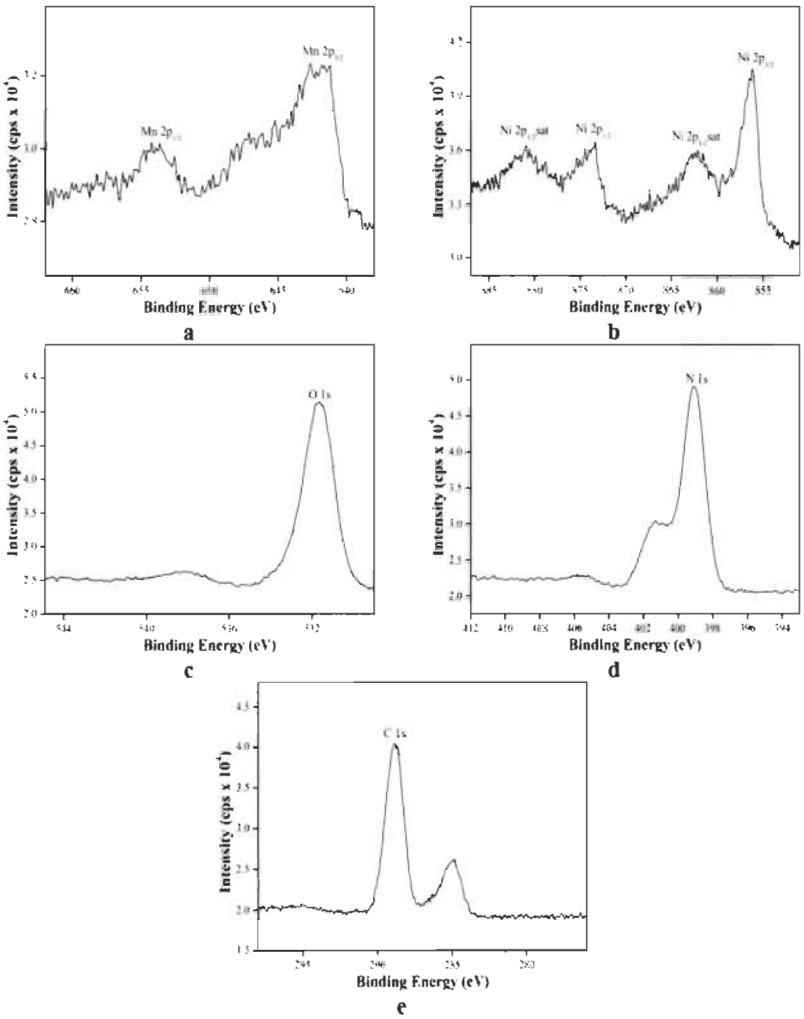

Figure S24. XPS patterns of MMOP-**6**. a)-e) Narrow survey XPS in MMOP-**6** of Mn $2p_{3/2}$ and $2p_{1/2}$; Ni $2p_{3/2}$, $2p_{3/2}$sat, $2p_{1/2}$ and $2p_{1/2}$sat; O 1s; N1s; C 1s.

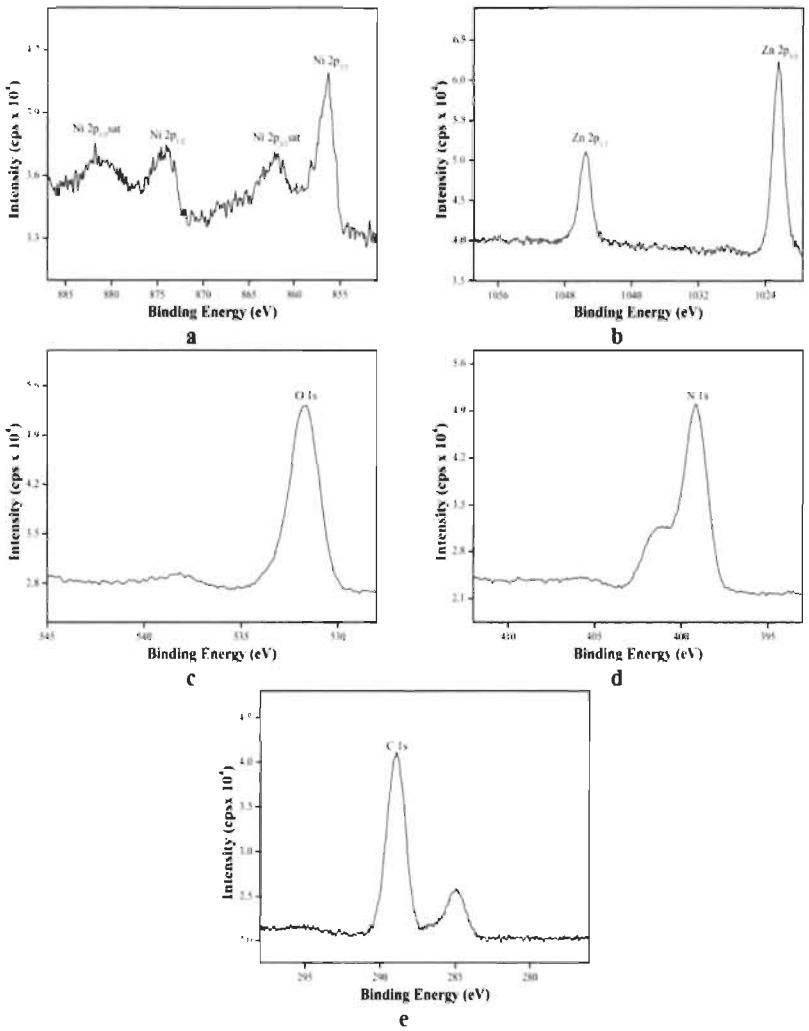

Figure S25. XPS patterns of MMOP-7. a)-e) Narrow survey XPS in MMOP-7 of Ni $2p_{3/2}$, $2p_{3/2}$sat, $2p_{1/2}$ and $2p_{1/2}$sat: Zn $2p_{3/2}$ and $2p_{1/2}$: O 1s: N1s: C 1s.

Table S13. Binding energy values (eV) of XPS elements peaks for MOPs-(**1-4**) and MMOPs-(**5-7**).

Element / Sample	Mn		Co				Ni				Zn		O	N	C
	$2p_{1/2}$	$2p_{3/2}$	$2p_{1/2sat}$	$2p_{1/2}$	$2p_{3/2sat}$	$2p_{3/2}$	$2p_{1/2sat}$	$2p_{1/2}$	$2p_{3/2sat}$	$2p_{3/2}$	$2p_{3/2}$	$2p_{1/2}$	1s	1s	1s
MOP-1	654	641		-				-			-		531	399	288
MOP-2		-	804	797	786	782		-			-		531	399	288
MOP-3		-		-			881	873	862	856			531	399	288
MOP-4		-		-				-			1022	1045	531	399	288
MMOP-5	654	641	804	797	786	782		-			-		531	399	288
MMOP-6	654	641		-			881	873	862	856	-		531	399	288
MMOP-7				-			881	873	862	856	1022	1045	531	399	288

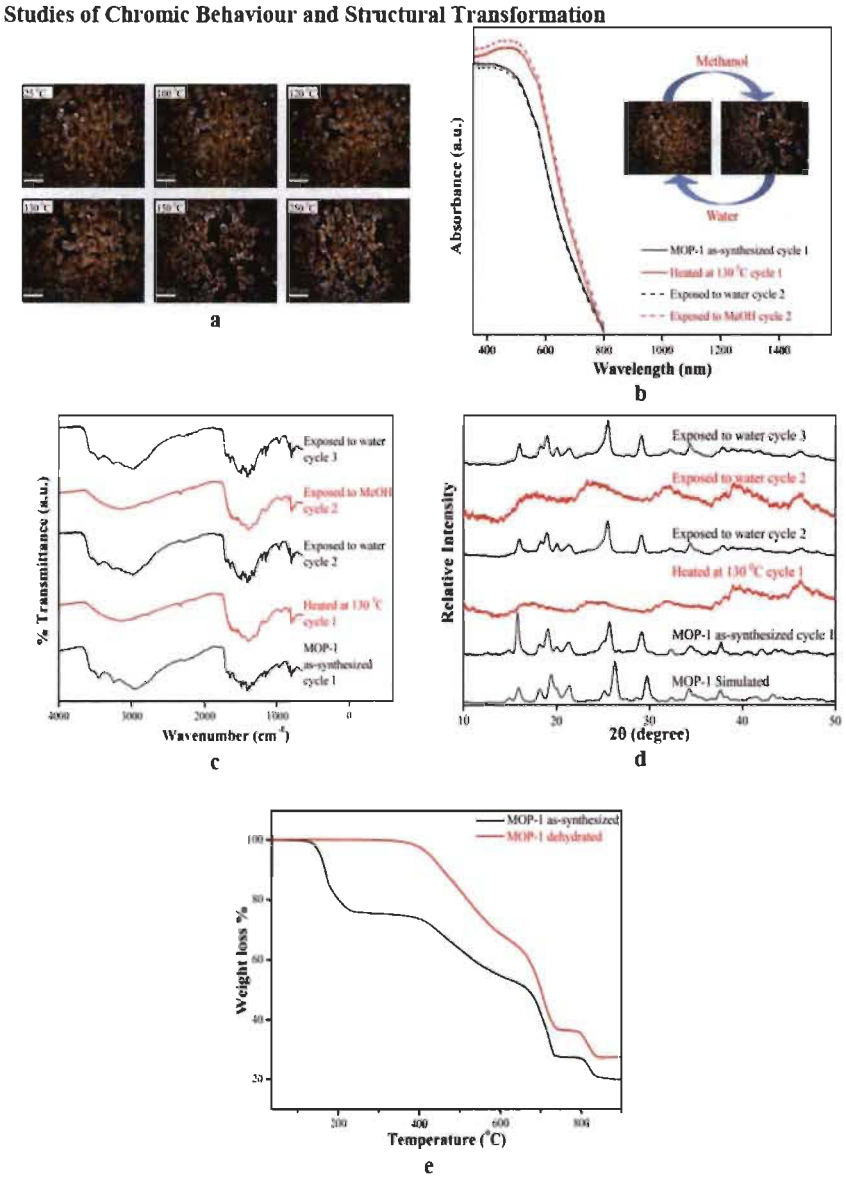

Figure S26. Chromic behaviour analysis of MOP-**1** using a) *In-situ* thermal microscopy images at different temperatures from 25-250 °C (scale bar: 500 μm); b) UV-Vis spectra changes for MOP-**1**. Black solid lines: MOP-**1** as synthesized; red solid lines: heated at 130 °C, black dash lines: sample on exposure in water and red dash lines: sample on exposure in methanol. Insert: chromism images of MOP-**1**; c) FTIR spectra of the MOP-**1** as-synthesized, heated at 130 °C, exposed to water and then exposed to methanol d) PXRD patterns of the samples taken at different cycles and the simulated patterns calculated from the single-crystal X-ray diffraction data. e) TG curves of MOP-**1** as synthesized and dehydrated. One cycle is referred to a process of dehydration followed by hydration.

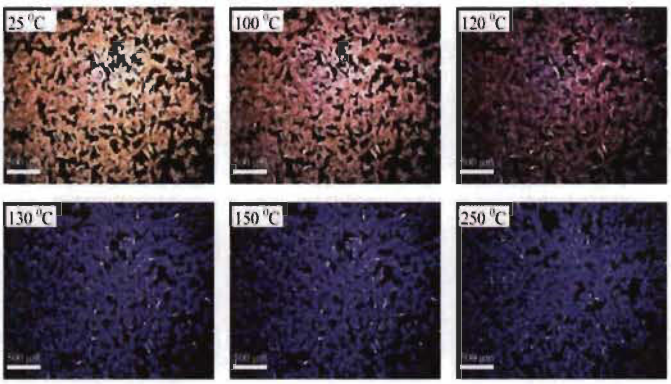

Figure S27. Chromic behaviour analysis of MOP-2 using *in-situ* thermal microscopy images at different temperatures from 25-250 °C (scale bar: 500 μm).

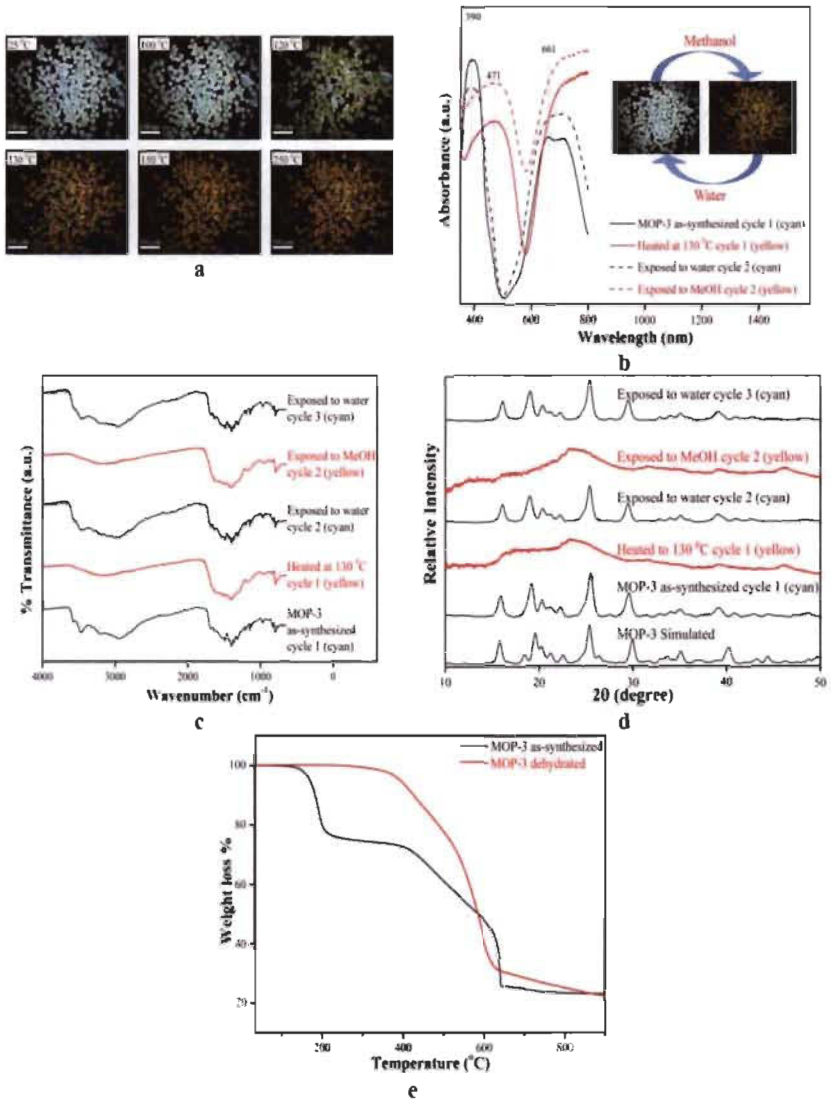

Figure S28. Chromic behaviour analysis of MOP-3 using. a) *In-situ* thermal microscopy images at different temperatures from 25-250 °C (scale bar: 500 μm); b) UV-Vis spectra changes for MOP-3. Black solid lines: MOP-3 as synthesized; red solid lines: heated at 130 °C, black dash lines: sample on exposure in water and red dash lines: sample on exposure in methanol. Insert: chromism images of MOP-3; c) FTIR spectra of the MOP-3 as-synthesized, heated at 130 °C, exposed to water and then exposed to methanol d) PXRD patterns of the samples taken at different cycles and the simulated patterns calculated from the single-crystal X-ray diffraction data. e) TG curves of MOP-3 as synthesized and dehydrated. One cycle is referred to a transformation that bring the cyan species to yellow species and return to the original colour.

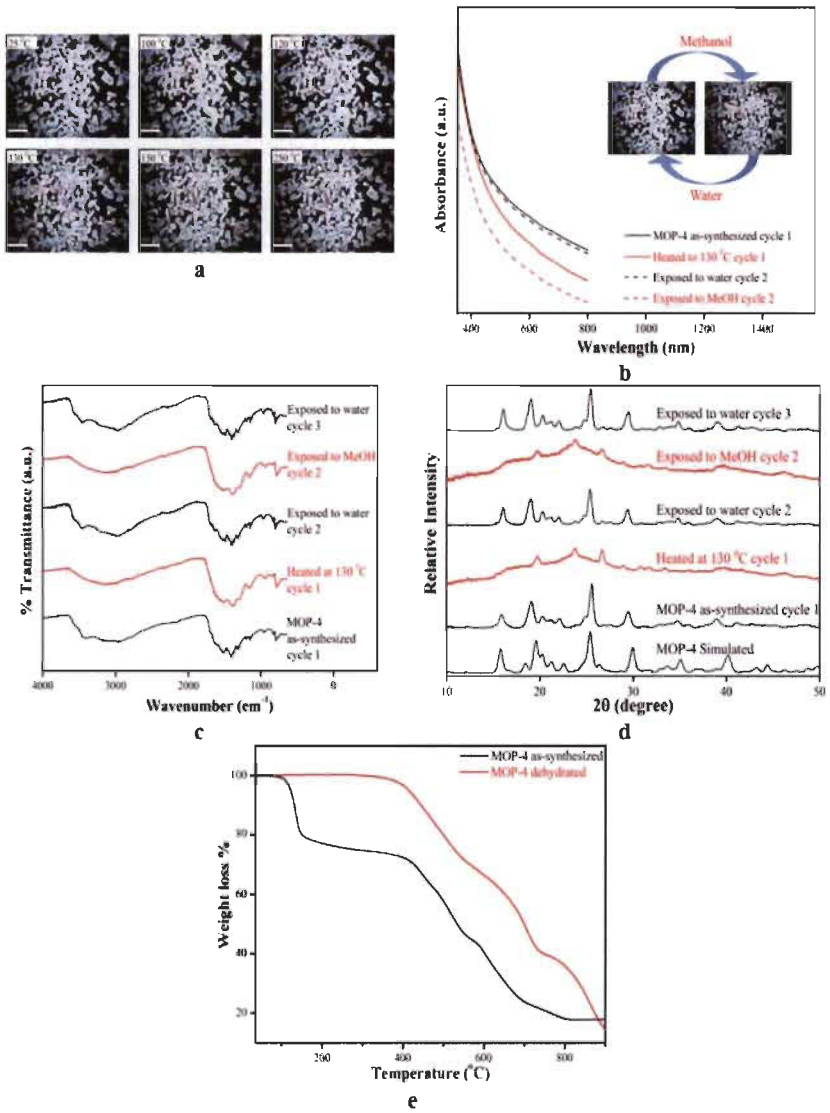

Figure S29. Chromic behaviour analysis of MOP-4 using. a) *In-situ* thermal microscopy images at different temperatures from 25-250 °C (scale bar: 500 μm); b) UV-Vis spectra changes for MOP-4. Black solid lines: MOP-4 as synthesized; red solid lines: heated at 130 °C, black dash lines: sample on exposure in water and red dash lines: sample on exposure in methanol. Insert: chromism images of MOP-4; c) FTIR spectra of the MOP-4 as-synthesized, heated at 130 °C, exposed to water and then exposed to methanol d) PXRD patterns of the samples taken at different cycles and the simulated patterns calculated from the single-crystal X-ray diffraction data. e) TG curves of MOP-4 as synthesized and dehydrated. One cycle is referred to a process of dehydration followed by hydration.

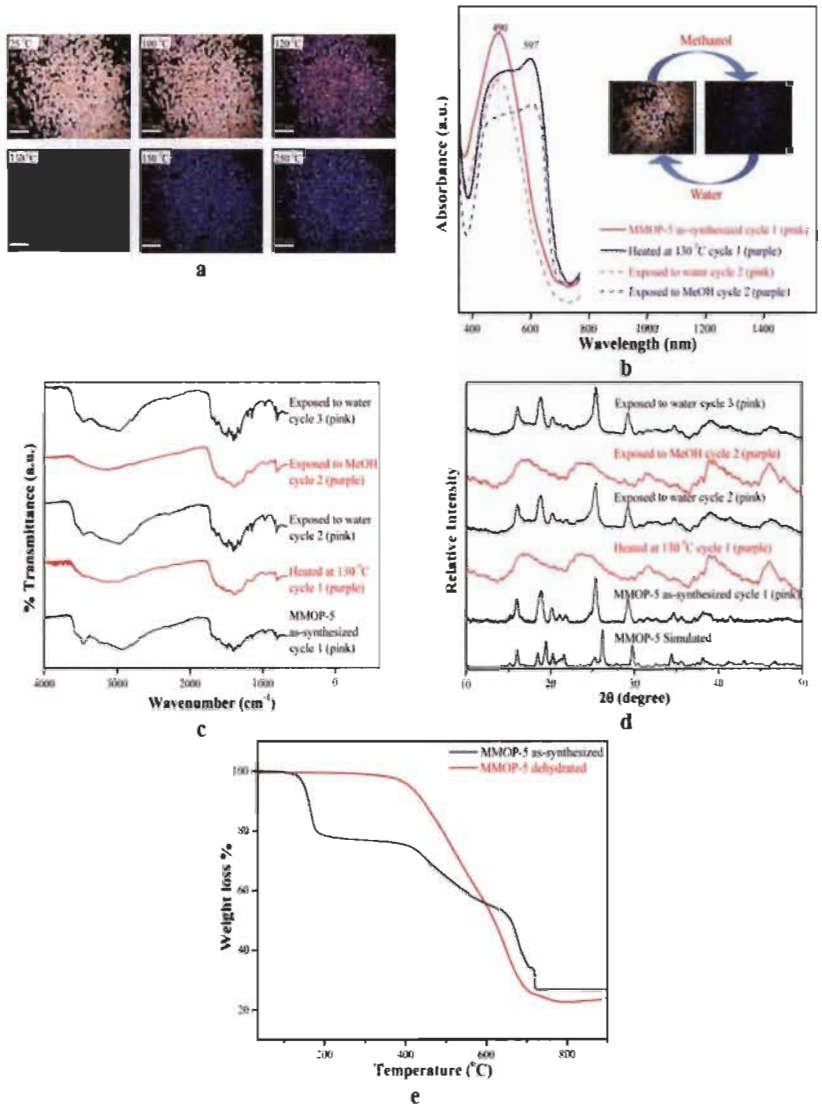

Figure S30. Chromic behaviour analysis of MMOP-**5** using. a) *In-situ* thermal microscopy images at different temperatures from 25-250 °C (scale bar: 500 μm); b) UV-Vis spectra changes for MMOP-**5**. Pink solid lines: MMOP-**5** as synthesized; purple solid lines: heated at 130 °C, pink dash lines: sample on exposure in water and purple dash lines: sample on exposure in methanol. Insert: chromism images of MMOP-**5**; c) FTIR spectra of the MMOP-**5** as-synthesized, heated at 130 °C, exposed to water and then exposed to methanol d) PXRD patterns of the samples taken at different cycles and the simulated patterns calculated from the single-crystal X-ray diffraction data. e) TG curves of MMOP-**5** as synthesized and dehydrated. One cycle is referred to a transformation that bring the pink species to purple species and return to the original colour.

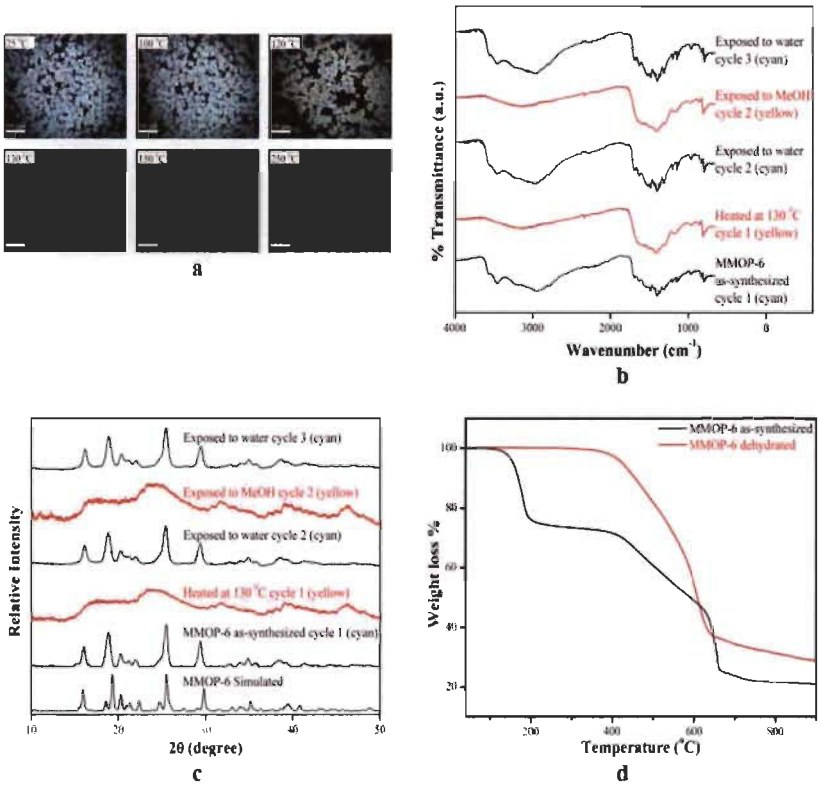

Figure S31. Chromic behaviour analysis of MMOP-6 using. a) *In-situ* thermal microscopy images at different temperatures from 25-250 °C (scale bar: 500 μm); b) FTIR spectra of the MMOP-6 as-synthesized, heated at 130 °C, exposed to water and then exposed to methanol c) PXRD patterns of the samples taken at different cycles and the simulated patterns calculated from the single-crystal X-ray diffraction data. d) TG curves of MMOP-6 as synthesized and dehydrated. One cycle is referred to a transformation that bring the cyan species to yellow species and return to the original colour.

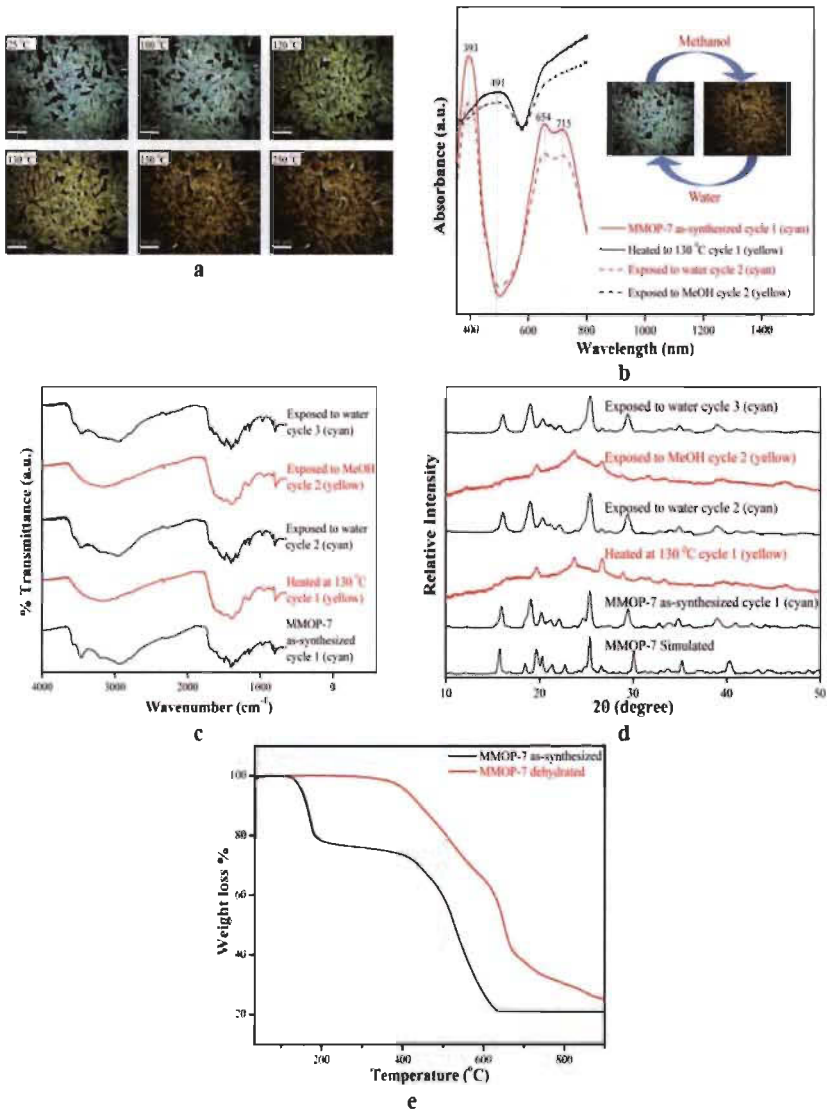

Figure S32. Chromic behaviour analysis of MMOP-7 using. a) *In-situ* thermal microscopy images at different temperatures from 25-250 °C (scale bar: 500 μm); b) UV-Vis spectra changes for MMOP-7. Black solid lines: MMOP-7 as synthesized; purple solid lines: heated at 130 °C, black dash lines: sample on exposure in water and red dash lines: sample on exposure in methanol. Insert: chromism images of MMOP-7; c) FTIR spectra of the MMOP-7 as-synthesized, heated at 130 °C, exposed to water and then exposed to methanol d) PXRD patterns of the samples taken at different cycles and the simulated patterns calculated from the single-crystal X-ray diffraction data. e) TG curves of MMOP-7 as synthesized and dehydrated. One cycle is referred to a transformation that bring the cyan species to yellow species and return to the original colour.

Appendix 5: Supplementary Information for Article 5

Supporting information

A Rational Design of Microporous Nitrogen-rich Lanthanide Metal-Organic Frameworks for CO_2/CH_4 separation

Midhun Mohan,[†] Mohamed Essalhi,[†] David Durette,[†] Love Karan Rana,[†] Follivi Kloutse Ayevide,[†] Thierry Maris[‡] and Adam Duong*[†]

[†]*Département de Chimie, Biochimie et physique* and *Institut de Recherche sur l'Hydrogène,* Université du Québec à Trois-Rivières, Trois-Rivières, Québec, G9A 5H7, Canada
[‡]*Département de Chimie,* Université de Montréal, Montréal, Québec, H3C 3J7, Canada

*To whom correspondence should be addressed. E-mail: adam.duong@uqtr.ca

Contents

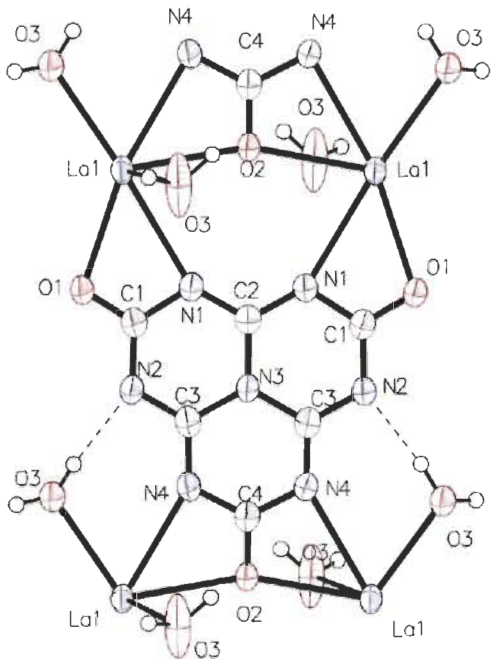

Figure S1. Thermal atomic displacement ellipsoid plot of **IRH-1.** The ellipsoids of non-hydrogen atoms are drawn at 50% probability level, and hydrogen atoms are represented by a sphere of arbitrary size.

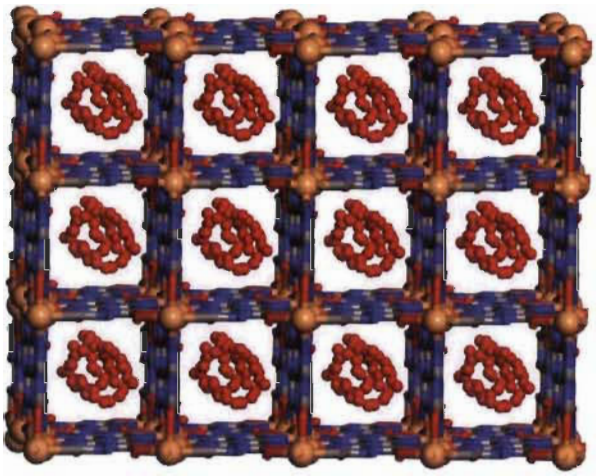

Figure S2. Crystal structure of **IRH-2.** Carbon atoms are shown in gray, oxygen atoms in red, nitrogen atoms in blue and Ce(III) ions in brown.

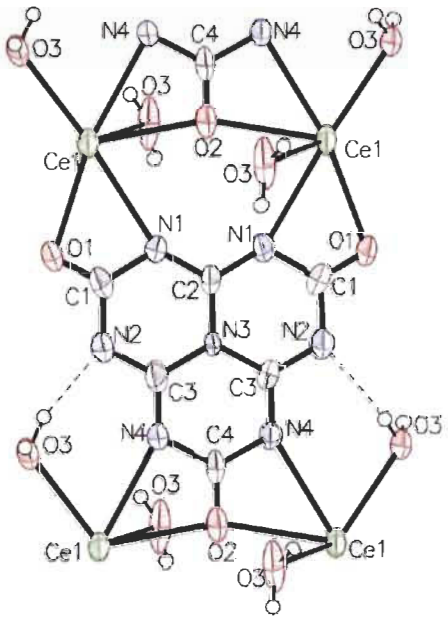

Figure S3. Thermal atomic displacement ellipsoid plot of **IRH-2**. The ellipsoids of non-hydrogen atoms are drawn at 50% probability level, and hydrogen atoms are represented by a sphere of arbitrary size.

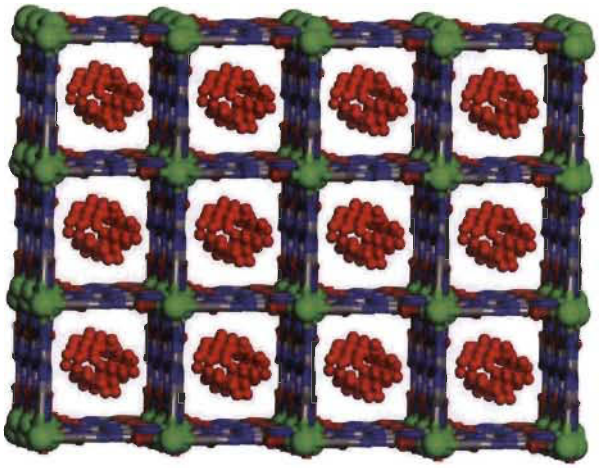

Figure S4. Crystal structure of IRH-**3**. Carbon atoms are shown in gray, oxygen atoms in red, nitrogen atoms in blue and Pr(III) ions in green.

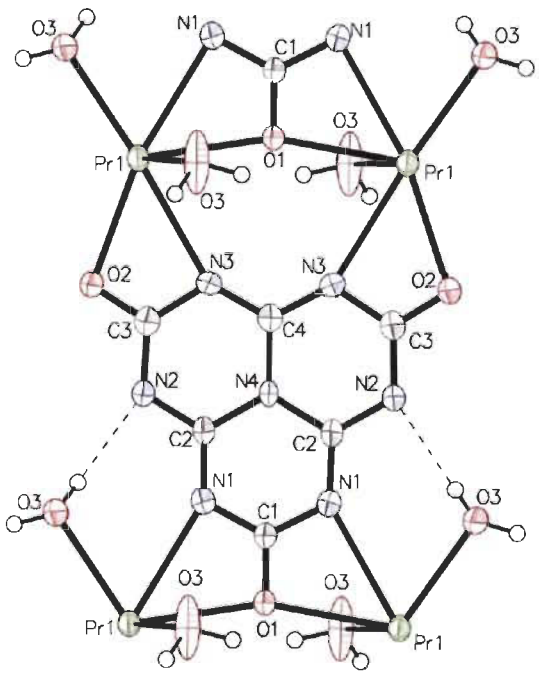

Figure S5. Thermal atomic displacement ellipsoid plot of **IRH-3**. The ellipsoids of non-hydrogen atoms are drawn at 50% probability level, and hydrogen atoms are represented by a sphere of arbitrary size.

Table S1. Crystallographic Data of IRHs-**(1-3)**.

	IRH-1	**IRH-2**	**IRH-3**
Cell Formula	$C_{24}H_{19}N_{28}O_{21.5}La_4$	$C_{24}H_{21}N_{28}O_{22.5}Ce_4$	$C_{24}H_{19}N_{28}O_{21.5}Pr_4$
Formula	$C_6H_{4.75}N_7O_{5.38}La$	$C_6H_{5.25}N_7O_{5.63}Ce$	$C_6H_{4.6}N_7O_{5.3}Pr$
CCDC Code	1880937	1880935	1880936
Crystal System	Tetragonal	Tetragonal	Tetragonal
Space group	$P4_322$	$P4_322$	$P4_322$
a /Å	8.7522(2)	8.7262(2)	8.6803(3)
b /Å	8.7522(2)	8.7262(2)	8.6803(3)
c /Å	20.2393(5)	20.1821(5)	20.1500(6)
α /°	90	90	90
β /°	90	90	90
γ /°	90	90	90
V /Å^3	1550.35(8)	1536.80(8)	1518.25(11)
Z	4	4	4
T (K)	150	150	150
x H_2O	0.38	0.63	0.30
Meas.	29243	44557	42995
Ind.	1772	1775	1748
Obs.	1736	1774	1745
R_{int}	0.0410	0.0358	0.0343
R_σ	0.0134	0.0098	0.0088
Param.	108	108	104
R_1 / I > 2s(I)	0.0289	0.0238	0.0161
wR_2 / I> 2s(I)	0.0736	0.0625	0.0436
R_1 (all data)	0.0294	0.0238	0.0162
wR_2 (all data)	0.0739	0.0625	0.0436
Flack parameter	0.473(19)	0.453(13)	0.417(11)

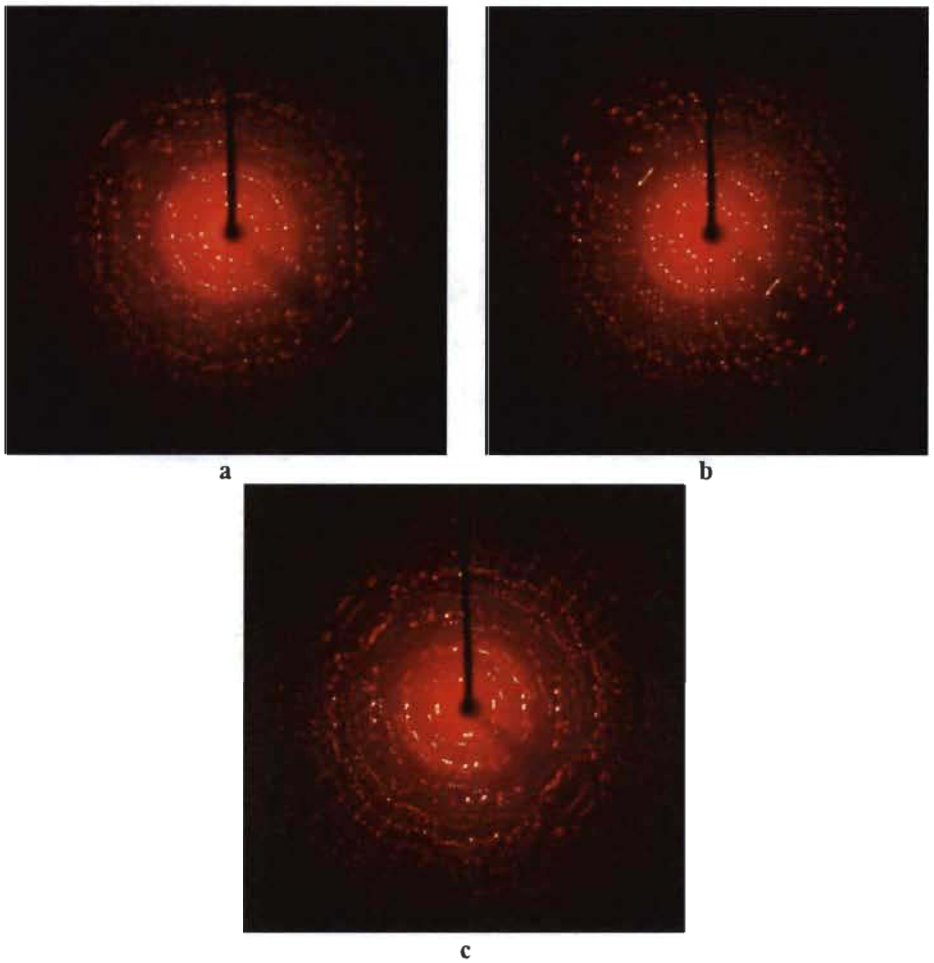

Figure S6. Diffraction patterns a)-c) IRHs-**(1-3)** respectively.

Table S2. Bond lengths (Å) observed in IRH-**1.**

Atoms	Length (Å)	Atoms	Length (Å)
La1 O1	2.561(3)	O1 C1	1.241(5)
La1 O1[1]	2.561(3)	O2 C4	1.254(7)
La1 O2[2]	2.5975(7)	N1 C1	1.371(5)
La1 O2[3]	2.5975(7)	N1 C2[6]	1.321(4)
La1 O3[1]	2.549(3)	N2 C1	1.364(5)
La1 O3	2.549(3)	N2 C3	1.313(5)
La1 N1	2.735(3)	N3 C2	1.400(8)
La1 N1[1]	2.735(3)	N3 C3[6]	1.400(5)
La1 N4[4]	2.705(4)	N3 C3	1.400(5)
La1 N4[5]	2.705(4)	N4 C3	1.329(6)
La1 C1	3.086(4)	N4 C4[6]	1.348(4)
La1 C1[1]	3.086(4)	O20 O2[2]	1.39(14)
La1 C4[3]	3.082(3)	O21 O2[3]	1.7(2)
La1 C4[2]	3.082(3)		

Symmetry codes : [1]1+y,-1+x,5/4-z; [2]+y,1-x,1/4+z; [3]2-x,-1+y,1-z; [4]+x,-1+y,+z; [5]+y,-1+x,5/4-z; [6]2-x,+y,1-z

Table S3. Bond angles ([0]) observed in IRH-**1.**

Atoms	Angle ([0])	Atoms	Angle ([0])
O1[1] La1 O1	95.7(2)	C1[1] La1 N4[4]	89.40(18)
O2[2] La1 O1[1]	63.71(6)	C1[1] La1 C1	85.9(2)
O2[3] La1 O1	63.71(6)	C4[2] La1 O1[1]	68.13(9)
O2[2] La1 O1	118.99(10)	C4[3] La1 O1[1]	142.53(11)
O2[3] La1 O1[1]	118.99(10)	C4[2] La1 O1	142.53(11)
O2[3] La1 O2[2]	176.43(11)	C4[3] La1 O1	68.13(9)
O3[1] La1 O1	126.20(9)	C4[2] La1 O2[3]	153.75(9)
O3[1] La1 O1[1]	100.1(2)	C4[3] La1 O2[3]	23.59(13)
O3 La1 O1[1]	126.20(9)	C4[3] La1 O2[2]	153.75(9)
O3 La1 O1	100.1(2)	C4[2] La1 O2[2]	23.59(13)
O3[1] La1 O2[3]	63.60(8)	C4[2] La1 O3	68.27(11)
O3 La1 O2[3]	114.14(11)	C4[3] La1 O3	90.66(11)
O3 La1 O2[2]	63.60(8)	C4[3] La1 O3[1]	68.27(11)
O3[1] La1 O2[2]	114.14(11)	C4[2] La1 O3[1]	90.66(11)
O3[1] La1 O3	110.3(3)	C4[3] La1 N1	111.23(10)
N1 La1 O1[1]	75.97(15)	C4[2] La1 N1[1]	111.23(10)
N1[1] La1 O1	75.97(15)	C4[2] La1 N1	93.18(11)
N1 La1 O1	49.45(9)	C4[3] La1 N1[1]	93.18(11)
N1[1] La1 O1[1]	49.45(9)	C4[2] La1 N4[4]	25.91(11)
N1 La1 O2[2]	69.60(10)	C4[3] La1 N4[5]	25.91(11)

$N1^{1}$ La1 $O2^{2}$	112.96(7)	$C4^{2}$ La1 $N4^{5}$	123.44(11)
$N1^{1}$ La1 $O2^{3}$	69.60(10)	$C4^{3}$ La1 $N4^{4}$	123.44(11)
N1 La1 $O2^{3}$	112.96(7)	$C4^{2}$ La1 C1	119.52(11)
$N1^{1}$ La1 $O3^{1}$	76.55(16)	$C4^{2}$ La1 $C1^{1}$	88.10(9)
$N1^{1}$ La1 O3	173.01(19)	$C4^{3}$ La1 $C1^{1}$	119.52(11)
N1 La1 $O3^{1}$	173.01(19)	$C4^{3}$ La1 C1	88.10(9)
N1 La1 O3	76.55(16)	$C4^{3}$ La1 $C4^{2}$	143.41(12)
$N1^{1}$ La1 N1	96.6(2)	C1 O1 $La1^{1}$	102.9(2)
$N4^{4}$ La1 $O1^{1}$	76.47(16)	$La1^{6}$ O2 $La1^{7}$	159.17(16)
$N4^{5}$ La1 $O1^{1}$	168.06(11)	C4 O2 $La1^{6}$	100.42(8)
$N4^{4}$ La1 O1	168.06(11)	C4 O2 $La1^{7}$	100.42(8)
$N4^{5}$ La1 O1	76.47(16)	C1 N1 La1	91.3(2)
$N4^{4}$ La1 $O2^{3}$	127.95(7)	$C2^{8}$ N1 La1	149.9(3)
$N4^{5}$ La1 $O2^{2}$	127.95(7)	$C2^{8}$ N1 C1	118.8(4)
$N4^{4}$ La1 $O2^{2}$	49.50(11)	C3 N2 C1	117.5(4)
$N4^{5}$ La1 $O2^{3}$	49.50(11)	$C3^{8}$ N3 C2	119.6(2)
$N4^{5}$ La1 $O3^{1}$	77.98(16)	C3 N3 C2	119.6(2)
$N4^{4}$ La1 $O3^{1}$	64.80(11)	C3 N3 $C3^{8}$	120.8(5)
$N4^{4}$ La1 O3	77.98(16)	C3 N4 $La1^{9}$	149.2(3)
$N4^{5}$ La1 O3	64.80(11)	$C4^{8}$ N4 $La1^{9}$	92.9(3)
$N4^{4}$ La1 N1	119.08(10)	$C4^{8}$ N4 C3	118.0(4)
$N4^{5}$ La1 $N1^{1}$	119.08(10)	O1 C1 La1	54.0(2)
$N4^{4}$ La1 $N1^{1}$	104.6(2)	N1 C1 La1	62.4(2)
$N4^{5}$ La1 N1	104.6(2)	N1 C1 O1	116.4(4)
$N4^{5}$ La1 $N4^{4}$	112.6(3)	N2 C1 La1	173.2(3)
$C1^{1}$ La1 $O1^{1}$	23.09(9)	N2 C1 O1	119.7(4)
C1 La1 O1	23.09(9)	N2 C1 N1	123.9(4)
$C1^{1}$ La1 O1	86.43(15)	N1 C2 $N1^{8}$	121.7(5)
C1 La1 $O1^{1}$	86.43(15)	N3 C2 $N1^{8}$	119.1(3)
$C1^{1}$ La1 $O2^{3}$	95.94(11)	N3 C2 N1	119.1(3)
C1 La1 $O2^{2}$	95.94(11)	$N3^{8}$ C3 N2	120.9(4)
$C1^{1}$ La1 $O2^{2}$	86.68(7)	N4 C3 N2	120.2(4)
C1 La1 $O2^{3}$	86.68(7)	N4 C3 $N3^{8}$	118.8(4)
C1 La1 $O3^{1}$	149.07(10)	$La1^{6}$ C4 $La1^{7}$	111.99(18)
C1 La1 O3	88.77(19)	O2 C4 $La1^{7}$	56.00(9)
$C1^{1}$ La1 O3	149.07(10)	O2 C4 $La1^{6}$	56.00(9)
$C1^{1}$ La1 $O3^{1}$	88.77(19)	$N4^{8}$ C4 $La1^{6}$	173.1(3)
C1 La1 $N1^{1}$	85.53(17)	$N4^{8}$ C4 $La1^{7}$	61.2(2)
$C1^{1}$ La1 $N1^{1}$	26.37(10)	N4 C4 $La1^{6}$	61.2(2)
C1 La1 N1	26.37(10)	N4 C4 $La1^{7}$	173.1(3)
$C1^{1}$ La1 N1	85.53(17)	$N4^{8}$ C4 O2	117.2(3)
C1 La1 $N4^{5}$	89.40(18)	N4 C4 O2	117.2(3)
$C1^{1}$ La1 $N4^{5}$	145.37(11)	N4 C4 $N4^{8}$	125.6(5)

C1 La1 N4[4]	145.37(11)	

Symmetry codes : [1]1+y,-1+x,5/4-z; [2]2-x,-1+y,1-z; [3]+y,1-x,1/4+z; [4]+x,-1+y,+z; [5]+y,-1+x,5/4-z; [6]1+y,+x,5/4-z; [7]2-x,1+y,1-z; [8]2-x,+y,1-z; [9]+x,1+y,+z

Table S4. Hydrogen bond geometry (Å, °) of IRH-**1.**

D—H···*A*	D—H	H···A	D···A	D—H···A
O3—H3a···N2[1]	0.8784	1.93(3)	2.769(5)	158(6)
O3—H3b···O1[2]	0.878	2.22(6)	2.798(4)	123(5)

Symmetry codes: [1]+y,-1+x,5/4-z; [2]1-y,-1+x,-1/4+z

Table S5. Bond lengths (Å) observed in IRH-**2.**

Atoms	Length (Å)	Atoms	Length (Å)
Ce1 O1[1]	2.565(10)	O1 C1	1.197(17)
Ce1 O1	2.565(10)	C1 N1	1.375(16)
Ce1 C1[1]	3.030(15)	C1 N2	1.40(2)
Ce1 C1	3.030(15)	N1 C2	1.334(14)
Ce1 N1[1]	2.709(11)	C2 C3	1.39(3)
Ce1 N1	2.709(11)	N2 C4	1.316(18)
Ce1 O2[2]	2.587(3)	O2 C5	1.23(3)
Ce1 O2[3]	2.587(3)	C3 C4	1.387(15)
Ce1 O3[1]	2.540(11)	C3 C4[5]	1.387(15)
Ce1 O3	2.540(11)	N3 C4	1.32(2)
Ce1 N3[2]	2.706(11)	N3 C5	1.383(15)
Ce1 N3[4]	2.706(11)		

Symmetry codes : [1]-y,-x,5/4-z; [2]+x,-1+y,+z; [3]1-y,+x,1/4+z; [4]1-y,-x,5/4-z; [5]-x,+y,1-z

Table S6. Bond angles ([0]) observed in IRH-**2**.

Atoms	Angle ([0])	Atoms	Angle ([0])
O1[1] Ce1 O1	95.5(7)	O3[1] Ce1 O2[2]	114.7(4)
O1 Ce1 C1	22.8(3)	O3 Ce1 O3[1]	110.7(9)
O1 Ce1 C1[1]	86.7(5)	O3[1] Ce1 N3[2]	64.6(3)
O1[1] Ce1 C1	86.7(5)	O3[1] Ce1 N3[4]	77.5(5)
O1[1] Ce1 C1[1]	22.8(3)	O3 Ce1 N3[4]	64.6(3)
O1[1] Ce1 N1	75.5(5)	O3 Ce1 N3[2]	77.5(5)
O1[1] Ce1 N1[1]	49.8(3)	N3[2] Ce1 C1[1]	89.8(6)

O1 Ce1 N1	49.8(3)	$N3^4$ Ce1 C1	89.8(6)
O1 Ce1 $N1^1$	75.5(5)	$N3^2$ Ce1 C1	146.3(3)
O1 Ce1 $O2^2$	118.8(4)	$N3^4$ Ce1 $C1^1$	146.3(3)
$O1^1$ Ce1 $O2^3$	118.8(4)	$N3^2$ Ce1 $N1^1$	105.5(7)
$O1^1$ Ce1 $O2^2$	63.6(2)	$N3^4$ Ce1 N1	105.5(7)
O1 Ce1 $O2^3$	63.6(2)	$N3^4$ Ce1 $N1^1$	119.4(3)
O1 Ce1 $N3^2$	168.8(4)	$N3^2$ Ce1 N1	119.4(3)
$O1^1$ Ce1 $N3^2$	77.5(5)	$N3^2$ Ce1 $N3^4$	110.7(8)
O1 Ce1 $N3^4$	77.5(5)	C1 O1 Ce1	101.0(8)
$O1^1$ Ce1 $N3^4$	168.8(4)	O1 C1 Ce1	56.2(7)
C1 Ce1 $C1^1$	86.4(7)	O1 C1 N1	119.5(13)
N1 Ce1 C1	27.0(3)	O1 C1 N2	118.9(12)
N1 Ce1 $C1^1$	85.4(5)	N1 C1 Ce1	63.4(7)
$N1^1$ Ce1 C1	85.4(5)	N1 C1 N2	121.6(13)
$N1^1$ Ce1 $C1^1$	27.0(3)	N2 C1 Ce1	174.7(11)
$N1^1$ Ce1 N1	96.4(8)	C1 N1 Ce1	89.6(8)
$O2^3$ Ce1 $C1^1$	96.0(4)	C2 N1 Ce1	151.5(10)
$O2^3$ Ce1 C1	86.3(3)	C2 N1 C1	118.8(13)
$O2^2$ Ce1 $C1^1$	86.3(3)	N1 C2 $N1^5$	118.9(18)
$O2^2$ Ce1 C1	96.0(4)	$N1^5$ C2 C3	120.5(9)
$O2^3$ Ce1 $N1^1$	69.0(4)	N1 C2 C3	120.5(9)
$O2^2$ Ce1 N1	69.0(4)	C4 N2 C1	118.5(13)
$O2^2$ Ce1 $N1^1$	113.2(3)	$Ce1^6$ O2 $Ce1^7$	159.8(7)
$O2^3$ Ce1 N1	113.2(3)	C5 O2 $Ce1^6$	100.1(3)
$O2^2$ Ce1 $O2^3$	176.8(5)	C5 O2 $Ce1^7$	100.1(3)
$O2^3$ Ce1 $N3^2$	127.4(2)	$C4^5$ C3 C2	119.4(9)
$O2^2$ Ce1 $N3^4$	127.4(2)	C4 C3 C2	119.4(9)
$O2^3$ Ce1 $N3^4$	50.3(4)	C4 C3 $C4^5$	121.1(17)
$O2^2$ Ce1 $N3^2$	50.3(4)	C4 N3 $Ce1^6$	150.6(10)
O3 Ce1 $O1^1$	125.9(3)	C4 N3 C5	118.6(13)
O3 Ce1 O1	100.3(6)	C5 N3 $Ce1^6$	90.8(9)
$O3^1$ Ce1 O1	125.9(3)	N2 C4 C3	121.1(13)
$O3^1$ Ce1 $O1^1$	100.3(6)	N2 C4 N3	119.3(13)
$O3^1$ Ce1 $C1^1$	88.6(6)	N3 C4 C3	119.5(14)
$O3^1$ Ce1 C1	148.5(3)	$Ce1^6$ C5 $Ce1^7$	112.9(7)
O3 Ce1 $C1^1$	148.5(3)	O2 C5 $Ce1^7$	56.5(3)
O3 Ce1 C1	88.6(6)	O2 C5 $Ce1^6$	56.5(3)
$O3^1$ Ce1 N1	172.8(6)	O2 C5 N3	118.8(9)
O3 Ce1 N1	76.5(5)	O2 C5 $N3^5$	118.8(9)
$O3^1$ Ce1 $N1^1$	76.5(5)	$N3^5$ C5 $Ce1^7$	62.3(6)
O3 Ce1 $N1^1$	172.8(6)	N3 C5 $Ce1^6$	62.3(6)
$O3^1$ Ce1 $O2^3$	63.3(2)	N3 C5 $Ce1^7$	175.2(12)
O3 Ce1 $O2^3$	114.7(4)	$N3^5$ C5 $Ce1^6$	175.2(12)

O3 Ce1 O2[2]	63.3(2)	N3 C5 N3[5]	122.4(18)

Symmetry codes : [1]-y, -x, 5/4-z; [2]+x, -1+y,+z; [3]1-y, +x, 1/4+z; [4]1-y, -x,5/4-z; [5]-x, +y,1-z; [6]-x,1+y,+z; [7]+y, 1-x, -1/4+z

Table S7. Hydrogen bond geometry (Å, °) of IRH-**2.**

D*—H···*A	**D—H**	**H···A**	**D···A**	**D—H···A**
O3—H3a···N2[1]	0.90	2.11	2.783(16)	131.1

Symmetry codes : [1]1-y, -x, 5/4-z

Table S8. Bond lengths (Å) observed in IRH-**3.**

Atoms	**Length (Å)**	**Atoms**	**Length (Å)**
Pr1 O1[1]	2.5789(8)	C1 O1	1.265(9)
Pr1 O1	2.5789(8)	C1 N1	1.344(6)
Pr1 N1	2.677(5)	C1 N1[5]	1.344(6)
Pr1 N1[2]	2.677(5)	N1 C2	1.314(8)
Pr1 C3[3]	3.046(6)	C2 N2	1.333(7)
Pr1 C3[4]	3.046(6)	C2 N4	1.407(6)
Pr1 N3[3]	2.686(5)	N2 C3	1.349(8)
Pr1 N3[4]	2.686(5)	C3 N3	1.364(7)
Pr1 O2[4]	2.519(4)	C3 O2	1.243(7)
Pr1 O2[3]	2.519(4)	N3 C4	1.325(6)
Pr1 O3[2]	2.496(5)	N4 C4	1.410(11)
Pr1 O3	2.496(4)		

Symmetry codes : [1]-1+y, 1-x, 1/4+z; [2]1-y, 1-x, 3/4-z; [3]1-y, 2-x, 3/4-z; [4]-1+x, +y, +z; [5]+x, 2-y, 1/2-z

Table S9. Bond angles ([0]) observed in IRH-**3.**

Atoms	**Angle ([0])**	**Atoms**	**Angle ([0])**
O1[1] Pr1 O1	177.52(15)	O3[2] Pr1 N1	65.22(15)
O1[1] Pr1 N1	128.05(11)	O3 Pr1 N1[2]	65.22(15)
O1[1] Pr1 N1[2]	50.16(15)	O3 Pr1 C3[3]	148.68(15)
O1 Pr1 N1	50.16(15)	O3[2] Pr1 C3[4]	148.68(15)
O1 Pr1 N1[2]	128.05(11)	O3[2] Pr1 C3[3]	88.2(3)
O1 Pr1 C3[3]	86.48(11)	O3 Pr1 C3[4]	88.2(3)
O1[1] Pr1 C3[3]	95.33(15)	O3 Pr1 N3[3]	172.6(3)
O1[1] Pr1 C3[4]	86.48(11)	O3[2] Pr1 N3[4]	172.6(3)

O1 Pr1 C3^{4}	95.33(15)	O3 Pr1 N3^{4}	76.1(2)
O1 Pr1 N3^{3}	113.05(10)	O3^{2} Pr1 N3^{3}	76.1(2)
O1 Pr1 N3^{4}	68.73(14)	O3^{2} Pr1 O2^{3}	99.6(3)
O1^{1} Pr1 N3^{4}	113.05(10)	O3^{2} Pr1 O2^{4}	125.47(13)
O1^{1} Pr1 N3^{3}	68.73(14)	O3 Pr1 O2^{3}	125.47(13)
N1^{2} Pr1 N1	111.8(4)	O3 Pr1 O2^{4}	99.6(3)
N1 Pr1 C3^{4}	145.46(15)	O3 Pr1 O3^{2}	111.2(4)
N1^{2} Pr1 C3^{3}	145.46(15)	Pr1^{5} C1 Pr1	112.7(2)
N1 Pr1 C3^{3}	89.6(3)	O1 C1 Pr1	56.34(11)
N1^{2} Pr1 C3^{4}	89.6(3)	O1 C1 Pr1^{5}	56.34(11)
N1^{2} Pr1 N3^{4}	105.2(3)	O1 C1 N1^{6}	117.4(4)
N1 Pr1 N3^{3}	105.2(3)	O1 C1 N1	117.4(4)
N1 Pr1 N3^{4}	118.88(14)	N1 C1 Pr1^{5}	173.7(4)
N1^{2} Pr1 N3^{3}	118.89(14)	N1^{6} C1 Pr1	173.7(4)
C3^{4} Pr1 C3^{3}	86.5(3)	N1^{6} C1 Pr1^{5}	61.0(3)
N3^{3} Pr1 C3^{4}	85.7(2)	N1 C1 Pr1	61.0(3)
N3^{4} Pr1 C3^{4}	26.60(14)	N1 C1 N1^{6}	125.2(7)
N3^{4} Pr1 C3^{3}	85.7(2)	Pr1^{5} O1 Pr1	160.9(2)
N3^{3} Pr1 C3^{3}	26.60(14)	C1 O1 Pr1	99.56(11)
N3^{4} Pr1 N3^{3}	96.6(3)	C1 O1 Pr1^{5}	99.56(11)
O2^{4} Pr1 O1^{1}	63.09(9)	C1 N1 Pr1	92.9(4)
O2^{4} Pr1 O1	118.76(14)	C2 N1 Pr1	148.8(4)
O2^{3} Pr1 O1	63.09(9)	C2 N1 C1	118.3(5)
O2^{3} Pr1 O1^{1}	118.76(14)	N1 C2 N2	121.1(5)
O2^{4} Pr1 N1	168.72(15)	N1 C2 N4	119.5(6)
O2^{4} Pr1 N1^{2}	76.2(2)	N2 C2 N4	119.3(5)
O2^{3} Pr1 N1	76.2(2)	C2 N2 C3	118.3(5)
O2^{3} Pr1 N1^{2}	168.72(15)	N2 C3 Pr1^{7}	173.6(5)
O2^{4} Pr1 C3^{4}	23.46(13)	N2 C3 N3	124.3(5)
O2^{4} Pr1 C3^{3}	87.3(2)	N3 C3 Pr1^{7}	61.8(3)
O2^{3} Pr1 C3^{4}	87.3(2)	O2 C3 Pr1^{7}	53.8(3)
O2^{3} Pr1 C3^{3}	23.46(13)	O2 C3 N2	120.1(5)
O2^{4} Pr1 N3^{3}	76.2(2)	O2 C3 N3	115.6(5)
O2^{3} Pr1 N3^{3}	50.06(13)	C3 N3 Pr1^{7}	91.6(3)
O2^{4} Pr1 N3^{4}	50.06(13)	C4 N3 Pr1^{7}	149.0(4)
O2^{3} Pr1 N3^{4}	76.2(2)	C4 N3 C3	119.4(5)
O2^{3} Pr1 O2^{4}	97.2(3)	C3 O2 Pr1^{7}	102.8(3)
O3 Pr1 O1^{1}	115.13(15)	C2^{6} N4 C2	119.2(7)
O3^{2} Pr1 O1	115.13(15)	C2^{6} N4 C4	120.4(3)
O3 Pr1 O1	63.31(11)	C2 N4 C4	120.4(3)
O3^{2} Pr1 O1^{1}	63.31(11)	N3^{6} C4 N3	123.5(7)
O3 Pr1 N1	77.6(2)	N3 C4 N4	118.3(4)
O3^{2} Pr1 N1^{2}	77.6(2)	N3^{6} C4 N4	118.3(4)

Symmetry codes : [1]-1+y, 1-x, 1/4+z; [2]1-y, 1-x, 3/4-z; [3]1-y, 2-x, 3/4-z; [4]-1+x, +y, +z; [5]1-y, 1+x, -1/4+z; [6]+x, 2-y, 1/2-z; [7]1+x, +y, +z

Table S10. Hydrogen bond geometry (Å, °) of IRH-**3.**

D—H···*A*	D—H	H···A	D···A	D—H···A
O3—H3a···O2[1]	0.88	1.96	2.790(6)	155.7
O3—H3b···N2[2]	0.88	2.19	2.771(6)	122.5

Symmetry codes : [1]1-y, +x, -1/4+z; [2]1-y, 1-x, 3/4-z

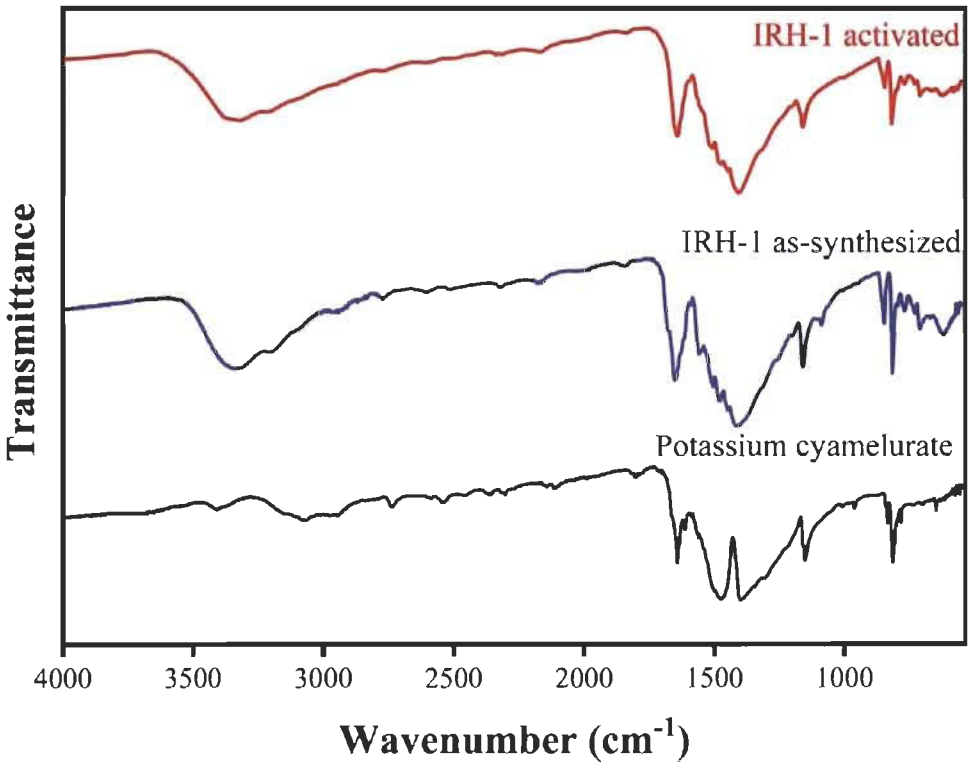

Figure S7. Comparison of FT-IR spectra of IRH-**1** as-synthesized and activated, and potassium cyamelurate.

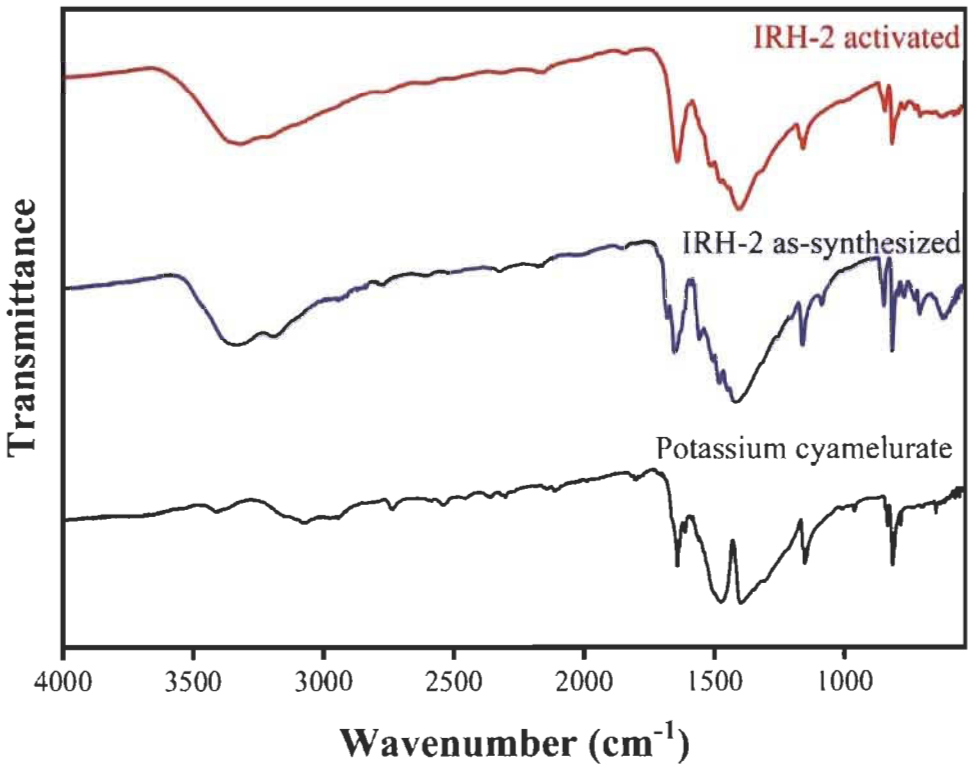

Figure S8. Comparison of FT-IR spectra of IRH-**2** as-synthesized and activated, and potassium cyamelurate.

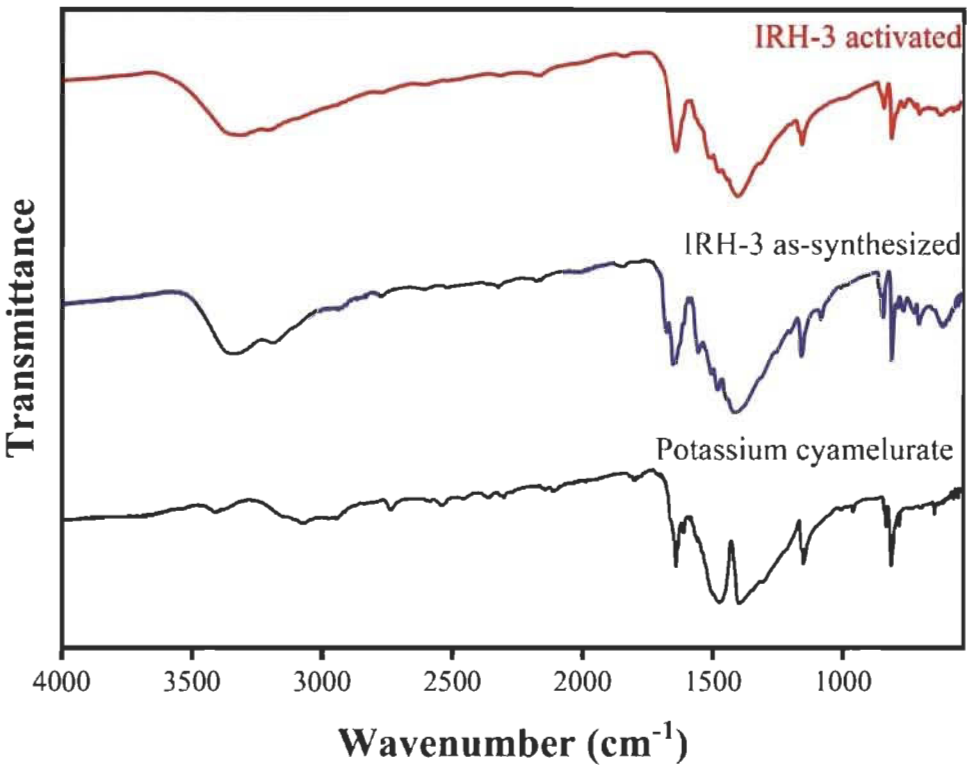

Figure S9. Comparison of FT-IR spectra of IRH-**3** as-synthesized and activated, and potassium cyamelurate.

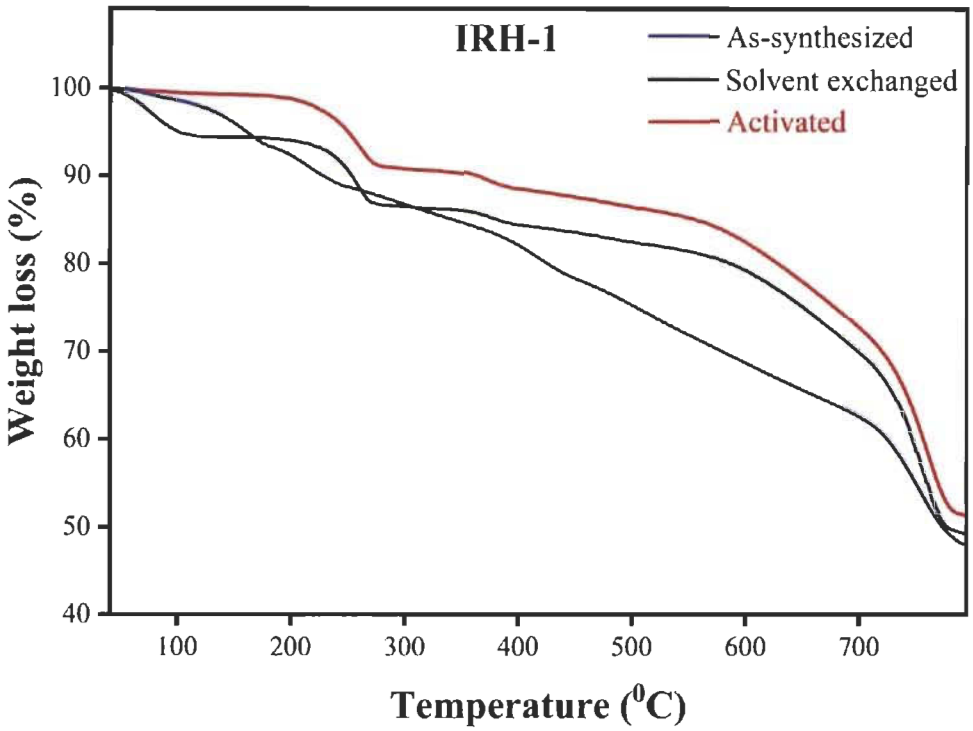

Figure S10. Thermogravimetric analysis curve of IRH-**1** as-synthesized, solvent exchange and activated.

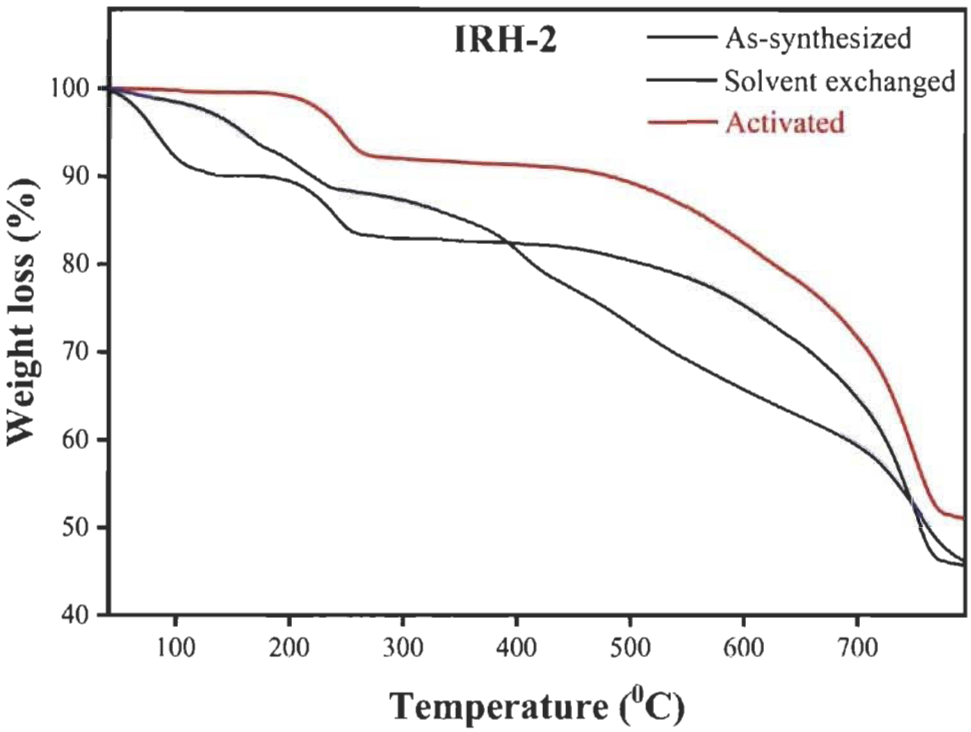

Figure S11. Thermogravimetric analysis curve of IRH-**2** as-synthesized, solvent exchange and activated.

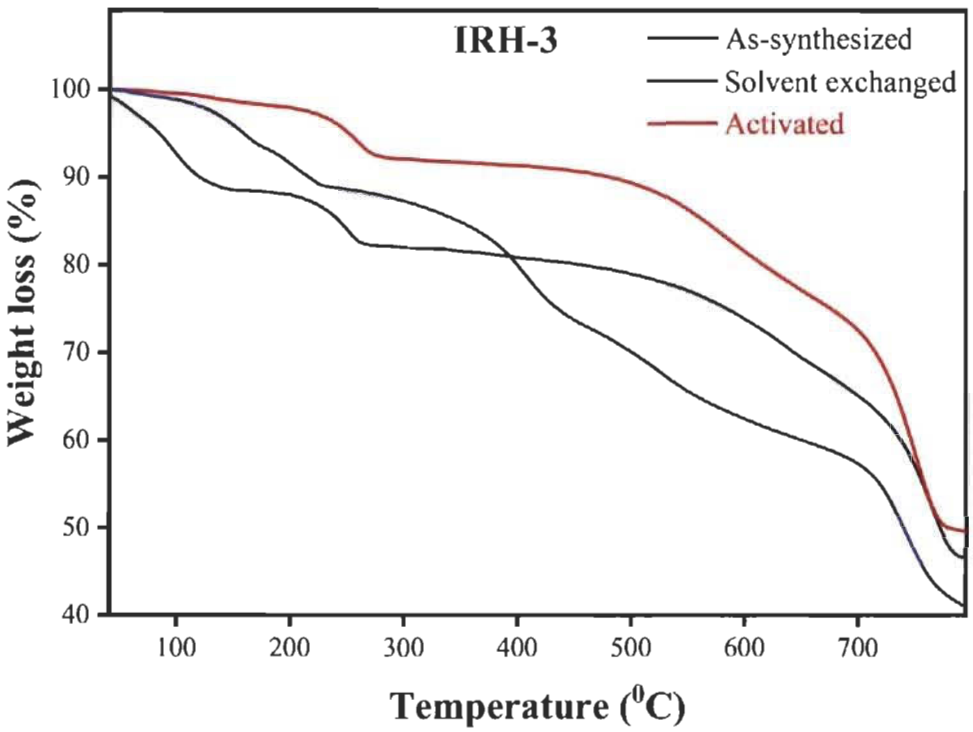

Figure S12. Thermogravimetric analysis curve of IRH-**3** as-synthesized, solvent exchange and activated.

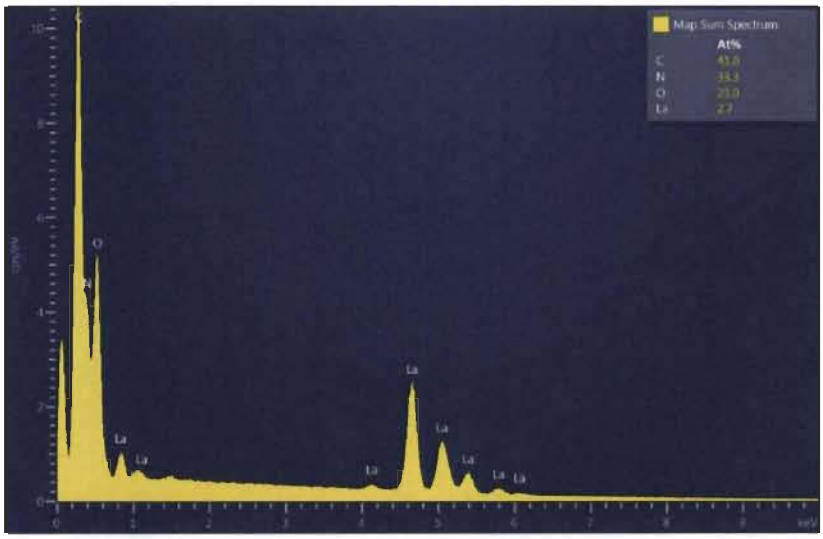

Figure S13. Energy Dispersive X-ray Spectra analysis of IRH-**1**.

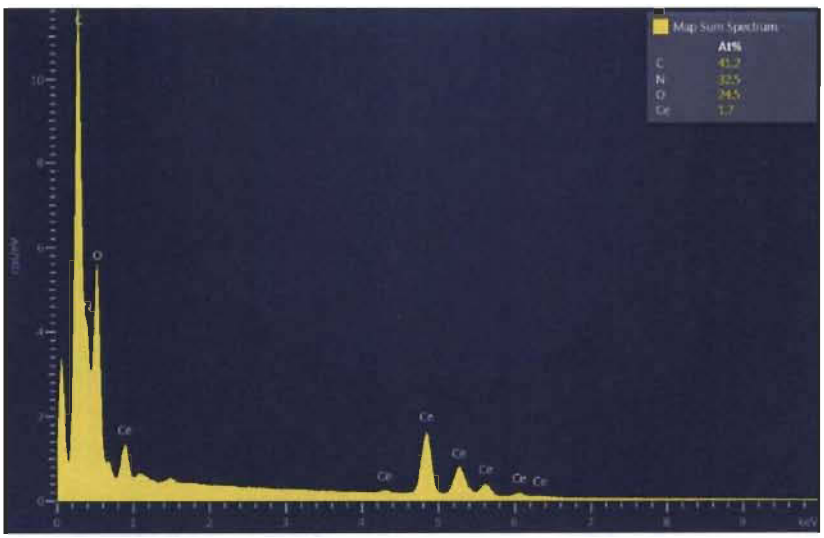

Figure S14. Energy Dispersive X-ray Spectra analysis of IRH-**2**.

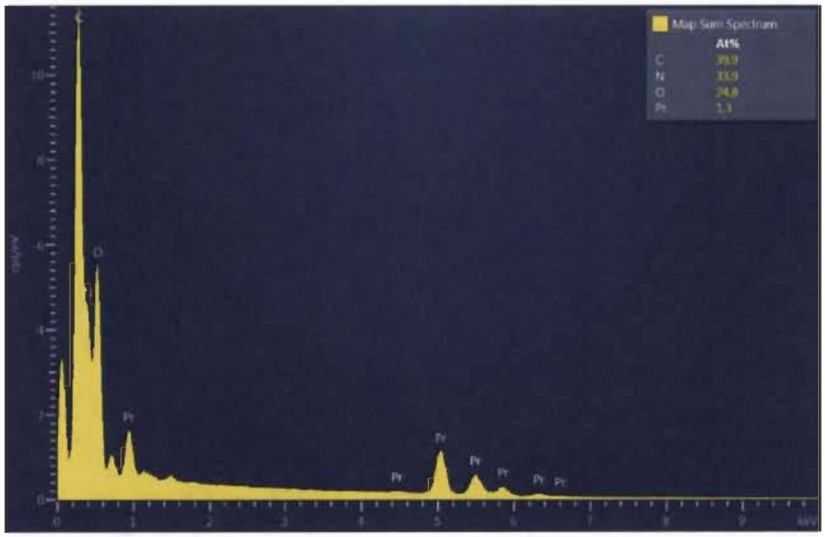

Figure S15. Energy Dispersive X-ray Spectra analysis of IRH-**3**.

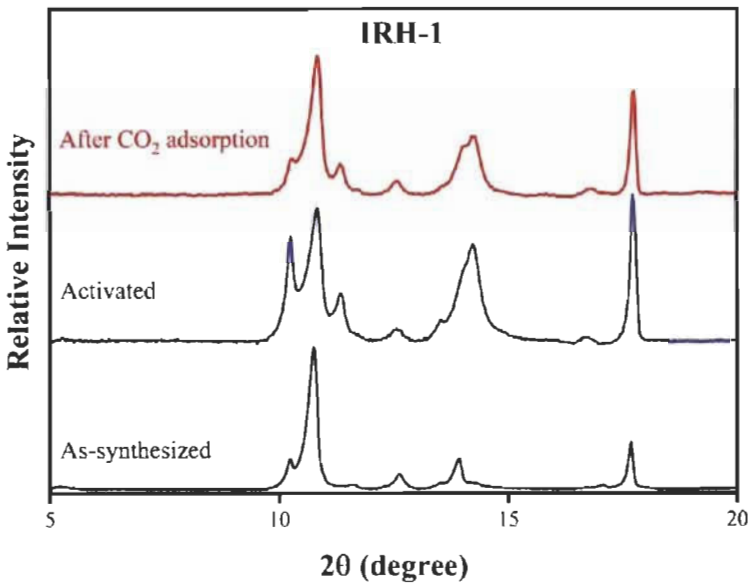

Figure S16. PXRD patterns of **IRH-1** as-synthesized, activated and after CO_2 adsorption.

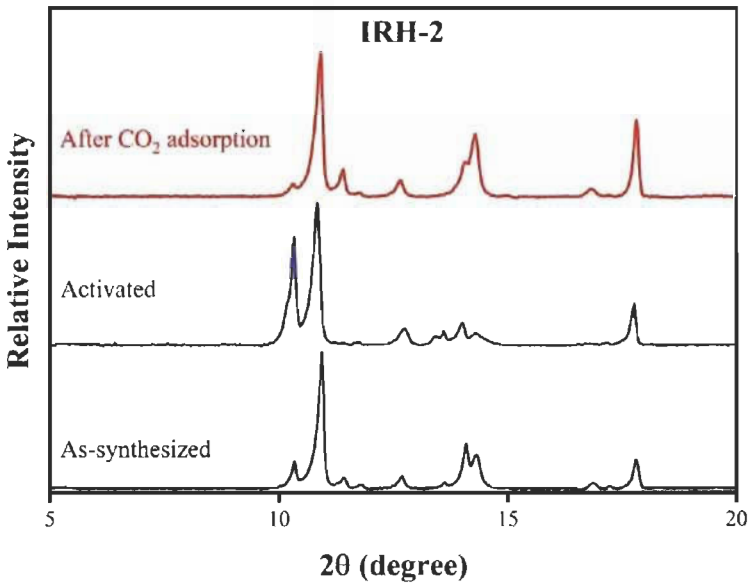

Figure S17. PXRD patterns of **IRH-2** as-synthesized, activated and after CO_2 adsorption.

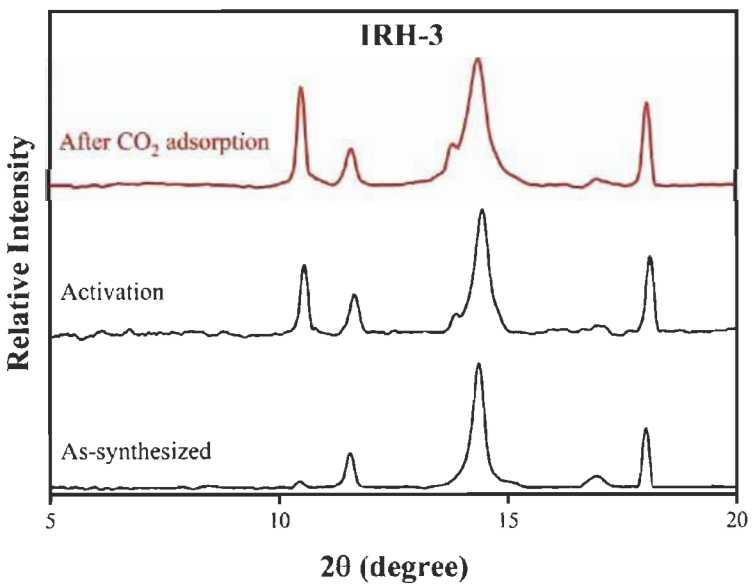

Figure S18. PXRD patterns of **IRH-3** as-synthesized, activated and simulated.

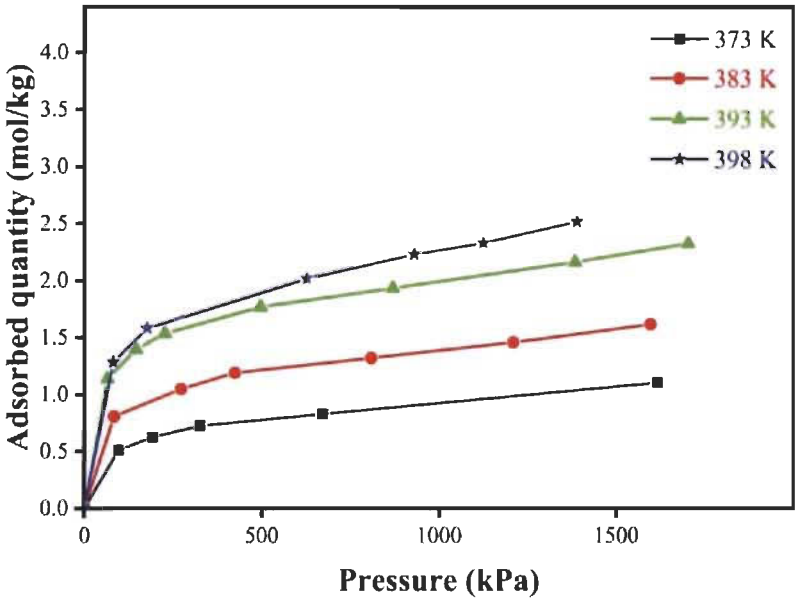

Figure S19. Effect of activation temperature on the adsorption of CO_2 on IRH-**1** at 373 K (black), 383 K (red), 393 K (green) and 398 K (blue).

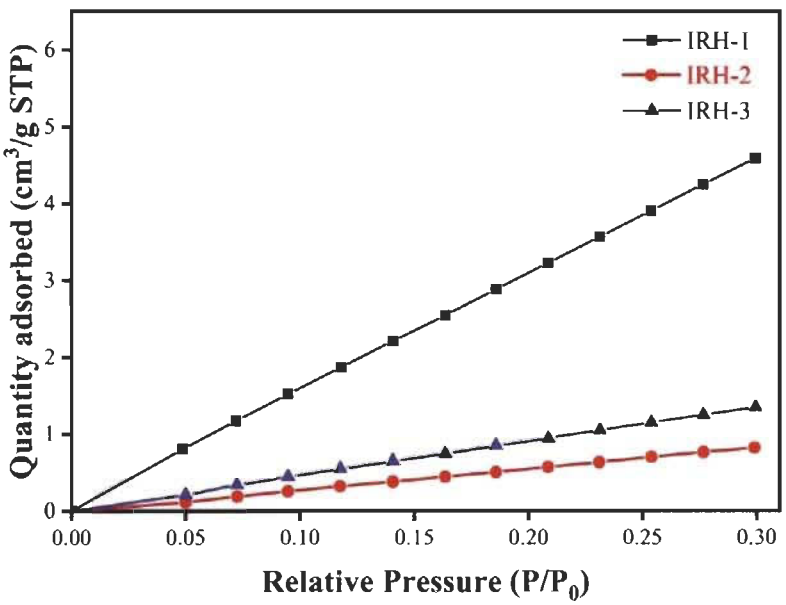

Figure S20. Ar sorption isotherm for IRHs-(**1**-**3**) at 87 K.

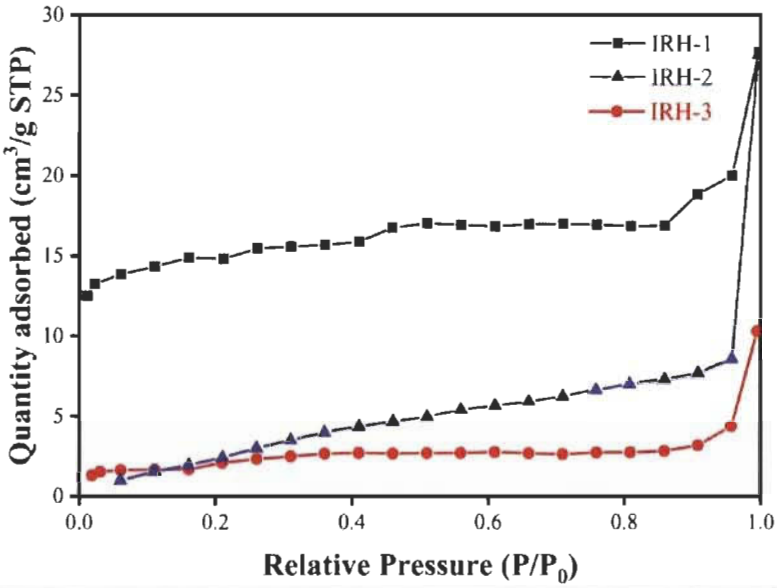

Figure S21. N_2 sorption isotherm for IRHs-(**1-3**) at 77 K.

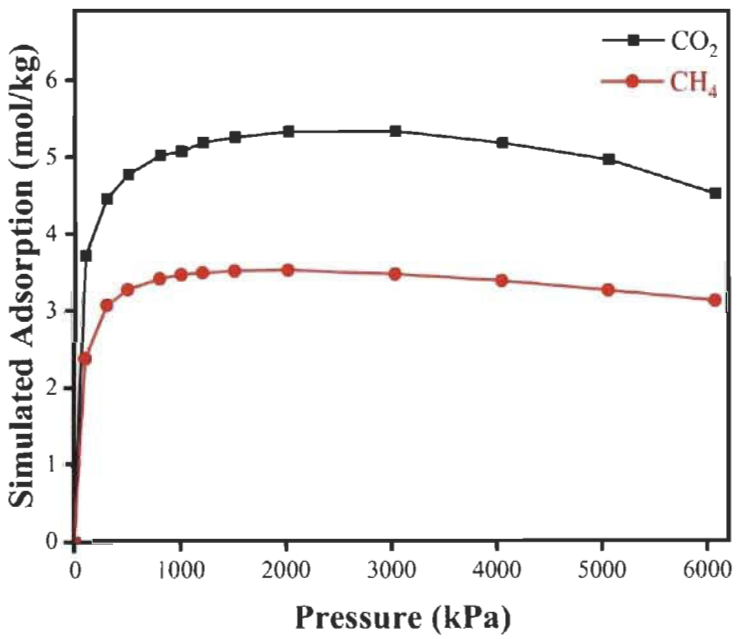

Figure S22. Simulated adsorption isotherms of CO_2 and CH_4 for IRH-**3** at 297 K.

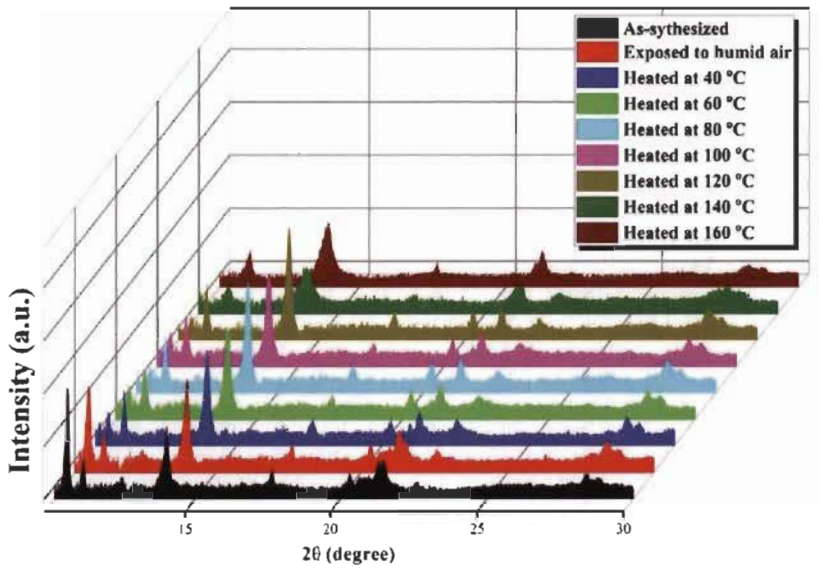

Figure S23. PXRD plots for analyzing the stability of IRH-**3** by heating at various temperature and exposing in humid air.

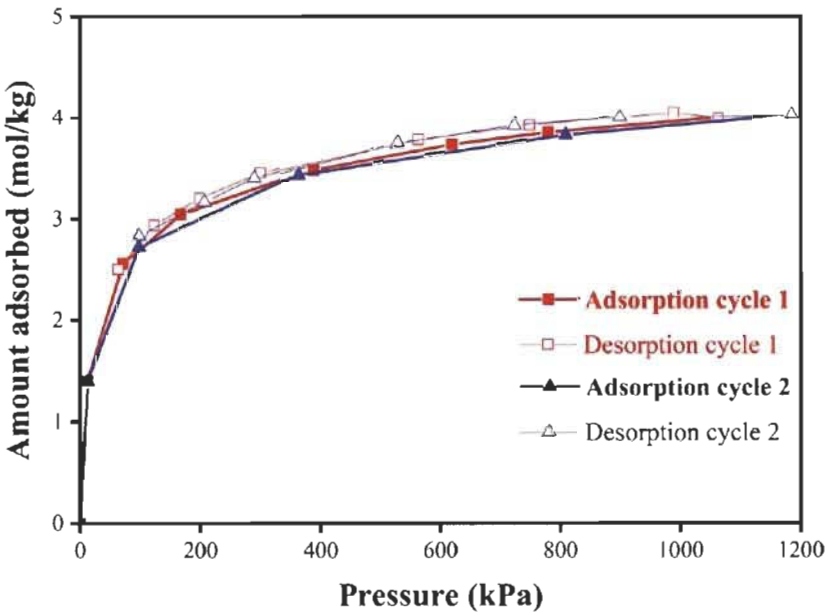

Figure S24. Adsorption and desorption cycles of CO_2 on IRH-**3** at 298 K.

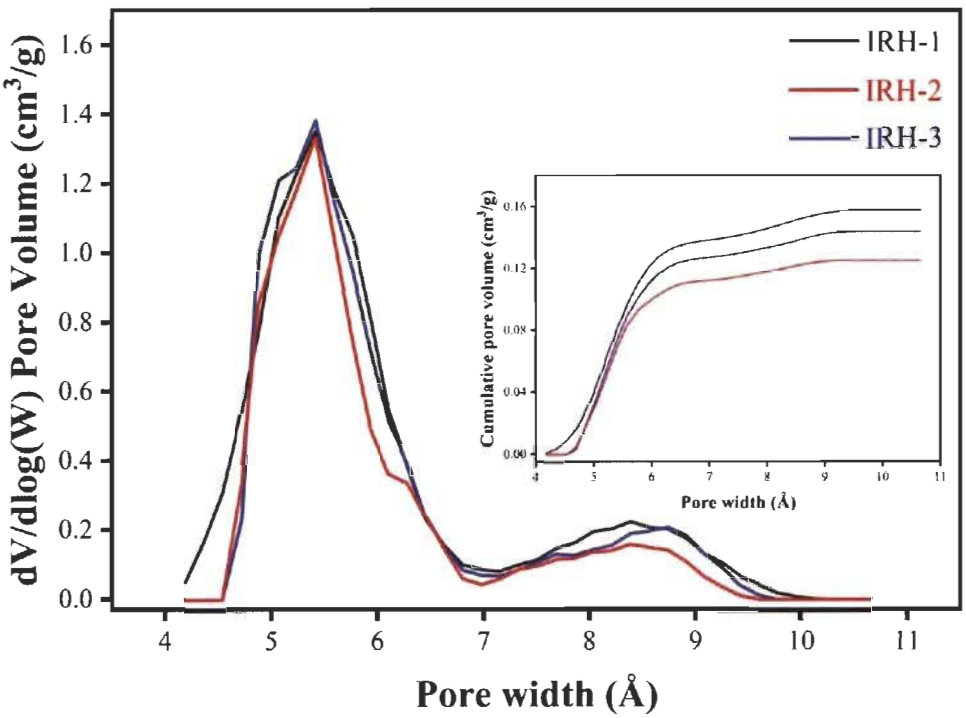

Figure S25. Pore size distribution curve for IHRs-(**1-3**). Inset image depicting raw data of cumulative pore volume against pore width.